ETH Diss. No 18374

Electrostatically Actuated All-Polymer Microbeam Resonators - Characterization and Application

Dissertation submitted to

ETH ZURICH

for the degree of

Doctor of Sciences

presented by

SILVAN SCHMID

Dipl. Ing. ETH, ETH Zurich

born 17.03.1977

citizen of Switzerland

accepted on the recommendation of

Prof. C. Hierold, examiner

Prof. A. Hierlemann, co-examiner

2009

"The most exciting phrase to hear in science, the one that heralds new discoveries, is not 'Eureka!' (I found it!) but 'That's funny ...' "

Isaac Asimov

US science fiction novelist & scholar (1920 - 1992)

Abstract

With recent advances in polymer science, the ability to customize the physical properties of polymers have pushed the application of these materials beyond simple processing layers and onto the center stage as active device materials in microelectromechanical systems, e.g. as soft hinges in micromirrors or as sensitive layers in chemical or biosensors. In this work, electrostatically actuated all-polymer resonant microbeams are mechanically characterized and applied as biosensors.

In order to actuate microstructures made from pure nonconductive polymers, a novel electrostatic actuation principle based on the Kelvin polarization force is developed. Single and double-clamped microbeams made from SU-8 which are actuated therewith are fabricated with a sacrificial layer technique. The samples are characterized by means of the resonant method.

The beamlike single-clamped microbeams are mainly damped by the internal material damping whereas the stringlike double-clamped microbeams are mainly damped by clamping loss. At atmospheric pressure, at low frequencies, the damping is dominated by air damping and at higher frequencies by the intrinsic damping.

Eventhough SU-8 is a highly crosslinked polymer, it shows a typical viscoelastic behavior. The mean Young's modulus is increasing from 4.54 GPa at 19 kHz to 5.24 GPa at 318 kHz. The modulus is linearly decreasing with temperature by -0.31 $\pm$0.01 %/ °C. Antiplasticization followed by a plasticization for low and high relative humidity values, respectively, were observed. The material also showed some significant aging of several percent in one month. The tensile stress in the double-clamped microbeams is changing with temperature (α_{th} = 47.9 $\pm$3.9 ppm/K) and humidity (α_{hyg} = 25.3 $\pm$1.0 ppm/%RH). The relaxation was measured over a period of 250 days. The tensile stress follows an exponential decay with a relaxation time of 114 days.

To demonstrate a potential application of polymer microresonators, the selective adsorption of streptavidin molecules on the biotinylated SU-8 microbeam surface in water was detected by measuring a shift in the self-excited oscillation frequency. A minimal concentration of 25 ng/ml of streptavidin was detected in 10–30 seconds. A main advantage of a resonant polymer microbeam biosensor is the possibility to directly adsorb the receptor biomolecules on the polymer without the need of an additional functional coating.

Zusammenfassung

Die Entwicklung von Polymeren mit vielfältigen physikalischen Eigenschaften hat das Anwendungsfeld dieser Materialien verändert von einfachen Prozess-Schichten hin zum aktiven mechanischen Bauteil in mikro-elektromechanischen Systemen. In dieser Arbeit werden elektrostatisch angeregte polymere Mikro-Schwingbalken mechanisch charakterisiert und als Biosensoren verwendet.

Um pure polymere Mikro-Strukturen zum Schwingen anzuregen wurde ein neues Aktuatorprinzip entwickelt welches auf der elektrostatischen Kelvin Polarisationskraft beruht. Einfach und doppelt eingespannte Mikro-Balken aus SU-8 wurden durch einen Opferschicht-Prozess hergestellt. Die mechanische Charakterisierung basiert auf der Resonanz-Methode.

Die balkenartigen einfach eingespannten Mikrobalken werden hauptsächlich durch die interne Materialdämpfung gedämpft und die saitenartigen doppelt eingespannten Mikrobalken hingegen durch Verluste über die Einspannungen. Bei atmosphären Druck und tiefen Frequenzen wird die Dämpfung durch die Luftdämpfung dominiert und bei hohen Frequenzen durch die intrinsische Dämpfung.

Trotz der starken Vernetzung zeigt SU-8 ein typische viskoelastisches Verhalten. Der mittlere E-Modul steigt von 4.54 GPa bei 19 kHz bis auf 5.24 GPa bei 318 kHz. Der E-Modul nimmt linear mit steigender Temperatur ab ($\alpha_{Y,T}$ = -0.31 $\pm$0.01 %/ °C). Antiplastifizierung gefolgt von einer Plastifizierung wurde beobachtet bei niedrigen beziehungsweise hohen relativen Luftfeuchtigkeits Werten. Das Material zeigte eine signifikante Alterung von mehreren Prozent in einem Monat. Die Zugspannung in den doppelt eingespannten Mikrobalken änderte sich mit der Temperatur (α_{th} = 47.9 $\pm$3.9 ppm/K) und der relativen Luftfeuchtigkeit (α_{hyg} = 25.3 $\pm$1.0 ppm/%RH). Die Relaxation der Zugspannung wurde über einen Zeitraum von 250 Tagen gemessen und folgt einer exponentiellen Abnahme mit einer Relaxationszeit von 114 Tagen.

Um eine mögliche Anwendung von polymeren Mikro-Resonatoren zu demonstrieren, wurde die selektive Adsorption von Streptavidin-Molekülen in Wasser auf der biotinylisierten SU-8 Oberfläche durch Messen der Schwing-Frequenz-Veränderung detektiert. Eine minimale Konzentration von 25 ng/ml Streptavidin wurde in 10 - 30 Sekunden detektiert. Ein wesentlicher Vorteil eines Biosenors aus polymeren Mikro-Schwinger ist die Möglichkeit die Rezeptor Biomoleküle direkt auf SU-8 zu adsorbieren ohne die Notwendigkeit einer zusätzlichen funktionellen Beschichtungen.

...

List of symbols

All parameters are given in SI units.

A	Cross section area
a_T	Shift factor in time-temperature equivalence
α_{hyg}	Coefcient of the humidity-induced volume expansion
α_m	Total sorption coefficient
α_{th}	Coefficient of thermal expansion
$\alpha_{Y,RH}$	Hygroscopic plasticizing coefcient
$\alpha_{Y,T}$	Coefcient of temperature induced change of the Youngs modulus
B	Oscillation amplitude
C	Capacitance
C_d	Capacitance in actuator material
C_{bias}	Bias capacitance
C_{ft}	Feedthrough capacitance
C_{fringe}	Capacitance of fringing field
C_g	Capacitance in the gap between actuator and electrodes
C_{g-d-g}	Capacitance in the parallel actuator where the dielectric slab is inserted
C_p	Parasitic capacitance
C_{ref}	Reference capacitance
C_{res}	Capacitance of resonators in the equivalent LCR circuit
C_{SA}	Streptavidin concentration
c	Coefficient of damping force
c_a	Amplitude variable
c_d	Factor representing the field reduction inside the dielectric material
c_p	Heat capacity
c_{wave}	Wave velocity
γ	Reduced time in time-temperature equivalence
Γ	Hydrodynamic function
d_0	Distance between beam and substrate
$\mathrm{d}s$	Stretched infinitesimal piece of string
$\mathrm{d}x$	Infinitesimal piece of string
D	Diffusion coefficient
δ	Phase angle between the stress and strain

δ_S	Thickness of surface layer
$\mathbf{d}$	Distance vector
ε	Strain
ε_0	Permittivity of free space
ε_d	Relative permittivity of the actuator material
ε_g	Relative permittivity of the gap between actuator and electrodes
ε_{hyg}	Hygroscopic strain
ε_r	Relative permittivity
ε_{pre}	Pre-stress of a string
E	Electric field intensity
E_α	Activation energy
E_0	Initial electric field intensity
E_d	Electric field intensity inside the dielectric material
$\mathbf{E}$	Electric field (vector)
f	Frequency
f_0	Natural frequency
f_{res}	Resonant frequency
$f_{r,str}$	Resonant frequency of a string
f_{trans}	Transition frequency
$\mathbf{f}_{KPFn}$	Kelvin polarization force density (vector)
f_{KPFn}	Kelvin polarization force density
F	Force
F_0	Constant force
$\mathbf{F}$	Force (vector)
F_{el}	Electrostatic force
F_{f-u}	Force per voltage ratio of the electrostatic actuation
F_{KPFn}	Kelvin polarization force normal towards the electrodes
F_{KPFp}	Kelvin polarization force parallel towards the electrodes
g	Gap distance between coplanar electrodes
G	Amplification factor
h	Beam thickness
h_d	Height of dielectric slab in parallel electrode design
h_g	Gap distance between dielectric slab and parallel electrodes
H	Transfer function of total system
H_{noRef}	Transfer function of the electronic circuit without the reference electrode
i	Imaginary number
I	Current
I_{out}	Output current

j	Integer
I_z	Geometric moment of inertia
$J_Y(t)$	Creep compliance
k	Spring constant
k_{beam}	Effective spring constant of a cantilever beam
κ	Thermal conductivity
L	Beam length
L_e	Effective beam length
L_g	Length of capacitor part which is unfilled
L_d	Length of capacitor part which is filled with the dielectric slab
L_p	Peripheral length
L_{res}	Inductance of resonators in the equivalent LCR circuit
λ_n	Solution of frequency equation
λ_j	Weighting coefficient
m	Mass
m_{eff}	Effective mass
M	Moisture content
M_m	Molar mass of gas
M_t	Total amount of moisture which has entered a plane sheet at time t
M_∞	Total amount of moisture which has entered a plane sheet after infinite time
μ	Viscosity
n	Mode number
n_c	Coefficient of damping
N	Number
N_p	Number of dipoles per unit volume
ν	Poisson ratio
ω	Angular frequency
ω_0	Angular natural frequency
ω_{osc}	Angular oscillation frequency of self-excitation
ω_r	Angular resonant frequency
p	Gas pressure
P_s	Saturated water vapor pressure
P_w	Water vapor pressure
π	Pi
$\mathbf{p}$	Dipole moment (vector)
$\mathbf{P}$	Macroscopic polarization (vector)
φ	Phase lag
φ_{osc}	Phase lag of self-excited oscillation

φ_r	Phase lag at resonance
q	Single charge
Q	Quality factor
Q_{air}	Quality factor due to air damping
Q_{clamp}	Quality factor due to clamping loss
Q_e	Charge
Q_{elong}	Quality factor due to elongational damping
Q_{flex}	Quality factor due to flexural damping
Q_{inter}	Quality factor due to internal damping
$Q_{intrinsic}$	Quality factor due to intrinsic damping
Q_{liq}	Quality factor in liquid
Q_{mat}	Quality factor due to material damping
$Q_{molecular}$	Quality factor due to air damping in the molecular pressure regime
$Q_{surface}$	Quality factor due to surface loss
Q_{str}	Quality factor of a string at atmospheric pressure
Q_{TED}	Quality factor due to thermoelastic damping
$Q_{viscous}$	Quality factor due to air dampign in the viscous regime
r	Radius
R	Coefficient of determination of a fit
R_f	Feedback resistance
R_{gas}	Universal gas constant
R_{res}	Resistance of resonators in the equivalent LCR circuit
R_{u-v}	Voltage per velocity ratio given by the decoder of the laser-Doppler vibrometer
RH	Relative humidity
ρ	Mass density
ρ_{liq}	Mass density of liquid
s	Complex frequency variable
S	Tension force
T	Temperature
T_0	Initial temperature
T_g	Glass transition temperature
T_{sta}	Thermal stability
t	Time
τ_r	Relaxation time
τ_ζ	Thermal relaxation time
σ	Stress
σ_s	Tensile strength
σ_{pre}	Pre-stress of a string

$u(t)$	Driving signal
U	Electric potential
U_{AC}	Sinusoidal driving voltage
U_{DC}	Bias voltage added to driving voltage
U_{in}	Input voltage
U_{out}	Output current
V	Volume
W	Energy
w	Beam width
w_p	Beam width in parallel actuator design
w_e	Energy density
w_n	Deflection of a string
W_e	Electrical energy
W_{elong}	Extensional energy
W_{flex}	Flexural energy
W_{pot}	Potential energy
x	Cartesian coordinate
ξ	Path
ξ_{TED}	Dimensionless variable in the TED theory
Y	Young's modulus
Y_0	Initial Young's modulus
$Y(t)$	Relaxation modulus
$Y^*(\omega)$	Complex Young's modulus
$Y'(\omega)$	Storage Young's modulus
$Y''(\omega)$	Loss Young's modulus
$Y''_S(\omega)$	Loss Young's modulus of surface layer
y	Cartesian coordinate
z	Cartesian coordinate
z_0	Amplitude of oscillation of a string
Z_f	Impedance of the transimpedance amplier
Z_{res}	Impedance of resonator
ζ	Damping ratio of the system

Contents

1 Introduction

Predominantly silicon-based materials, but also glass, ceramics, and metals have been applied in MEMS with great success [1] during the last two decades. However, it is not clear if they are always the best choice for a specific application. Particularly their high modulus hampers the development of specific MEMS devices which involve comparatively large displacements of mechanically active parts [2–4]. Obviously the application of soft materials with lower modulus would be the preferred choice if great flexibility is a prerequisite for the functionality of a mechanically active microstructure [5]. Thus, organic polymers are potential candidates for such applications, since they are available with tailored moduli within the range of less than 1 MPa up to several GPa [6]. For example, the modulus of chemically cross-linked elastomers can be tuned over one or even more orders of magnitude by controlling the amount of cross-linkings between the polymer chains [7].

On a research level, numerous examples of MEMS exist which benefit from the great flexibility of these soft materials. In particular polymer actuators, e.g. for biomedical applications like cell manipulation [4,8,9], mimicking of muscle-like movements [10,11], or for large movements of micro-valves in micro-fluidic systems [2,12, 13], have attracted great attention in recent years. Complementary, polymers have also been used successfully as MEMS sensing material for deflecting cantilevers for chemical [14] or biosensing [15, 16] and stress sensing applications [17, 18], for auditory prostheses [19], or for soft probes in scanning force microscopy [20]. Respecting polymer actuators, they usually make use of special electrical, magnetic, thermal, or electrochemical properties of certain functional polymers, e.g. polypyrrole [11,21–24], polyaniline [8,24–26], or high performance epoxys [4,9,13]. Thus, the general benefit from polymer materials offered by their exceptional variety of properties has not yet been used to full capacity due to the restriction to a rather small class of highly functional materials. For example, technologies which would allow for the actuation of polymers with only poor electrical or magnetic properties, such as low-cost thermoplastics, are still lacking.

Beside the quasistatic applications of polymers in MEMS, polymers have also been used as structural material for dynamic devices. Soft polymeric hinges for resonant silicon structures [27] such as resonant micromirrors with polymeric hinges [28] have been designed and successfully applied. Polymer microbeam resonators have been

built and actuated by electrostatic forces [29]. These devices show the feasibility to fabricate and operate microresonators made of polymer materials. Tamayo et al. have studied the effect of adsorbates on the stiffness of microbeam resonators [30]. They found that the softness of polymer microresonators make them two orders of magnitude more sensitive to the stiffness of the adsorbed film than silicon cantilevers. This effect potentiates the application of polymer microresonators as highly sensitive chemical or biochemical sensors. So far, polymers have played a key role in chemical resonant sensors based on high Q silicon cantilevers which are covered with a functional polymer layer [31].

Mechanical testing of micro-scaled specimens can be performed on test structures which are either integrated with the active mechanical devices or non-integrated. The motivation for integrated testing is to obtain a measure of mechanical properties from test structures that are on the same chip or wafer as the manufactured MEMS. This is very attractive for process monitoring and control as it allows for inspection of wafers between process steps. Another reason is the fact, that it is essentially impossible to handle components with dimensions in the micrometer regime and that most MEMS materials are unavailable in standard form. Electrostatically actuated single and double-clamped silicon microbeams are well suited to evaluate material properties such as the Young's modulus and residual stress by static deflection measurements [32, 33] or by vibration measurements [34]. Dynamic mechanical properties, damping effects in particular, have been thoroughly examined using resonating silicon micro-cantilever beams [35–37]. Micro-fabrication processes can alter the mechanical properties significantly [38, 39], particularly for polymer materials [40]. Furthermore, for the application of polymer microresonators at ambient atmosphere, the influence of the air damping and the humidity on the resonance behavior are of interest. Water is known to diffuse into polymer materials thereby changing the material properties [41].

Because the material properties of polymers are expected to be very different compared to stiff and brittle silicon based crystalline materials, further research is needed in order to quantify the potential benefits and limitations of polymer based materials for microsystem actuators. Because of the high actuation frequency of micro structures a potential exists for a detailed study of polymer viscoelasticity at small length and time scales that cannot be performed using bulk testing techniques. The dependence of properties like elastic stiffness on the rate of applied stress is widely known by polymer researchers. Macroscopic polymer samples can be characterized by forced vibration non-resonance methods at frequencies up to approximately 100 Hz. This method is often called dynamic mechanical analysis (DMA). DMA allows the determination of the viscoelastic behavior as a function of frequency and

temperature. The most simple and most accurate method which allows the characterization of macroscopic samples at frequencies up to approximately 10 kHz is the resonance method [42]. With polymer microresonators, the frequency range of the mechanical characterization can be expanded to frequencies of up to approximately 10 MHz [29] by means of the resonance method.

Besides the material properties, the micro-machining capabilities are of similar importance for the effective implementation of a certain material into MEMS. Meanwhile great advances have been made in soft lithographic technologies for polymers, which make either use of their low softening temperature or their sensitivity to radiation [43, 44]. In particular photosensitive polymers like SU-8 have attracted great attention for the fabrication of micro-structures with high aspect ratios [45]. Further, "hot"-embossing has turned out to be a well suited tool for micro and nanostructuring of those polymers, which soften above a certain processing temperature [46–49], so called thermoplastics. But a standard fabrication process for an integrated fabrication of polymer microresonators by means of surface micromachining is still missing.

In summary, the promising evaluation of polymers according to the crucial criteria for a proper material selection, i.e. material properties, micro-processability and cost-efficiency, encourages a more comprehensive exploration of these soft materials for future MEMS applications.

1.1 Objective and outline of this work

The objective of this work is to develop fabrication and actuation techniques for electrostatic polymer microactuators. With it, the influence of frequency, temperature, time, and relative humidity on the resonance behavior of polymer microbeams is evaluated. To show a potential application, the microactuators are used to detect biomolecules in aqueous solution.

The thesis is subdivided into two parts, a part presenting the characterization of the polymer microbeams and a part presenting the chapters which are important for the application of polymer microbeams for the detectino of biomolecules.

In chapter 2, a method is developed which is based on the *Kelvin polarization force*, a dielectric force, which allows for the direct actuation of non-metalized, dielectric polymer microstructures which thus do not need any connection to the electronic circuit.

In chapter 3, two fabrication techniques based on a polymer sacrificial layer, which allow for the fabrication of SU-8 microstructures actuated by the *Kelvin polarization force*, are presented. All the subsequent measurements are performed with samples made with one of the two processes.

In chapter 4, the main mechanical models are presented which are needed to analytically describe the dynamic mechanical behavior of beams and strings.

In chapter 5, the experimental setup and approach are explained.

In chapter 6, the damping mechanisms of the single-clamped and the prestressed double-clamped microbeams are studied in high vacuum and at atmospheric pressure.

In chapter 7, the SU-8 electrostatically actuated resonant microbeams are mechanically characterized for varying resonant frequencies and different temperatures. The parameters that are evaluated are the storage Young's modulus by means of the single-clamped microbeams and the intrinsic stress in double-clamped beams.

In chapter 8, the influence of the relative humidity on the resonant behavior on the SU-8 microresonators is investigated.

In chapter 9, the application of Q-enhancement and self-excitation by means of a positive feedback-loop with the polymer microresonators is studied. The self-excitation technique allows the detection of the resonant frequency and its variation in gaseous and aqueous environment, enabling the application of polymer microresonators as chemical or biosensors.

In chapter 10, the SU-8 microbeam resonators are used for the detection of streptavidin molecules in aqueous solution. The actuation of the polymer microbeams is done by means of the before introduced self-excitation technique.

In chapter 11, the electronic readout by means of a transimpedance amplifier of the presented all-polymer microresonators is presented clearing the way for a future applications as chemical or biosensors.

In chapter 12, conclusions are drawn and an outlook for future projects is given.

2 Dielectric force actuation scheme

Microscaled polymer actuators are usually restricted to a rather small group of polymers with special intrinsic properties allowing for direct electrostatic [29], electrochemical [23, 24, 50], or thermal actuation [4]. In contrast, the majority of polymers are not well suited for direct actuation, but rather for indirect actuation, e.g. by actuation of a functional layer attached to the polymer structure [51, 52]. However, besides the more complex fabrication process, degradation of the adhesion of the functional layer at high actuation cycles must be expected [53]. In this chapter, a method is presented which is based on the *Kelvin polarization force* (KPF), a dielectrophoretic force, which allows for the *direct* actuation of non-metalized, dielectric polymer microstructures which thus do not need any connection to the electronic circuit.

2.1 Electrostatic forces on macroscopic media

[1] Considering an electroquasistatic system with only one mechanical degree of freedom ξ, only one electrical terminal pair with constant potential U and the assumption that there is no dissipation of energy, the electrical energy input $U\mathrm{d}Q_e$ to the system must either result in a change in the electrical energy stored $\mathrm{d}W_e$ or mechanical energy expended $F\mathrm{d}\xi$. Thus we write the statement of energy conservation [54]

$$U\mathrm{d}Q_e = \mathrm{d}W_e + F\mathrm{d}\xi \tag{2.1}$$

where Q_e is the net charge on the electrical terminal. Here, $F(Q, \xi)$ is the as yet unknown force. Solved for $\mathrm{d}W_e$, this energy conservation statement is

$$\mathrm{d}W_e(Q_e, \xi) = U\mathrm{d}Q_e - F\mathrm{d}\xi \tag{2.2}$$

The incremental change in $W_e(Q_e, \xi)$ associated with incremental changes of $\mathrm{d}Q_e$ and $\mathrm{d}\xi$ in the independent variables is (total derivative)

$$\mathrm{d}W_e = \frac{\partial W_e}{\partial Q_e}\mathrm{d}Q_e + \frac{\partial W_e}{\partial \xi}\mathrm{d}\xi \tag{2.3}$$

Because Q_e and ξ can be independently specified, (2.2) and (2.3) must hold for any combination of $\mathrm{d}Q_e$ and $\mathrm{d}\xi$, and so it follows that the coefficients of $\mathrm{d}Q_e$ in (2.2) and

[1] The presented theory in this section is mainly based on [54] chapter 11.6.

(2.3) must be equal to each other, as must be the coefficients of $\mathrm{d}\xi$.

$$U = \frac{\partial}{\partial Q_e} W_e(Q_e, \xi) \qquad F = -\frac{\partial}{\partial \xi} W_e(Q_e, \xi) \tag{2.4}$$

For a given total stored energy, defined in terms of the independent variables Q and ξ, the second of these relations provides the desired force.

The electrical energy W_e can be derived by integration of the energy density w_e

$$w_e = \frac{1}{2}\varepsilon_r \varepsilon_0 E^2 \tag{2.5}$$

over the volume V of the system.

Another expression for the electrical energy is given by the capacitance of the system

$$W_e = \frac{1}{2}\frac{Q_e^2}{C} \tag{2.6}$$

where the capacitance C is defined as

$$C(\xi) = \frac{Q_e}{U}. \tag{2.7}$$

The desired force is obtained by substituting (2.6) into the second term of (2.4).

$$F = -\frac{1}{2}Q_e^2 \frac{\mathrm{d}C^{-1}}{\mathrm{d}\xi} = -\frac{1}{2}Q_e^2 \left(-\frac{1}{C^2}\frac{\mathrm{d}C}{\mathrm{d}\xi}\right) \tag{2.8}$$

By using the definition of the capacitance (2.7), the force can be written in terms of the voltage U.

$$F = \frac{1}{2}U^2 \frac{\mathrm{d}C}{\mathrm{d}\xi} \tag{2.9}$$

2.2 The Kelvin polarization force density

To derive a model for the electrostatic dielectric force exerting on dielectric materials, the net force on a small physical dipole is estimated. A dipole of opposite charges $+q$ and $-q$ spaced a distance $\mathbf{d}$ apart, is located in an electric field with the field $\mathbf{E}$. A schematic drawing of the dipole is depicted in Fig. 2.1. We assume that the contribution of the dipole to the electric field is zero. In an inhomogeneous electric field, the two charges will experience a different field vector and the dipole will experience a net force $\mathbf{F}$. Thus, the sum of the two forces acting on the dipole is [55]

$$\mathbf{F} = q\mathbf{E}(\mathbf{r} + \mathbf{d}) - q\mathbf{E}(\mathbf{r}) \tag{2.10}$$

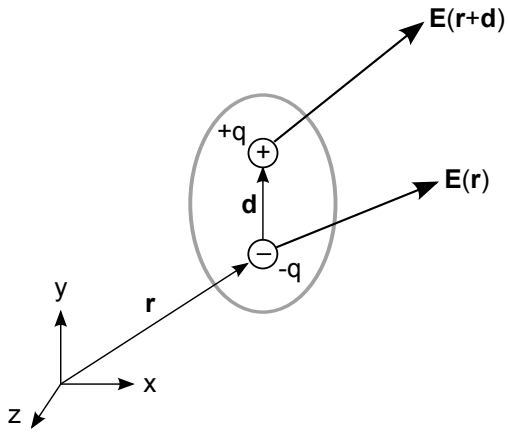

Figure 2.1: The nonuniform electric field exerted upon a small dipole of strength $\mathbf{p} \equiv q\mathbf{d}$. Image adapted from [55].

where $\mathbf{r}$ is the vector to the negative charge $-q$. Assuming that the distance $|\mathbf{d}|$ is small compared to the characteristic dimension of the field nonuniformity, the electric field at the positive charge $+q$ can be simplified by a Taylor series expansion, that is

$$\mathbf{E}(\mathbf{r}+\mathbf{d}) \approx \mathbf{E}(\mathbf{r}) + \mathbf{d} \cdot \nabla \mathbf{E}(\mathbf{r}) \tag{2.11}$$

thereby neglecting all terms of order two or higher. Using (2.11) with (2.10), the force on an infinitesimal dipole ($|\mathbf{d}| \to 0$) becomes [55]

$$\mathbf{F} = q\mathbf{d} \cdot \nabla \mathbf{E} = \mathbf{p} \cdot \nabla \mathbf{E} \tag{2.12}$$

where $\mathbf{p}$ is the dipole moment. Equation (2.12) teaches that an electric field has to be inhomogeneous in order to exert a net force on a dipole.

Infinitesimal dipoles situated in an electric field experience a force that they pass on to the medium as a whole. For a medium with one particle type only, so called *Kelvin polarization force density* [54] is

$$\mathbf{f}_{KPF} = \mathbf{P} \cdot \nabla \mathbf{E} \tag{2.13}$$

with the macroscopic polarization

$$\mathbf{P} = N_p \mathbf{p} \tag{2.14}$$

where N_p is the number of dipoles per unit volume and $\mathbf{p}$ is the polarization of the individual dipoles.

With the polarization of a linear dielectric material

$$\mathbf{P} = \varepsilon_0(\varepsilon_r - 1)\mathbf{E} \tag{2.15}$$

the KPF density can be written as [54]

$$\mathbf{f}_{KPF} = \frac{1}{2}\varepsilon_0(\varepsilon_r - 1)\nabla(\mathbf{E} \cdot \mathbf{E}) \tag{2.16}$$

Equation 2.16 depicts that in order to create a force acting on a dielectric material, an inhomogeneous electric field is required where the *Kelvin polarization force* (KPF) acts towards the field gradient. The strength of the KPF depends on the polarizability and the volume of the attracted medium and the field intensity squared.

The *Kelvin polarization force* is defined by the bulk material properties of the involved dielectrics. In an aqueous environment, charges, bound ions (Stern layer), and a diffuse double layer create electric shells at the interface between the polymer and the water [56]. These surface layers have a distinct dielectric behavior which is important in dielectrophoresis, but are not taken into account in this work. The introduction of foreign particles or bio-molecules into the water can change its permittivity [57]. A change in the polarizability of the surrounding medium results in a change of the driving force which consequently changes the oscillation amplitude of the microresonator. In order to actuate by means of the KPF in water, the aqueous medium has to be dielectric. Furthermore, if the ion concentration is too high and the aqueous solution becomes conductive, the electric field in the the water becomes zero and the Kelvin polarization force diminishes.

2.3 Actuator designs

There are two principle designs with which a micro actuator based on the *Kelvin polarization force* can be realized. The electrode configuration can be parallel or coplanar and the force on the dielectric is directed parallel (KPFp) to the electrodes or normal (KPFn) to the electrodes, respectively. The two designs are schematically shown in Fig. 2.2. The parallel plate capacitor design (Fig. 2.2a) needs a demanding fabrication process. In order to get such a sandwich structure, a bonding process is needed. But the parallel design has the advantage that it is possible to develop an analytical model based on energy considerations without knowing the fringe fields at the edge of the capacitor plates. The design with the coplanar electrodes (Fig. 2.2b) has the advantage that it can be fabricated by means of surface micromachining. But finite element method simulations are needed for the exact calculation of the magnitude of the force.

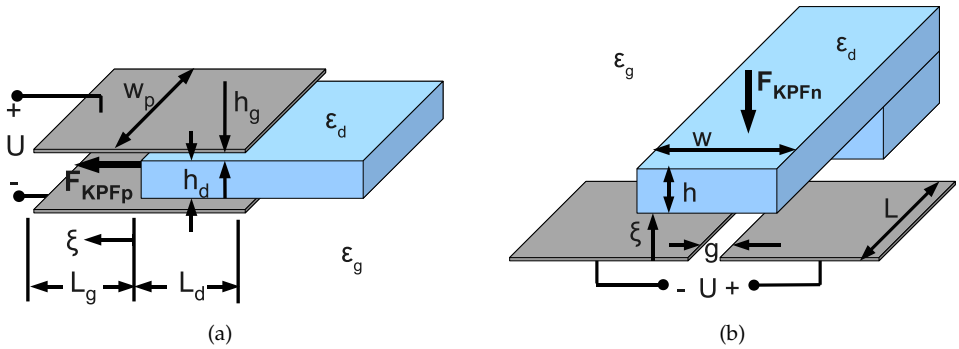

Figure 2.2: Actuation schemes (a) of a dielectric slab experiencing the *Kelvin polarization force* parallel (*KPFp*) in-between two capacitor plates and (b) of a dielectric beam experiencing the *Kelvin polarization force* normal (*KPFn*) towards the electrodes. Reprinted with permission from [58]. Copyright [2006], American Institute of Physics.

In section 2.3.1 an analytical expression for the KPF in the parallel design is developed. The force values calculated based on FEM simulations are then verified by a comparison with the analytical model. In section 2.3.2 a qualitative analytical model of the KPF is developed. The magnitude of the force is obtained by the FEM method that was validated before.

2.3.1 KPF acting parallel to electrodes (KPFp)

The Pellat's experiment has shown that a dielectric fluid rises against gravity in between two capacitor plates when a voltage is applied. The same effect can be used to design a polymer based micro actuator where a dielectric slab is pulled inside two electrode plates. A schematic of the KPFp design is shown in Fig. 2.2a.

In Fig. 2.3 it can be seen, that the electric field in the capacitor away from the edge is homogeneous. The capacitor with three dielectric layers (air gap - dielectric plate - air gap) can be modeled as three single serial capacitors with the capacitance in the gap of $C_g = \frac{\varepsilon_0 \varepsilon_g w_p L_g}{h_g}$ and the capacitance in the dielectric of $C_d = \frac{\varepsilon_0 \varepsilon_d w_p L_d}{h_d}$. The total capacitance where the dielectric plate is inserted thus is

$$C_{g-d-g} = \left(\frac{1}{C_g} + \frac{1}{C_d} + \frac{1}{C_g} \right)^{-1} = \frac{C_g C_d}{2C_d + C_g} = \frac{\varepsilon_0 w_p L_d \varepsilon_g \varepsilon_d}{2\varepsilon_d h_g + \varepsilon_g h_d}. \tag{2.17}$$

Provided that the dielectric slab is very long compared to the electrode distance and that it is located well in between the capacitor plates away from the fringing fields

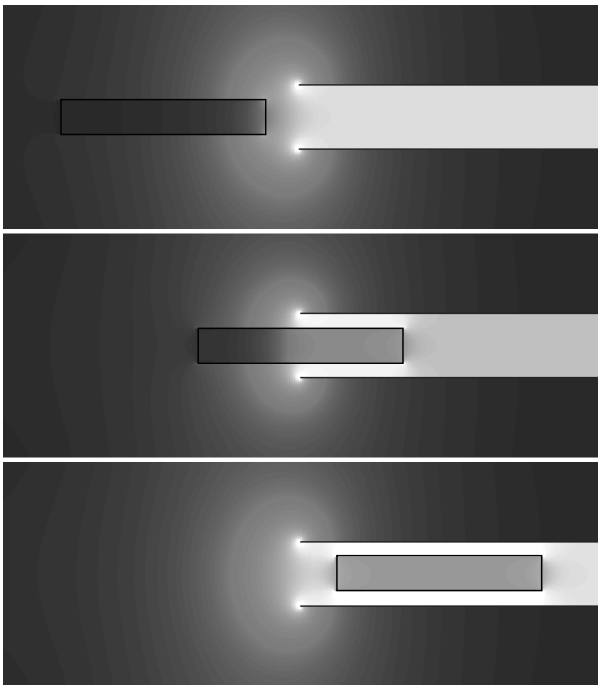

Figure 2.3: Electric field of the KPFp design simulated with FEM. The force is approximately zero for the case when the dielectric slab is fully outside or fully inside of the capacitor plates. When the slab is placed in the region of the electric fringe field at the edge of the capacitor plates it experiences a force pulling it inside the capacitor.

at the edges of the electrodes, the fringing field is assumed to stay unchanged for a changing overlapping distance ξ. Consequently, the capacitance due to the fringing field C_{fringe} remains constant too. The capacitance with respect to ξ then is

$$\begin{aligned} C(\xi) &= C_{g-d-g}(\xi) + C_g(\xi) + C_{fringe} \\ &= \frac{\varepsilon_0 w_p \varepsilon_g \varepsilon_d}{2\varepsilon_d h_g + \varepsilon_g h_d}(L_d + \xi) + \frac{\varepsilon_0 \varepsilon_g w_p}{h_g}(L_g - \xi) + C_{fringe} \end{aligned} \tag{2.18}$$

and the derivative becomes

$$\frac{\mathrm{d}C}{\mathrm{d}\xi} = \frac{w_p \varepsilon_0 \varepsilon_g \varepsilon_d}{2\varepsilon_d h_g + \varepsilon_g h_d} - \frac{w_p \varepsilon_0 \varepsilon_g}{2h_g + h_d}. \tag{2.19}$$

(2.19) deployed in (2.9), the force acting on the dielectric slab inbetween the parallel capacitor plates is

$$F_{KPFp}(h_g, h_d) = \frac{1}{2} U^2 \varepsilon_0 w_p \left(\frac{\varepsilon_d \varepsilon_g}{2h_g \varepsilon_d + h_d \varepsilon_g} - \frac{\varepsilon_g}{2h_g + h_d} \right). \tag{2.20}$$

Even though the physical origin of the acting force is confined to the fringing field at the edge of the electrodes, the force can be modeled as shown by assuming that it remains constant. Hence, the highly inhomogeneous fringing field does not need to be known. This theoretical setup was used to validate the applied FEM method. The simulated energy density was integrated over the entire area for discrete distances ξ. For the region where the dielectric slab overlaps the electrode edge, the field energy was linear with respect to ξ. The force was then obtained by means of (2.4). A comparison of the simulated F_{KPFp} with (2.20) is shown in Fig. 2.4. The forces determined by FEM coincide with the values from the analytical expression.

If the gap h_g is zero, (2.20) simplifies to the idealistic electric capillary force which can be found in literature [59]:

$$F_{KPFp}(0, h_d) = \frac{1}{2} \varepsilon_0 (\varepsilon_d - \varepsilon_g) \frac{w_p}{h_d} U^2 \tag{2.21}$$

In this equation, the influence of the dielectric constants of the materials on the direction of the force becomes obvious. In air or vacuum, with $\varepsilon_r \approx 1$, a dielectric material experiences a force pulling into the capacitor plates. In water, with a very high permittivity of $\varepsilon_r \approx 80$, most dielectric materials with a lower permittivity are pushed out of the capacitor plates.

2.3.2 KPF acting normal to electrodes (KPFn)

Another polymer actuator design based on the *Kelvin polarization force*, as shown in Fig. 2.2b, is the dielectric beam that is attracted towards the highest electric field intensity between the gap of the two coplanar electrodes on which a potential difference

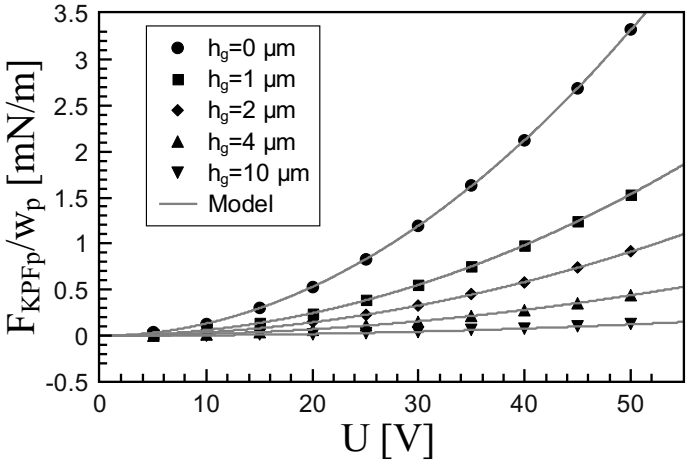

Figure 2.4: FE simulation of F_{KPFp} based on principle of virtual work assuming a relative dielectric constant $\varepsilon_d = 4$, $\varepsilon_g = 1$, and a dielectric slab thickness of h_d=10 μm for a varying gap distance h_g. The grey lines represent the force calculated with (2.20) for the corresponding parameters.

is applied. Other than for the KPFp, it is more difficult to derive an analytic model for this "out of plane" actuator.

First, an analytical expression will be derived for the qualitative description of the KPFn in air or vacuum. Fig. 2.5 depicts the actuator design and the corresponding ideal electric field. Assuming the electrode gap g to be infinitesimal small, the electric field produced by the two electrodes without the presence of the dielectric can be written as

$$E_0 = \frac{U}{\pi r} = \frac{U}{\pi\sqrt{x^2 + y^2}} \tag{2.22}$$

When the dielectric beam is introduced into the electric field it will be polarized and in return it modifies the field. At the boundary between the dielectric with ε_d and the surrounding medium with ε_g a polarization surface charge is induced by the field. If $\varepsilon_d > \varepsilon_g$ the charge weakens the field inside the dielectric relative to the field of the surrounding medium and for $\varepsilon_d < \varepsilon_g$ the field inside the dielectric is strengthened. Assuming the field inside the dielectric to have the same form but not the same force we write

$$E_d = c_d E_0 \tag{2.23}$$

where factor c_d represents the field reduction inside the dielectric material $c_d < 1$. In air or vacuum the permittivity is $\varepsilon_g \approx 1$. With (2.16), the *Kelvin polarization force*

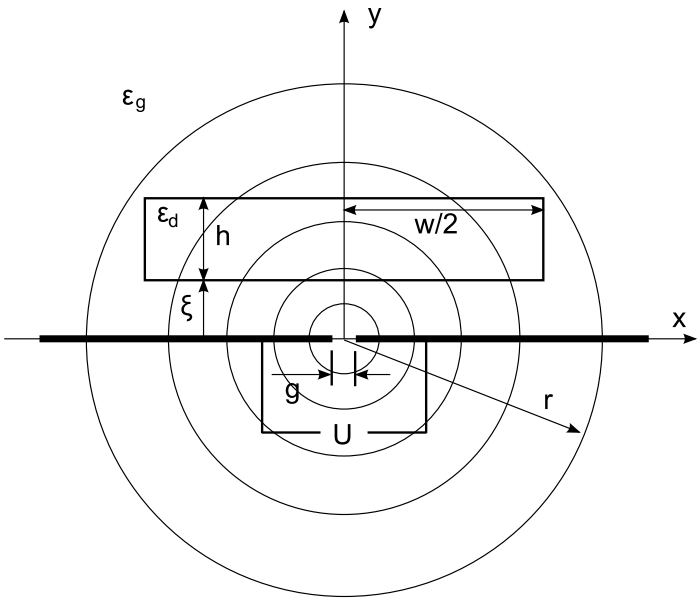

Figure 2.5: Schematic drawing of the electric field for the modeling of the F_{KPFn}.

density in the normal direction to the electrodes inside the dielectric is

$$\begin{aligned} f_{KPFn} &= -\frac{1}{2}\varepsilon_0(\varepsilon_d - 1)\frac{\partial E_d^2}{\partial y} \\ &= -\varepsilon_0(\varepsilon_d - 1)\frac{c_d^2 U^2 y}{\pi^2(x^2+y^2)^2}. \end{aligned} \tag{2.24}$$

To obtain the force acting on the dielectric beam, the force density has to be integrated over its volume.

$$\begin{aligned} F_{KPFn}(\xi) &= L\int_{\xi}^{\xi+h}\int_{-w/2}^{w/2} f_{KPFn}\,\mathrm{d}x\,\mathrm{d}y \\ &= -\varepsilon_0(\varepsilon_d - 1)c_d^2 U^2 L\int_{\xi}^{\xi+h}\frac{\frac{wy}{2(w^2/4+y^2)} + \arctan\frac{w}{2y}}{\pi^2 y^2}\,\mathrm{d}y \\ &= \varepsilon_0(\varepsilon_d - 1)c_d^2 U^2 L\frac{\xi\arctan\frac{w}{2(\xi+h)} - (\xi+h)\arctan\frac{w}{2\xi}}{\pi^2\xi(\xi+h)}. \end{aligned} \tag{2.25}$$

Assuming the beam width to be large compared to its height and its distance to the electrodes, the force can be simplified to

$$F_{KPFn}(\xi) \approx -\varepsilon_0(\varepsilon_d - 1)c_d^2 U^2 L\frac{1}{2\pi}\frac{h}{\xi(\xi+h)}. \tag{2.26}$$

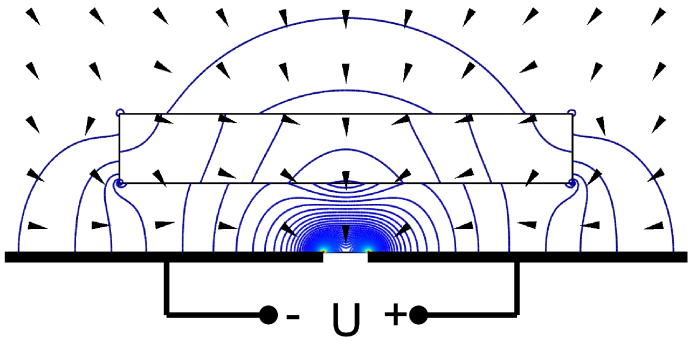

Figure 2.6: Electric field **E** over the electrodes gap $g = 2\mu m$ for a dielectric beam ($w = 20\ \mu m, h = 3\mu m, U = 10\ V, \varepsilon_r = 4$ (dielectric constant for SU-8 [60])), simulated with FEM (Comsol). The cones indicate the trend of the gradient field $\nabla(\mathbf{E} \cdot \mathbf{E})$. Reprinted with permission from [58]. Copyright [2006], American Institute of Physics.

One can see that in vacuum or air, the F_{KPFn} is negative, that means it acts towards the electrodes. To finally use this expression to define the KPFn, the weighting factor c_d has to be known. This factor not only includes the field reduction inside the dielectric beam but also the correction of the influence of the non ideal behavior of the electric field, as shown in Fig. 2.6.

With a finite element method the KPFn can be directly calculated for any geometry by integrating the *Kelvin polarization force density* (2.16) over the volume. Therefore, the simulated electric field first has to be deviated and then integrated over the volume which requires a high mesh density resulting in long computation time in order to obtain exact data. The exact calculation of the energy stored in the electric field W_e is easier. According to the right term in (2.4), the electrical energy in the system can be written as

$$\begin{aligned} W_e(\xi) &= -\int F_{KPFn}(\xi)\ \mathrm{d}\xi \\ &= a - \varepsilon_0(\varepsilon_d - 1)c_d^2 U^2 L \frac{1}{2\pi}\left(\ln(\xi) - \ln(\xi + h)\right). \end{aligned} \tag{2.27}$$

The simulated values of W_e can now be fitted with (2.27) and so the factor c_d can be determined. Fig. 2.7a shows the KPFn in air or vacuum calculated by means of the field energy simulation. The force was determined for different electrode gap sizes. Eventhough the gap size has a strong influence on the magnitude of the field energy it has only little influence on the force.

Water has a very high polarizability ($\varepsilon_g = 80$) and the area with the field intensity maximum is preferably occupied by the water. So, according to (2.5), the electric

field intensity close to the gap and therewith the total energy stored in the electric field is minimized. Consequently, the dielectric beam experiences a force away from the electrodes. Nevertheless, the same energy method which is based on the model of the KPFn in air (2.27) was used to derive the KPFn in water. The force in water qualitatively shows a behavior which is similar to the behavior in air or vacuum and the fit of the simulated energy values W_e in water was of good quality (see insert of Fig. 2.7b). In Fig. 2.7b it can be seen, that the force not only has an opposite sign, it is also around 50 times stronger in water than in air or vacuum.

The validation of the electrostatic nature of the actuation force is presented in appendix A.

Kelvin polarization force for the actuation of a polymer microresonator. The presented designs have to evaluated with respect to their actuator properties, their suitability as dynamic mechanical test structures and the feasibility of fabrication.

The normal force acting on parallel capacitor plates is given by [61]

$$F_{el} = -\frac{wL\varepsilon_g\varepsilon_0}{2\xi^2}U^2. \tag{2.28}$$

Fig. 2.8 shows the ratio between the calculated F_{KPFn} and the theoretical electrostatic force F_{el} acting normal to comparable parallel electrode plates in vacuum and in water, where w and L are the plate dimensions, ξ is the distance between the plates and U the potential difference. Obviously, F_{KPFn} is much weaker than F_{el}, particularly at small distances. However, in vacuum or air, at distances $\xi \gtrsim 1$ μm, i.e. $F_{el}/F_{KPFn} \lesssim 40$, the static deflection of a beam made of a polymer material actuated by F_{KPFn} will be larger than the deflection of a beam made of Si of the same dimensions ($w = 20\mu m, h = 3\mu m$) actuated by F_{el} at the same voltage. This is due to the fact, that the lower modulus of polymers such as SU-8 [62], i.e. $Y_{SU-8} = 4\ GPa \simeq Y_{Si}/40$, compensates for the lower actuation force at $\xi \gtrsim 1$ μm. Note that the specific relation F_{el}/F_{KPFn} as shown in Fig. 2.8 is a function of the beam dimensions such as the thickness and the permittivity of the polymer.

polarization force is presented in appendix A.

2.4 Conclusion

In summary, an electrostatic actuation method based on the Kelvin polarization force has been developed. Finite element model simulations show that the Kelvin polarization force F_{KPFn} is significantly weaker than a conventional electrostatic force acting normal on parallel capacitor plates for a comparable setup. However, the F_{KPFn} is suitable to actuate soft polymer microbeams. The presented actuator design demonstrates an alternative solution to drive micro structures made from arbitrary polymer

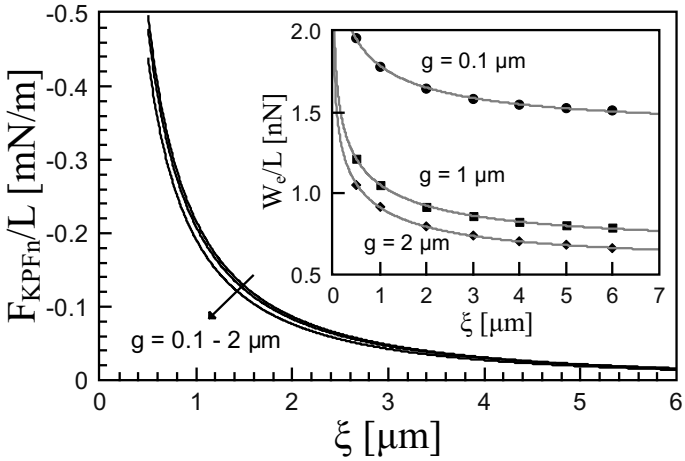

(a) In air or vacuum ($\varepsilon_g = 1$)

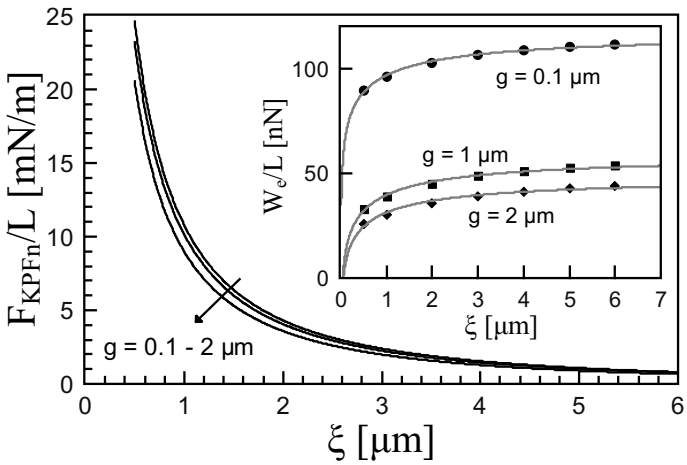

(b) In water ($\varepsilon_g = 80$)

Figure 2.7: F_{KPFn} plotted against the distance ξ of the dielectric with w=20μm, h=3μm and $\varepsilon_d = 4$ from the coplanar electrodes with an applied potential of $U = 10V$ (see Fig. 2.2b) in air or vacuum (a) and in water (b). The three curves represent F_{KPFn} for different electrode gap sizes g. The insert shows the stored electrical field energy W_e simulated with FEM. The simulated values are fitted with (2.27) with the fitting parameter c_d. In air or vacuum, the values of c_d are 0.826, 0.811, and 0.776 for gaps g of 0.1, 1, and 2 μm, respectively. The fit was of high quality with coefficients of determination $R^2 > 0.999$. In water, the fit quality was $R^2 > 0.982$.

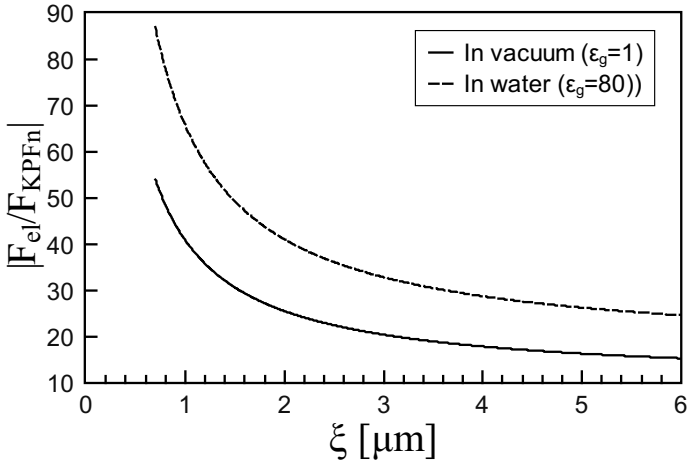

Figure 2.8: Comparison of the electrostatic force between two parallel capacitor plates F_{el} and the Kelvin polarization force F_{KPFn} for w= 20 μm, $h = 3$ μm, $\varepsilon_d = 4$, and U=10 V in vacuum ($\varepsilon_g = 1$) and in water ($\varepsilon_g = 80$). Reprinted with permission from [58]. Copyright [2006], American Institute of Physics.

materials. Thus, the greater flexibility in terms of material selection virtually allows for the full exploration of the exceptional variety of polymer materials for microscaled actuators and sensors without the need of a conducting layer by means of a metalization.

3 Device fabrication

In order to fabricate polymer microresonators based on the actuation technique of using the Kelvin polarization force, a method is needed which allows the fabrication of suspended microbeams which are placed over an electrode gap, as shown in the schematic in Fig. 2.2a. Several methods have been reported which allow for the fabrication of suspended polymer microstructures. Full release techniques have been reported [15, 17]. Other techniques work by controlling the UV penetration depth via UV exposure dosage [63] or by means of absorbing the UV light with a polymer layer [64] or with a metallic "buried" mask [65–69]. The use of a serial direct-writing technique has been reported by two-photon fabrication [70]. Other methods are based on a bonding process [71–73].

The sacrificial layer technique is a well established fabrication method in surface micromachining. The top layer is processed over a sacrificial layer material that can be selectively removed, yielding a freestanding structure. The most common sacrificial layer for silicon or silicon-nitride surface micromachining is silicon-dioxide which can be selectively etched with hydrofluoric acid (HF) [74]. Because HF etches [75] or diffuses [76] through many organic polymers, alternative sacrificial layer techniques for polymer materials are applied. Metals also provide a suitable class of materials as sacrificial layer materials to form freestanding polymer microstructures [29, 77]. Polymers can be used as sacrificial materials which are either heat-decomposed [78, 79] or dissolved in a selective solvent [65] or in water [75].

The use of a heat-decomposable sacrificial material [79] would be very advantageous, but it is not applicable since only a high performance polymer material can withstand the required high temperatures in the range of 220 °C to 280 °C without thermal degradation. Furthermore, the exposure of the structure polymer to high temperatures would significantly influence the mechanical and chemical properties. The opposite way around, a suitable sacrificial layer material must withstand the processing temperatures of the polymer structural material which is around 100 °C to 180 °C for polymers like SU-8 (an epoxy type polymer) or PMMA (polymethylmethacrylate) but can be as high as 400 °C for polyimide. Further, the sacrificial material should not intermix with the polymer material. In order to release the sacrificial layer material, a very selective solvent is needed, which must be compatible with all the other materials on the microsystem, such as metallic electrodes used for

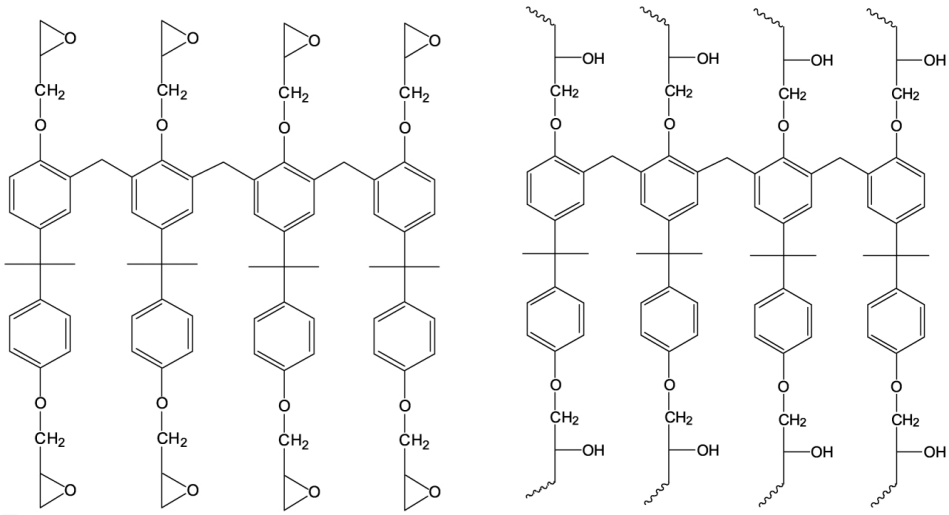

(a) Monomoer (b) Polymerized monomer

Figure 3.1: Chemical formula of SU-8.

electrostatically actuated polymer micro structures [29]. Thus, the use of aluminum as sacrificial layer material as used by Zhang et al. [29] is not applicable, since Al is etched with an etch solution based on phosphoric acid that would also etch other metals and polymers [80].

Varying solution of LOR can be purchased with which layers of $10nm - 6\mu m$ can be applied by spin coating in a single coat. LOR does not intermix with other photoresists and can be dissolved in an aqueous alkaline solution which is compatible with most polymer materials. The adhesion to most common substrates such as Si is excellent. The glass transition temperature of LOR is at around 190 °C, thus it withstands the processing temperatures of most common polymers. LOR layers can be patterned by using a photoresist etch mask. The etch rate of the lift-off resist can be well controlled by the concentration of the aqueous alkaline solution.

SU-8 combines good chemical resistance, good thermal stability, and excellent microprocessability by means of photolithography [81] and was therefore chosen as the polymer structural material. All structures are made of SU-8 2000 from Microchem GmbH. SU-8 is an epoxy-based negative-type photoresist. SU-8 is a highly crosslinked amorphous polymer built of monomers with eight epoxy binding sites. One monomer is based on four bisphenol-A units connected to each other at the phenyl rings [82]. The chemical formula is shown in Fig. 3.1. The material properties of SU-8 are listed in Table 3.1.

Table 3.1: Material properties of SU-8.

Mass density	ρ	1218	kg/m^3	[83]
Young's modulus	Y	4.02	GPa	[62]
Poisson ratio	ν	0.26		[84]
Plane strain modulus	$Y/(1-\nu^2)$	4.30	GPa	[85]
Heat capacity	c_p	1200	J/(kg K)	[86]
Thermal conductivity	κ	0.3	W/(m K)	[87]
Coeff. therm. exp.	α_{th}	52, 87.1, 102	ppm/K	[40,45,83]
Glass temperature	T_g	210	°C	[87]
Thermal stability	T_{sta}	≈ 300	°C	[87]
Tensile strength	σ_s	60	MPa	[87]
Dielectric constant (1 GHz)	ε_r	4.1		[87]

In this chapter, two fabrication techniques based on lift-off resist (LOR) from Microchem Corp. as a sacrificial layers, which allow for the fabrication of electrostatically actuated SU-8 microstructures, are presented. All the subsequent measurements are performed with samples made with one of the two processes.

Two different processes were used to fabricate suspended single and double-clamped microbeams. Both fabrication processes are on glass substrates offering Ti/Au electrodes which also offer the alignment marks for further photolithography steps. The electrodes are deposited by e-beam evaporation and patterned by a lift off process. For both methods, the final structures are dried in a critical point dryer to prevent the fragile suspended polymer structures from sticking to the substrate.

For the application in water, the electrodes are additionally covered with a 120 nm thick layer of aluminum oxide (Al_2O_3) which was deposited using atomic layer deposition (ALD). The ALD deposition temperature was 300 °C and was performed in a Picosun tool.

The detailed runsheets are listed in appendix B.

3.1 Fabrication of thin microbeams

In the process for thin microbeams, the sacrificial layer (LOR) remains unstructured and the structural polymer layer (SU-8) is applied subsequently. At the end, the LOR layer is part of the anchors. The anchor areas are large compared to the structure dimensions. The SU-8 layer is structured and the sacrificial layer is dissolved until the beams are suspended. The anchors are large enough so that they are not released,

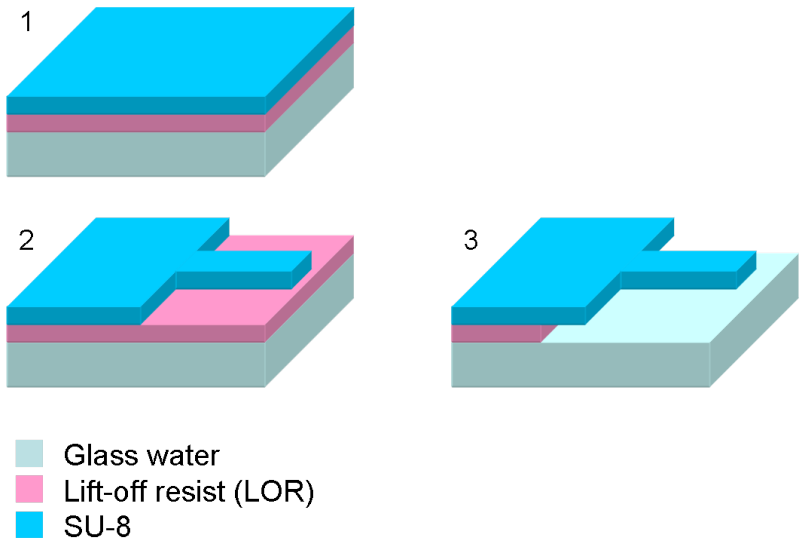

Figure 3.2: Schematic representation of the fabrication process for the thin SU-8 microbeams.

and the structures stay attached to the substrate. Although the anchors are attached to the substrate, they are partially suspended around the edge. A schematic drawing of the fabrication process of the thin SU-8 microbeams is shown in Fig. 3.2. A layer of SU-8 2002 was spin coated over a 3 μm thick layer of LOR 30B which before was baked for 15 min at 170 °C (Fig. 3.2 (1)). After a softbake at 100 °C, the SU-8 layer was exposed to 120 mJ/cm^2 followed by a post exposure bake at 100 °C. After developing the SU-8 layer in PGMEA (Fig. 3.2 (2)), a hard bake at 170 °C for 15 min was performed. A profile of the structured SU-8 layer over the LOR layer is shown in Fig. 3.3. Finally, the LOR was dissolved in aqueous alkaline solution until the beams were suspended (Fig. 3.2 (3)).

Fig. 3.4 shows SU-8 microbeams fabricated with this process. The samples used for this work are taken from two wafers. The beams are 14 μm wide and have varying lengths from 30 to 300 μm and a thickness of 1.45 $\mu m \pm 0.04$ μm and 1.31 $\mu m \pm 0.04$ μm for the particular wafers. The advantage of this process is the very homogeneous film thickness. The disadvantage is the underetching at the anchor sites which is more difficult to model than the anchors of the thick beams. The microbeams fabricted with this process are thinner than the beams fabricated with the other process. They are referred to as *thin microbeams*.

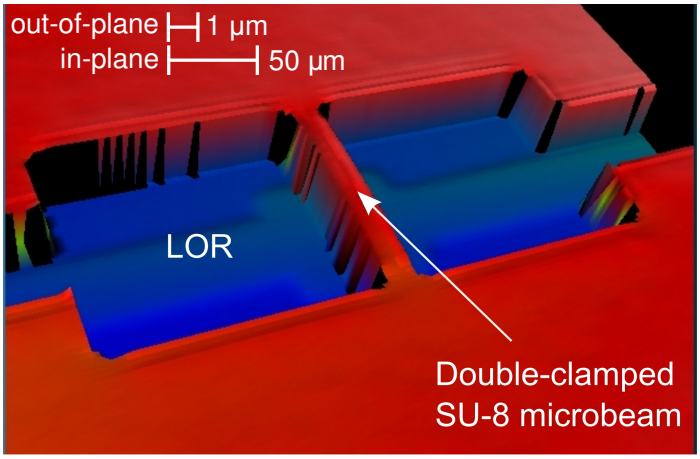

Figure 3.3: Profile of an unreleased double-clamped thin SU-8 microbeam (100 μm long, 1.5 μm thick) patterned over a LOR layer measured with a white-light interferometer. The scale in the out-of-plane direction (structure thickness) is strongly exaggerated. This image corresponds to the fabrication step 2 in Fig. 3.2.

3.2 Fabrication of thick microbeams

In the fabrication process for thick microbeams, the sacrificial layer (LOR) is patterned prior to the application of the structural polymer layer (SU-8) and the LOR is fully dissolved at the end, resulting in released beams. Structuring of the LOR allows anchoring of the SU-8 beams on the substrate. A schematic drawing of the fabrication process of the thick SU-8 microbeams is shown in Fig. 3.5. LOR is not photosensitive, thus it was patterned by covering it with a photoresist film acting as a mask for the subsequent concurrent development of both layers. Therefore, a 0.5 μm thick layer of ma-N 405 from Microresist was spin coated over a 3 μm thick layer of LOR 30B which before was baked for 15 min at 170 °C (Fig. 3.5 (1)). After softbake, the negative resist ma-N 405 was exposed with 600 mJ/cm^2. Now, both layers were developed in an aqueous alkaline solution, until the LOR was fully structured (Fig. 3.5 (2)). After the photoresist was stripped in acetone (Fig. 3.5 (3)), the SU-8 structure layer was spin coated over the LOR bumps followed by a 20 min long softbake at 100 °C (Fig. 3.5 (4)). That way the polymer can reflow and the layer gets planar, levelling off the sacrificial layer bumps. Then the SU-8 layer was exposed to 150 mJ/cm^2 followed by a post exposure bake for 2 min at 95 °C and the subsequent development in PGMEA (Fig. 3.5 (5)). A profile of the structured SU-8 layer over the LOR bump is shown in Fig. 3.6. Finally, the sacrificial LOR layer was removed in an

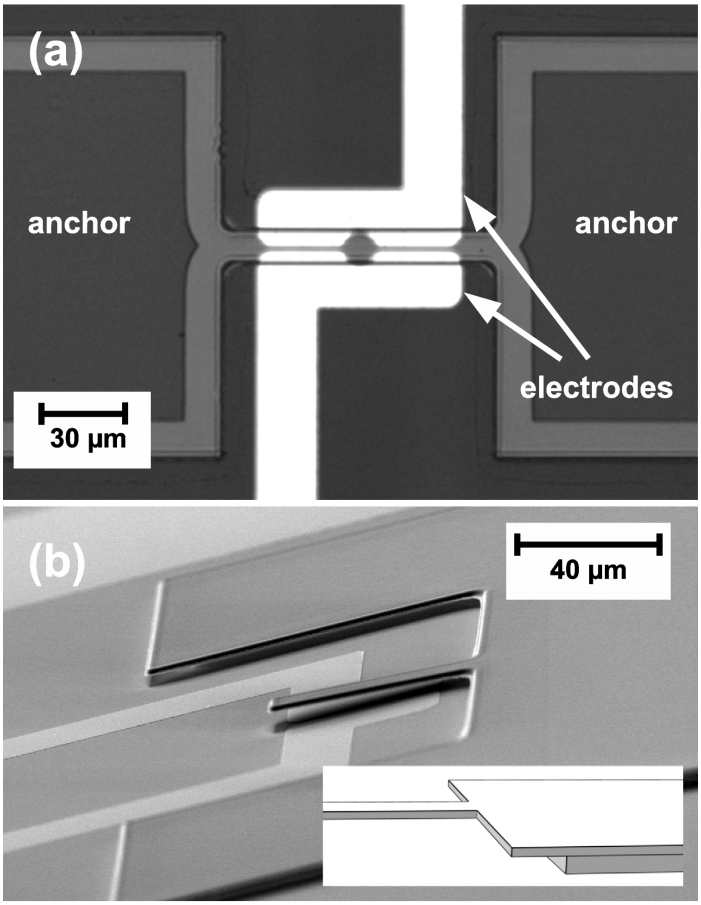

Figure 3.4: (a) Microscope image of a double-clamped and (b) a SEM image of a single-clamped microbeam made of SU-8. The anchors of these structures yield an underetched suspended plate. Single-clamped (s-c) and double-clamped (d-c) microbeams of this type are labelled in this paper as *thin s-c microbeams* and *thin d-c microbeams*, respectively. Insert of (b) shows the anchors with the partially suspended SU-8 plate structure at its edge.

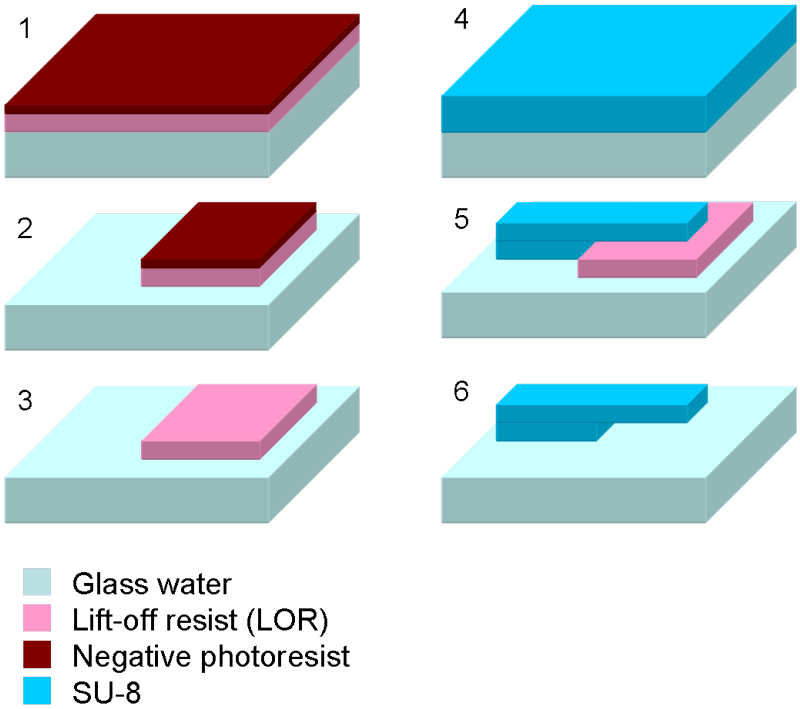

Figure 3.5: Schematic representation of the fabrication process for the thick SU-8 microbeams.

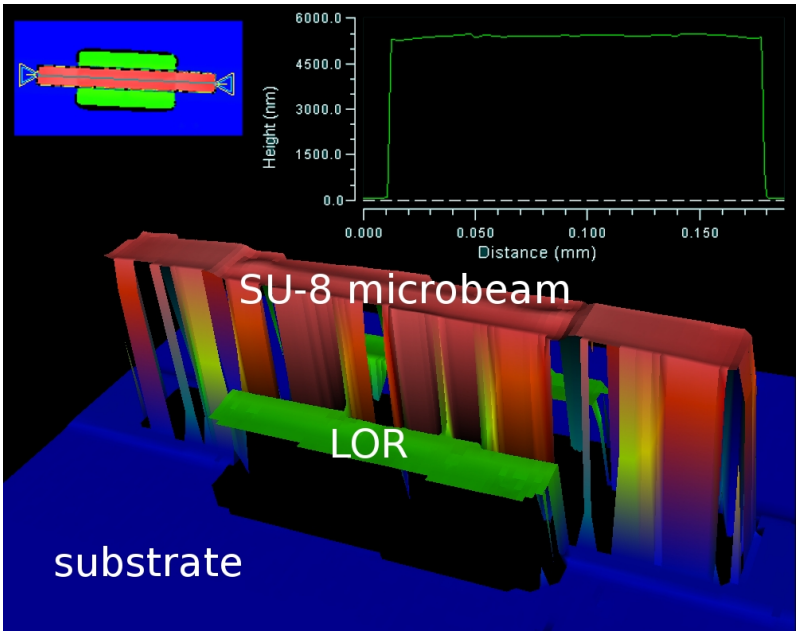

Figure 3.6: Profile of an unreleased double-clamped thick SU-8 microbeam patterned over a LOR bump measured with a white-light interferometer. This image corresponds to the fabrication step 5 in Fig. 3.5.

aqueous alkaline solution (Fig. 3.5 (6)).

Fig. 3.7 shows SU-8 beams fabricated with this process. The samples used for this work are all taken from one wafer. The beams are 12 μm and 20 μm wide and have varying lengths from 15 to 185 μm and a varying thickness of 3.6 to 5.6 μm. The advantage of this process is the anchor geometry which makes it easier for analytical or finite element modelling. The drawback of the structures made with this process is the varying thickness along the beam length, as can be seen in Fig. 3.7. Furthermore, the minimal thickness of the beams is limited by the thickness of the sacrificial layer. If the LOR bumps are too high compared to the structural SU-8 layer, the SU-8 layer does not fully cover the sacrificial layer islands. The microbeams fabricated with this process are thicker than the beams fabricated with the other process. They are referred to as *thick microbeams*.

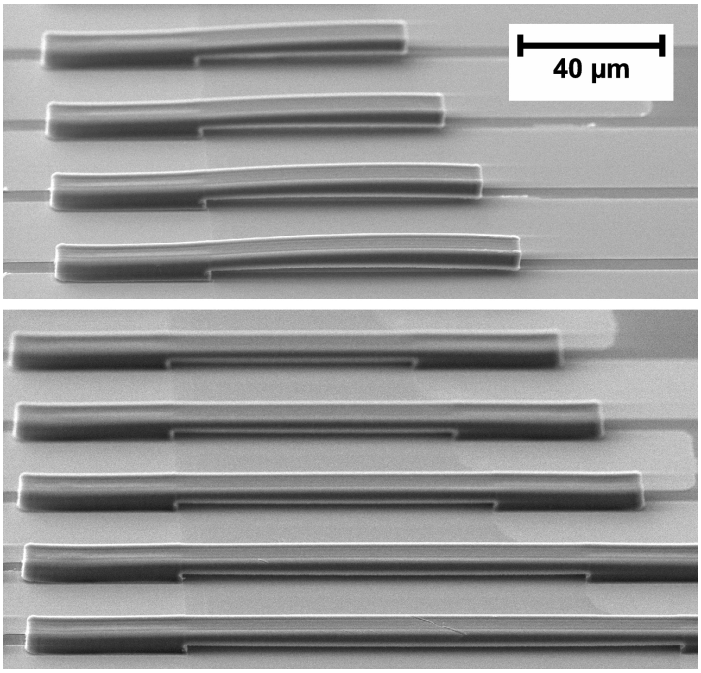

Figure 3.7: SEM image of thick single and double-clamped microbeams made of SU-8. Single-clamped (s-c) and double-clamped (d-c) microbeams of this type are labelled in this paper as *thick s-c microbeams* and *thick d-c microbeams*, respectively.

Part I

Characterization

4 Mechanical models

4.1 Damped and forced vibration

Mechanical vibrations in physical systems are associated with the periodic conversion of kinetic to potential energy and vice versa. Elastic elements such as beams, strings, and plates are able to store potential energy in terms of the deformation energy. If the system comes out of its position of rest, restoring forces accelerate the mass of the system towards the rest position thereby generating kinetic energy. Due to the kinetic energy, the physical system traverses the position of rest, generating new deflection energy that is potential energy. This periodic energy conversion would continue forever if the present mechanical energy would not be resisted by dissipative forces.

[1] The forced vibration of a damped system with a single degree of freedom can be modelled with a one dimensional oscillator based on a zero mass spring, a linear damping element, and a mass, as depicted in Fig. 4.1. Assuming a periodic driving force $F(t) = F_0 \sin \omega t$, the second order differential equation of the system is

$$m\ddot{x} + c\dot{x} + kx = F_0 \sin \omega t \tag{4.1}$$

where m is the mass, k is the spring constant and c is the coefficient of damping force.

The solution of Eq. 4.1 consists of a specific solution and the general solution to the homogeneous differential equation of the damped system. Using

$$\omega_0^2 = \frac{k}{m} \tag{4.2}$$

and

$$n_c = \frac{c}{2m} \tag{4.3}$$

the characteristic equation can be written as

$$\ddot{x} + 2n_c\dot{x} + \omega_0^2 x = 0 \tag{4.4}$$

where ω_0 is the natural vibration frequency of the system without damping and n_c is the coefficient of damping.

[1] This section is mainly based on [61] chapter 2.5.

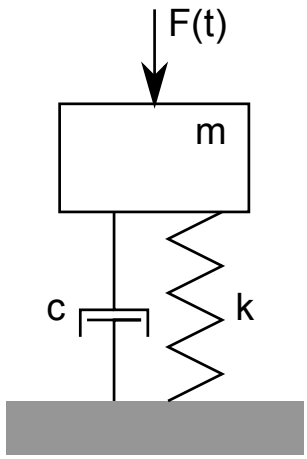

Figure 4.1: Damped one dimensional oscillator with one degree of freedom.

The ratio

$$\zeta = \frac{n_c}{\omega_0} \tag{4.5}$$

is called the damping ratio of the system which together with ω_0 describes the performance of a damped oscillator. If $\zeta < 0.707$ the system is slightly damped and it shows a resonance behavior. For $\zeta \geq 0.707$ the system is overdamped and the resonance peak disappears. The damping ratio $\zeta = 0.707$ is called critical damping condition.

For slight damping, the amplitude B and the phase lag φ of the steady vibration are [61]

$$B = \frac{F_0/m}{\sqrt{(\omega_0^2 - \omega^2)^2 + 4n_c^2\omega^2}} \tag{4.6}$$

and

$$\varphi = \arctan \frac{2n_c\omega}{\omega_0^2 - \omega^2}. \tag{4.7}$$

The resonance of a mechanical structure can be characterized by two specific parameters, the natural frequency f_0 and the damping ratio of the system which often given by the quality factor Q.

4.1.1 Resonant frequency

From Eq. 4.6 it can be seen, that the amplitude of a slightly damped system has a maximum near the natural frequency ω_0. The frequency of the highest amplitude is

called resonant frequency ω_r and it can be found by using $\partial B/\partial\omega = 0$. The resonant frequency is

$$\omega_r = \omega_0\sqrt{1-2\zeta^2}. \tag{4.8}$$

For slight damping, the resonant frequency is very close to the natural frequency of the damped system $\omega_r \approx \omega_0$. If $\zeta \geq 1/\sqrt{2}$ value under the square root becomes negative and the resonance disappears, as already mentioned above.

4.1.2 Quality factor

The quality factor (Q) is a value indicating the sharpness of the resonance peak. There are several definitions of Q, all equivalent for slight damping.

The physical definition is the ratio between the energy stored and energy lost during one cycle at resonance

$$Q = 2\pi\frac{W}{\Delta W} = \frac{\sqrt{1-2\zeta^2}}{2\zeta} \tag{4.9}$$

where W is the total energy stored in the system and ΔW is the energy loss during one cycle of oscillation. For slight damping, the quality factor becomes $Q \approx \frac{1}{2\zeta}$.

For electrical resonant circuits the quality factor is defined by [61]

$$Q = \frac{\omega_r}{\Delta\omega} = \frac{1-2\zeta^2}{2\zeta} \tag{4.10}$$

where $\Delta\omega$ is the frequency difference between the two frequencies at which the amplitude curve (Eq. 4.6) has the half maximum energy $B/\sqrt{2}$ (-3dB). For slight damping, this definition of the quality factor is equal to the physical definition.

4.2 Eigenfrequency of a bending beam

Here the Euler-Bernoulli beam theory is presented. For a thin beam ($L/h > 10$) (see Fig. 4.2), the rotational inertia and the shear deformation can be neglected. The equation of motion of a thin beam can be derived by means of the equilibrium of forces for an infinitesimal piece of beam. Assuming a linear elastic material and small deflections $w(x,t)$, the equation of motion of a thin beam is [88]

$$\rho A\frac{\partial^2 w}{\partial t^2} + YI_z\frac{\partial^4 w}{\partial x^4} = 0 \tag{4.11}$$

where ρ is the mass density, A is the cross sectional area, Y is the Young's modulus, and I_z is the geometric moment of inertia. The equation of motion can be solved with

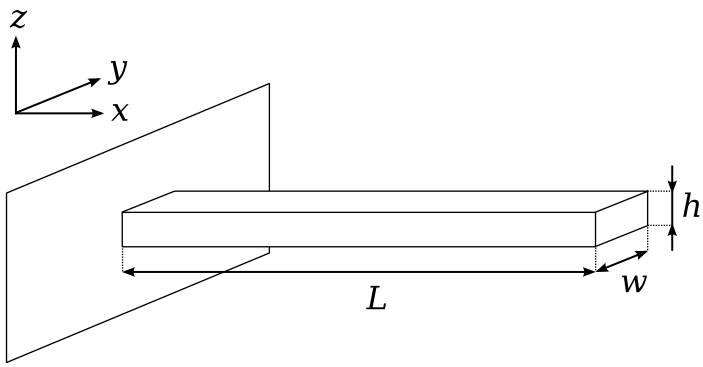

Figure 4.2: Schematic drawing of a single-clamped beam.

the variable separation ansatz and the eigenfrequency of a thin beam becomes

$$\omega_{0,beam} = 2\pi f_{0,beam} = \lambda_n^2 \sqrt{\frac{YI_z}{A\rho}} \frac{1}{L^2}, \quad n = 1, 2, \ldots \tag{4.12}$$

where λ_n is the solution of the frequency equation. For a single-clamped beam, the frequency equation becomes $1 + \cos\lambda \cosh\lambda = 0$ and the solutions for $n = 1, 2, 3, n > 3$ are 1.8751, 4.6941, 7.8548, $(2n-1)\pi/2$, respectively. For a double-clamped beam the frequency equation is $1 - \cos\lambda \cosh\lambda = 0$ and the solutions for $n = 1, 2, 3, n > 3$ are 4.7300, 7.8532, 7.10.9956, $(2n+1)\pi/2$, respectively.

For a beam with rectangular cross section the geometrical moment of intertia is

$$I_z = \frac{Ah^2}{12} \tag{4.13}$$

and (4.12) becomes

$$f_{0,beam} = \frac{\lambda_n^2}{2\pi} \frac{h}{L^2} \sqrt{\frac{Y}{12\rho}}, \quad n = 1, 2, \ldots \tag{4.14}$$

where h is the thickness of the beam.

4.2.1 Effective mass and spring constant

For small deflections in the first resonant mode, a bending beam behaves like a linear spring and its dynamic behavior can be modelled by the discrete linear model discussed in section 4.1. In order to calculate the spring constant and the effective mass of a beam, the potential energy of the string is compared to the potential energy of a spring-mass system which is

$$W_{pot} = \frac{1}{2} y_0^2 k. \tag{4.15}$$

The potential energy of an Euler Bernoulli beam is given by the flexural strain energy [61]

$$W_{flex} = \frac{1}{2} Y I_z \int_0^L \left(\frac{\partial^2 w_n}{\partial x^2} \right)^2 \mathrm{d}x \tag{4.16}$$

and the deflection w of a single-clamped beam with a distributed loading is given by [61]

$$w(x) = c_a x^2 (x^2 - 4Lx + 6L^2). \tag{4.17}$$

By setting $w(L) = y_0$ the amplitude variable c_a becomes

$$c_a = \frac{y_0}{3L^4} \tag{4.18}$$

and by integrating(4.16) with (4.18) and (4.17) the potential energy of a single-clamped beam with a distributed load is

$$W_{pot,beam} = \frac{8 Y I_z y_0^2}{5L^3}. \tag{4.19}$$

Comparing the potential energies of the spring-mass system (4.15) and a single-clamped beam (4.19) yields the spring constant of a beam

$$k_{beam} = \frac{16 Y I_z}{5L^3}. \tag{4.20}$$

To obtain the effective mass of a single-clamped beam, the resonant frequency of the spring-mass oscillator (4.2) with the spring constant (4.20) is compared with the first mode resonant frequency of a beam (4.12), the effective mass of a beam with a rectangular cross-section (4.13) becomes

$$m_{eff,beam} = \frac{16}{5\lambda_1^4} A L \rho \tag{4.21}$$

which gives with $\lambda_1 = 1.8751$

$$m_{eff,beam} = 0.259 A L \rho. \tag{4.22}$$

4.3 Eigenfrequency of a lateral oscillating string

A string is a prestressed thread-like elastic continuum without flexural rigidity. The bending deflection $w(x,t)$ is assumed to be small and the prestress is big enough so that its change due to the string deflection can be neglected. The equation of motion of a string can be obtained by the equilibrium of forces for an infinitesimal piece of string and it is [89]

$$\rho A \frac{\partial^2 w}{\partial t^2} - S \frac{\partial^2 w}{\partial x^2} = 0 \tag{4.23}$$

where ρ is the mass density, A is the cross-section area, and S is the tension force. This differential equation is the so called wave equation with the wave propagation velocity $c_{wave}^2 = \frac{S}{\rho A}$. For the boundary conditions of a clamping at both ends the wave equation can be solved by variable separation and the eigenfrequency of a string is [89]

$$\omega_{0,string} = 2\pi f_{0,string} = \pi n \sqrt{\frac{\sigma}{\rho}} \frac{1}{L}, \quad n = 1, 2, \ldots \tag{4.24}$$

where $\sigma = \frac{S}{A}$ is the prestress.

4.4 Linear viscoelasticity

There are two types of ideal material models, the elastic solid and the viscous liquid. Real materials, polymers in particular, show a mechanical behavior which is intermediate between the two ideal cases. Polymers have distinct viscoelastic behavior. They show a wide range of properties, from a viscous liquid to an elastic solid depending on the temperature and the time scale.

[2] If a linear viscoelastic material is subjected to a constant strain ε, the stress σ decays with time which is called *relaxation*, unlike for an ideal elastic materials where the stress remains constant. Assuming a linear behavior, the stress-strain behavior for tension and flexure can be written as

$$\sigma(t) = \varepsilon \, Y(t) \tag{4.25}$$

where $Y(t)$ is the *relaxation modulus*. The other case is when a viscoelastic material is slowly deforming under a constant stress. This is called creep and the stress-strain relation for tension and flexure can be written as

$$\varepsilon(t) = \sigma \, J_Y(t) \tag{4.26}$$

where $J(t)$ is the *creep compliance*. Experimentally obtained curves for $Y(t)$ and $J_Y(t)$ can be represented by simple exponential decay functions. But usually, they only hold good for limited time intervals.

The *Boltzmann superposition principle* postulates a linear stress-strain relation, and the possibility to add deformation steps with a relaxation modulus always having the same time response, that is, the material does not age. With these assumptions, the constitutive equation of linear viscoelastic behavior for the uniaxial stress condition in tension and flexure is [90]

$$\sigma(t) = Y(0)\varepsilon(t) + \int_0^t \varepsilon(t-\tau)\dot{Y}(\tau)\mathrm{d}\tau. \tag{4.27}$$

[2] This section is mainly based on [90] chapter 3.

For an infinite observation period $t \to \infty$ and a sinusoidal strain $\varepsilon(t) = \varepsilon_0 e^{i\omega t}$ the constitutive equation becomes

$$\sigma(t) = \left[Y(0) + \int_0^\infty e^{-i\omega\tau} \dot{Y}(\tau) \mathrm{d}\tau \right] \varepsilon_0 e^{i\omega t}. \tag{4.28}$$

The *complex Young's modulus* is now defined as

$$Y^*(\omega) = Y(0) + \int_0^\infty e^{-i\omega\tau} \dot{Y}(\tau) \mathrm{d}\tau \tag{4.29}$$

and the stress-strain relation is

$$\sigma(t) = Y^*(\omega)\varepsilon(t) = (Y'(\omega) + iY''(\omega))\varepsilon(t). \tag{4.30}$$

where $Y'(\omega)$ and $Y''(\omega)$ are the real and an imaginary part of the complex Young's modulus, respectively. $Y'(\omega)$ is called *storage Young's modulus*, it is the part that is in phase with the applied strain. $Y''(\omega)$ is the *loss Young's modulus*, it is the part that is $\pi/2$ out phase with the applied strain. The *loss tangent* is defined by

$$\tan\delta(\omega) = \frac{Y''(\omega)}{Y'(\omega)}. \tag{4.31}$$

The stress-strain relation (4.30) can be written as

$$\sigma(t) = \|Y^*(\omega)\| e^{i\delta} \varepsilon(t) = \|Y^*(\omega)\| \varepsilon_0 e^{i(\omega t + \delta)}. \tag{4.32}$$

which reveals that δ is the phase angle between the stress and strain.

The storage and the loss modulus define the energy that is stored and the energy that is lost during one cycle, respectively. Calculating the energy dissipated during one cycle gives [91]

$$\Delta W = \oint \sigma \mathrm{d}\varepsilon = \int_0^{2\pi/\omega} \sigma \frac{\mathrm{d}\varepsilon}{\mathrm{d}t} \mathrm{d}t = \pi Y''(\omega)\varepsilon_0^2 \tag{4.33}$$

and taking the integral for (4.33) over a quarter cycle only, the maximum stored energy W can derived as

$$W = \frac{1}{2} Y' \varepsilon_0^2. \tag{4.34}$$

With (4.33) and (4.34), the loss tangent (4.31) can be rewritten as

$$\tan\delta = \frac{\Delta W}{2\pi W} = Q_{mat}^{-1} \tag{4.35}$$

which is equal to the definition of the quality factor (4.9) and thus represents the material damping Q_{mat}^{-1}.

The complex Young's modulus can be represented by the absolute value

$$\|Y^*\| = \sqrt{Y'^2 + Y''^2} \tag{4.36}$$

and the phase angle δ. With (4.31), the magnitude of Y^* can be written as

$$\|Y^*\| = Y'\sqrt{1 + (\tan\delta)^2}. \tag{4.37}$$

Solid polymers below their glass transition temperature usually exhibit only a low viscoelastic behavior ($\tan\delta < 0.1$), and thus the dynamic mechanical characteristic can be defined in terms of the Young's modulus $\|Y^*\| \approx Y' = Y$ and the loss tangent $\tan\delta$.

5 Experimental

5.1 Evaluation of resonance parameters

As introduced in section 4.1, the resonance behavior of a damped and forced oscillator is determined by the resonant frequency and the quality factor. In order to evaluate these two parameters, the single and double-clamped microbeams were actuated with a periodic chirp signal. This signal excites all frequencies over a given bandwidth resulting in steady resonance curves. The vibration was monitored with a microscope based laser-Doppler vibrometer (MSA-400) from Polytec GmbH with a frequency range from 0 to 10 MHz (shown in Fig. 5.1). The applied driving voltages ranged from 0.5 to 30 V according to the following requirements: The vibration amplitude was always kept as low as possible in order to stay in the linear regime but high enough to still have a good signal to noise ratio. Being in the linear regime, the measured amplitude and phase responses of the first resonant mode were fitted with the amplitude and phase curves of a linear mass-damper model (4.6). The resonant frequency and the -3dB bandwidth of the peak, which defines the quality factor, were determined from the fit parameters. Fig. 5.2 shows such an amplitude response of the first resonant mode of a thin d-c microbeam fitted with the linear oscillator model. Fig. 5.3 displays the measured first resonant mode of a thin d-c microbeam.

5.2 Temperature control

A Peltier element was placed on the backside of the sample to control the temperature of the polymer microstructures. The backside of the Peltier element itself was cooled with an external water-cooling loop passing water of 0 °C. With this setup, the sample temperature can be controlled from -20 to 130 °C. The temperature sensor is placed at the site of the Peltier element. For calibration, the temperature of the sample (T_{sample}) was compared to the temperature at the Peltier element ($T_{peltier}$), see Fig. 5.4. For this calibration measurement a temperature sensor was glued with a temperature-conducting glue into an empty chip-carrier.

The total systematic error of the temperature control does not exceed ±1.1 °C. This error is caused by the following effects. First, the influence of the resistance of the electrical connection to the resistive temperature sensors (PT1000, 1kOhm at 0 °C) on

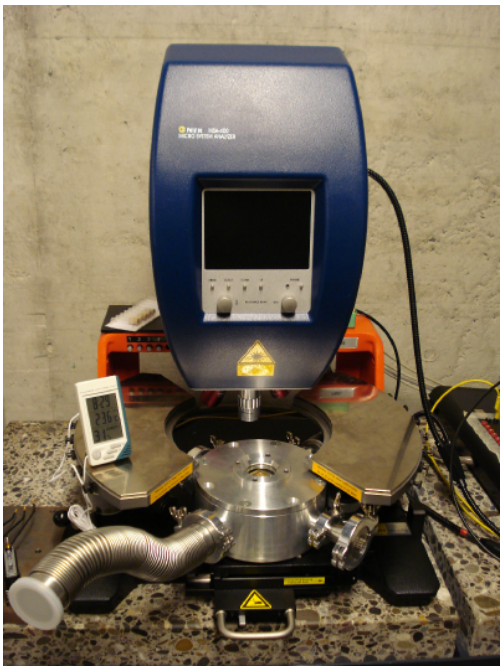

Figure 5.1: Photography of laser-Doppler vibrometer with vacuum chamber.

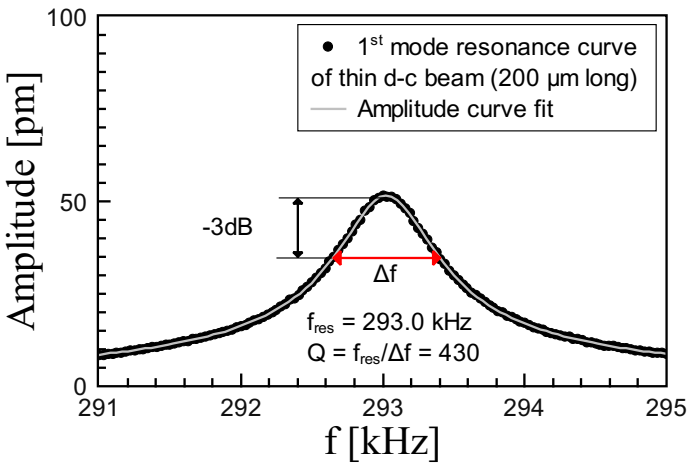

Figure 5.2: Resonance curve (first mode) of a 200 μm long and 1.45 μm thick SU-8 microbeam at 20 °C. The measured data was fitted with the amplitude curve of a linear vibration system with damping.

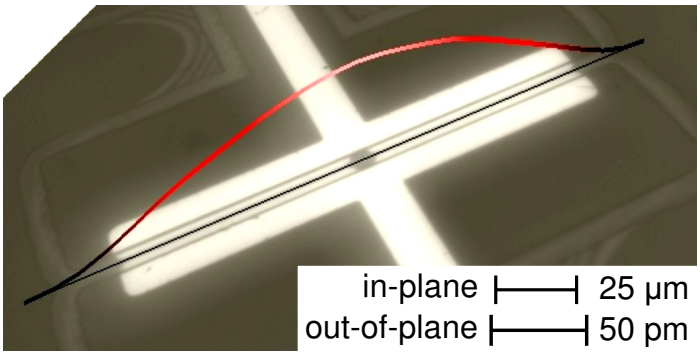

Figure 5.3: Scan measured with the laser-Doppler vibrometer of a first resonant mode of the thin double-clamped microbeam with $L = 200\ \mu$m. The out-of-plane scale is highly exaggerated.

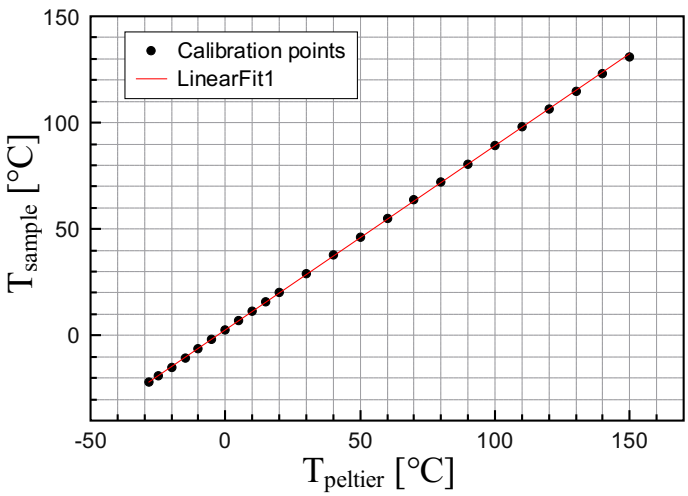

Figure 5.4: Temperature calibration.

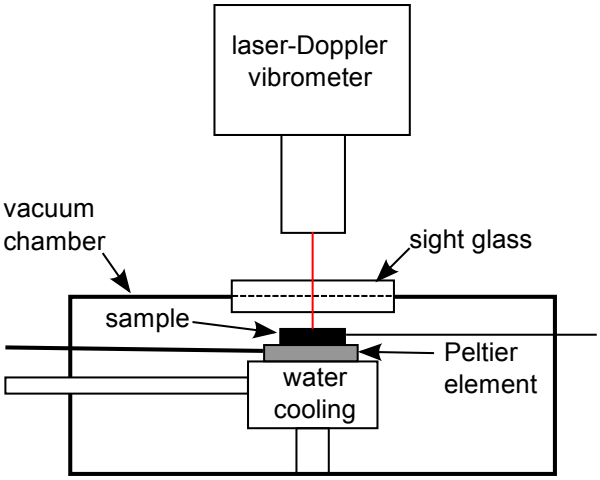

Figure 5.5: Schematic drawing of the measurement setup.

the total resistance causes a systematic error of less than 0.02 °C. Second, the PT1000 sensor has a systematic error of 0.2 °C at -20 °C, and up to 0.7 °C at 100 °C is possible. Third, the linearization of the PT1000 response in the thermocontroller causes an error of less than 0.1 °C. Fourth, the varying amount of thermo-conductive paste can influence the temperature difference between the sample and the Peltier element by 0.1 °C. Fifth, the aging of the thermo-conductive paste results in a temperature difference of less than 0.2 °C.

The samples were measured in a vacuum chamber which was pumped down with a turbomolecular pump and a membrane forepump. A schematic drawing of the setup is shown in Fig. 5.5.

5.3 Packaging

The glass wafer is diced into single chips of 5.5 × 6.5 mm which are then glued with a two component epoxy adhesive into a chip carrier. The chips were then wire-bonded to the chip-carrier. A photo of such a dye- and wire-bonded chip is shown in Fig. 5.6. For the measurements, an appropriate chip-socket is positioned inside a vacuum chamber. This procedure allows a quick change of the samples.

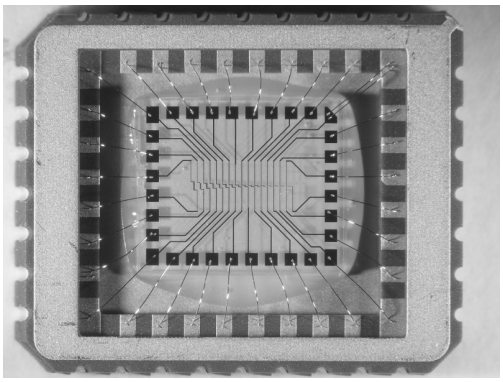

Figure 5.6: Die and wire-bonded glass chip containing the Cr/Au electrodes and the SU-8 microresonators.

5.4 Relative humidity control

The relative humidity (RH) and temperature were measured with a reference humidity sensor (SHT11 from Sensirion AG) with a humidity accuracy of 3 %RH and a temperature accuracy of 0.4 °C. The sensor has a time response of typically 8 seconds. The relative humidity was controlled by moisturizing dry air by passing it through a bubbler filled with water. Different levels of the RH are adjusted by a specific mixing of the wet air with the dry air. A constant flow of humid air through the measurement chamber was ensured. A humidity sensitivity of the air temperature of 0.003 °C/%RH is determined. This allows the assumption of isothermal measurements. A schematic of the measurement setup is shown in Fig. 5.7.

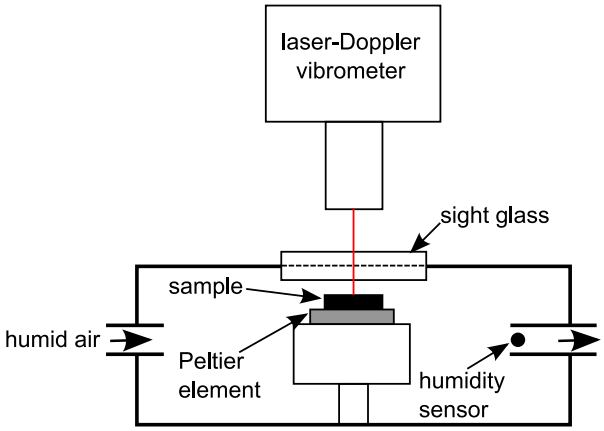

Figure 5.7: Schematic drawing of the measurement setup of the humidity measurements.

6 Damping

[1] A high quality factor is crucial for most resonator applications, for resonant sensors in particular. The total Q factor measured in a vibration test of cantilever beams is the sum of the air damping and the intrinsic damping of the microstructure

$$\frac{1}{Q} = \frac{1}{Q_{air}} + \frac{1}{Q_{intrinsic}}. \tag{6.1}$$

The intrinsic damping itself is the sum of internal damping mechanisms such as thermoelastic damping, surface loss or material damping and external damping mechanisms such as clamping loss.

$$\frac{1}{Q_{intrinsic}} = \frac{1}{Q_{mat}} + \frac{1}{Q_{TED}} + \frac{1}{Q_{surface}} + \frac{1}{Q_{clamp}}. \tag{6.2}$$

In this work, the material damping is represented by $\tan\delta$ correspondig to (4.35) as introduced in chapter 4.4. The understanding of the intrinsic dissipation and its influence on the damping behavior at atmospheric pressure of polymer microresonators is of great interest from a technological but also from a fundamental point of view.

The intrinsic energy dissipation in silicon-based single-clamped microbeams has been thoroughly investigated. Surface-related relaxation mechanisms have been found to be responsible for the damping in submicron-thick silicon-nitride, polysilicon and single-crystal silicon cantilevers [35,93,94]. In micron-thick silicon-nitride cantilevers, thermoelastic dissipation was found to be significant [35,94] and support loss was determined to damp silicon cantilevers with a small length to thickness ratio [35,95].

Investigations of the intrinsic damping of double-clamped single-crystal GaAs and Si microbeams indicate that internal defect motion is the main loss mechanism [93]. Surface loss has been found to be the dominant loss mechanism in double-clamped amorphous silicon microbeams [96]. Recently, large quality factors have been measured in highly prestressed silicon-nitride nanostrings [97] and the thermoelastic damping (TED) was determined to be the dominant loss mechanism. But further investigations indicated that TED is not the limiting factor of the nanostrings. Neither the dominant dissipation nor the precise source of the increased quality factor resulting from additional tension could be determined [98]. In prestressed double-clamped polymer microbeams made of conducting PMMA the dominant dissipation was attributed to the internal material damping of the structural polymer [99].

[1] Reprinted with permission from [92]. Copyright [2008], American Institute of Physics.

The aspect of the understanding of the intrinsic dissipation in polymer microresonators and its influence on the quality factors at atmospheric pressure is the subject of this chapter. The damping mechanisms of single and double-clamped polymer microbeams with different thicknesses and varying lengths made of SU-8 are investigated. The intrinsic quality factors at high vacuum of the single-clamped (s-c) and the double-clamped (d-c) microbeams show values with a large discrepancy which was also observed between highly prestressed d-c and s-c silicon-nitride nanobeams [97]. It is evident that different intrinsic damping mechanisms are responsible for the dominant dissipation in single and prestressed d-c beams. It is shown that internal damping effects, such as TED or material damping, can not be directly applied to prestressed d-c microbeams.

For the experiments, samples made from two different fabrication processes, allowing the fabrication of two different sample thicknesses and different anchor geometries, were used. This makes it possible to investigate the damping of polymer microbeams with different flexural rigidities. In this way, samples of d-c microbeams can be obtained which show a more beam or stringlike mechanical behavior, whose mechanical model essentially differ. Whereas the s-c microbeams represent pure beamlike structures. The diverse beam lengths enables the measurement of quality factors over a wide range of frequencies.

The sample fabrication technique and the experimental details are provided, and then air damping in rarefied air is discussed, which is relevant for both single and d-c microbeams. To investigate the intrinsic damping mechanisms, the measurements have been made in high vacuum where air damping can be neglected. The damping mechanisms of the s-c and d-c polymer microbeams are analyzed separately.

The intrinsic damping values of the s-c microbeams are compared to various possible loss mechanisms such as clamping loss, thermoelastic damping, surface loss or material damping. The discussion will indicate that the s-c microbeams are mainly damped by the high material loss of the viscoelastic polymer.

The measured intrinsic quality factors of the prestressed d-c microbeams have values that are an order of magnitude higher than the material damping. Furthermore, the thermoelastic damping conflicts the measured data. It is shown that the influence of the internal dissipation due to flexure or elongation is small. The corresponding weighting factor is calculated. The discussion will indicate that the d-c polymer microbeams are dominantly damped by elastic waves propagating into the anchors.

Finally, the quality factors of single- and d-c microbeams are measured at atmospheric pressure. The damping behavior is explained by the sum of the squeeze-film air damping and the specific intrinsic damping.

6.1 Measuring the intrinsic damping

Damping of a system caused by the surrounding air is related to the surface area of the moving parts. In micromechanical systems, the ratio of surface area to volume becomes large and air damping can become the main source of energy dissipation. The pressure range can be divided into three regions where different damping mechanisms are dominant, namely the viscous, molecular and intrinsic region. Close to atmospheric pressure, the damping results by the viscous flow of the air caused by the movement of the vibrating microbeams which is discussed in section 6.4. In low vacuum, the mean free path of the gas molecules becomes larger than the typical dimensions of the damping structure. In this molecular region, the damping is caused by the collision of noninteracting air molecules with the microbeam. In the intrinsic region, the vacuum is low enough that air damping can be neglected. In order to get insight into the intrinsic damping mechanisms, the transition pressure between the molecular and the intrinsic region needs to be known.

Because of the requirement for electrostatic actuation, the vibrating polymer structures are close to the electrodes which are located on the substrate. The gas molecules which are trapped between the substrate and the lower beam side are responsible for the main air damping, the so called squeeze-film damping. A second part of the damping is due to gas molecules colliding with the upper side of the beam which corresponds to the damping of an isolated plate. The squeeze-film air damping and the damping of an isolated plate in low vacuum can be modeled by calculating the energy transfer from the plate to the gas molecules as done by Bao et al. [100] and by Christian [101], respectively. The energy transfer models are based on rigid oscillating plates. The air damping model for an isolated plate by Christian has been shown to also be valid for flexible beams [102]. For this work we assume that Baos model for squeeze-film damping of a rigid plate is also valid for flexible beams.

For a microbeam with a peripheral length L_p, thickness h and a distance d_0 to the substrate and a mass density ρ, the quality factor for squeeze-film damping in low vacuum by the energy transfer model (Baos model) is [100]

$$Q_{molecular,sq}(p) = (2\pi)^{\frac{3}{2}} \rho h \omega \frac{d_0}{L_p} \sqrt{\frac{R_{gas} T}{M_m}} \frac{1}{p} \tag{6.3}$$

and the damping of an isolated plate in rarefied air (Christians model) is [101]

$$Q_{molecular,iso}(p) = \frac{\rho h \omega}{4} \sqrt{\frac{\pi}{2}} \sqrt{\frac{R_{gas} T}{M_m}} \frac{1}{p} \tag{6.4}$$

where ω, T, M_m and R_{gas} are the oscillation frequency, temperature, Molar mass of the gas and the universal molar gas constant, respectively. Both damping effects are

reciprocally proportional to the pressure p. At the bottom side of the beam, squeeze film damping predominates while on the top side the damping of an isolated beam is added to the total air damping. The total damping including intrinsic and molecular damping can then be expressed by

$$Q^{-1} = Q^{-1}_{intrinsic} + Q^{-1}_{molecular,sq} + \frac{1}{2} Q^{-1}_{molecular,iso}. \tag{6.5}$$

In Fig. 6.1, the measured quality factors of a thin s-c and d-c microbeam are plotted against the air pressure. The quality factor values are fitted with $Q^{-1}(p) = Q^{-1}_{intrinsic} + C^{-1}_{molecular}\ p$ based on (6.5).The material properties used for the calculations are listed in Table 3.1. The values of the air damping parameter $C_{molecular}$ obtained by fitting and by calculation based on the molecular models are in a similar range for the d-c microbeam ($C_{molecular,calc} = 59315$ and $C_{molecular,fit} = 79308$) whereas they differ more for the s-c microbeam ($C_{molecular,calc} = 96605$ and $C_{molecular,fit} = 51488$). The discrepancy of the fit and the model for the s-c microbeam can be explained by the uncertain gap distance d_0 which probably is not constant due to a slight bending of the beam. It can be seen that the influence of air damping begins to vanish at pressures below 10 Pa and the quality factor reaches a plateau which is dominated by the intrinsic damping. All intrinsic damping measurements were performed at pressures below 0.05 Pa. At that pressure, the quality factor due to air damping is higher than 1×10^6.

The first resonant mode of thin and thick single and d-c SU-8 microbeams were measured at 25 °C. Due to the different beam lengths of the samples, Q values for a frequency range from 10 kHz to 5 MHz could be obtained. The measurement results are shown in Fig. 6.2. Obviously, the measured Q values of the s-c microbeams show a different behavior than the d-c microbeams. The specific dissipation mechanisms of the s-c and d-c microbeams are discussed in section 6.2 and 6.3, respectively.

6.2 Intrinsic damping mechanisms of single-clamped beams

From Fig. 6.2 it can be seen that the thin and thick s-c SU-8 microbeams have relative low quality factors which slightly increase from 30 at high frequencies to around 120 at lower frequencies. This behavior is discussed in this section.

6.2.1 Clamping loss

Loss due to radiation of vibrational energy through the anchor was determined by means of a 2D finite element model. The simulation was performed with HiQLab [103,104], a tool to compute clamping loss in microelectromechanical systems. It was

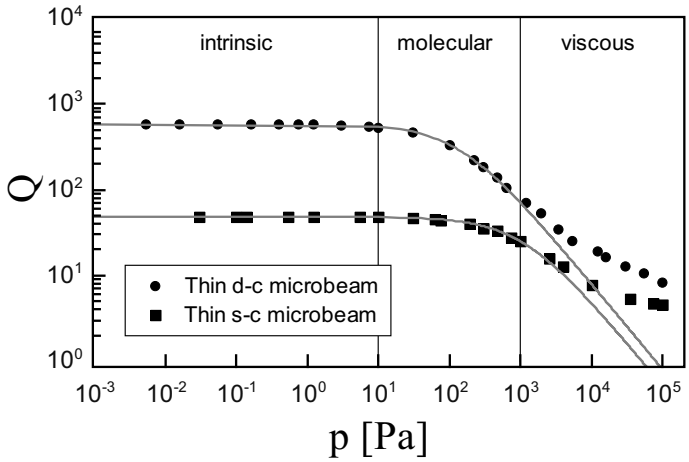

Figure 6.1: Quality factor plotted against air pressure, for a thin s-c (55 μm, long, 1.45 μm high, 14 μm wide) and thin d-c (250 μm long, 1.45 μm high, 14 μm wide) SU-8 microbeam, with a gap between substrate and beam of around 3 μm, resonating at 138.3 kHz and 222,7 kHz, respectively, and measured at 25 °C. The gray lines represent a fit with the damping model for the molecular region (6.5).

assumed that all elastic waves radiating into the substrate would not be reflected and thus would be lost. Therefore, the substrate was modelled as a semi-infinite domain by means of a perfectly matched layer (PML) at the boundaries. A PML absorbs waves of any angle of incident. Fig. 6.3 shows the displacement field of a s-c microbeam with an anchor terminated with a PML which absorbs all incoming elastic waves. The PML parameters were chosen by a heuristic method [105] in order to minimize unwanted reflections at the PML boundaries. The source code of the HiQLab FEM simulation is given in appendix C. Fig. 6.4 shows the comparison of the measured Q values and the simulated Qs due to clamping loss.

For the quality factor due to elastic wave radiation into an infinite anchor the following geometrical dependence was found [38, 106]

$$Q_{clamp} \propto \left(\frac{L}{h}\right)^3 . \tag{6.6}$$

The Q values obtained with the HiQLab simulation qualitatively coincide with (6.6), as can be seen by the fit in Fig. 6.4.

From the FEM simulation it is obvious, that clamping loss is too small to play a dominant role in damping behavior of the s-c beams. This finding is confirmed by the fact that clamping loss is a pure geometrical effect which is temperature indepen-

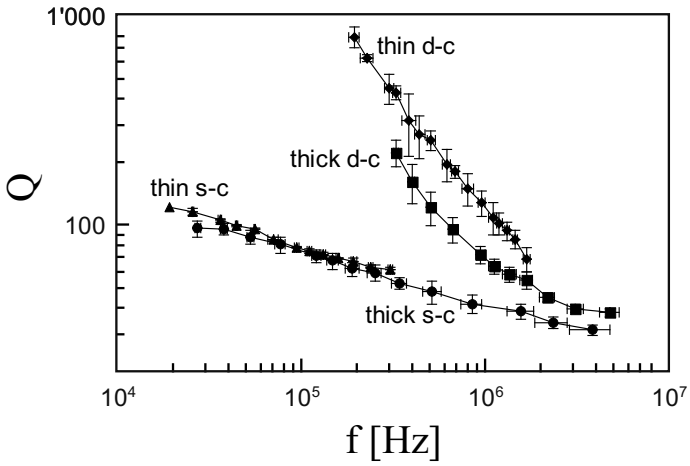

Figure 6.2: Quality factors plotted against the frequency for the 4 different types of structures that were fabricated. 32 thin s-c (4 × 13 microbeams with varying lengths, 20 beams were defect), 54 thin d-c (4 × 16 microbeams with varying lengths, 10 beams were defect), 126 thick s-c (9 × 14 microbeams with varying lengths), and 77 thick d-c (7 × 11 microbeams with varying lengths) microbeams have been measured at a pressure below 0.05 Pa at a temperature of 25 °C. The error bars represent the standard deviation of the obtained values from the different microbeams.

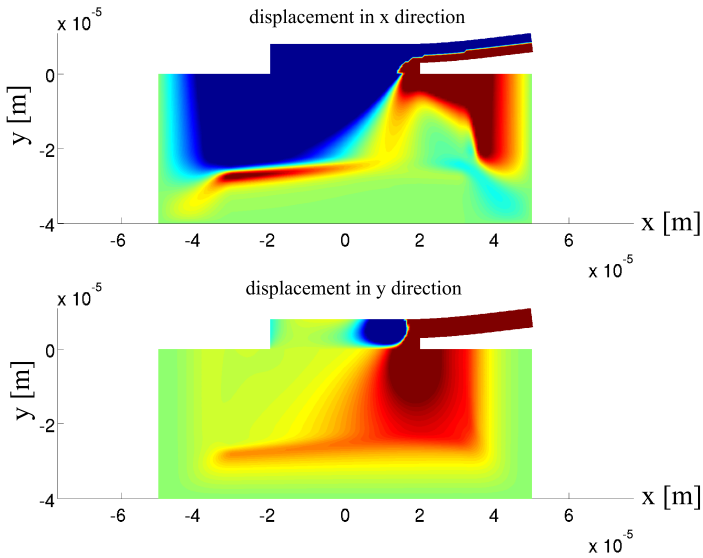

Figure 6.3: Displacement of a thick s-c microbeam simulated with HiQLab. The anchor is modelled as a semi-infinite domain by terminating it with a PML. Red areas experience a positive displacement blue areas a negative displacement.

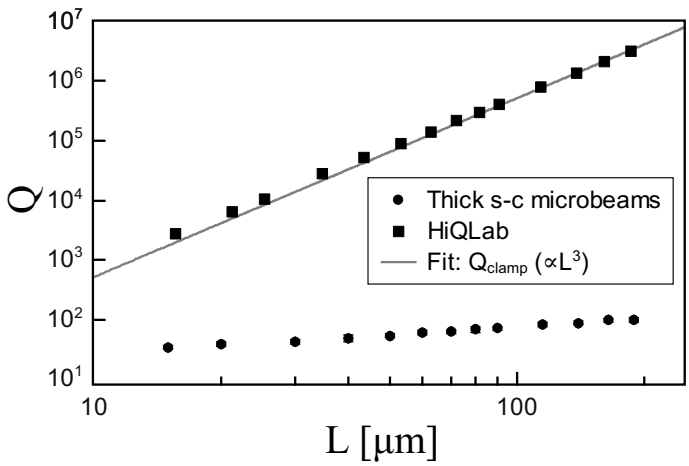

Figure 6.4: Comparison of the quality factors of thick single-clamped SU-8 microbeams (*thick s-c microbeams* from Fig. 6.2) and the calculated clamping loss values. The 2D finite element calculations were performed with HiQLab. The HiQLab values were fitted with the clamping loss model (6.6).

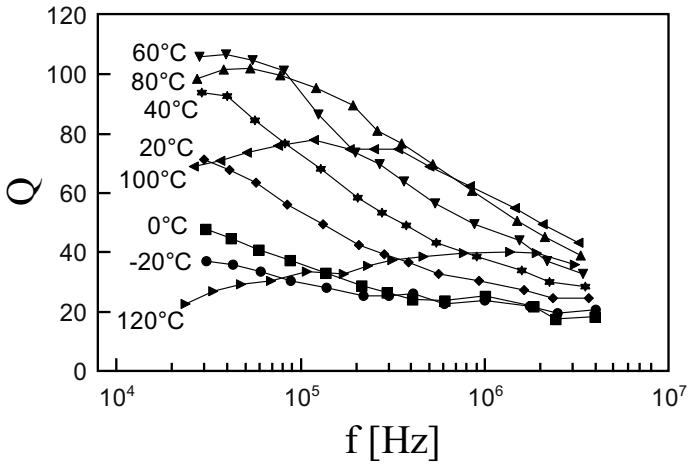

Figure 6.5: Quality factors of thick s-c SU-8 microbeams with a width of 12 μm and lengths from 15 to 185 μm at different temperatures from -20 to 120 °C measured at a pressure below 0.05 Pa.

dent assuming a constant Young's modulus. That means, if clamping loss would be the dominant source of energy dissipation in the thick s-c microbeams, the damping would not change with temperature. But temperature obviously has a large influence on the measured quality factors, as can be seen in Fig. 6.5 where for an array of thick s-c SU-8 microbeams, the quality factors were measured for temperature steps from -20 to 120 °C. Due to their smaller height to length ratio, the impact of the clamping loss on the total damping is even smaller for thin s-c microbeams than for the thick s-c microbeams.

6.2.2 Thermoelastic damping

Thermoelastic damping (TED) is caused by irreversible heat flow across the beam thickness. During vibration of a beam, one side is under compression while the other side is under tension. The strain field is coupled to the temperature field by the material's thermal-expansion coefficient α_{th}. The side under compression becomes warmer while the side with tension becomes colder. This temperature gradient across the beam thickness causes the energy loss. The maximum energy in an oscillation cycle is lost if the cycle time of the resonating beam is similar to τ_Z which is the time the heat needs to relax over the beam thickness. For lower vibration frequencies, the system stays more or less in equilibrium (isothermal state) and only little energy is lost. If the frequency of vibration is higher than the relaxation rate of the heat flow,

the heat has no time to relax (adiabatic state) and again very little energy is lost. An approximation for the thermoleastic model in beams was developed by Zener [107, 108] where the dissipation exhibits a Lorentzian behavior as a function of $\omega\tau_Z$ with a maximum value at $\omega\tau_Z = 1$. The Zener's model is very practical for the quantitative discussion of the TED. The exact expression for thermoelastic damping in vibrating thin beams was obtained by Lifshitz and Roukes [108]:

$$Q_{TED}^{-1} = \frac{Y\alpha_{th}^2 T_0}{\rho c_p}\left(\frac{6}{\xi_{TED}^2} - \frac{6}{\xi_{TED}^3}\frac{\sinh\xi_{TED} + \sin\xi_{TED}}{\cosh\xi_{TED} + \cos\xi_{TED}}\right) \tag{6.7}$$

where

$$\xi_{TED} = h\sqrt{\frac{\omega\rho c_p}{2\kappa}}. \tag{6.8}$$

This derivation of the expression for TED is based on the Euler-Bernoulli beam assumptions. Furthermore, in equilibrium, the beam is unstrained, unstressed and at temperature T_0.

Q_{TED} has a minimum peak at $\xi_{TED,0} = 2.225$ with a minimal value [108]

$$Q_{TED,min} \simeq 2.02\frac{\rho c_p}{Y\alpha_{th}^2 T_0} \tag{6.9}$$

which is independent of the dimensions of the beam. With the SU-8 material properties from Table 3.1 a minimal quality factor $Q_{TED,min}$ of 239 results. This is more than twice the maximal measured quality factor of the s-c microbeams.

In Fig. 6.6, the comparison of the measured quality factors of the thick and thin s-c microbeams with the TED model (6.7) is shown. In particular at the lowest measured frequency, the stagnation of the quality factor could be caused by the influence of TED. But for the quality factors measured above that frequency, a limitation due to thermoelastic effects in s-c SU-8 beams seems not to be significant. Comparing the quality factors of the thin with the thick s-c microbeams, it can be seen that the thin beams do not show the kink at the lowest frequency. Because they are thinner, the relaxation time τ_Z becomes shorter and the peak of the TED is located at a higher frequency (see gray TED lines in Fig. 6.6) where the effect on the total damping becomes small.

The measured Q values for the thin d-c microbeams also plotted in Fig. 6.6 overlap the curves of the corresponding TED model (6.7). This fact will be discussed in section 6.3.

6.2.3 Surface loss

Surface loss can be the dominant source of damping in submicrometer thick beams when the surface-to-volume ratio increases. Surface loss is assumed to be caused by

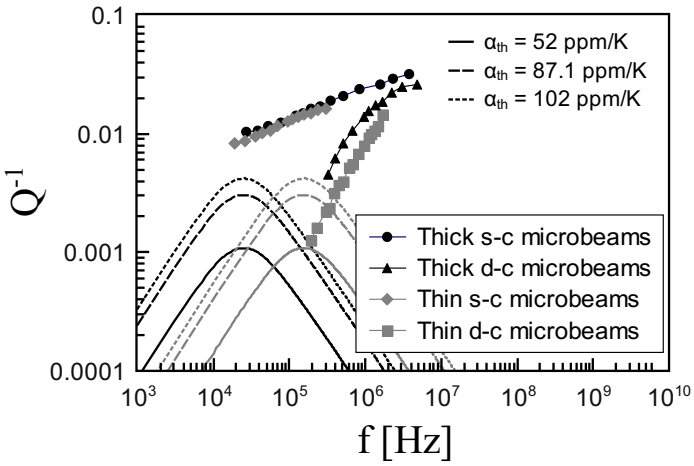

Figure 6.6: Comparison of the average quality factors of thick s-c (*thick s-c microbeams* from Fig. 6.2), thick d-c (*thick ds-c microbeams* from Fig. 6.2), thin s-c (*thin s-c microbeams* from Fig. 6.2) and thin d-c SU-8 microbeams (*thin d-c microbeams* from Fig. 6.2) with the corresponding thermoelastic damping for these structures at 25 °C. Because the reported values of the thermal-expansion coefficient α_{th} vary, three values that were reported [40, 45, 83] were used for the model calculations.

adsorbates on the surface modifying the surface stress [35] or by surface roughness interacting with surface waves [93]. The surface loss is given by [35, 94]

$$Q_{surface} = \frac{bh}{2\delta_S(3b+h)} \frac{Y}{Y_S''} \tag{6.10}$$

where δ_S and Y_S'' are the thickness and the loss Young's modulus of the surface layer and b is the beam width. For a thin beam ($b \gg h$), surface damping is proportional to the inverse of the beam thickness

$$Q_{surface} \propto \frac{h}{\delta_S}. \tag{6.11}$$

If surface loss would be the limiting damping mechanisms, the thin microbeams should have lower Q values than the thick beams. But the quality factor of the thin and thick s-c microbeams show similar values. Limiting quality factor values of around 1×10^4 have been measured in 170 nm thick single-crystal silicon cantilevers [35], which is more than two orders of magnitude higher than the measured Q values for s-c polymer beams. Surface loss can thus be neglected as an important damping mechanism of the measured SU-8 beams.

6.2.4 Material damping

SU-8 is an epoxy-type highly crosslinked polymer with a glass temperature T_g = 210 °C (Table 3.1). Polymers show a viscoelastic behavior. Not all the energy that is stored in the deformation of a viscoelastic material by external forces is available to restore the initial form when the external forces are released. That means that energy is lost in every vibrational cycle and the vibration gets damped. According to (4.35), the material damping is expressed by the loss tangent $\tan\delta$.

A comparison of our results with the measurement of Hossenlopp et al. [109] (Fig. 6.7) confirms the conclusion that the dominant damping mechanisms in the measured s-c SU-8 beams is the material damping. The loss tangent measured at 9 MHz by Hossenlopp et al. [109] completes the line of measured values from this work.

The material damping depends on the molecular structure of the polymer. SU-8 is a highly crosslinked amorphous polymer built of monomers with eight epoxy binding sites. One monomer is based on four bisphenol-A units connected to each other at the phenyl rings as shown in Fig. 3.1. Polymers containing the bisphenol-A compound, such as bisphenol-A polycarbonate (BPA-PC) (see Fig. 6.8a) or diglycidyl ether of bisphenol A (DGEBA) (see Fig. 6.8b), have an unusual toughness. Therefore, such polymers have been subject of numerous investigations of the dynamic mechanical behavior. Most polymers based on bisphenol-A show a distinct secondary transition at a vibrational frequency of 1 Hz at a temperature of -100 °C [110–112].

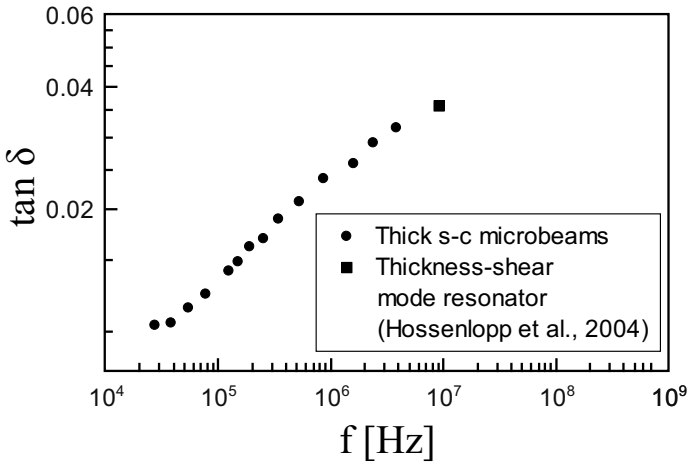

Figure 6.7: Comparison of the measured loss tangent of thick s-c SU-8 microbeams (*thick s-c microbeams* from Fig. 6.2) with a measured value of another group. Hossenlopp et al. [109] has mechanically characterized SU-8 thin films (10 - 20 μm) using a thickness-shear mode resonator at 9 MHz.

An associated activation energy of 60 kJ mol^{-1} can be determined for this secondary relaxation process. Thorough investigations based on dielectric analysis, dynamic mechanical analysis, different NMR techniques and atomistic modelling come to the conclusion that the molecular motions of the dynamic mechanical secondary transition of bisphenol-A polycarbonate originates mostly from the motion of the phenyl rings and its perturbation of the surrounding molecular structures [110]. Thus, the energy loss mainly comes from the oscillation and conformation flipping (π-flips) of the phenyl rings in the bisphenol-A.

For transitions occurring below the glass transition temperature, the frequency-temperature dependence obeys the Arrhenius law:

$$f_{trans,T} = f_{trans,0} \exp\left(-E_\alpha / R_{gas} T\right), \tag{6.12}$$

where E_α is the activation energy of the transition and R_{gas} is the universal gas constant. Assuming that the same submolecular relaxation mechanisms are responsible for the secondary solid-state transition in SU-8 and in bisphenol-A, (6.12) can be used to calculate the transition frequency or temperature, respectively, by using the corresponding activation energy of 60 kJ mol^{-1} reported in [110].

In Fig. 6.7, we see that the loss tangent is still increasing at the highest measured frequency of 3.8 MHz. A secondary transition due to phenyl ring motion at 25 °C

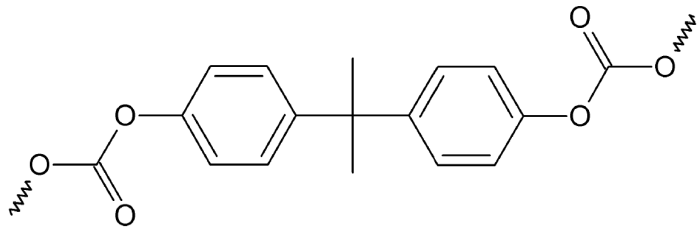

(a) Bisphenol-A polycarbonate (BPA-PC)

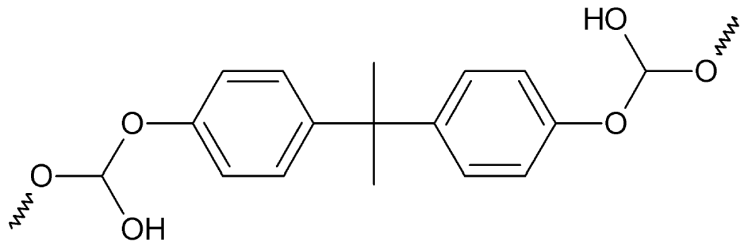

(b) Diglycidyl ether of bisphenol A (DGEBA)

Figure 6.8: Chemical structure of bisphenol-A polycarbonate (BPA-PC) (a) and diglycidyl ether of bisphenol A (DGEBA) (b).

would occur at a frequency $f_{trans,T} = 40$ MHz.

In Fig. 6.9, the loss tangent of thick s-c SU-8 microbeams with different length, and thus different resonant frequencies, are plotted against the temperature. The resonant frequency of the s-c microbeams are temperature dependent. Therefore, the average values are given in the legend. The calculated secondary transition due to the phenyl group motion would occur at -43.7 °C for 28.2 kHz and at -2.0 °C for 3.54 MHz.

The increasing loss starting at 100 °C could be the beginning of the primary transition, the so called glass transition.

The explanation of the material damping behavior of SU-8 with the secondary solid-state transition of the similar bisphenol-A compound seems to be plausible. But the loss tangent curves do not show pronounced transition peaks at the measured temperature and frequency range. In order to get certainty that the calculated transition peaks really coincide with the measured loss tangent, the temperature and frequency range would have to be extended.

6.3 Intrinsic damping mechanisms of double-clamped beams

The measured quality factors of the d-c microbeams are one order of magnitude higher than the Qs of s-c microbeams (see Fig. 6.2). Furthermore, in Fig. 6.6 the over-

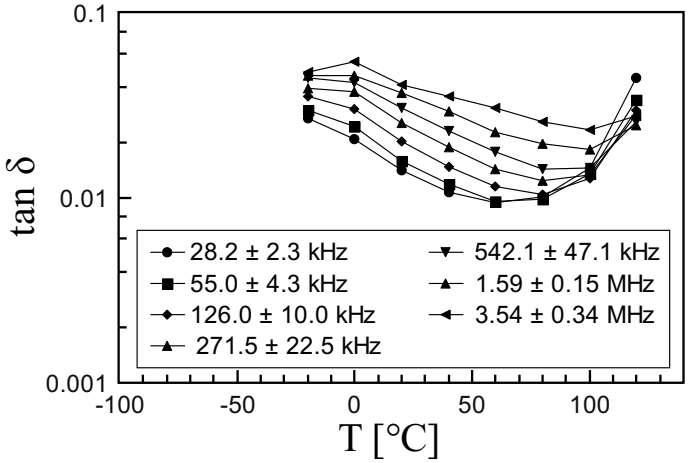

Figure 6.9: Average loss tangent of thick s-c SU-8 microbeams with a width of 12 μm and lengths from 15 to 185 μm at plotted against temperature measured at a pressure below 0.05 Pa (same data as shown in Fig. 6.5). The resonant frequency of the beams are temperature dependent. The average frequency values are given in the legend.

lap of the limiting thermoelastic damping and the data of the thin d-c microbeams is shown. The measured values enter the region limited by the thermoelastic damping. The damping of the d-c beams seems to be caused by different loss mechanisms than the damping of s-c beams. Therefore, the damping behavior of the d-c beams will be treated here separately.

6.3.1 String or beam

The eigenfrequency of a simply supported d-c beam with a tensile stress σ is given by [113]

$$f_0 = \frac{n^2\pi}{2L^2}\sqrt{\frac{YI_z}{\rho A}}\sqrt{1+\frac{\sigma A L^2}{n^2 Y I_z \pi^2}} \tag{6.13}$$

where n is the resonant mode number, A is the cross section and I_z is the geometrical moment of inertia. For low stress, (6.13) yields the equation of a simply supported unstressed Euler-Bernoulli beam whose eigenfrequency is proportional to the inverse to the beam length squared (4.12). If the thickness to length ratio of the beam is small and the resonant frequency is mainly defined by the tensile stress, the influence of the flexural rigidity diminishes and the eigenfrequency can be described by the model of a stretched string (4.24). In this case, the resonant frequency is proportional to the

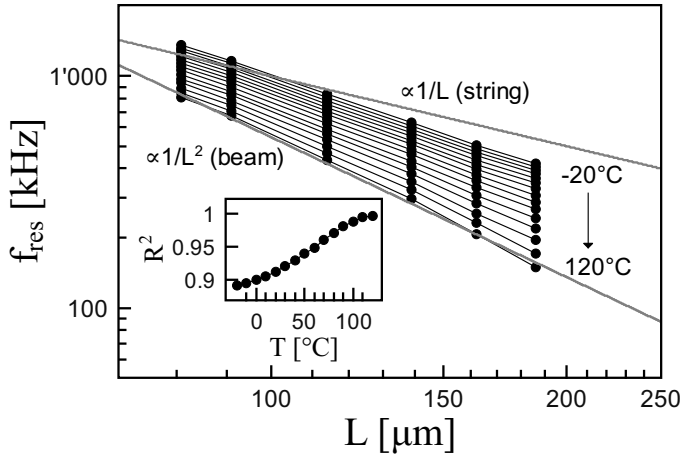

Figure 6.10: Resonant frequencies of thick d-c microbeams with different lengths plotted against their length L for a temperatures range from -20 to 120 °C at a pressure below 0.05 Pa. The upper fit represents the resonant frequency behavior of a string (4.24) and the lower fit represents the resonant frequency behavior of a beam (6.13) for $\sigma = 0$. The insert shows the coefficient of determination R^2 which represent the fit quality with the beam model.

inverse of the length.

The resonant frequency of d-c microbeams with different lengths were measured at different temperatures. The glass substrate has a smaller coefficient of thermal expansion than SU-8. Hence, the tensile stress in the beams increases with decreasing temperature and vice versa. Therewith, the prestress in the beams can be varied.

Fig. 6.10 shows that the thick d-c microbeams act like Euler-Bernoulli beams at elevated temperatures above 100 °C. The insert shows the coefficient of determination R^2 representing the fit quality of the beam model with the measured resonant frequencies. It depicts that at a temperature of 120 °C, that is with low prestress, the thick microbeams show a beamlike behavior. At lower temperatures, they mechanically behave somewhere inbetween a string and a beam.

Fig. 6.11 shows the stringlike behavior of the thin d-c beams at temperatures below 60 °C. The insert shows the coefficient of determination R^2 representing the fit quality of the string model with the measured resonant frequencies. It depicts that above a temperature of around 60 °C, the thin beams loose that distinct string behavior.

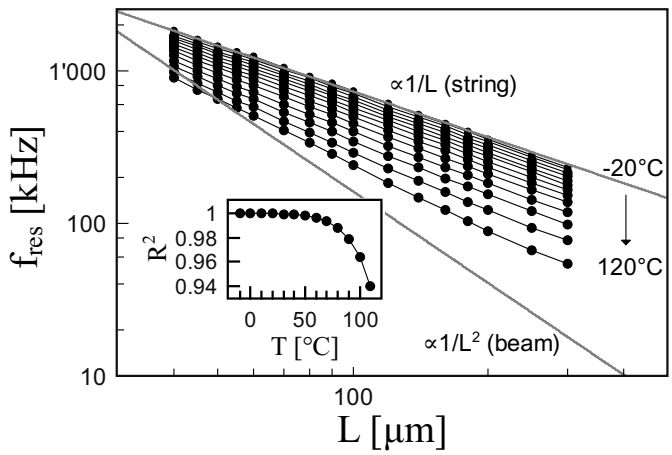

Figure 6.11: Resonant frequency of thin d-c microbeams with different lengths plotted against their length L for a temperature range from -10 to 110 °C at a pressure below 0.05 Pa. The upper fit represents the resonant frequency behavior of a string (4.24) and the lower fit represents the resonant frequency behavior of a beam (6.13) for $\sigma = 0$. The insert shows the coefficient of determination R^2 which represent the fit quality with the string model.

6.3.2 Internal damping of stretched strings

A string is a prestressed thread-like elastic continuum without flexural rigidity. The bending deflection $w(x,t)$ is assumed to be small and the prestress is big enough so that its change due to the string deflection can be neglected. That is, the effect of the elongation on the tensile force is neglected. Using these assumptions, the resonant behavior of a stretched string can be sufficiently modelled. But it would also predict the damping of a vibrating string to be zero in vacuum, due to the lack of extensional and flexural loss factors, which of course is not the case. In order to obtain the damping of a stretched string, the extensional and flexural strain energies coming from the elongation and curvature of the string in a deflected position have to be taken into account.

Following the definition of the quality factor (Eq. 4.35), the internal damping of a stretched string due to flexure and elongation can be written as [114]

$$Q^{-1}_{inter,str} = \frac{\Delta W_{elong} + \Delta W_{flex}}{2\pi(W_{pot} + W_{elong} + W_{flex})} \tag{6.14}$$

where W_{pot}, W_{elong} and W_{flex} are the potential, extensional and flexural energy of the oscillating string, respectively. ΔW_{elong} and ΔW_{flex} are the extensional and flexural energies lost during one cycle. Assuming the potential energy of a string to be significantly larger than the flexural or extensional energy, (6.14) can be written as

$$Q^{-1}_{inter,str} = \left(\frac{W_{elong}}{W_{pot}}\right) Q^{-1}_{elong} + \left(\frac{W_{flex}}{W_{pot}}\right) Q^{-1}_{flex} \tag{6.15}$$

with $Q^{-1}_{elong} = \Delta W_{elong}/(2\pi W_{elong})$ and $Q^{-1}_{flex} = \Delta W_{flex}/(2\pi W_{flex})$. The weighting factors in Eq. (6.15) are less than unity. Thus, the system damping of a stretched string is smaller than the internal damping due to flexure and elongation. Consequently, stretched strings are interesting structures for the fabrication of resonators made from highly damped materials such as polymers. The effect of a very small system damping of stretched strings was also observed in silicon nitride nano strings [97].

The explicit form of (6.15) can be calculated. The deflection in z-direction of a double clamped stretched string aligned in x-direction is [89]

$$w_n(x,t) = z_0 \sin\left(\frac{n\pi}{L}x\right) e^{i\omega t} \quad n = 1, 2, 3, \ldots \tag{6.16}$$

where z_0 is the amplitude of the oscillation.

The potential energy of a stretched string is defined by the work done against the tension force $S = \sigma A$ for a given deflection w_n. For a piece of string with an infinites-

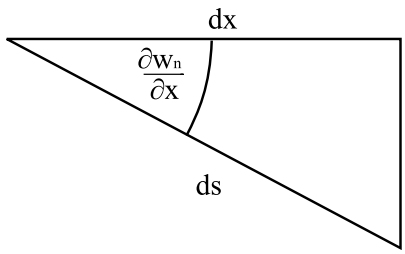

Figure 6.12: Schematic drawing of an infinitesimal piece of string.

imal length dx the potential energy is

$$\mathrm{d}W_{pot} = S(\mathrm{d}s - \mathrm{d}x) = S\left(\sqrt{1+\left(\frac{\partial w_n}{\partial x}\right)^2} - 1\right)\mathrm{d}x \tag{6.17}$$

where ds is the stretched length of dx when deflected. Using the Taylor series representation of the square root, neglecting all orders ≥ 2, the potential energy of a stretched string becomes

$$\begin{aligned} W_{pot} &= \int_0^L S\left(\sqrt{1+\left(\frac{\partial w_n}{\partial x}\right)^2} - 1\right)\mathrm{d}x \\ &\approx \int_0^L S\left(1+\frac{1}{2}\left(\frac{\partial w_n}{\partial x}\right)^2 - 1\right)\mathrm{d}x = \frac{1}{2}\sigma A\int_0^L\left(\frac{\partial w_n}{\partial x}\right)^2\mathrm{d}x. \end{aligned} \tag{6.18}$$

By inserting (6.16), the potential energy (6.18) becomes at $t = 0$

$$W_{pot} = \frac{1}{4}\frac{\sigma A(z_0 n\pi)^2}{L}. \tag{6.19}$$

The elongational strain energy W_{elong} can be derived by integrating the elongational energy stored in a infinitesimal piece of string with the length dx over the length of the string. The energy stored in an infinitesimal piece of string dx when strained to the length ds is

$$\mathrm{d}W_{elong} = \int_0^{\mathrm{d}s-\mathrm{d}x}\sigma(\zeta)A\mathrm{d}\zeta = \int_0^{\mathrm{d}s-\mathrm{d}x}\varepsilon(\zeta)YA\mathrm{d}\zeta \tag{6.20}$$

where ζ is the additional length which is added to dx due to the elongation. With the strain $varepsilon = \zeta/\mathrm{d}x$, (6.20) becomes

$$\mathrm{d}W_{elong} = \frac{1}{2}YA\frac{(\mathrm{d}s-\mathrm{d}x)^2}{\mathrm{d}x} \tag{6.21}$$

By using the Taylor series approximation, as done for (6.18), the energy stored in an infinitesimal piece of string becomes

$$\begin{aligned} \mathrm{d}W_{elong} &= \frac{1}{2}YA\left(\sqrt{1+\left(\frac{\partial w_n}{\partial x}\right)^2}-1\right)^2 \mathrm{d}x \\ &\approx \frac{1}{2}YA\left(1+\frac{1}{2}\left(\frac{\partial w_n}{\partial x}\right)^2-1\right)^2 \mathrm{d}x = \frac{1}{8}YA\left(\frac{\partial w_n}{\partial x}\right)^4 \mathrm{d}x. \end{aligned} \tag{6.22}$$

By integrating over the length L, the elongational energy stored in a string reads

$$W_{elong} = \frac{1}{8}YA\int_0^L \left(\frac{\partial w_n}{\partial x}\right)^4 \mathrm{d}x. \tag{6.23}$$

Inserting (6.16), we obtain for the elongational energy at $t = 0$

$$W_{elong} = \frac{3}{64}\frac{YA(n\pi z_0)^4}{L^3}. \tag{6.24}$$

Taking (6.15) and inserting (6.19) and (6.24), the system damping due to elongational dissipation of a stretched string is

$$Q^{-1}_{elong,str} = \frac{3(n\pi)^2}{16}\frac{Y}{\sigma}\left(\frac{z_0}{L}\right)^2 Q^{-1}_{elong}. \tag{6.25}$$

The weighting factor is dependent on the vibration amplitude z_0, thus the influence of the string damping due to elongation can be minimized by driving the vibration at low amplitudes.

The flexural strain energy is given by [61]

$$W_{flex} = \frac{1}{2}YI_z\int_0^L \left(\frac{\partial^2 w_n}{\partial x^2}\right)^2 \mathrm{d}x. \tag{6.26}$$

Assuming a rectangular cross section and inserting (6.16), (6.26) becomes at $t = 0$

$$W_{flex} = \frac{1}{48}\frac{YA(hz_0)^2(n\pi)^4}{L^3}. \tag{6.27}$$

With Eq. (6.15) and inserting (6.19) and (6.26), the system damping due to flexural dissipation of a stretched string with a rectangular cross section is given by

$$Q^{-1}_{flex,str} = \frac{(n\pi)^2}{12}\frac{Y}{\sigma}\left(\frac{h}{L}\right)^2 Q^{-1}_{flex}. \tag{6.28}$$

Unlike the weighting factor of the damping due to elongation (6.25), the weighting factor of the flexural damping is independent of the vibration amplitude but dependent on the height h. For $z_0 \ll h$, $Q^{-1}_{elong,str}$ is very small compared to $Q^{-1}_{flex,str}$. In

all of the measurements made during this work, the ratio between the vibration amplitude and beam thickness has always been $(z_0/h)^2 < 10^{-6}$. Thus neglecting the elongational damping is well justified and the damping of a stretched string can be represented by (6.28) only.

$$Q^{-1}_{inter,str} \approx Q^{-1}_{flex,str} \tag{6.29}$$

This result depicts that flexural damping effects such as TED, surface- and material damping can not be applied directly to stretched string structures. For stretched strings, the internal flexural damping mechanisms have to be represented by (6.28).

If the measured quality factors of the thin d-c microbeams are compared to $Q_{flex,str}$, it can be seen that the minimal damping of a string without any external loss factors would be significantly lower than the measured values (Fig. 6.13). It is not only the magnitude, but also the proportionality of the quality factors, that do not fit. Thus, the limiting damping factor of the thin d-c microbeams must be an external damping mechanism. This finding is further confirmed by the measurements presented in Fig. 6.14 where for an array of thin d-c SU-8 microbeams, the quality factors were measured for temperature steps from -10 to 110 °C. The quality factors are independent of temperature for temperatures below 60 °C. Eq. 6.28 predicts an increasing Q for an increasing tensile stress, which is the case when lowering the temperature, as shown in the insert of Fig. 6.14 (The tensile stress behavior in theses structures will be discussed in detail in section 7.2.1). In the insert of Fig. 6.11 the stringlike behavior of the thin d-c beams is depicted by the coefficient of determination R^2 of the fit with the string model. At around the same temperature of 60 to 70 °C, the beams start to act like strings. That means, the damping is not limited by the internal flexural damping anymore and an external loss mechanisms becomes dominant.

6.3.3 Clamping loss

As discussed before, it appears that an external damping mechanism must be responsible for the stagnating quality factors measured for the thin d-c microbeams at temperatures below 60 °C. This external loss mechanisms seems to be temperature independent. As already mentioned above, clamping loss is a pure geometrical and therefore temperature independent damping mechanism.

Cross and Lifshitz have modelled the elastic wave transmission at an abrupt junction in a thin plate [115]. The geometry that was modelled is composed of a small floating bridge of rectangular cross section. The bridge is connected to two larger blocks of the same thickness at both ends. This geometry is schematically depicted in Fig. 6.15. The boundary conditions of this model come very close to the geometry of the structures used in this work where the beams are anchored at a suspended

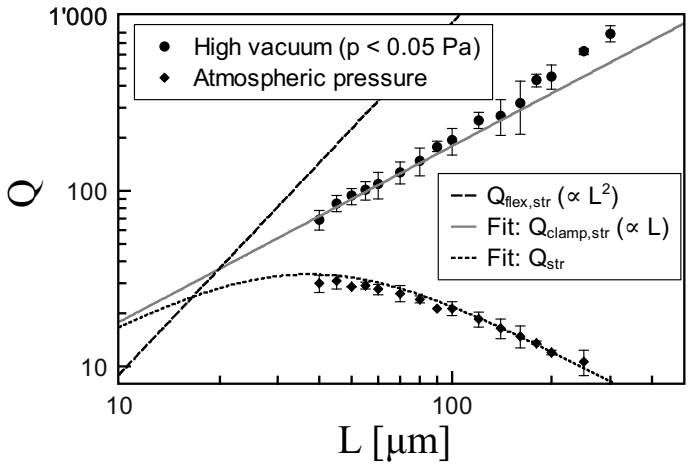

Figure 6.13: Quality factors of thin d-c microbeams at high vacuum (*thin d-c microbeams* from Fig. 6.2) and at atmospheric pressure measured at 25 °C. The intrinsic loss at high vacuum is fitted with $Q_{clamp,str}$ (6.30) and compared to $Q_{flex,str}$ (6.28) assuming $Q_{flex} = 30$. The axial stress σ of 20.9 MPa and 18.1 MPa was determined for the measurements in high vacuum and at atmospheric pressure, respectively. For the calculation of Q_{str} (6.33) the following values were used $d_0 = 3\mu m$, $b = 14\mu m$, $h = 1.45\mu m$ and $\mu = 18.4 \times 10^{-6}$ Pa sec.

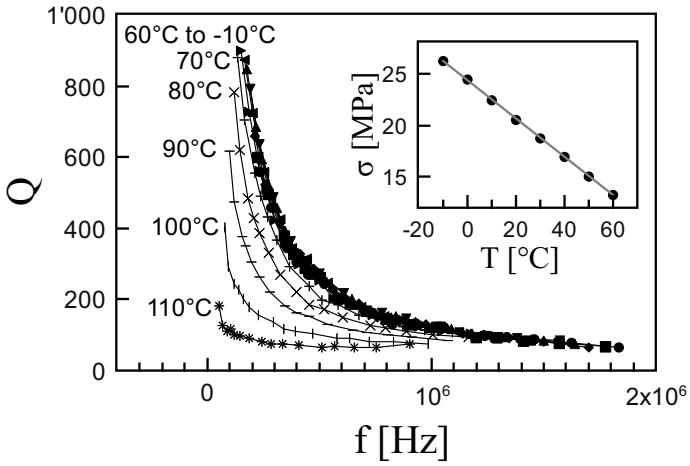

Figure 6.14: Quality factors of thin d-c SU-8 microbeams with lengths from 40 to 300 μm measured at different temperatures from -10 to 110 °C at a pressure below 0.05 Pa. The insert shows the prestress σ obtained with the corresponding resonant frequencies (4.24) for the temperature range from -10 to 60 °C where the string model is valid (see insert in Fig. 6.11). More details about the evaluation of the prestress is presented in section 7.2.1.

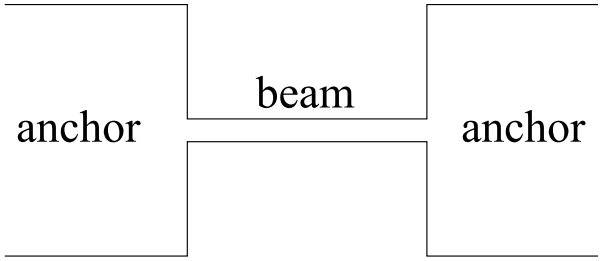

Figure 6.15: Schematic of boundary conditions of the elastic wave transmission at an abrupt junction in a thin plate by Cross and Lifshitz [115].

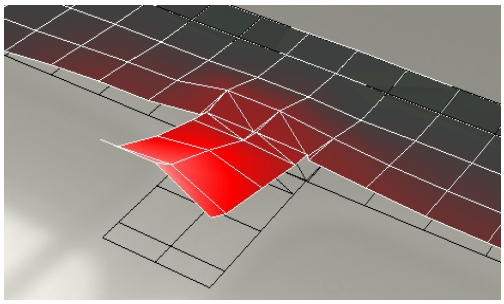

Figure 6.16: Scan with the laser-Doppler vibrometer of the deflection of the suspended anchor plate at the first resonant vibration of a 100 μm long thin d-c microbeam. The anchor features an undercut length of 11.04 μm and is 1.45 μm thick.

plate (see Fig. 3.4). In Fig. 6.16, the deflection of the suspended anchor during vibration of a stringlike double-clamped microresonator is shown. The model predicts a flexural vibration energy loss with a quality factor which is proportional to the beam length [115]

$$Q_{clamp,str} \propto L. \tag{6.30}$$

The anchor features an undercut length of 11.04 μm and a thickness of 1.45 μm and has a measured resonant frequency $f_{res,AP} = 3.41 \pm 0.02$ MHz and a measured quality factor $Q_{AP} = 36.3 \pm 2.2$. The insert shows the scan of the deflection of the freestanding anchor site at the first resonant vibration of a 100 μm long thin d-c microbeam.

Fig. 6.13 shows the measured quality factors of the thin d-c microbeams fitted with (6.30). The length proportionality (6.30) coincides well with the measured quality factors. Hence, the quality factors of the stringlike thin d-c SU-8 microbeams seem

evidently to be limited by the energy dissipating into the suspended anchor plates.

6.4 Damping at atmospheric pressure

After the determination of the intrinsic damping mechanisms in the previous sections, in this section the samples are measured at atmospheric pressure. Because of the small gap distance d_0 between the beams and the substrate compared to the beam width b the main damping source in the viscous pressure region (see Fig. 6.1) is the squeeze film damping. When a plate is moving perpendicular towards a wall, the air film in between the plate and the wall is squeezed, causing an increasing pressure. In the movement away of the wall, the pressure is reduced. In both cases, the built up pressure induces a damping force on the plate. The quality factor due to squeeze-film air damping of a long rectangular beam ($L \gg w$) oscillating in the normal direction to the substrate is [61]

$$Q_{viscous} = \frac{\rho h d_0^3 2\pi f_{res}}{\mu b^2} \tag{6.31}$$

where μ is the viscosity of the gas surrounding the beam and f_{res} is the resonant frequency.

In Fig. 6.17 and Fig. 6.13 the measured quality factors at atmospheric pressure of thick s-c and thin d-c microbeams, respectively, are compared to the intrinsic damping measured at high vacuum. The quality factors are increasing with increasing frequency for both types of microbeams having a low resonant frequency and a long length L, respectively, according to (6.31). At high frequencies or with short beam lengths, respectively, the Q values are limited by the particular intrinsic damping. The quality factors of the thick s-c microbeams are limited by the material damping and the quality factor of the thin d-c microbeams are limited by the clamping loss. The total damping is the sum of the intrinsic damping and the air damping. This behavior was also observed with s-c silicon microbeams [95] where clamping loss was found to be the dominant intrinsic damping mechanism at high frequencies.

The total damping of the stringlike thin d-c microbeams at atmospheric pressure can be expressed by

$$Q_{str}^{-1} = Q_{viscous}^{-1} + Q_{clamp,str}^{-1}. \tag{6.32}$$

With (6.31), (4.24) and (6.30) the total damping (6.32) can be written with respect to the string length L as

$$Q_{str}(L)^{-1} = (C_{viscous}\ \frac{1}{L})^{-1} + (C_{clamp}\ L)^{-1} \tag{6.33}$$

with

$$C_{viscous}(\sigma) = \frac{n\pi h d_0^3 \sqrt{\rho}}{\mu b^2}\sqrt{\sigma}. \tag{6.34}$$

A fit of the model for the total damping according to (6.33) of the thin d-c microbeams is shown in Fig. 6.13. The parameter C_{clamp} is obtained by fitting the intrinsic damping at high vacuum. The value of the squeeze-film damping parameter obtained by fitting $C_{viscous,fit} = 0.0025$ is smaller than the calculated value of $C_{viscous,calc} = 0.0051$. This discrepancy possibly comes from the model imprecisions and from geometrical uncertainties such as the gap distance d_0 which strongly influences the damping value. Unlike at high vacuum where the smallest damping was measured for the longest string structures, the quality factors of the thin d-c microbeams at atmospheric pressure are maximal for

$$L_{max}(\sigma) = \sqrt{\frac{C_{viscous}(\sigma)}{C_{clamp}}} \tag{6.35}$$

with a maximum quality factor of

$$Q_{str,max}(\sigma) = \frac{1}{2}\sqrt{C_{viscous}(\sigma)\ C_{clamp}}. \tag{6.36}$$

This damping model indicates that quality factors at atmospheric pressure can be maximized by increasing the resonant frequency of long stringlike d-c microbeams. This could either be done by increasing the tensile stress σ [98] or by actuating the beams at a higher resonant mode [95]. But the maximum intrinsic stress is limited by the relative low tensile strength of polymers which for SU-8 in particular is 60 MPa (Table 3.1). The drawback of increasing the resonant mode is the resulting rise of the internal damping in strings due to flexure which is proportional to n^2 (6.28). Another way to increase the quality factors for both s-c and d-c microbeams is to minimize air damping which can be done by an optimal design featuring a large gap distance d_0 (6.31).

6.5 Conclusion

The quality factors of single and d-c polymer microbeams with different lengths were measured and the corresponding damping mechanisms were investigated. In order to get insight into the intrinsic energy dissipation mechanisms, the pressure at which air damping can be neglected was evaluated. At a pressure below 10 Pa the intrinsic damping is dominant. The quality factors due to intrinsic damping of s-c and prestressed d-c SU-8 microbeams showed quality factors of 60 and 790, respectively, at a frequency of around 200 kHz at a pressure below 0.05 Pa and a temperature of 25 °C. The dominant damping mechanisms of s-c and prestressed d-c polymer microbeams which differ more than one order of magnitude were investigated for both types of structures separately.

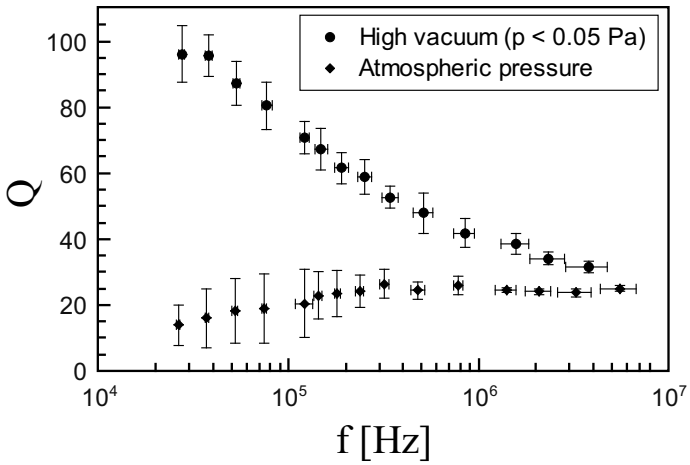

Figure 6.17: Quality factors of thick s-c microbeams at atmospheric pressure and at a high vacuum (*thick s-c microbeams* from Fig. 6.2) measured at 25 °C.

After excluding thermoelastic damping, surface damping and clamping loss as potential dominant damping mechanisms for the s-c SU-8 microbeams it was shown that they are mainly damped by the high material damping. The measured quality factors from 30 at 3.8 MHz to 120 at 19.1 kHz are in agreement with a material damping measurement of SU-8 made by another group. Furthermore, the temperature dependent damping behavior could be plausibly explained by a solid-state transition theory for a well-known bisphenol-A compound which has a similar chemical structure like SU-8.

Plotting the resonant frequency against the beam length revealed that the thin d-c microbeams act like strings. String-like beams have a system damping which is lower than the flexural damping. Therefore, quality factor values of more than 720 at 20 °C were measured with structures made of SU-8 with an material damping of $Q = 70$ at the corresponding frequency and temperature. It is important that internal damping mechanisms such as TED, surface loss or material damping can not be directly applied to stringlike microbeams. The quality factors of the d-c microbeams was found to be limited by the energy loss due to radiation of the elastic waves into the suspended anchor plates which is proportional to the beam length.

When the quality factors were measured at atmospheric pressure, at low frequencies, the dominant damping mechanism of polymer microbeams was found to be air damping which is proportional to the resonant frequency. At higher frequencies, the s-c microbeams are mainly damped by the internal material damping and the thin d-

c microbeams are mainly damped by the intrinsic clamping loss. A maximal Q value for the thick s-c microbeams in air of 26 at a frequency of 783 kHz and for thin d-c microbeams of 31 at a frequency of 1.38 MHz (beam with a length of $L = 45\mu m$) was measured. The quality factor of beamlike resonators made from polymer materials are low due to the dominant internal material damping, therefore an optimization of Q is difficult. But prestressed stringlike polymer microresonators are promising devices which theoretically can overcome the high material damping. The limiting intrinsic damping and air damping can be minimized by using long strings with a high resonant frequency. This demand can be achieved by applying a high tensile stress to the long string or by the actuation at a higher mode. But polymer materials have a relatively low tensile strength which limits the maximum tensile stress they can bear and the actuation at a higher resonant mode would increase the internal damping in strings with a factor of n^2. The maximization of the quality factor at atmospheric pressure of polymer microresonators would be an interesting investigation that is important for the future application of polymer materials in resonant MEMSs.

7 Tensile stress and Young's modulus

In this chapter, the influence of temperature and time on the resonant frequency of beamlike and stringlike polymer microbeams is investigated. For a given geometry, the eigenfrequency of an undamped beam (4.14) and an undamped string (4.24) are exclusively defined by the Young's modulus and the tensile stress, respectively. Therefore, the investigations are strongly focused on these two parameters. Determining the natural frequency of resonant beamlike and stringlike microstructures permits the evaluation of the Young's modulus [34, 39] and residual stress [39, 53], respectively.

Damping can lead to significant differences between the natural and the measured resonant frequency. With (4.9), the resonant frequency of a damped resonator (4.8) can be written as

$$\omega_r = \omega_0 \sqrt{1 - \frac{1}{2Q^2 + 1}}. \tag{7.1}$$

In Fig. 6.5, the quality factors of s-c microbeams for a frequency range of 20 kHz to 4 MHz and a temperature range of -20 °C to 120 °C is shown. The quality factor is always > 20. Inserting this minimal Q value in (7.1) gives a maximum discrepancy of

$$\omega_r = 0.9994 \cdot \omega_0. \tag{7.2}$$

Thus, for all subsequent measurements performed in high vacuum ($p < 0.05$ Pa), the resonant frequency can be assumed to the equal to the undamped natural frequency or eigenfrequency of the microbeams.

7.1 Young's modulus of single-clamped microbeams

The s-c SU-8 microbeams can be modelled as Euler-Bernoulli beams (4.14). For a constant geometry, the eigenfrequency of the beams is proportional to the square root of the Young's modulus Y. All the data presented in this section was measured with s-c beamlike microbeams. First, the frequency dependent Young's modulus is evaluated. Then, the temperature influence and aging of the Young's modulus are investigated.

As already discussed, in Fig. 6.5 it can be seen, that the lowest quality factors for a frequency range of 20 kHz to 4 MHz and a temperature range of -20 °C to 120 °C

have a value of around 20. This quality factor of the s-c microbeams is a result of the material damping. Therefore, a maximum loss tangent of $\tan\delta < 0.05$ has to be assumed. Inserting this value into (4.37), the magnitude of the complex Young's modulus becomes

$$\|Y^*\| = 1.0012 \cdot Y'. \tag{7.3}$$

Thus, the magnitude of the complex Young's modulus can be approximized by the storage Young's modulus that is the general Young's modulus. In the subsequent subsections, the Young's modulus is used instead of the complex Young's modulus.

7.1.1 Frequency dependence of the Young's modulus

SU-8 is a crosslinked amorphous polymer which is expected to show viscoelastic behavior. The relaxation mechanisms in the material are strongly dependent on the time scale. For increasing vibration frequencies the time scales become shorter and the viscoelastic material has no time to relax. Consequently, the Young's modulus is expected to increasing with frequency [42, 116].

The frequency dependent Young's modulus is evaluated with thin s-c microbeams. These structures have the advantage that the film thickness is very homogeneous compared to the thick s-c microbeams whose thickness vary over the beam length.The drawback of the thin s-c microbeams is the suspended anchor plate. The Bernoulli-Euler beam theory assumes perfectly clamped ends which is not given in these structures. Thus, an extended model was developed which includes the typical nonideal suspended anchors. This model, which is presented in appendix E, calculates the effective beam length L_e thereby taking the effect of the suspended anchors into account. With the effective length, the structures can be analyzed by the Euler-Bernoulli model (4.14). This analytical model yields a transcendental frequency equation which is simple to solve analytically. For short beams ($L = 50\ \mu$m), the extended model yield errors of up to 5% whereas for long beams (200 μm) the error is $< 1\%$. Applying the plain Euler-Bernoulli model, errors of 100% and 20% for short and long beams are obtained. Nevertheless, because the extended model requires a numerical solver and still producing errors, the Young's modulus is determined by a model based analysis based on an finite element method (FEM). The first mode resonant frequencies of single-clamped microbeams with varying lengths are measured and the Youngs modulus is calculated by an iterative FEM simulation [117]. The eigenfrequency of the beam for a given geometry is computed for an assumed Young's modulus. The obtained eigenfrequency is then compared to the measured resonant frequency and the Young's modulus is iteratively adjusted until the difference of the computed and measured frequency value are below a defined threshold of 0.1% of the measured resonant frequency. The accuracy of the finite element simulation was determined to

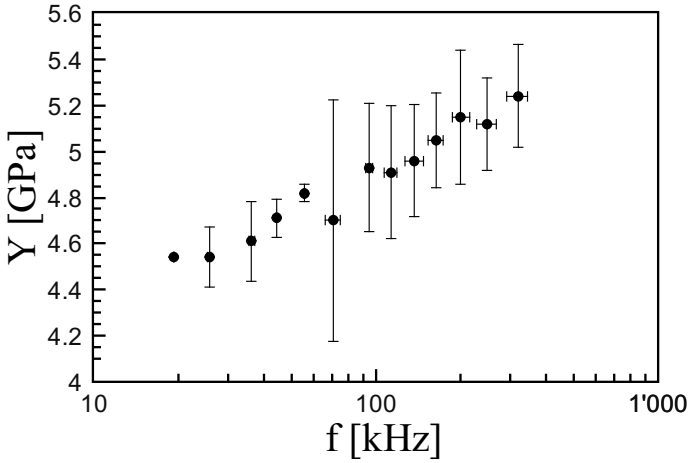

Figure 7.1: The mean Young's modulus of 38 thin s-c microbeams (from 5 different samples with 2 to 15 beams each) with lengths from 30 to 140 μm evaluated by iterative FEM from resonant frequencies measured at a pressure below 0.05 Pa at a temperature of 25 °C. For the FEM simulations, a Poisson's ratio of 0.26 and a mass density of 1200 kg m^{-3} were assumed. The error bars represent the standard deviation of the obtained values.

be $< 0.2\%$ by means of a convergence analysis. The algorithm which was developed to adjust the values of the Young's modulus is presented in appendix D.

Fig. 7.1 shows the Young's modulus determined from the resonant frequencies of single-clamped SU-8 beams. The average values are slightly increasing with frequency. This gradual increase with increasing frequency is a typical behavior for a polymeric glass [118] and was also observed for microbeams made of blended PMMA [119]. According to this, the values of the measured dynamic Young's modulus are higher than the static value for SU-8 of 4.02 GPa measured by a tensile test [62].

The high error of the calculated values of the Young's modulus mainly comes from uncertainties in the determination of the exact dimensions of the microbeams. The mean error for all samples is 0.21 GPa. The deviation of the SU-8 film thickness of $\pm$ 40 nm (measured with the white light interferometer) and the beam length of $\pm$ 1 μm (measured with an optical microscope) results in a mean modulus deviation of $\pm$ 0.23 GPa. This random error is determined by the Gauss error propagation [120] for a corresponding Euler-Bernoulli beam (4.12). The rise of the errors for the modulus above 100 kHz might come from differences in the optical determination of the sample geometry of a chip which only has microbeams with resonant frequencies

>100 kHz.

In addition to the random error, the absolute values for the frequency dependent Young's modulus have a systematic error. The uncertainties of the assumed material properties, by assuming relative errors for the Poisson's ratio of 0.26 ± 10% and the mass density of 1200 kg/m^3 ± 3%, lead to a systematic error of the Young's modulus of + 6.48% and -6.21%. These values are obtained by including the material property errors into the FEM simulation. Even if the error of the dimensions would be neglected, the error due to uncertainties of the assumed material properties would be relatively large. Therefore, the obtained values of the modulus are of interest for a qualitative discussion of the frequency dependence and to a lesser extend for a quantitative determination.

7.1.2 Temperature dependence of the Young's modulus

In polymer materials there are molecular rearrangement processes whose speed depend on the motion of the participating molecules and thus on the temperature. An increase of the temperature accelerates relaxation mechanisms and hence a temperature change is equal to a shift in the effective time scale. This phenomenon is called *time-temperature equivalence*. If the speed of all relaxation processes are influenced by the same extent by a temperature change, the material is called *thermorheologically simple* and the relaxation Young's modulus can be written as [90]

$$Y(t,T) = Y(\gamma, T_0), \quad with\ \gamma = \frac{t}{a_T(T)} \tag{7.4}$$

where γ is called the reduced time, T_0 is a reference temperature, and a_T is the shift factor. If the temperature is increased, the relaxation processes are accelerated and consequently the Young's modulus is expected to decrease.

From (4.14) the Young's modulus can be defined by the eigenfrequency of the beam for a given beam dimension $Y \propto f_{0,beam}^2$. The relative change of the Young's modulus with respect to a reference temperature T_0 can thus be written as

$$\delta Y_{T_0}(T) = \frac{f_{0,beam}^2(T) - f_{0,beam}^2(T_0)}{f_{0,beam}^2(T_0)}. \tag{7.5}$$

The resonant frequency of thin and thick s-c SU-8 microbeams were measured at different temperatures. The average relative change of the resonant frequency δf and of the Young's modulus δY by means of (7.6) for a reference temperature of 20 °C are plottet in Fig. 7.2. Both, the relative frequency and modulus change are fitted with a linear function. This linear fit is not based on a material model. It only is an approximation for the description of the Young's modulus behavior between -20 and

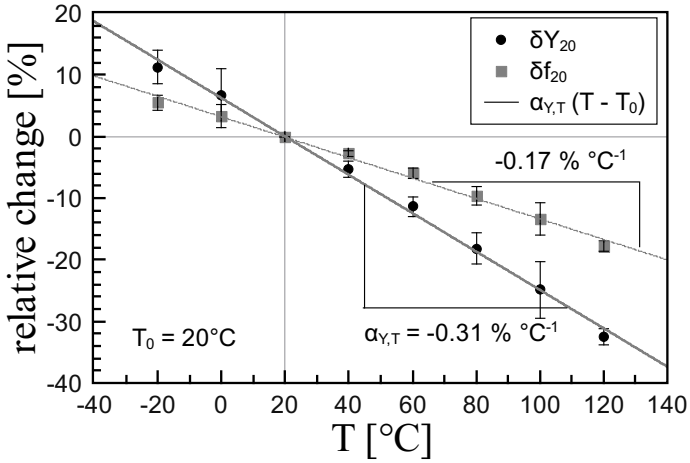

Figure 7.2: The average relative Young's modulus and resonant frequency change of 22 thin s-c SU-8 microbeams with lengths from 30 to 140 μm and 13 thick s-c SU-8 microbeams with lengths from 13 to 180 μm with respect to the reference temperature $T_0 = 20\,°\mathrm{C}$. The measurements were performed at a pressure below 0.05 Pa. The gray line is the linear model (7.6) fitted to the measurement data δY and the dotted line is a linear fit for δf.

120 °C. δY is thus described by a linear coefficient of temperature induced change of the Young's modulus $\alpha_{Y,T}$

$$\delta Y_{T_0}(T) = \alpha_{Y,T}(T - T_0). \tag{7.6}$$

Beside the softening of the polymer, an increasing temperature also induces a change of the dimensions of the structure due to thermal expansion of the material. This geometry change also results in a shift of the resonant frequency. This effect is evaluated by means of the Euler-Bernoulli beam theory. The geometrical dimensions of the beam are expanding by the factor $\alpha_{th}\Delta T$ where $\Delta T = T - T_0$ is the temperature difference between the temperature T and the reference temperature T_0. But also the mass density changes with the thermal expansion. Consequently, (4.12) can be written as

$$\begin{aligned} f_{0,beam}(T) &= \frac{\lambda_j^2}{2\pi}\frac{h_0(1+\alpha_{th}\Delta T)}{L_0^2(1+\alpha_{th}\Delta T)^2}\sqrt{\frac{Y}{12\rho_0(1+\alpha_{th}\Delta T)^{-3}}} \\ &= f_{0,beam}(T_0)\sqrt{1+\alpha_{th}\Delta T} \end{aligned} \tag{7.7}$$

where $f_{0,beam}(T_0)$ is the natural frequency at the reference temperature. The frequency of an Euler-Bernoulli beam experiences a positive shift when the beam ex-

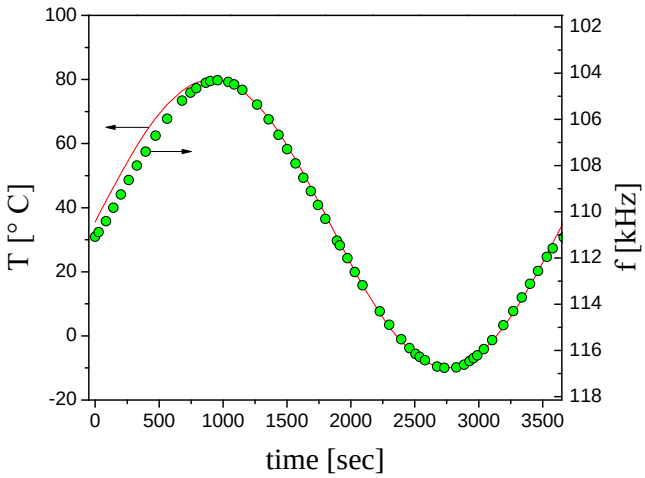

Figure 7.3: The resonant frequency of a thin s-c SU-8 microbeam with a length of 50 μm measured at a pressure below 0.05 Pa for a temperature cycle.

pands. For a coefficient of thermal expansion of $\alpha_{th} = 52$ ppm/K [45], a maximal relative frequency shift of +0.0026%/ °C results. This relative frequency shift due to thermal expansion is two orders of magnitude smaller compared to the measured relative frequency shift of -0.17%/ °C (see Fig. 7.2) and is thus neglected.

The resonant frequency change with respect to the temperature shows an approximately linear behavior for the temperature range from -20 to 100 °C. The linear fit in Fig. 7.2 reveals that the Young's modulus of SU-8 in average is changing by $\alpha_{Y,T} = -0.31 \pm 0.01$ %/ °C.

Fig. 7.3 shows the resonant frequency of a thin s-c microbeam for a sinusoidal temperature cycle from -10 to 80 °C. In this measurement, the linear behavior of the resonant frequency with respect to the temperature is evident.

The temperature sensitivity of the Young's modulus of SU-8 with $\alpha_{Y,T} = -0.31$%/ °C is high. To compare, the temperature dependence of Si microresonators is more than two orders of magnitude smaller ($\alpha_{Y,T}$ = -0.0013% [121]). This high temperature dependence of the material properties of SU-8 has to be taken into account for any resonant applications based on mechanical SU-8 structures.

7.1.3 Aging of the Young's modulus

Beside the chemical aging which occurs during polymerization and crosslinking of a polymer material, the physical aging is the material property change with time due to thermodynamic processes. In amorphous glassy polymers, aging is the slow continuation of the glass formation below the glass transition temperature T_g. If an amorphous material is quenched below T_g it is not in a thermodynamic equilibrium. The material has a higher volume and a higher entropy than it would have in the equilibrium state. Thus, quenched amorphous glass slowly approaches equilibrium. During aging, the material becomes more dense, stiffer, and more brittle [122].

Aging can be affected by mechanical deformation [118]. Therefore, to accelerate the physical aging, in one experiment thin s-c microbeams were actuated at an oscillation with high amplitudes, and in another experiment the temperature was cycled. This cycling causes the material to periodically expand and contract due to thermal expansion resulting in a periodic mechanical deformation. Fig. 7.4 shows the relative change of the Young's modulus and of the resonant frequency of thin s-c microbeams that were driven by a sinusoidal driving signal in ambient air at room temperature for 46 days. The resonant frequency was measured in a vacuum at any one time.

Fig. 7.5 shows the relative change of the Young's modulus and of the resonant frequency of thin s-c SU-8 microbeams for which the temperature was cycled while stored in vacuum for 36 days.

In both mid term experiments, the Young's modulus is increasing with time. The increase of the stiffness of the samples that were actuated at a high amplitude (Fig. 7.4) is steady. The resonant frequency of the samples exposed to temperature cycles (Fig. 7.5) increased faster in the beginning and after 10 days the change slows down and continues uniformly. At the start of the long time measurement, there still could be a few unbound epoxy groups that crosslink at the maximum cycle temperature of 80 °C. This final curing could lead to the observed fast stiffening and thus fast increase of the resonant frequency in the beginning of the experiment.

Despite the high crosslink density the Young's modulus of SU-8 is changing with time. Consequently, resonant s-c microbeams made of SU-8 can have a changing resonant frequency of up to one percent in one month due to aging.

7.2 Tensile stress of double-clamped microbeams

The thin d-c SU-8 microbeams can be modelled as strings (4.24) as shown in section 6.3.1. For a constant length L, the eigenfrequency of the strings is proportional to the square root of the tensile stress σ. All the data presented in this section was measured with the thin d-c microbeams. In a first subsection the influence of the

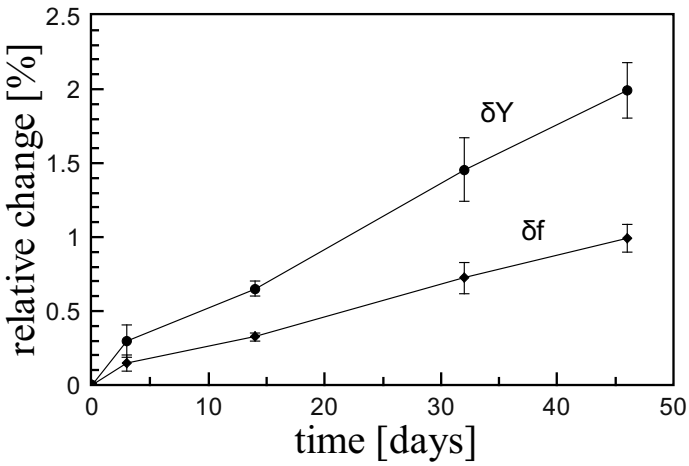

Figure 7.4: The relative change of the Young's modulus and of the resonant frequency of 10 thin s-c SU-8 microbeams (all 60 μm long and 1.4 μm thick). The average resonant frequency at $t = 0$ was 107.3 kHz $\pm$1.2 kHz. They were driven at atmospheric pressure at room temperature at frequency of 100 kHz and with an average displacement amplitude of 111 nm $\pm$14 nm for 1104 h. The measurements were done at a temperature of 25 °C and a pressure of p $<$ 0.05 Pa for any one time.

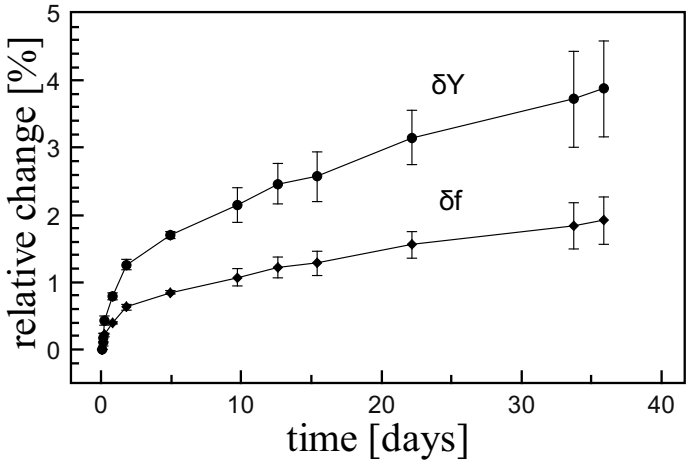

Figure 7.5: The relative change of the Young's modulus and of the resonant frequency of 9 thin s-c SU-8 microbeams with lengths from 30 to 140 μm, stored in a vacuum with a pressure $p < 0.01$ Pa. The temperature was sinusoidally cycled from -10 to 80 °C in a time interval of 60 min. The measurements were done at a temperature of 20 °C for any one time.

temperature on σ is investigated. In the second subsection, the change of σ as a function of time and temperature is determined.

7.2.1 Temperature dependence of tensile stress

The resonant frequency of a string is given by (4.24) and it is mainly defined by the pre-stress σ. As discussed in section 6.3.1, the strings have a certain strain which comes from the different coefficient of thermal expansion of the substrate and the polymer. If the volume of the polymer expands due to the thermal expansion, the strain in the string is released which results in a resonant frequency decrease. Assuming the volume expansion to be a linear function of the temperature, the total strain in the string can be written as

$$\varepsilon = \varepsilon_{pre} - (\alpha_{th,str} - \alpha_{th,sub})(T - T_0) \tag{7.8}$$

where ε_{pre} is the pre-strain of the string, $\alpha_{th,str}$ and $\alpha_{th,sub}$ are the coefficients of thermal expansion of the string material and the substrate material, respectively. Beside the change of the strain, the temperature also influences the Young's modulus $Y(T)$ as shown in section 7.1.2. Using the linear stress-strain relation and neglecting the

transverse strain, the stress in the polymer string as a function temperature becomes

$$\begin{aligned}\sigma(T) &= Y(T)\left(\varepsilon_{pre} - (\alpha_{th,str} - \alpha_{th,sub})(T - T_0)\right)\\ &= Y_0(1 + \alpha_{Y,T}(T - T_0))\left(\varepsilon_{pre} - (\alpha_{th,str} - \alpha_{th,sub})(T - T_0)\right)\\ &= (1 + \alpha_{Y,T}(T - T_0))\left(\sigma_{pre} - Y_0(\alpha_{th,str} - \alpha_{th,sub})(T - T_0)\right).\end{aligned} \tag{7.9}$$

Beside the tensile stress, the resonant frequency of a string is also a function of the mass density. Due to the thermal expansion of the volume, the mass density changes with temperature and the eigenfrequency (4.24) can be written as

$$f_{0,str}(T) = \frac{1}{2L}\sqrt{\frac{\sigma(T)}{\rho(1 + \alpha_{th}(T - T_0))^{-3}}}. \tag{7.10}$$

The eigenfrequency shift due to a mass density change assuming $\alpha_{th} = 52$ ppm/K [45] can be calculated and a value of 0.0078%/ °C is obtained. It is too small to contribute significantly to the total frequency shift and the mass density is assumed to be constant over the measured temperature range.

Calculating the influence of the softening of the Young's modulus assuming $\alpha_{Y,T} = -0.31\%/\ ^\circ\mathrm{C}$, as determined in section 7.1.2, gives a shift factor of -1.6%/ °C, which is high enough to be taken into account. Thus finally, the eigenfrequency of a string as a function of temperature can be approximized by

$$f_{0,str,T_0}(T) = \frac{1}{2L}\sqrt{\frac{(1 + \alpha_{Y,T}(T - T_0))\left(\sigma_{pre} - Y_0(\alpha_{th,str} - \alpha_{th,sub})(T - T_0)\right)}{\rho}} \tag{7.11}$$

and the relative change of the eigenfrequency then is

$$\delta f_{0,str}(T) = \sqrt{\frac{(1 + \alpha_{Y,T}(T - T_0))\left(\sigma_{pre} - Y_0(\alpha_{th,str} - \alpha_{th,sub})(T - T_0)\right)}{\sigma_{pre}}} - 1. \tag{7.12}$$

The prestress of a string can be determined from the resonant frequency (4.24). The average prestress determined from 16 thin d-c microbeams at each temperature step is shown in Fig. 7.6. The coefficient of thermal expansion of SU-8 can be extracted from the fit of the tensile stress presented in Fig. 7.6 with (7.9). This yields a value of $\alpha_{th,SU-8} = 47.9 \pm 3.9$ ppm/K for a fit in the temperature range from -10 to 60 °C (where the string model is valid, see insert in Fig. 6.11). The error is obtained by fitting (7.9) to the sum of the average prestress values and the corresponding standard deviation. The substrate is a borosilicate glass wafer with $\alpha_{th,glass} = 3.25$ ppm/K. The obtained value for the coefficient of thermal expansion of SU-8 is close to the published value of 52 ppm/K [45].

Fig. 7.7 shows the relative change of the resonant frequency δf of thin d-c SU-8 microbeams with respect to temperature. The reference temperature is chosen to be

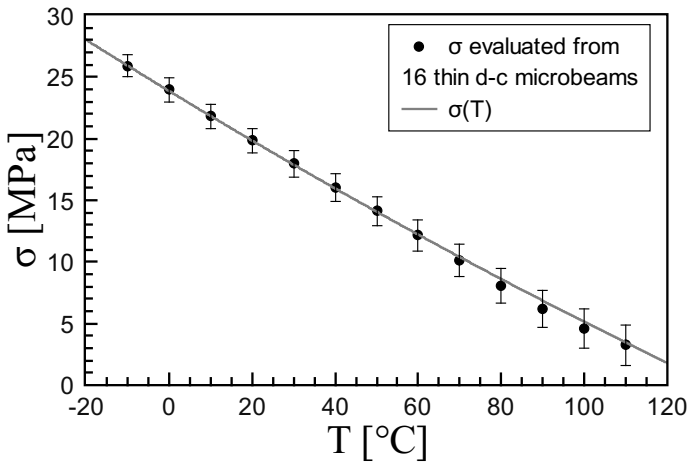

Figure 7.6: The average prestress σ obtained from 16 thin d-c microbeams (lengths from 40 to 300 μm) measured at a vacuum of 0.05 Pa assuming a mass density of $\rho =$ 1218 kg/m^3. The gray line is the fit with $\sigma(T)$ (7.9) for the temperature range from -10 to 60 °C for $\alpha_{th,sub} = 3.25$ ppm/K for silicon, a Young's modulus of Y_0 =4 GPa. From the fit, a coefficients of thermal expansion of $\alpha_{th,str} = 47.86 \pm 3.9$ ppm/K is obtained. The error bars represent the standard deviation obtained from the 16 different microbeams.

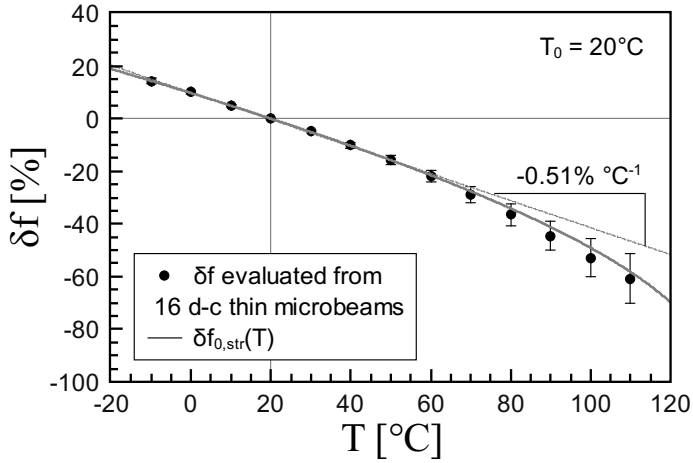

Figure 7.7: The relative change of the resonant frequency δf of 16 thin d-c microbeams (same whose data are shown in Fig. 7.6) with respect to temperature change. The relative change is calculated for a reference temperature $T_0 = 20$ °C. The measurements were performed at a pressure below 0.05 Pa. The gray line represents the model (7.12) for the parameter extracted from the fit of the prestress in Fig. 7.6. The error bars represent the standard deviation from the 16 different microbeams.

T_0=20 °C. The function of the relative frequency change (7.12) is plotted for the parameters extracted from the fit in Fig. 7.6. Over the temperature range from -10 to 60 °C, the relative frequency change is fitted with a linear function obtaining a frequency shift of -0.51% per °C. The temperature dependence concerning the resonant frequency of the d-c microbeams (-0.51%/ °C) is significantly higher than of the s-c microbeams (-0.16%/ °C) (see Fig. 7.2). This is because the prestress is influenced more by the temperature than the Young's modulus.

7.2.2 Relaxation of tensile stress

Relaxation is a fundamental phenomenon for viscoelastic materials. As explained in section 4.4, if a viscoelastic material is subjected to a constant strain, the stress decays with time.

$$\sigma(t) = \varepsilon Y(t) \tag{7.13}$$

The relaxation behavior can be described on an empirical basis by mechanical linear spring-dashpot models. The simplest transient response function involve a single

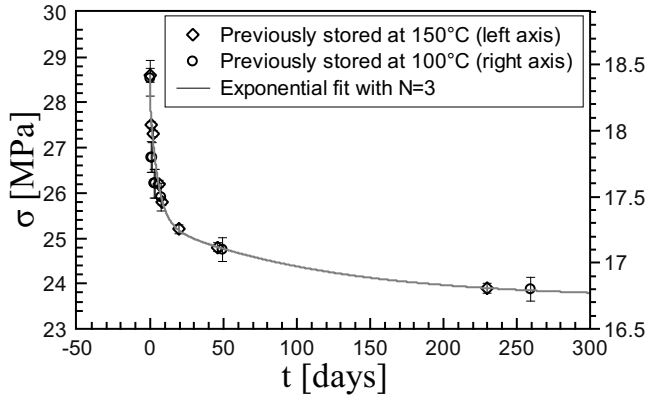

Figure 7.8: Relaxation of the intrinsic stress of 2 samples. One with 10 and the other with 15 double-clamped SU-8 microbeams measured at 25 °C with lengths from 40 to 250 μm. One sample was previously stored at 100 °C for 134 hours and the other was stored at 150 °C for 163 hours. The data of the sample which was stored at 150 °C was fitted with (7.15) with $N = 3$ with a longest relaxation time of $\tau_3 = 113.7$ days. The measurements were performed at a pressure below 0.05 Pa.

exponential and the relaxation modulus $Y(t)$ is written as

$$Y(t) = Y_0 e^{-t/\tau_r} \tag{7.14}$$

where Y_0 the initial Young's modulus and τ_r is called the relaxation time. But real materials in general can not be described by first order exponential decay functions. If there are multiple internal relaxation mechanisms, the relaxation function can be described by the sum of N exponentials [90]

$$Y(t) = \sum_{j=0}^{N} \lambda_j e^{-t/\tau_n}. \tag{7.15}$$

Here, the λ's are weighting coefficients.

Fig. 7.8 shows the prestress decay at 25 °C of thin d-c microbeams that previously were stored at elevated temperatures at which the material relaxed and got stress free. The sample stored at 150 °C expands more than the sample stored at 100 °C and it therefore yields a higher stress after cool down. Both samples however show a similar relaxation behavior which is fitted with a third order exponential decay function (7.15).

Fig. 7.9 shows the relaxation of a thick d-c SU-8 microbeam that was stored at 130 °C. The temperature was quenched to 20, 60, and 100 °C each time starting at

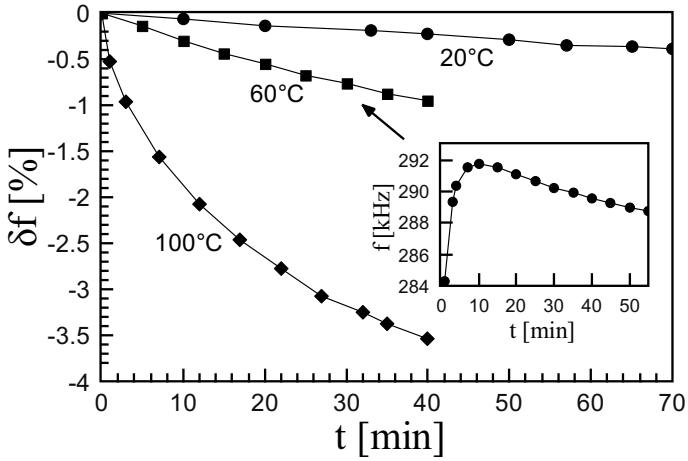

Figure 7.9: Relative resonant frequency change of a thick d-c microbeam (200 μm long and 12 μm wide). The structure was heated up to 130 °C and the cooled down to 20, 60, and 100 °C, with resonant frequencies at t=0 of 364.9 kHz, 291.5 kHz, and 202.8 kHz, respectively. The insert shows the resonant frequency gradient after cooling down to 60 °C. The measurements were performed at a pressure below 0.05 Pa. The black lines are a guide to the eye.

130 °C. Due to the different pre-stress at different temperatures, the resonant frequencies differ strongly for each cooling temperature. In order to compare the relaxation behavior at different temperatures, the relative frequency changes are plotted against time. Directly after cooling down, the frequency increases due to an increasing tensile stress. If the target temperature is reached, the material starts to relax and the frequency slowly starts to decrease (see insert in Fig. 7.9). The relative frequency shifts shown in Fig. 7.9 are started at the top dead center when relaxation begins.

Eventhough SU-8 is a highly crosslinked thermoset, pronounced stress relaxation has been observed in d-c microbeams which confirms the relaxation measurements of SU-8 membranes by Bernd Schöberle [85]. The relaxation curves obey a third order exponential decay with a maximum relaxation time of 114 days at a temperature of 25 °C. The relaxation time can be decreased by increasing the temperature. This can be concluded indirectly by measuring the resonant frequency gradient of a prestressed thick d-c microbeam at different temperatures. Even though the stress is smaller at elevated temperatues, the relaxation time is accelerated. Also for highly cross-linked polymers, the elastic energy storage appears to be based largely on an entropy effect [123] as it is the case for amorphous glassy polymers. In microstruc-

tures, the crosslinks seem to play a minor role in the glassy state.

7.3 Conclusion

The Young's modulus is frequency dependent, as it is expected for a viscoelastic material. The modulus is increasing from around 4.54 GPa at 19 kHz to 5.24 GPa at 318 kHz. Corresponding to the time-temperature equivalence, temperature has the opposite effect and the Young's modulus is decreasing with increasing temperature. A linear relative change of the Young's modulus of -0.31% per °C is determined. Temperature and frequency have a relatively large influence on the stiffness of SU-8 and has to be taken into account when designing a polymer MEMS. Furthermore, SU-8 show a pronounced aging behavior. The modulus was increasing up to 4% over a period of around a month when the temperature was cycled from -10 to 80 °C in a time interval of 60 min. By actuating the samples at room temperature, also a stiffening of up to 2% is observed.

Due to the different coefficient of thermal expansion of the substrate and the structural polymer, the tensile stress in 16 d-c SU-8 microbeams is varying from 25.9 MPa to 12.2 MPa for temperatures from -10 to 60 °C. By subtracting the expansion of the substrate and by taking the softening of the polymer into account, a coefficient of thermal expansion of 47.9 $\pm$3.9 ppm/K is obtained by assuming a static Young's modulus of 4.0 GPa. As polymers in general, SU-8 is also strongly expanding with increasing temperature. Therefore, the resonant frequency of d-c polymer microbeams is highly sensitive to temperature changes. Relative frequency shifts of d-c SU-8 microbeams of -0.51% per °C were measured for a temperature change from 20 to 60 °C.

The relaxation of the tensile stress of stringlike d-c SU-8 microbeams was investigated over a period of around 250 days. Two samples with different thermal history and hence with different tensile stress values showed a similar relaxation behavior. The relaxation was fitted with a third order exponential decay function with a maximum relaxation time of 114 days. The stress relaxation can be accelerated if the samples are stored at elevated temperatures. SU-8 shows a pronounced relaxation behavior even though it is highly crosslinked.

Over all, the tensile stress and with it the resonant frequency of d-c SU-8 microbeams are highly sensitive to temperature changes. This temperature sensitivity has to be taken into account when designing polymer based microsystems. The temperature influence can be minimized by choosing a substrate material with a similar coefficient of thermal expansion as the polymer structural material.

8 Influence of air humidity

[1]It is well known, that polymer materials are sensitive to humidity. Polymers are therefore often used as sensitive materials in humidity sensors [125]. There are several transduction techniques [126] such as the gravimetric technique which detects the mass load due to the absorbed water [31,127,128], the capacitive technique which measures the change of the dielectric constant [127, 129, 130], the calorimetric technique which detects the amount of heat that is generated in the polymer during absorption [127], the resistive technique which measures the resistance change of a conductive polymer [130], and the hygrometric technique where the change of the volume of the polymer due to the absorbed water vapor is detected [31, 131, 132].

In this chapter, the influence of the relative humidity (RH) on the resonant frequency of the resonant microbeams made from SU-8 is investigated. The resonance behavior is modelled based on the specific mechanical property changes due to the moisture uptake such as swelling, mass loading and plasticization and the dominant effects for different mechanical structures are determined.

Glassy polymers are in a frozen non-equilibrium state and the movement of the polymer chain backbones is largely restricted. Nevertheless, inbetween the frozen molecular chains, there are holes and voids, the "free volume"', which provides the sorption sites to accommodate penetrants and to allow the movements through the polymer matrix. The permeation of a liquid or a vapor can induce a swelling of the polymer, which consequently alters its properties. For liquids in polymers, the sorbed volume can reach 20% and more. Liquids are able to open up intermolecular bonds in the polymer. Therefore, the absolute flux of a liquid or a vapor through a polymer can be 2 to 3 orders of magnitude higher than for a noncondensible gas [41]. Water in particular has the ability to form hydrogen bonds with other water molecules but also with polar groups in the polymer. The amount of water which is absorbed by a polymer is called "moisture". The moisture content M at equilibrium is related to the mass of the sorbed water to the mass of the dry polymer.

$$M(RH, T) = \frac{m_{water}}{m_{dry\ polymer}} \tag{8.1}$$

The moisture content is a function of the absolute humidity but also of the temperature. Thus, the sorption behavior has to be determined isothermally.

[1] Reprinted with permission from [124]. Copyright [2009], IOP Publishing.

Relative humidity (RH) is defined by the ratio of the mass of water vapor in a unit volume compared to the maximum mass of water vapor which would be held in that volume when it is saturated at a given temperature. The relative humidity RH for a given temperature is given in percentage

$$RH = 100\frac{P_w}{P_s} \tag{8.2}$$

where P_w is the water vapor pressure and P_s is the saturated water vapor pressure.

8.1 Water vapor absorption in polymers

A cornerstone of the theory of water transport is based on the superposition of three distinct sorption mechanisms [41] as schematically shown in Fig. 8.1. The main phenomena is the dissolution of water in the polymer based on Henry's law. This law predicts a linear relationship between the RH and the moisture in the polymer. A second mechanism is adsorption of water molecules filling microvoids. This adsorption mechanism can be described by a Langmuir isotherm. The effect occurs at low RH concentrations. A third phenomenon is based on the formation of clusters inside the polymer matrix at higher RH concentrations ($> 60\%$). Water clusters can increase the diffusion coefficient resulting in a higher water transport through the polymer at higher RH concentrations. The cluster formation can be described by an exponential function [132]. It can be concluded that very hydrophilic polymers form large water clusters. As a result, the polymer is highly swollen and the diffusion coefficient becomes large. Polymer with a well balanced hydrophilicity and hydrophobicity form small clusters and the water diffusion if reasonably high. Highly hydrophobic polymers form large clusters where water separates from the polymer matrix. The diffusion coefficient decreases. SU-8 is slightly hydrophilic with a contact angle of 65.8 °C ±6.1 °C (see Appendix F). Thus, the water diffusivity is high and the formation of small clusters at high RH has to be expected. Crosslinked epoxy resins, such as SU-8, offer hydroxyl groups as can be seen in Fig. 3.1b. Epoxy resins have a relatively high water absorption capacity which results from the presences of -OH groups attracting the polar water molecules.

8.1.1 Mass load

The mass load of the polymer matrix is directly related to the moisture content in the polymer (8.1) and thus follows the theory of water transport as introduced before. Despite the nonlinearity of the moisture content isotherm it has been found for polyimide, that the uptake of water is dominated by Henry's law and therefore it can be

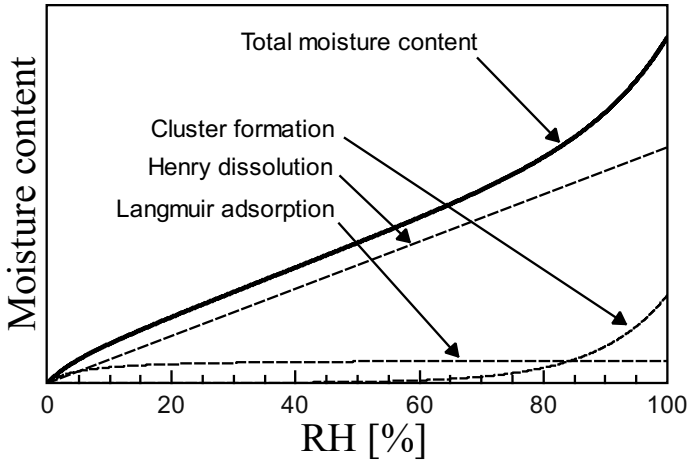

Figure 8.1: Isothermal moisture content as the superposition of three distinct sorption mechanisms at room temperature. Image adapted from [132].

approximated by a linear regression [132]. From the diffusion model (Fig. 8.1) it can be seen that the error from a linearization of the moisture content in particular for RHs below 60% is small. For polyimide, the moisture concentration is linear up to a concentration of 70% [133]. Only at larger RH levels, the moisture uptake is accelerated which might be explained by the clustering of water molecules. Hence, the linearized moisture content M is written as

$$M(RH) = \alpha_m RH \tag{8.3}$$

where α_m is the total sorption coefficient. For polyimide, values for α_m from 1.9×10^{-4} /%RH up to 4.3×10^{-4} /%RH [132] and $\alpha_m = 2.5 \times 10^{-4}$ /%RH were measured [133]. Sorption coefficients for epoxy resins based on diglycidyl ether of bisphenol A (DGEBA), which is a component of SU-8, were determined at 25 °C and values from 2.5×10^{-4} /%RH up to 3.1×10^{-4} /%RH were obtained [134]. It was found that the diffusion parameters of DGEBA such as the sorption coefficient are systematically increasing for an increasing crosslink density. The highest values of the sorption coefficient thus belongs to the epoxy with the highest crosslink density. The same effect of an enhanced water absorption for an increasing crosslink density was also observed for polyimide [135], crosslinked poly(vinyl cinnamate) (PVCA) [136] and for crosslinked poly(methyl metacrylate) (PMMA) [137]. The moisture penetration into polymer is affected by the availability of free volume within the polymer in the first state and by the attraction forces between the water molecules and the polymer in the

second state. In epoxy resins it was found that the latter effect, namely the polarity of the polymer, is the dominant factor for the water uptake [138].

8.1.2 Volume expansion

As already mentioned above, the water uptake can result in a volume change of the polymer. Hydrophilic polymers tend to swell for an increasing moisture content. Only a fraction of the sorbed water causes swelling [132]. The volume expansion with respect of the moisture content has been found to be linear to a good approximation for polyimide [132], different epoxies [139, 140] and also for SU-8 [40]. Therefore, the hygroscopic strain ε_{hyg} can be related to a linear coefficient α_{hyg} of the humidity-induced volume expansion according to [132]

$$\varepsilon_{hyg} = \alpha_{hyg} RH. \tag{8.4}$$

Values of the hygroscopic expansion coefficient were determined for different polyimides at 23 °C. Typical values of α_{hyg} that were obtained reached from 22 ppm/%RH to 58 ppm/%RH [132]. A hygroscopic strain of $\varepsilon_{hyg} = 0.22M$ was determined for an epoxy resin based on DGEBA [140]. Applying this relation to the sorption coefficients found for DGEBA [134], values for α_{hyg} of 57.2 ppm/%RH to 79.2ppm/%RH are obtained.

8.1.3 Modulus change

For many different polymer materials it is known that water changes the interactions between polymer chains and acts as a plasticizer which lowers the Young's modulus [141–144]. At low concentrations however, some plasticizers have shown to increase, rather than decrease, the modulus of polymers. This effect is called antiplasticization. At higher plasticizer concentrations the polymer begins to soften again. Epoxy based thermosets were found to antiplasticize by adding low concentrations of phosphate additives [145]. The Young's modulus could most efficiently be increased with the smallest additive molecules. Further, it was observed that the most tightly crosslinked materials produce the highest increase in strength and stiffness. Humidity was found to increase the stiffness in hydrophilic thermoplasts such as diglycerol and quadrol [146]. The effect of humidity-induced antiplasticization of polyamide was investigated by studying the free-volume in the polymer [147]. For low to medium relative humidity levels, the free-volume in the polyamide was decreasing (antiplasticization), that is the preexisting free volume holes are filled by water molecules. At relative humidities $> 50\%$, the free-volume is increasing again, indicating a plasticization. In thermosets such as polyimide, the modulus showed a stiffening response at low relative humidity levels [135].

8.2 Response time

In order to determine the influence of the RH on the resonance behavior of the polymer microbeams at equilibrium, the response time of the measurement setup has to be evaluated. First the response time due to the diffusion of the water vapor into the polymer microbeams is calculated. Second, the response time of the measurement chamber is measured.

The width of the microbeams is larger than the thickness. Neglecting the diffusion into the polymer from the sidewalls of the beam, the beam can be treated as a plane sheet and the diffusion law (Fick's law) becomes one-dimensional

$$\frac{\partial M(z,t)}{\partial t} = D\frac{\partial^2 M(z,t)}{\partial z^2}. \tag{8.5}$$

If the moisture concentration in a plane sheet with thickness h ($-h/2 < z < h/2$) is initially uniform and the surfaces are kept at constant concentrations, the solution of Fick's law becomes [148]

$$\frac{M_t}{M_\infty} = 1 - \sum_{j=0}^{\infty} \frac{8}{(2j+1)^2\pi^2} \exp - \frac{D(2j+1)^2\pi^2 t}{h^2} \tag{8.6}$$

where M_t denotes the total amount of moisture which has entered the plane sheet at time t, and M_∞ the corresponding quantity after infinite time. Fig. 8.2 shows a plot of (8.6) for the thin and thick SU-8 microbeams using a diffusion coefficient $D = 1.25 \times 10^{-13}$ m^2/sec for water into SU-8 [149]. For a thin microbeam, 95% and 99% of the moisture content is diffused after $t < 5$ sec and $t < 8$ sec, respectively. For a thick microbeam, 95% and 99% of the moisture content is diffused after $t < 30$ sec and $t < 46$ sec, respectively.

The response time of the measurement chamber is determined by increasing and decreasing the RH in the chamber as a step function. The RH humidity in the chamber is continuously measured with the reference sensor with a particular response time of 8 sec. The response to a rectangular RH pulse is shown in Fig. 8.3. 95% and 99% of the RH is reached after $t < 30$ sec and $t < 60$ sec, respectively.

The response time of the measurement chamber is larger then the response time of the diffusion into the thin polymer microbeams and it is of the same order of magnitude as the diffusion response time of the thick microbeams. The fact that the response time of the measurement chamber is larger than of the gas or humidity sensors itself is observed in most cases [150]. All humidity measurements were performed after the measurment setup reached steady state, which was always longer than 60 seconds.

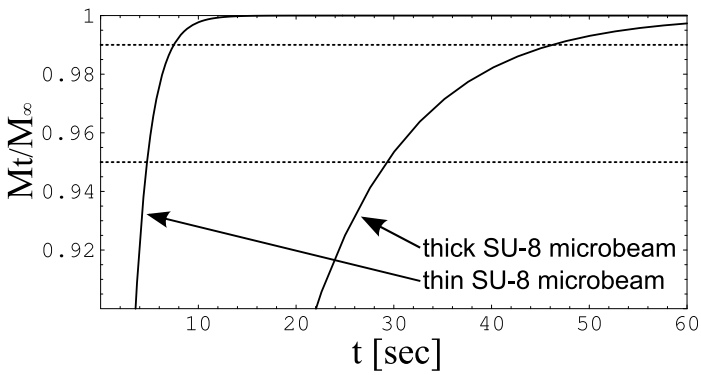

Figure 8.2: Ratio of total amount of moisture which has entered the plane sheet at time t compared to the corresponding quantity after infinite time for a thin ($h = 1.45\ \mu m$) and a thick ($h = 3.6\ \mu m$) SU-8 microbeam corresponding to (8.6).

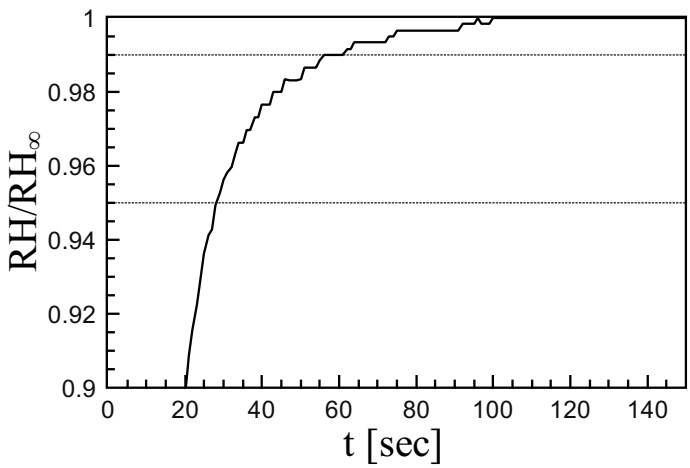

Figure 8.3: Response time of the measurement chamber demonstrated by the ratio of the measured RH compared to the RH at saturation as a response to a RH step from 4.2%RH to 25.8%RH.

8.3 Extended mechanical models

The influence of air humidity is investigated by means of beamlike s-c SU-8 microbeams and stringlike thin d-c SU-8 microbeams. In this section, the mechanical models presented in chapter 4 are extended with the introduced water diffusion models in polymer materials (section 8.1).

8.3.1 Eigenfrequency of a beam as a function of RH

If the one-dimensional hygroscopic strain is given by ε_{hyg} (8.4), the eigenfrequency of a beam (4.12) as a function of the relative humidtiy becomes

$$f_{0,beam}(RH) = \frac{\lambda^2 h}{2\pi L^2}\sqrt{\frac{Y(RH)(1+\alpha_{hyg}RH)}{12\rho(1+\alpha_m RH)}} \tag{8.7}$$

where $Y(RH)$ is the Young's modulus as a function of the relative humidtiy.

8.3.2 Eigenfrequency of a string as a function of RH

If the volume of the polymer expands due to the absorption of water, the strain in a string is released which results in a resonant frequency decrease. Assuming the volume expansion to be a linear function of the relative humidity (8.4), the total strain in a string can be written as

$$\begin{aligned} \varepsilon &= \varepsilon_{pre} - \varepsilon_{hyg} \\ &= \varepsilon_{pre} - \alpha_{hyg}RH \end{aligned} \tag{8.8}$$

where ε_{pre} is the pre-strain of the string. Beside the change of the strain, the humidity also influences the Young's modulus and the mass density of the stringlike microbeam. Using the linear stress-strain relation and neglecting the transverse strain, the stress in a polymer string as a function of the relative humidity becomes

$$\sigma(RH) = Y(RH)(\varepsilon_{pre} - \alpha_{hyg}RH). \tag{8.9}$$

With (8.3), the eigenfrequency of a string as a function of the relative humidity can be written as

$$f_{0,string}(RH) = \frac{1}{2L}\sqrt{\frac{Y(RH)(\varepsilon_{pre} - \alpha_{hyg}RH)}{\rho_0(1+\alpha_m RH)(1+\alpha_{hyg}RH)^{-3}}}. \tag{8.10}$$

8.4 Results & discussion

In Fig. 8.4, the relative resonant frequency changes of SU-8 microstrings, microbeams and the micromirror are shown for relative humidity levels between 3 and 60%. The

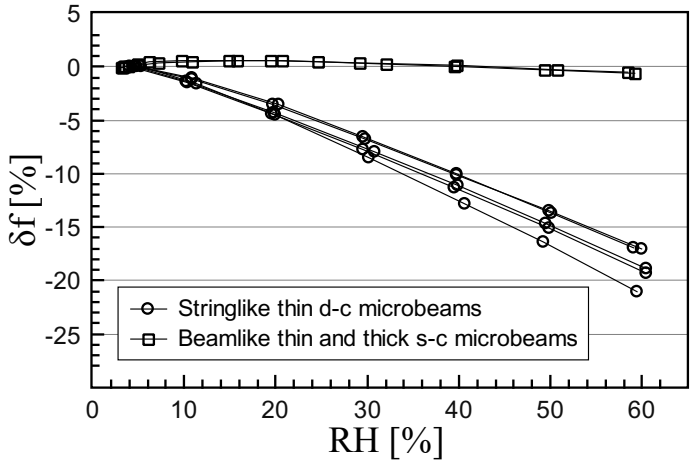

Figure 8.4: Relative resonant frequency shifts of SU-8 stringlike thin d-c microstrings and beamlike thin and thick s-c microbeams for a varying relative humidity measured at 24 °C.

relative frequency shifts show significant differences for the different structures and modes. In order to determine the moisture effect that dominantly influences the resonant frequency, the influence of effects such as mass loading, volume expansion, or plasticizing on the frequency change are examined based on the mechanical models introduced in section 8.3.

8.4.1 Beamlike s-c microbeams

In Fig. 8.5, the relative frequency shifts of a thin and a thick s-c microbeam are shown. In order to find the significant effects contributing to the resonant frequency shift, the individual influences are evaluated based on (8.7). The influence of the hygroscopic strain on the eigenfrequency $f_{0,beam}(RH) \propto \sqrt{(1+\alpha_{hyg}RH)}$ is estimated with $\alpha_{hyg} =$ 79.2 ppm/%RH of DGEBA [40]. This yields a $\delta f \approx +0.0040\%/\%\text{RH}$. This is too small to have a significant influence on the measured resonant frequency shift of the SU-8 microbeams. The change of the mass density due to mass load yields the following proportionality $f_{0,string}(RH) \propto \sqrt{(1+\alpha_m RH)^{-1}}$. With $\alpha_m = 3.1 \times 10^{-4}/\%\text{RH}$ for an epoxy resin [134], $\delta f \approx -0.015$ %/%RH. This is in the order of the measured frequency changes and is thus taken into account. Finally, the eigenfrequency of

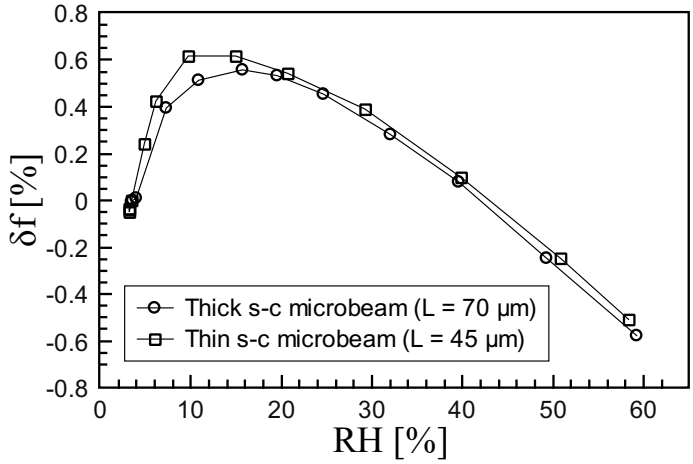

Figure 8.5: Relative resonant frequency shifts of a thick s-c SU-8 microbeam ($L = 70\ \mu$m, $w = 12\ \mu$m, $f_{res} = 281.5$ kHz at RH=3.5%) and a thin s-c SU-8 microbeam ($L = 45\ \mu$m, $w = 14\ \mu$m, $f_{res} = 171.8$ kHz at RH=3.4%) as a function of relative humidity measured at 24 °C. The structures were at equilibrium for every measurement.

microbeams as a function of RH can thus be approximated by

$$f_{0,beam}(RH) \approx \frac{\lambda^2 h}{2\pi L^2}\sqrt{\frac{Y(RH)}{12\rho(1+\alpha_m RH)}}. \tag{8.11}$$

In Fig. 8.5 it can be seen, that the relative frequency shift of a thick and a thin s-c microbeams shows the same qualitative but also quantitative behavior. That let's conclude, that not a geometrical effect such as a volume expansion is causing the measured frequency shifts, but rather a material property change. As given in (8.11), the mass load due to water absorption would cause a steady frequency drop. Consequently, the measured frequency increase at low RH levels seems to be caused by an antiplasticization of SU-8 by water molecues as introduced in section 8.1. SU-8 is highly crosslinked and the small water molecules increase the stiffness by filling the free volume in the material. At higher RH levels, the increased moisture content starts to soften the material which together with the concurring mass uptake results in a frequency decrease.

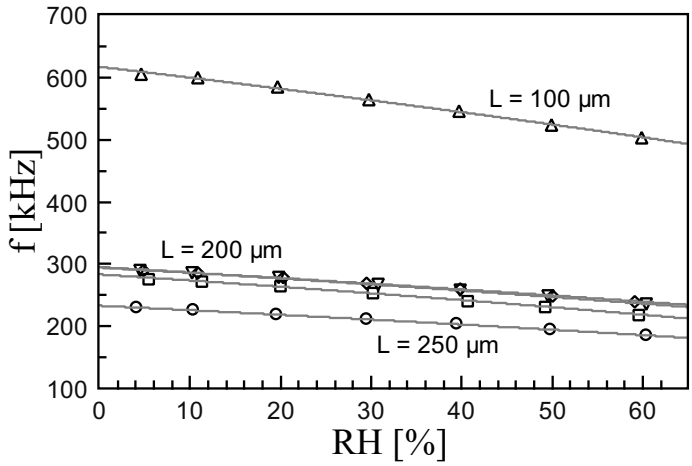

Figure 8.6: Resonant frequency shifts of the 5 stringlike thin d-c SU-8 microbeams shown in Fig. 8.4 with length from 100 to 250 μm for a varying relative humidity measured at 24 °C. The gray lines show the fit of the measured resonant frequency values with the model (8.13) with ρ=1218 kg m^{-3}. The average fit parameter are $Y\alpha_{hyg}$ = 101108±3873 Pa/%RH and σ_{pre}=16.92±1.05 MPa.

8.4.2 Stringlike d-c microbeams

From Fig. 8.4 it can be seen, that the microstrings show the largest relative change of the resonant frequency as a function of the RH. Linearizing the measured frequency shift, a relative change of 0.34%/%RH in average is obtained. The individual resonant frequency shifts of the SU-8 microstrings are shown in Fig. 8.6.

The influence of the individual effects causing the resonant frequency change are evaluated by means of (8.10). Because the exact values of the different coefficients of SU-8 are unknown, values for similar polymers are used as an estimation. The change of the mass density due to the volume expansion yields the following proportionality $f_{0,string}(RH) \propto \sqrt{(1+\alpha_{hyg}RH)^3}$. With $\alpha_{hyg} = 79.2$ ppm/%RH of DGEBA [40], $\delta f \approx +0.012$%/%RH. This is one order of magnitude smaller than the measured -0.34%/%RH and is thus neglected. The change of the mass density due to mass load yields the same proportionality as the microbeams discussed in section 8.4.1 and $\delta f \approx -0.015$ %/%RH. This is one order of magnitude smaller than the measured δf and is thus neglected. From the microbeams it can be seen, that the change of the Young's modulus is significantly lower and plasticization follows antiplasticization whereas the resonant frequency of the microstrings is decreasing over the whole RH range. Therefore, the Young's modulus is approximized as a constant. Hence, (8.9)

can be written as

$$\sigma(RH) = (\sigma_{pre} - Y\alpha_{hyg}RH) \tag{8.12}$$

and (8.10) reduces to

$$f_{0,string}(RH) \approx \frac{1}{2L}\sqrt{\frac{\sigma_{pre} - Y\alpha_{hyg}RH}{\rho_0}}. \tag{8.13}$$

The frequency change by the moisture uptake of SU-8 microstrings is thus mainly caused by a change of the tensile stress. The stress is relieved by the swelling of the polymer which results in a drop of the eigenfrequency. The pre-stress in string-like d-c microbeams shows a distinct relaxation behavior as shown in section 7.2.2. It is assumed that the pre-stress does not relax and thus stays constant over the time of the air humidity experiments. In Fig. 8.6, the measured resonant frequencies are fitted with (8.13). The model was fitted to the data by two fit parameters, that are $Y\alpha_{hyg}$ and the pre-stress σ_{pre}. The obtained fit parameter values are $Y\alpha_{hyg}$ = 101108±3873 Pa/%RH and σ_{pre}=16.92±1.05 MPa. With a Young's modulus of SU-8 of $Y = 4.0$ GPa [62, 85], a coefficient of humidity-induced expansion of $\alpha_{hyg} = 25.3 \pm 1.0$ ppm/%RH is obtained.

A sample containing SU-8 microstrings was stored at 150 °C for 150 hours in nitrogen atmosphere. In Fig. 8.7, their relative resonant frequency change is compared to the frequency change of the samples stored at room temperature which are shown in Fig. 8.6. The microstrings stored at 150 °C are more sensitive to air humidity than the microstrings stored at room temperature, as can be seen in Fig. 8.7. The linearized measured relative frequency change for the microbeams stored at 150 °C is -0.78%/%RH which is around twice the value as for the strings stored at room temperature with -0.34%/%RH. By fitting with (8.13), the following fit parameters are obtained $Y\alpha_{hyg}$ = 210330±1980 Pa/%RH and σ_{pre}=18.0±0.05 MPa. With $Y = 4.0$ GPa, a coefficient of humidity-induced volume expansion of $\alpha_{hyg} = 52.3 \pm 0.5$ ppm/%RH is obtained. The storage at elevated temperature seems to significantly change the material parameters. This high temperature storage can be seen as an extended hard-bake which fully cures the material and therewith increases the crosslink density. In SU-8, at every crosslink, a hydroxyl group is formed which increased the polarity. This increases the affinity to water molecules which can form hydrogen bonds to the unreacted polar hydroxyl groups. The polarity of the polymer seems to be dominant over the free volume which is related to the cross-link density which is in agreement with the results obtained for epoxy resins [138].

In Fig. 8.8, the resonant frequency of two SU-8 microstrings as a function of relative humidity is shown. The frequency was measured by first increasing the relative humidity up to around 60% and then subsequently decreasing the relative humidity down to the initial value. The individual resonant frequencies were measured at

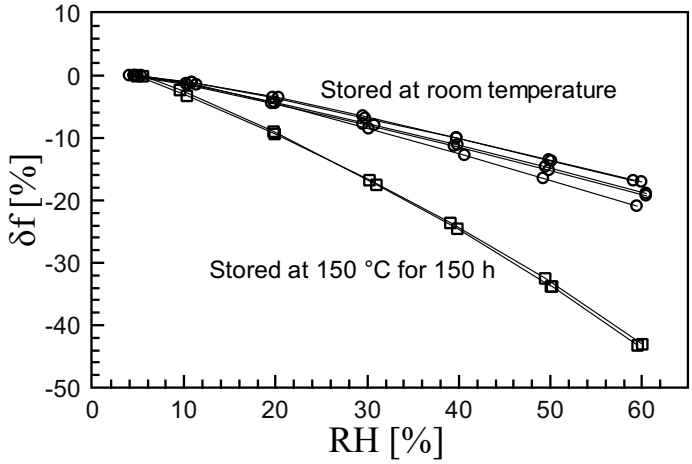

Figure 8.7: The relative resonant frequency shifts of stringlike thin d-c SU-8 microbeams stored at room temperature and stored at 150 °C. The 5 strings that were stored at room temperature are from 3 different samples. The 2 strings that were stored at 150 °C are from the same sample. Measured at 24 °C. The structures were in equilibrium for every measurement.

equilibrium which usually was reached after 2 minutes. From this measurement it can be seen, that no significant hysteresis is observable. Therefore, the absorption and desorption of water molecules in and out of the polymer matrix is reversible. It can therefore be assumed that the water-polymer interaction is of pure physical nature, so called physisorption. The water absorption was also found to be reversible for polyimide [132], DGEBA [134] and also for SU-8 [40].

8.5 Conclusion

The resonant frequency response of two different polymeric resonators are measured and shown to obey different mechanisms, as summarized in Table 8.1. The structures whose resonant frequencies are defined by a pre-stress, such as the stringlike d-c microbeams, show a high humidity sensitivity which is caused by a reversible relief of the pre-stress by the moisture absorption. In contrast, the resonators whose resonant frequencies are mainly defined by the modulus of the polymer material, such as the beamlike s-c microbeams, show a small sensitivity to moisture. The relative resonant frequency change due to plasticization between 3 and 60% RH was always smaller than ±0.7%. Values of the linear coefficient of the humidity-induced volume expan-

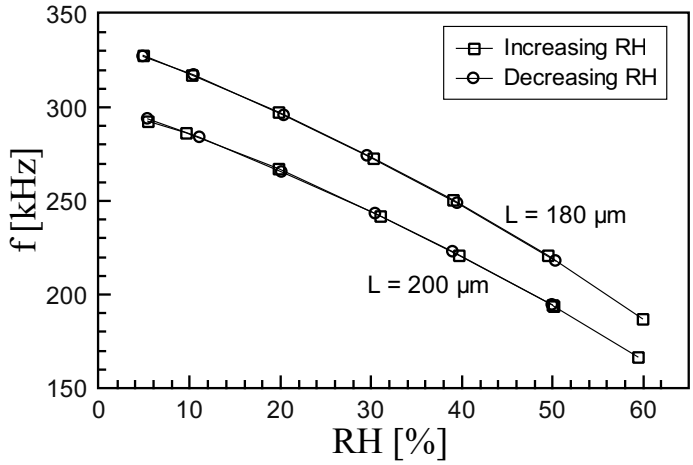

Figure 8.8: The resonant frequencies of two stringlike thin d-c SU-8 microbeams for an increasing (absorption) and a subsequently decreasing (desorption) relative humidity. Measured at 24 °C. The structures were in equilibrium for every measurement which usually was reached after 2 minutes.

Table 8.1: Summary of results. The material parameter are extracted assuming a Young's modulus of 4.0 GPa [62] and a mass density of 1218 kg/m^3 [83] for SU-8.

Structure	Beamlike s-c SU-8 microbeams	Stringlike d-c SU-8 microbeams	
Mode	flexural	lateral	
$f_0^2(\mathrm{RH}) \propto$	$Y(\mathrm{RH})\rho(\mathrm{RH})^{-1}$	$\sigma(\mathrm{RH})$	
Temp history after fabrication	room temp	room temp	150 °C for 150 h
δf [%]	$< \pm 0.7$ (3 - 60%RH)	-0.34 /%RH	-0.78 /%RH
α_{hyg} [ppm/%RH]	n.a.	25.3	52.3

sion of $\alpha_{hyg} = 25.3$ ppm/%RH and $\alpha_{hyg} = 52.3$ ppm/%RH of SU-8 are determined. The coefficient strongly depends on the history of the polymer, in particular on the temperature history. SU-8 becomes more sensitive to humidity if it is exposed to elevated temperatures. The modulus of SU-8 was found to increase for low moisture concentrations. This antiplasticization is followed by a softening at higher relative humidity values. Consequently, in addition to the influence of temperature and time (as discussed in chapter 7), the influence of the humidity on the resonance behavior of polymer microstructures, microstrings in particular, can be significant and needs to be taken into account for the design of polymer microsystems that are operated at ambient air.

The very quick response of the microstructures on a change of humidity presents an exceptional fast polymer test for the evaluation of the humidity influence. Polymer microresonators are able to significantly decrease the long waiting times in humidity test of hours to seconds compared to macroscopic samples. In appendix G, the feasibility of the application of stringlike polymer microresonators as humidity sensors is investigated in a case study.

Part II

Application

9 Positive feedback

In microelectromechanical systems (MEMSs), organic polymers are a class of promising materials due to their vast variety of properties, and because of their low cost and simple processing [2, 23]. By virtue of the low Youngs modulus [17], the ability of surface modifications [151] and the absorption of chemicals [31], polymer materials often play a key role in chemical sensing [31] and biosensing [151] applications. Many of these sensor systems provide micro transducers based on the principle of oscillating cantilevers [152, 153]. Typically, such microresonators are made of silicon which is covered with a functional polymer layer [31].

Polymer microresonators are promising devices for sensing applications. The relatively low mass of polymer microstructures results in a high mass sensitivity. Due to their softness, polymer microstructures are very sensitive to changes in surface stress [30] produced by analyte molecules attaching to the surface. Usually, polymer microresonators are restricted to a rather small group of polymers with special intrinsic properties allowing for direct electrostatic [29], thermal [4], or piezoelectric [23] actuation. In contrast, the majority of polymers are not well suited for direct actuation but rather for indirect actuation, e.g., by actuation of a metallic layer attached to the polymer structure [51]. However, besides the more complex fabrication process and the issue of degradation of the adhesion of the functional layer at high actuation cycles, conductive or metalized microresonators need to be electronically connected to a driving circuit.

In this chapter, the application of the concept of a positive feedback with the electrostatically actuated all-polymer microresonators is investigated by means of the readout with a laser-Doppler vibrometer. In air, but particularly in water, the frequency determination of a microbeam resonator is difficult because of the broad resonance peak due to the high damping. In order to work against viscous and intrinsic damping in gaseous or aqueous environments, a positive feedback can be used [31,154–157]. Usually, the readout signal represents the micromechanical deflection. By measuring the vibration with a laser-Doppler vibrometer, the readout signal represents the velocity of the vibrating microstructure. Therefore, the approaches for positive feedback circuits which are based on the deflection signal have to be adapted. Here, the application of Q-enhancement and self-excitation with the electrostatically actuated polymer microresonators measured with a laser-Doppler vibrometer in air

and in DI-water is investigated and compared. In the last section, the actual self-excitation circuit used for the subsequent measurements is presented.

9.1 Q-enhancement

For microresonators, the quality factor is an important parameter in the resonance characteristics. The quality factor (Q) determines the sharpness of the resonant peak and thus the frequency stability of the resonator. Q of a harmonic oscillator can be defined by the ratio of the vibrational energy stored in the system and the total energy lost per cycle (see section 4.1.2). However, the quality factor of polymer based microresonators in air or in vacuum is low [58]. In liquids, the quality factor of microresonators in general is very low, e.g. $Q = 1.8$ at 13 kHz for a silicon nitride cantilever [157]. It has been shown that positive feedback can be used to increase the quality factor in gaseous and in aqueous environment [153, 158]. Therefore, the oscillation signal is shifted 90° and amplified before it is added to the driving signal. Here we use a laser-Doppler vibrometer to measure the oscillation of the polymer microbeams. The output signal of the vibrometer represents the oscillation velocity $\dot{z}(t)$ of the resonator. The first derivation of a sinusoidal oscillation signal already has a 90° phase shift compared to the oscillation signal $z(t)$. Thus, a 90° phase shifter is theoretically not needed for a velocity signal feedback. Fig. 9.1 shows the schematic representation of the setup with positive feedback for Q-enhancement where the measured signal $R_{u-v} \cdot \dot{z}(t)$ is amplified with a variable amplifier (G) and then added to the driving signal $u(t)$.

The motion of a polymer microresonator can be described by the differential equation of a damped harmonic oscillator:

$$\ddot{z}(t) + 2\zeta\omega_0\dot{z}(t) + \omega_0^2 z(t) = \frac{1}{m_{eff}} F(t) \tag{9.1}$$

where ω_0 is the free vibration frequency, m_{eff} is the effective mass and ζ is the damping ratio of the system. An electrostatic force is proportional to the applied voltage squared. The driving force $F(t)$ in air or vacuum is:

$$F(t) = -F_{f-u}[u(t) + G[R_{u-v}\dot{z}(t)]]^2 \tag{9.2}$$

where $u(t)$ is the external driving signal, F_{f-u} is a factor representing the force per voltage ratio of the electrostatic actuation, G is the amplification factor of the variable amplifier and R_{u-v} is the voltage per velocity ratio given by the decoder of the laser-Doppler vibrometer. For the application in water, the Kelvin polarization force $F(t)$ would be positive. For the application in air or vacuum, (9.1) can be rewritten and

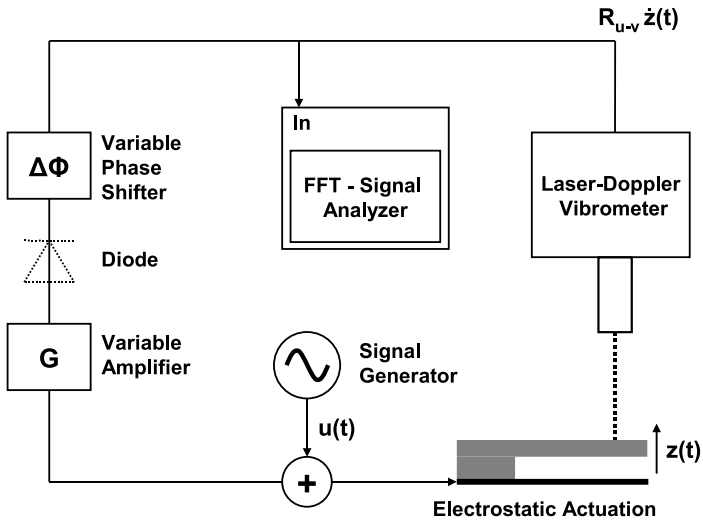

Figure 9.1: Schematic representation of the oscillator setup with feedback for Q-enhancement.

becomes a nonlinear differential equation of the following form:

$$\ddot{z}(t) = c_1\dot{z}(t) + c_2 u(t)\dot{z}(t) + c_3\dot{z}^2(t) + c_4 z(t) + c_5 u^2(t) \tag{9.3}$$

with the parameters

$$\begin{aligned} c_1 &= -2\zeta\omega_0 \\ c_2 &= -\frac{2F_{f-u}GR_{u-v}}{m_{eff}} \\ c_3 &= -\frac{F_{f-u}G^2R_{u-v}^2}{m_{eff}} \\ c_4 &= -\omega_0^2 \\ c_5 &= -\frac{F_{f-u}}{m_{eff}}. \end{aligned}$$

The solution of (9.3) is not trivial, thus it was simulated with Matlab/Simulink. The Simulink models are depicted in appendix H. In doing so, the phase shifter was neglected for all the simulations. Fig. 9.2 shows the simulated amplitude response of the oscillator system to a sinusoidal sweep signal $u(t)$. The value of the force factor F_{f-u} was obtained by finite element analysis for the beam being in the starting position. Assuming small vibration amplitudes, the dependency of the force on the beam deflection is neglected. All the other parameter were chosen such as to fit the real parameters in the experiments in air. The simulation indicates, that the effective damping of the system can be decreased by increasing the amplification factor G of the feedback amplifier.

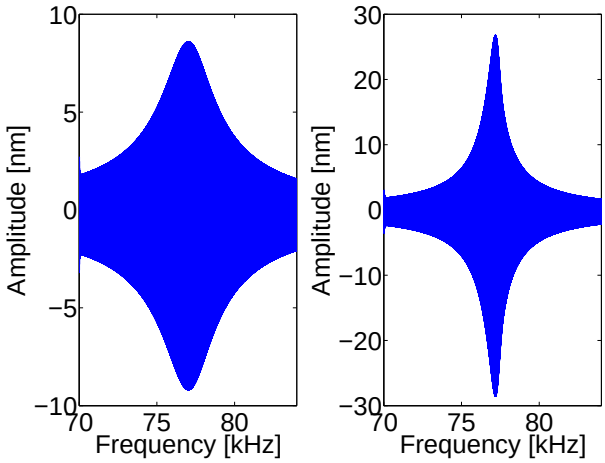

Figure 9.2: Amplitude response of oscillator setup in air or vacuum without a diode in the feedback loop with a driving voltage $U_{AC} = 5$ V, $U_{DC} = -5$ V and an amplification factor (a) $G = 0$ and (b) $G = 1.25$ simulated with Matlab/Simulink. The parameters are: $\zeta = 0.02$, $\omega_0 = 77$ kHz, $m_{eff} = 6 \times 10^{-12}$ kg, $R_{u-v} = 500$ Vs/m, $F_{f-u} = 1 \times 10^{-11}$ N/V^2.

The electrostatic nature of the actuation technique creates a force component with double the frequency of the sinusoidal driving voltage. This is because an electrostatic force is proportional to the square of the applied voltage, i.e. $F_{el} \propto U^2 \sin^2(\omega t)$, which can be rewritten to $F_{el} \propto U^2(1 - \cos 2\omega t)/2$. The standard procedure to solve this electrostatic driving problem is to add a DC component to the AC driving signal, as presented in [158]. This creates a constant force component, a dominant alternating force component with the same frequency as the driving voltage and a third force component with a double frequency [61]. Here we use an alternative method which is to cut off all positive parts of the driving signal by means of a diode. The use of a diode produces higher harmonics too. But because the device is actuated at resonance, the effect of the component with the same frequency is much larger than that of the force components with higher frequencies. This method has a similar effect as adding a DC component to the driving voltage and it is very simple to implement. If no diode or no DC component is used to drive the oscillator, the double frequency of the driving force accelerates the resonant structure when it is moving towards the electrodes but it also slows the oscillation down when the resonator is moving upwards, away from the electrodes.

Fig. 9.3 shows the simulated effective quality factors with respect to the amplification factor G for a feedback loop, as shown in Fig. 9.1, with a diode (dashed symbol in Fig. 9.1) and without. The influence of the diode in the feedback path was taken into account in the Matlab/Simulink simulation (see appendix H). The simulations show that the Q-enhancement is strongly nonlinear. The system becomes instable for higher amplification factors G, that is the damping becomes negative. At the instability point, the feedback signal starts to dominate the oscillation. This instability can be used to let the polymer microresonator self-oscillate at its resonant frequency. The simulations reveal that the instability of the system is reached a lot faster if a diode is implemented in the feedback path, which avails for the application of the self-excitation technique. The slower enhancement of the effective quality factor without a diode can be explained by the negative acceleration in the upward movement of the beam due to the double frequency of the feedback signal.

In Fig. 9.4, the effect of a diode in the feedback loop cutting off all positive signal parts is schematically illustrated. This is needed if the polymer microbeam is actuated in air or vacuum, that is if the force acts in the negative z direction. Then, the polymer beam gets accelerated when moving downwards and it experiences no electrostatic force when it is moving upwards, away from the electrodes. Because the feedback signal has only negative peaks as a result of the diode, in air or vacuum the actuation voltage $u(t)$ has to be negative too (negative DC part). Otherwise, it would not be a positive feedback. The signals would cancel each other out and the

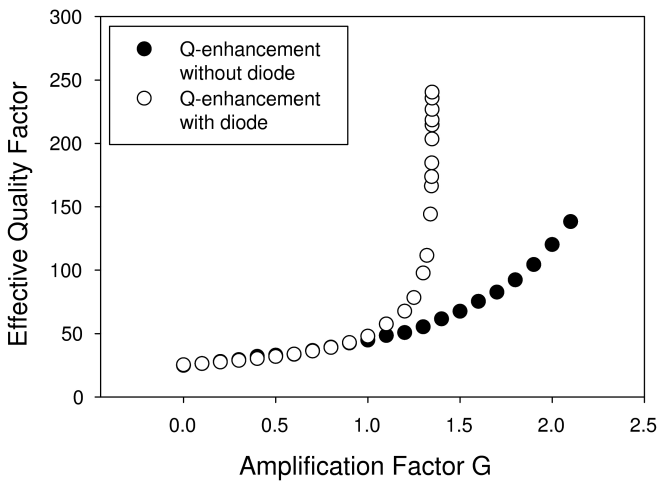

Figure 9.3: Effective quality factors for the application in air or vacuum simulated with Matlab/Simulink for an increasing amplification factor G. The parameters are: $U_{AC} = 5$ V, $U_{DC} = -5$ V, $\zeta = 0.02$, $\omega_0 = 77$ kHz, $m_{eff} = 6 \times 10^{-12}$ kg, $R_{u-v} = 500$ Vs/m, $F_{f-u} = 1 \times 10^{-11}$ N/V^2.

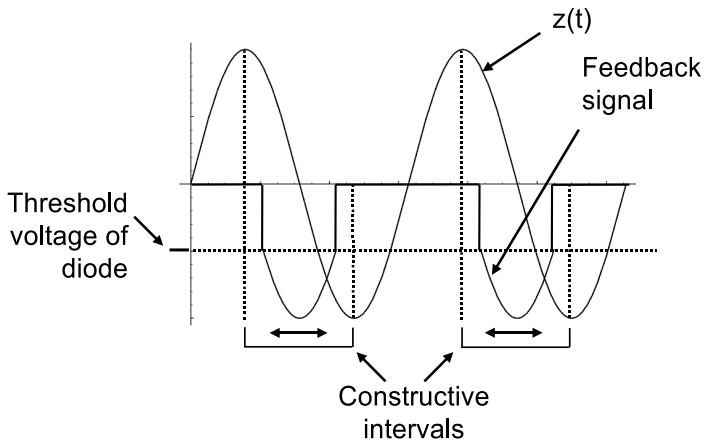

Figure 9.4: Illustration of the effect of a diode in the feedback loop in air or vacuum, that is for an actuation force acting in the negative z direction.

resonance peak enhancement would not work. In water, the direction of the diode needs to be changed to cut off all the negative signal parts of the feedback because of the force acting in the positive z direction. Consequently, in water, the actuation signal $u(t)$ needs to have a positive DC part.

9.1.1 Experiments

The polymer microresonators based on the *Kelvin polarization force*, as described in section 2.3.2, are actuated by applying a periodic chirp signal $u(t)$, with a DC amplitude U_{DC} and an AC amplitude U_{AC}, over the coplanar electrodes. The oscillation was monitored with a laser-Doppler vibrometer (Polytec MSA-400). The signal from the vibrometer, representing the velocity $\dot{z}(t)$ of the polymer microstructure, was amplified with a variable gain amplifier and added to the driving signal. The positive parts of the feedback signal was cut off by a diode. The phase shift was adjusted such that the feedback signal was in the constructive interval as depicted in Fig. 9.4 for the application in air. For the application in water, the phase of the feedback was shifted 180 degree compared to the application in air. If the phase shift is not set correctly, the oscillation frequency of the system does not match the resonant frequency of the polymer microresonator. Furthermore, the driving force can act at the upward moving of the polymer beam and the oscillation gets damped causing a drop of the quality factor. The low-pass filter was set to 100 kHz and to 200 kHz for the self-excitation measurements in air and in water, respectively. If the filter cut-off

frequency is set too low, the feedback signal gets damped. The velocity signal was analyzed using FFT analysis. The polymer microresonators were actuated in ambient air and in DI-water at room temperature. The feedback amplification was manually adjusted until a stable oscillation with a maximal effective quality factor was reached. For the self-excitation technique, the amplification factor was increased beyond the point of instability, then the thermal noise was enough to start the self-oscillation. The driving voltage of the self-excitation was 10 and 15 V in air and in water, respectively.

A SU-8 microcantilever was actuated in air at atmospheric pressure. Without any feedback, the resonance of the structure showed a quality factor of $Q = 28$. Applying Q-enhancement, an effective quality factor of $Q_{eff} = 115$ was obtained. The amplitude responses of the microcantilever are shown in Fig. 9.5a. Fig. 9.5b shows the amplitude response of a SU-8 microcantilever in DI-water. The very low quality factor of $Q \approx 1$ was increased to an effective quality factor of $Q_{eff} = 31$ by means of Q-enhancement. The vertical lines dropping from the amplitude response curves are measurement artifacts coming from frequency points where the oscillation amplitude during the sweep was not measured. The electrodes on this sample were not covered with aluminum oxide.

9.2 Self-excitation

For the self-excitation technique [157–159] there is no driving signal needed. In fact, the oscillation is driven by the amplification of the thermal noise of the polymer microresonator via the feedback amplifier. Fig. 9.6 shows the schematic of the setup which was used for the self-excitation technique. Additionally to the variable phase shifter and the variable amplifier, a diode is added to cut off all the positive signal parts that would damp the oscillation.

To obtain a stationary sustained oscillation, a correct phase adjustment and a feedback gain control are required [160]. The phase shift determines the frequency of oscillation (phase-controlled oscillator) and the damping behavior of the system. The oscillation frequency of the system is only at the resonant frequency of the polymer beam if the phase of the feedback exactly matches the phase of the velocity signal of the resonator at its resonance frequency. In order to stabilize the amplitude, a comparator comparing to ground followed by a low-pass filter are implemented in the signal path [156]. In order to continuously measure the frequency, the FFT-analyzer can be replaced by a frequency counter.

For soft polymeric microstructures using a sensitive displacement sensor, such as a laser vibrometer, thermal noise of the oscillating structure is dominant under most conditions. With this assumption, the frequency resolution $\delta\omega$ of the self-excitation

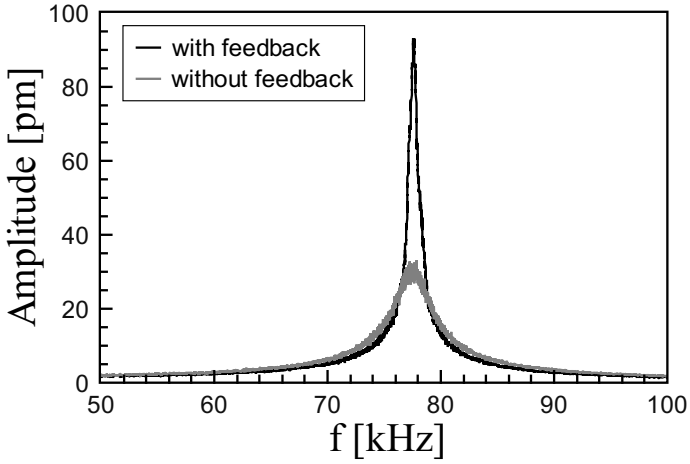

(a) In air

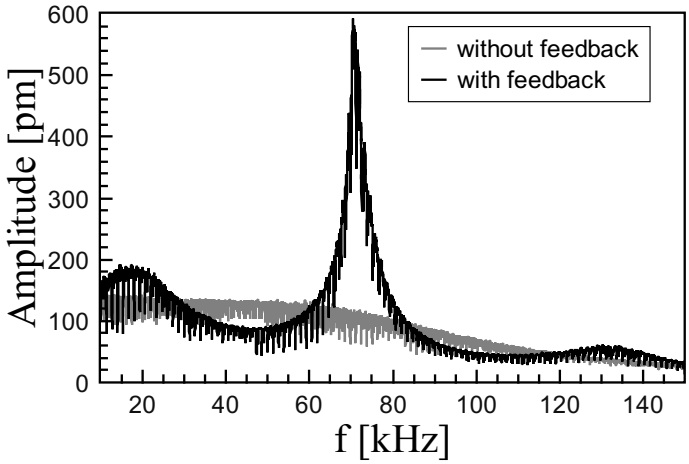

(b) In water

Figure 9.5: (a) Amplitude response of a SU-8 cantilever (12 μm wide, 125 μm long and 3 μm thick) in air at atmospheric pressure. The amplitude of the measurement signal were averaged ten times. The resonance curves of the microresonator with (black curve) and without (grey curve) Q-enhancement. The microresonator was driven by a periodic chirp signal with a driving voltage of U_{AC}=5 V and U_{DC}=5 V. (b) Amplitude response of a SU-8 cantilever (10 μm wide, 80 μm long and 3 μm thick) in water to a frequency sweep (U_{AC}=3 V and U_{DC}=0 V) without (grey curve) and with (black curve) Q-enhancement.

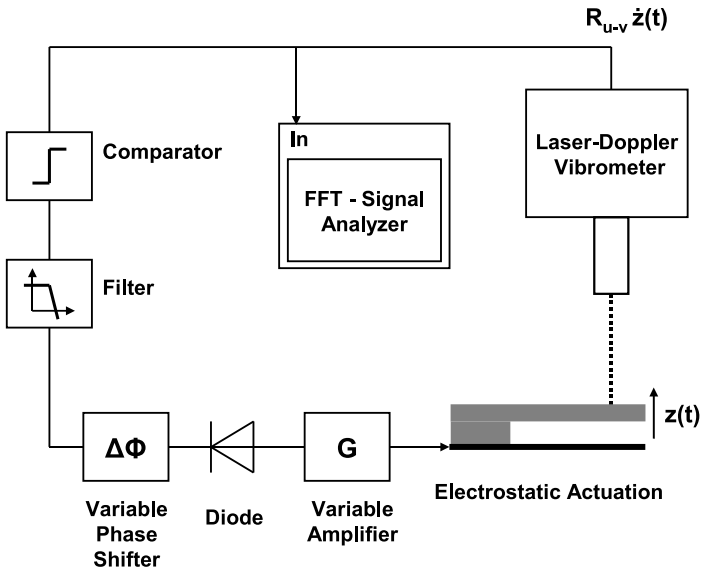

Figure 9.6: Schematic representation of the oscillator setup with self-excitation feedback.

technique shows the following proportionality [161]:

$$\delta\omega^2 \propto \frac{\omega_0 B}{Q\langle z_{osc}^2\rangle} \tag{9.4}$$

where B denotes the readout measurement bandwidth and $\langle z_{osc}^2\rangle$ is the mean-square amplitude of the self-oscillating microbeam. From (9.4) it is obvious that the frequency stability mainly depends on the quality factor of the resonator in open-loop actuation. Further more, the frequency noise can also be reduced by increasing the vibration amplitude.

9.2.1 Experiments

Again, the oscillation of the electrostatically actuated polymer microbeams is monitored with a laser-Doppler vibrometer (Polytec MSA-400). The signal from the vibrometer is put through the amplitude control stage consisting of a comparator and a low-pass filter as depicted in Fig. 9.6. The phase of the feedback signal was set by the phase shifter as depicted in Fig. 9.4. The velocity signal was analyzed using FFT analysis. The polymer microresonators were actuated in ambient air and in DI-water at room temperature. The amplification factor was increased beyond the point of in-

stability, then the thermal noise was enough to start the self-oscillation. The driving voltage of the self-excitation was 10 and 15 V in air and in water, respectively.

Applying the self-excitation technique, an effective quality factor of > 40000 in air was obtained. Fig. 9.7a shows the resonance curve of the self-excited oscillation and the thermal noise of the polymer cantilever, respectively. The total harmonic distortion (THD) of the measured signal at self-excitation was as low as 0.3%, regarding the first four harmonics.

A single clamped SU-8 beam with isolated electrodes was driven in DI-water. Applying the self-excitation technique, an effective quality factor of 4200 was obtained. The resonance curve of the cantilever is shown in Fig. 9.7b. A THD of 9% was obtained, regarding the first six harmonics in the measurement bandwidth from 0 to 350 kHz defined by the decoder of the laser-Doppler vibrometer.

9.3 Comparison

In the previous sections, the application of a positive feedback using the velocity signal from the laser-Doppler vibrometer is elaborated. In air and in water, the effective quality factor of the oscillator system was enhanced more than one order of magnitude by means of Q-enhancement. The value of the effective quality factor with Q-enhancement in air is close to the critical value simulated with Matlab/Simulink (Fig. 9.3). If the amplification factor was increased further, the damping becomes negative and the oscillation becomes instable. The measured maximum amplitude is lower than the simulated amplitude. Among other things, this might be due to the periodic chirp signal which was used to drive the resonator, whereas the simulations were performed with a sweep signal. The periodic chirp signal has a root mean square (RMS) to peak of only 0.5.

For both environments, gaseous and aqueous, the highest effective quality factors were obtained by applying the self-excitation technique. With it, very stable oscillations were obtained with effective quality factor three orders of magnitude higher than the quality factor of the uncontrolled polymer microresonators. The comparator of the amplitude control stage amplified very small measurement signals. This effect helped to spontaneously start the self-excitation in air as well as in water. In air, self-excitation was also possible without amplitude control. The oscillation was then limited by the saturation of the opamp of the variable amplifier. The obtained oscillations showed equally low THD values as with the amplitude control stage. A drawback of not using a gain control stage is the fixed oscillation amplitude which is defined by the supply voltage of the opamp in the variable amplifier. The oscillation of the self-excitation remained at resonance until the amplification factor was

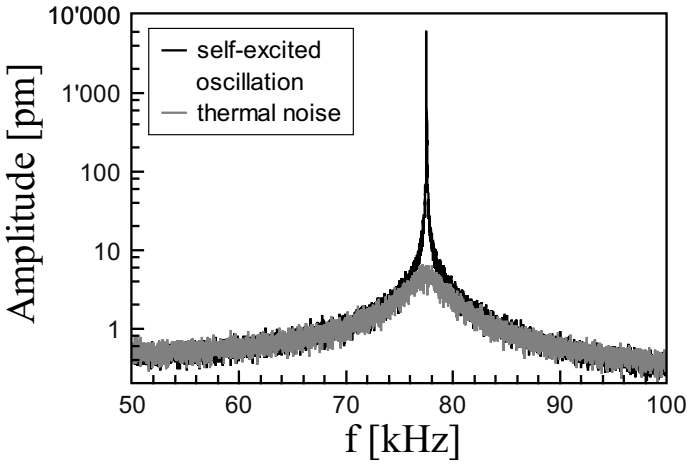

(a) In air

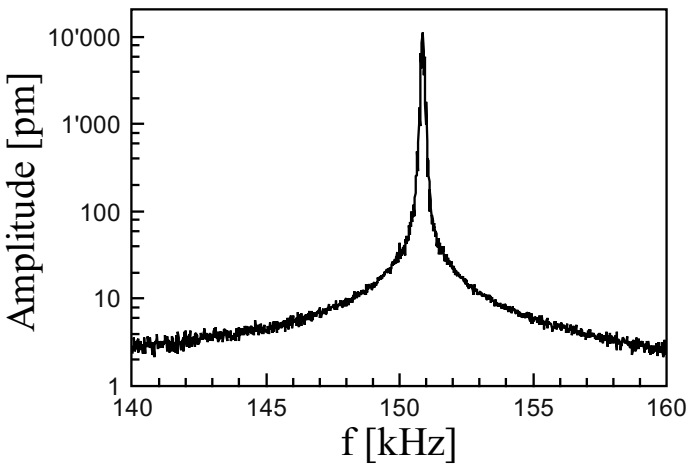

(b) In water

Figure 9.7: (a) Measurement of the thermal noise of the polymer thick s-c microbeam (12 μm wide, 125 μm long) and the resonance curve of the self-excited oscillation. The amplitude of the self-excitation was set to 10 V. (b) Self-excited oscillation of a single clamped SU-8 beam (90 μm long, 1.3 μm thick and 14 μm wide) in DI-water. The amplitude of the self-excitation was set to 15 V.

decreased under a critical value. Then the self-excitation stopped.

The Q-enhancement can be used for the so called slope detection technique where the vibration amplitude change is determined at a fixed driving frequency. But it was shown, that the sensitivity of the slope detection can not be enhanced by using a positive feedback loop which is due to the amplification of the noise [159]. The self-excitation technique on the other hand applied with electrostatically actuated polymer microresonators allows the direct detection of the resonant frequency and its variation with very high sensitivity [159] in gaseous and aqueous environment. The frequency resolution (9.4) can be obtimized by driving the oscillation with high vibration amplitudes. In particular in water, the self-excitation technique potentiates the application of polymer microresonators as chemical sensors or biosensors [162]. The application of the Q-enhancement technique is less suitable in aqueous environment. Furthermore, the oscillation with Q-enhancement becomes instable if a specific gain is exceeded and the damping becomes negative. Consequently, all subsequent sensor measurements are performed by letting the polymer microbeams vibrate in a self-sustained oscillation by means of a positive feedback. In the next section 9.4, the self-excitation circuitry which is used for the subsequent measurements is presented.

9.4 Optimized feedback circuit for self-excitation

The oscillation is monitored with a laser-Doppler vibrometer and the resulting velocity signal is used to drive the polymer microresonator by means of a positive feedback [163], as explained in section 9.2. The structures are again electrostatically actuated in air and in water by means of the Kelvin polarization force [58] (chapter 2). In air or vacuum, the electrostatic force is positive, that is the polymer microbeam is pulled towards the electrodes. Unlike in air or vacuum, the net force in an aqueous environment is negative. The highly polar water is attracted towards the electric field intensity maximum at the electrodes' gap, pushing away the polymer microbeam. That means, in air, the feedback-loop has to be designed such that the actuation voltage is coherent with the negative measured velocity signal $\dot{z}(t)$ (see blue signal in Fig. 9.8) whereas in water, the actuation voltage is coherent with the positive velocity peaks (see red signal in Fig. 9.8). Rectangular pulses as driving signal allow a maximum energy transfer to the vibration of the microbeam which is important to counteract the high damping in water. In order to shape the feedback-signal based on these requirements, a feedback-circuit by means of a comparator comparing to ground is realized which allows a self-sustained excitation.

As a basic principle in an aqueous or gaseous environment, a force is asked pushing the polymer beam away from the electrodes when it is veering away from them

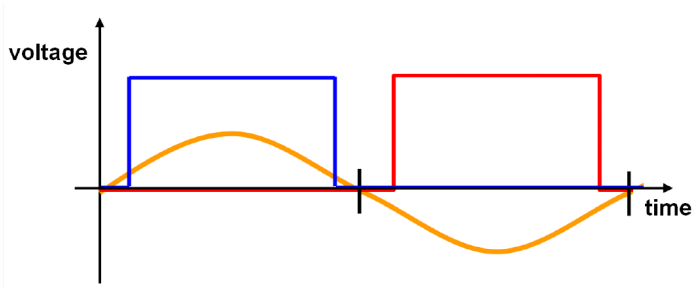

Figure 9.8: Demand on the feedback circuit. Orange signal: given velocity signal of the resonant structure, red signal: actuation signal in air or vacuum, blue signal: actuation signal in water.

or pulling the beam toward the electrodes when it is approaching them, respectively. An electrostatic force is proportional to the applied voltage squared. So, for an electrostatic actuation only half of the frequency is required. In section 9.2, the frequency is divided by adding a diode to the circuit to cut off the positive peaks of the measured sinusoidal signal but this is not possible for higher frequencies. Furthermore, the phase offsets produced by the components (mainly the phase-shift introduced by the low-pass filter in the amplitude control stage) in the signal path are corrected with a phase-shifter (all-pass filter). The use of an all-pass filter has the disadvantage that it is sensitive to frequency changes, that means, the set phase shift changes with frequency. But it is exactly the goal to measure frequency changes. Thus a frequency shifter based on an all-pass filter would affect the frequency measurement. In section 9.2 it was shown that a self-excited oscillation can be obtained by directly feedback the velocity signal. A circuit is realized without the usage of a diode or a phase shifter for the direct feedback of the velocity signal. The schematic representation of the circuit for the application in water is shown in Fig. 9.9. The function of the diode is transfered to a comparator which amplifies only positive signals, consequently dividing the frequency. For the application in air or vacuum, the comparator amplifies only the negative signals (circuit details shown in appendix I). The comparator has a delay due to its given switching time. In order to take account of this delay, the decreasing slope of the rectangular signal is triggered with a high-pass filter which is placed in front of a Schmitt-trigger [164] – a comparator circuit with variable threshold. When the input is higher than a certain chosen threshold, the output is high; when the input is below another (lower) chosen threshold, the output is low; when the input is between the two, the output retains its value. This dual threshold action is called hysteresis and implies that the Schmitt-trigger has some memory.

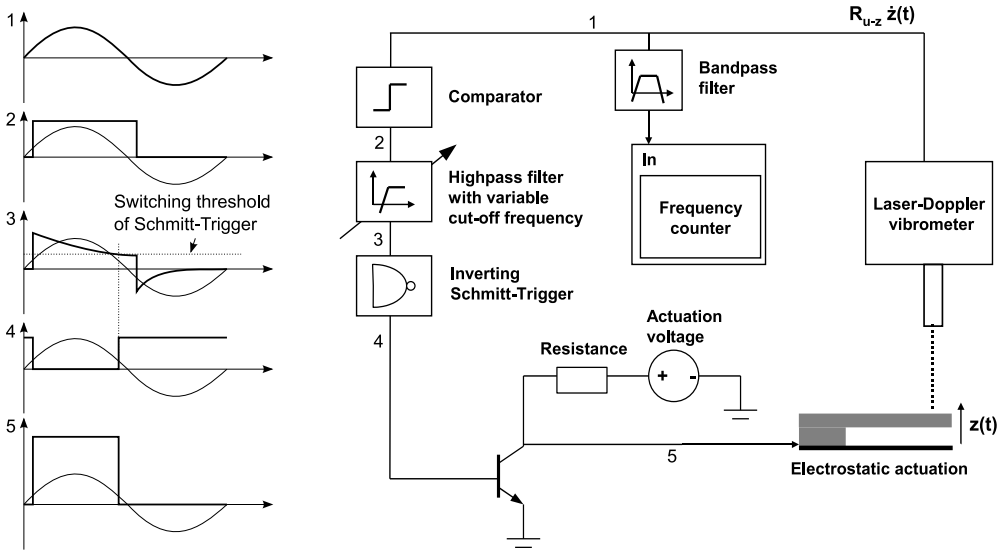

Figure 9.9: Schematic representation of the final oscillator setup with self-excitation feedback for the application in water.

The advantage of a Schmitt-trigger over a circuit with only a single input threshold is also greater stability (noise immunity). The switching point of the Schmitt-trigger can now be controlled by controlling the cut-off frequency of the high-pass filter. The resulting signal is used to trigger a bipolar transistor which switches the actuation voltage of the polymer microresonator. The details of the used circuit are presented in the attachment I.

9.4.1 Results and discussion

In Fig. 9.10 and Fig. 9.11, the resulting measured velocity signal from the vibrometer and the feedback driving signal of a SU-8 microbeam in a self-sustained oscillation in air and water is shown, respectively.

As can be seen in Fig. 9.10b, the self-excited oscillation frequency is lower than the resonant frequency of the microbeam which is due to the driving signal delay caused by the comparator. That means, that the driving signal is not fully in phase with the vibration of the microbeam. Assuming a Lorentzian line shape for the resonance response of a microbeam, the frequency ω_{osc} of a self-excited oscillation by means of a positive-feedback as a function of the operating point (phase angle φ_{osc}) of the

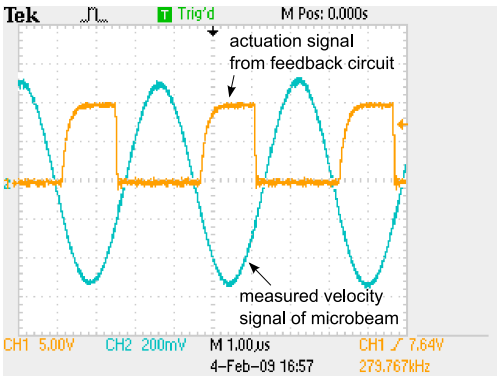

(a) Oscillation and actuation signal in time domain

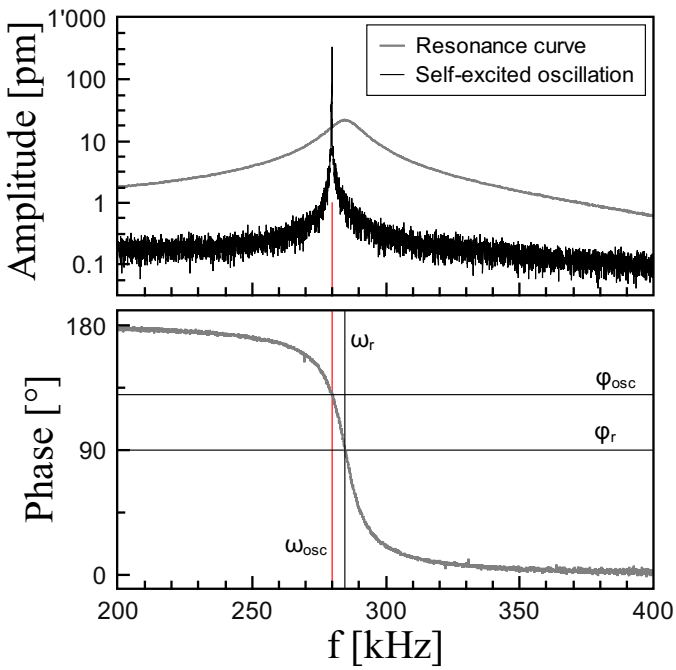

(b) Oscillation signal in frequency domain

Figure 9.10: Self-excited oscillation in air with a feedback circuit as shown in Fig. 9.9 of a thick s-c microbeam with a length of 70 μm and width of 12 μm by applying a driving voltage of 10 V. In (b), the self-excited oscillation is compared to the resonance curve obtained by applying a periodic chirp signal with U_{AC}=10 V and U_{DC}=10 V. The oscillation frequency of the self-excited oscillation is always lower than the resonant frequency.

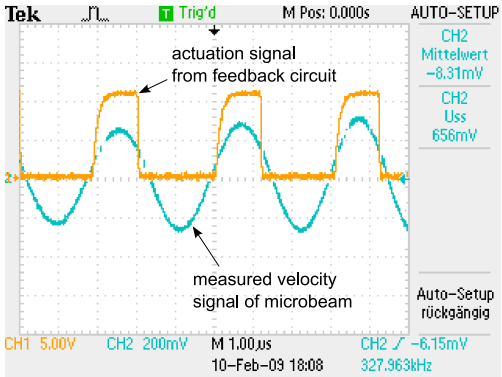

(a) Oscillation and actuation signal in time domain

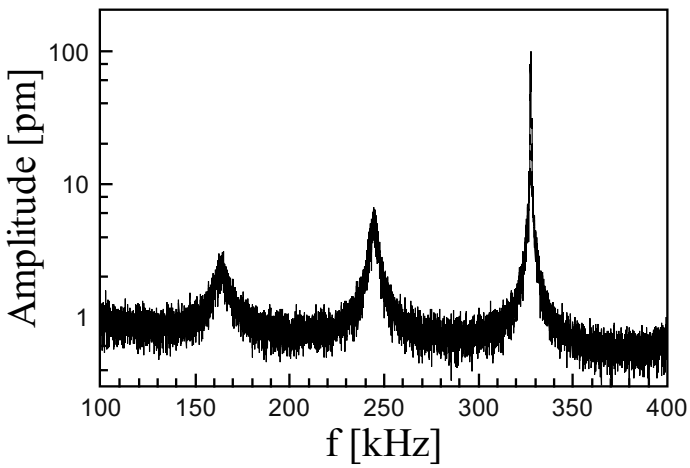

(b) Oscillation signal in frequency domain

Figure 9.11: Self-excited oscillation in water with a feedback circuit as shown in Fig. 9.9 of a thin d-c microbeam with a length of 300 μm and width of 14 μm by applying a driving voltage of 11 V.

sinusoidal feedback signal can be approximated by [160]

$$\omega_{osc} \simeq \omega_r \left(1 - \frac{\varphi_{osc} - \varphi_r}{2Q}\right) \tag{9.5}$$

where ω_r and φ_r are the resonant frequency and the phase angle at resonance of the microbeam, respectively. For a given microbeam resonance response, the oscillation frequency ω_{osc} thus depends on the operating point but also on the system damping represented by Q. The operating point can be influenced by changing the driving signal pulse width. If the pulse width is decreased, the oscillation frequency ω_{osc} increases. This effect can be observed for the self-excited oscillation in air and in water. In air, a maximum oscillation frequency shift of +1.4% was measured for a total pulse width variation from full pulse width to the smallest pulse width (almost zero) at which the oscillation sustained. The oscillation frequency was 279.8 kHz (same microbeam as measured in Fig. 9.10). Consequently, it is important to fix the pulse width during a measurement.

In liquid environment, the surrounding water is strongly coupled to the microbeams which results in an inertial loading (virtual mass). Therefore, the resonant frequencies of a microbeam are lower in a fluid compared to the frequencies in air or vacuum. Consequently, there are more resonance modes detectable in the measurable frequency bandwidth (0 Hz to 350 kHz given by the low noise digital decoder of the vibrometer) as there would be in a less dense medium. Higher order resonance modes in water are known to show higher quality factors [165]. Hence, the most stable self-excitation with a high frequency resolution was obtained at a higher order resonance mode. The most pronounced peak with the lowest total harmonic distortion (see Fig. 9.11) was typically obtained just below the cut off frequency at 350 kHz given by the vibrometer decoder.

The frequency of the self-sustained oscillation during the measurement is continuously monitored with a frequency counter measuring the frequency every second. The frequency counter counts zero-crossings. To minimize noise and select a single resonant mode, the measurement frequency was separated by means of a bandpass filter.

The use of Ti/Au electrodes in water limited the maximum voltage values that could be applied. Electrolysis reaction took place when the electrodes were in direct contact with water at voltages above 3 V. This resulted in a fast degradation of the electrodes. This drawback was solved by covering the electrodes with a 120 nm thick layer of Al_2O_3. With the alumina layer, voltages of up to 15 V could be applied without damaging the electrodes. After storing the samples for a few weeks in DI-water, electrolysis reaction started already at around 7 to 10 V. The insulation seemed to decrease over time. An insulating layer covering the electrodes has an effect on

the electrostatic actuation [166]. Finite element model simulations showed that the driving force decreases by around 5% when using such a layer, assuming a relative permittivity of $\varepsilon_r = 10$ for aluminum oxide [167] and a distance of 3 μm between the beam and the electrodes. Thus, the small screening due to the aluminum oxide layer does only slightly affect the electrostatic actuation in water.

In order to test the application of the feedback circuit, the oscillation frequency of a SU-8 microbeam is determined for varying concentrations of ethanol dissolved in water. This self-excitation in aqueous environment is shown in appendix J.

9.5 Conclusion

The use of a self-excited oscillation based on a positive feedback is more suitable than the application of the Q-enhancement technique which is also based on a positive feedback. With the self-excitation technique, the polymer microbeams can be driven in a stable oscillation in air but also in water. The final feedback circuit based on a Schmitt-trigger enables the self-excitation in air and in water and allows the direct detection of the resonant frequency and its variation, potentiating the application of polymer microresonators as chemical sensors or biosensors.

10 Detection of biomolecules

Microcantilever based biosensors are typically made of silicon microbeams which change their resonant frequency or deflection as a cause of analyte molecules adsorbing on the surface [152]. For the application of the deflection method, only one side of the cantilever has to be functionalized with the receptor molecules. This can be done by coating the upper surface with a gold layer which can be functionalized by thiol-conjugated receptor molecules [16, 168–170]. Besides gold, functional layers of chemical sensors but also such for biosensing applications often consist of polymer coatings [171]. Polymer microcantilevers with and without a gold layer have been used as deflecting biosensors because of their softness which results in high deflection for a induced surface stress, detecting 2 μM thiolated ssDNA [16] and 5 μg/ml streptavidin [172]. Tamayo et al. [30] predicted a superior sensitivity of soft polymeric resonant cantilevers based on an increasing stiffness due to the adsorbed molecular layer resulting in a positive frequency shift. Furthermore, oscillating polymer microbeam sensors made from bare SU-8 can be directly functionalized with receptor biomolecules [151, 173, 174], thereby covering the complete surface which simplifies the pre-treatment procedure.

In water, the quality factor of resonant microbeams is dominated by the damping of the aqueous environment. The quality factors of silicon and polymer micro cantilevers in water have similar low values of Q = 1.8 at 13 kHz for a silicon nitride cantilever [157] and Q = 1.4 at 7.3 kHz for SU-8 cantilevers [16]. In order to overcome the high damping in water, the microbeams are typically actuated in a self-excited oscillation by a positive feedback-loop [157] which has shown to be also feasible for polymer microbeams in aqueous environment [163], as introduced in chapter 9. Typically, minimum frequency changes of around 10-20 Hz can be measured for a cantilever resonator in water [152] limited by the broad resonance peaks due to the high damping in liquid environment. Therefore, it is important that the resonant sensor is sensitive enough in order to obtain frequency shifts which can be resolved. Soft polymer resonant biosensors are predicted to be up to one order of magnitude more sensitive compared to a silicon microresonator [30]. Consequently, resonant polymer microbeams have a high potential as low-cost system for disposable and label-free (that means the biomolecules are not labelled with a fluorescent molecule or magnetic particles for detection) biosensing applications.

To test the feasibility of a new sensor for protein detection, often the reliable and well characterized biotin/streptavidin ligand-receptor system is used. With biotin as a receptor molecule, streptavidin has been label-free detected with a gravimetric thin-film bulk acoustic resonator [175], gravimetric silicon-based micro cantilevers [176], optical methods based on an evanescent field [177, 178], surface plasmon resonance [179, 180], a porous silicon-based optical interferometric biosensor [181], a method based on the transmembrane movement of a polymer chain which is modulated by streptavidin [182], silicon nanostructures [183–185], and carbon nanotubes [186, 187].

Here, single- and double-clamped resonant all-polymer microbeams made from SU-8 are used for the detection of streptavidin. The polymer microstructures are functionalized by immersing them into the solution containing the receptor biomolecules which directly bind to the polymer surface.

10.1 Models

10.1.1 Mass loading near critical damping

As given by (4.8), the resonant frequency of a damped oscillator is a function of the damping ratio of the system. For small damping, the resonant frequency approximately is equal to the natural frequency. But for high damping, as it is the case in an aqueous environment, the resonant frequency can be significantly lower than the natural frequency and it is highly sensitive to changes of the damping ratio. The lower the damping the higher is the resonant frequency. With (4.2) and (4.3), the damping ratio (4.5) can be written as follows

$$\zeta = \frac{c}{2\sqrt{k\, m_{eff}}} \tag{10.1}$$

where c is the coefficient of damping force, m_{eff} is the effective mass and k is the spring constant. The effective mass includes the mass of the water around the microbeam which is coupled to the vibration. With (10.1) and (4.2), the resonant frequency of a damped oscillator (4.8) can be expressed as a function of c, m_{eff}, and k

$$\omega_{res} = 2\pi f_{res} = \sqrt{\frac{k}{m_{eff}} - \frac{1}{2}\left(\frac{c}{m_{eff}}\right)^2}. \tag{10.2}$$

From (10.2) it can be seen, that the resonant frequency obviously increases for an increasing stiffness k. By differentiating with respect to the effective mass m_{eff}

$$\frac{\partial \omega_{res}}{\partial m_{eff}} = \frac{c^2 - k\, m_{eff}}{\sqrt{2}\, m_{eff}^2 \sqrt{2k\, m_{eff} - c^2}} \tag{10.3}$$

it can be seen that the resonant frequency change is positive for an increasing mass if $c^2/(k\,m_{eff}) > 1$ (which is equal to $\zeta > 0.5$) and it is negative if $c^2/(k\,m_{eff}) < 1$. When $c^2/(k\,m_{eff}) = 2$, the system has reached its critical damping condition where $\zeta = 0.707$ and the change of the resonant frequency becomes infinite. That means, for the condition $1 < c^2/(k\,m_{eff}) < 2$ or $0.5 < \zeta < 0.707$, the resonant frequency is highly sensitive to an additional mass resulting in a positive frequency shift. For a system which has a small damping ($c^2/(k\,m_{eff}) \ll 1$), the resonant frequency response to an additional mass is negative. If $c^2/(k\,m_{eff}) > 2$ the oscillator system is over-damped and thus has no resonance. In Fig. 10.1, the influence of the effective mass on the resonant frequency in a highly damped system is plotted.

Summing up, the adsorption of biomolecules on the surface of a resonant microbeam can increase the stiffness which causes an increasing resonant frequency. In addition, the mass added to a soft and light polymeric microbeam oscillating in water can also cause a strong positive resonant frequency shift if the damping ratio is close to critical damping.

10.1.2 Eigenfrequency of multilayered beams

The eigenfrequency of a multilayered beam is given by [188]

$$f_0 = \frac{\lambda_n^2}{2\pi}\frac{1}{L^2}\left(\frac{\int_h Y(z-z_0)^2 \mathrm{d}z}{\sum_{j=1}^{N}(h_i\rho_i)}\right)^{1/2} \tag{10.4}$$

where Y is the Young's modulus of the individual layers, λ_n is the solution of the frequency equation, L is the length, h_j are the layer heights, ρ_i are the layer mass densities, and z_0 is the position of the neutral axis (this is the axis whose length remains constant during deflection). The case of biomolecules adsorbing on a microbeam is schematically depicted in Fig. 10.2.

The numerator under the square root in (10.4) represents the total geometrical moment of inertia of the beam. Assuming that the additional layers have the same height h_a, Young's modulus Y_a, and mass density ρ_a, the neutral axis is in the middle of the beam and $z_0 = 0$. The numerator can be written as

$$\int_{-h/2}^{h/2} Yz^2 \mathrm{d}z + 2\int_{h/2}^{h/2+h_a} Y_a z^2 \mathrm{d}z \tag{10.5}$$

and by integrating, the eigenfrequency of a thin microbeam with identical additional layers then becomes

$$f_0 = \frac{\lambda_n^2}{2\pi}\frac{1}{L^2}\left(\frac{\left(Yh^3 + 2Y_a h_a(4h_a^2 + 6hh_a + 3h^3)\right)}{12(h\rho + 2h_a\rho_a)}\right)^{1/2}. \tag{10.6}$$

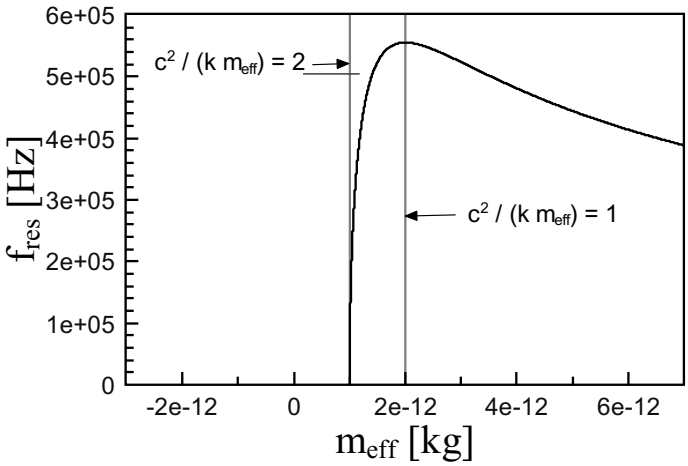

(a) Plot of (10.2)

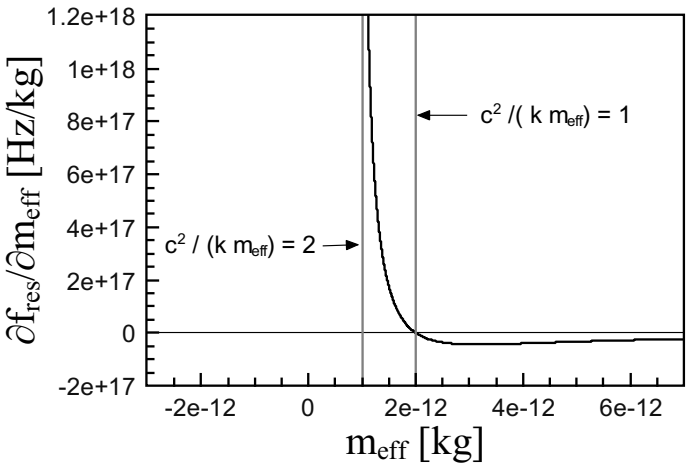

(b) Plot of (10.3)

Figure 10.1: Plot of (10.2) and (10.3) for $k = 0.5\,\mathrm{N/m}$ and $c = 1 \times 10^{-6}$ Pa s.

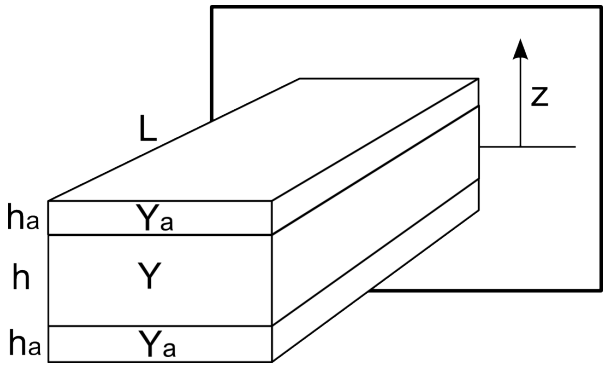

Figure 10.2: Schematic of a beam with additional layers on the top and bottom surface with different material properties.

10.1.3 Frequency response of microbeams immersed in water near a solid wall

In water, the effective mass of a vibrating microbeam is the sum of the beam mass and the mass of the water layer which is coupled to the beam vibration. This additional mass significantly decreases the resonant frequency which can be analytically modelled accounting the viscous effects for a beam immersed in a liquid of infinite extent [189]. For a rectangular microbeam immersed in water and lying parallel to a planar wall and whose distance to the wall is smaller than its width w, the frequency response is primarily defined by the gap distance between beam and wall [190, 191]. For a decreasing gap distance, the resonance peak strongly broadens and shifts to lower resonant frequencies. Thus, the resonant frequency and the damping of a microbeam near a planar surface in water are strongly influenced by the squeeze film effect. This strong effect is primarily caused by the significant fluid shear in the gap between microbeam and planar surface which adds to the localized fluid shear at the microbeam edges. The additional mass from the coupled water only plays a minor role for the frequency response [190].

For the case where dissipative effects in the fluid are small ($Q_{liq} \gg 1$) the flexural frequency response of the first few modes of a microbeam immersed in water near a planar surface can be described by [190]

$$\omega_{0,liq} = \omega_0 \left(1 + \frac{\pi \rho_{liq} w}{4\rho h} \Gamma_r(\omega_{0,liq})\right)^{(-1/2)} \tag{10.7}$$

and

$$Q_{liq} = \frac{\frac{4\rho h}{\pi \rho_{liq} w} + \Gamma_r(\omega_{0,liq})}{\Gamma_i(\omega_{0,liq})} \tag{10.8}$$

where ω_0 is the eigenfrequency of the beam and ρ_{liq} is the mass density of the liquid. Γ_r and Γ_i are the real and the imaginary part of the hydrodynamic function which depends on the Reynold's number and the ratio between beam width to gap distance. Solutions of Γ based on numerical calculations is presented in [190]. As can be seen, the resonant frequency in water (10.7) depends on itself and thus needs to be solved iteratively. But as described in chapter 9, the quality factor of the polymer microresonators are expected to have quality factors values around 1. Thus, the constraint of low damping is not given and the model for the frequency response of a beam near a solid wall is not valid.

The simulations of microbeams near a solid surface [192] have shown that the quality factor of the first mode falls from $Q > 3$ for a gap distance of 30 μm to $Q < 1$ for a gap distance of 6 μm. The simulated Q-values decrease significantly upon approaching towards the substrate. The second mode shows higher quality factors which also rapidly decrease for smaller gap distances ($Q < 2$ at gap distance of 5 μm). The added mass coefficient defined as

$$\alpha_m = \left(\frac{\omega_0}{\omega_{liq}}\right)^2 - 1 \tag{10.9}$$

increases from $\alpha_m = 6$ far away from the surface up to $\alpha_m = 14$ for a gap distance of 5 μm for the second mode. Interestingly, the first torsional mode was less sensitive to the squeeze film effect than the bending modes.

10.2 Experimental

The microbeams used for the biosensing experiments are of the thin type with a structure thickness of 1.45 μm. The substrate with the Cr/Au electrodes is coated with a 120 nm thick aluminum oxide layer.

Due to the small fluid sample volumes, the tests with biomolecules are performed in a small dish (volume of around 5 ml) covered with a glass slide. The wire-bond pads of the chips with the resonant polymer structures are electrically contacted with probe needles. Usually, biomolecules are dissolved in buffer solutions. These buffers are lightly conductive and the electrostatic field between the electrodes is attenuated. In order to keep the electrostatic force constant which is acting on the polymer microbeam when placed in a buffer, the voltage has to be increased. But higher voltages accelerate the degradation of the gold electrodes, even if they are covered with an alumina film. Therefore, the buffer concentrations were kept as low as possible.

10.2.1 Surface functionalization

For the demonstration of the capability of SU-8 microresonators as biosensors, biotin and streptavidin was chosen as a reliable and well characterized ligand-receptor system. Biotin and streptavidin have a very high affinity and selectivity and are often used in immunohistochemistry to label and localize proteins in cells of a tissue. Biotin, also known as vitamine B7, is a relatively small molecule of about 0.5 nm which can be covalently attached to molecules and surfaces. This process is called biotinylation. Streptavidin is a tetrameric protein with a molecular weight of 58 kDa. Each of the four subunits is able to bind one biotin molecule. The non-covalent bond formed between streptavidin and biotin is one of the strongest and approaches the strength of a covalent bond. The formation of the complex involves hydrogen bonds, electrostatic and hydrophobic interactions. The biotin-streptavidin complex is very stable and shows a high thermal stability [193]. The diameter of a streptavidin protein is about 5.5 to 6.5 nm.

Immunoglobulin G (IgG) is an antibody composed of 4 peptides showing a characteristic Y-like shape of an antibody. It is known, that IgG type proteins can be immobilized on bare SU-8 [173,174]. Therefore, biotinylated anti-mouse IgG has been used as receptor molecules. The IgG antibodies are conjugated with 3-5 biotin molecules, each. In order to biotinylate the SU-8 sensor surface, biotinylated IgG antibodies are immobilized as receptor molecules. The target molecules, streptavidin, binds to the biotin molecules at the sensor surface. Here, IgG has the function of a linker molecule attaching the receptor molecules on the polymer surface.

As a negative test, bovine serum albumin (BSA) is used. In mammals, BSA is the most abundant protein in plasma. It's molecular weight is similar to the molecular weight of streptavidin and it shows an elliptic structure with a diameter of about 7 nm. BSA is water soluble and can reversibly bind anions and cations showing a so called ampholytic characteristic. The main function of albumin is to sustain the osmotic pressure in blood vessels. It is also responsible for the transport of non water-soluble molecules as for example hydrophobic hormones, vitamines of fatty acids by non specific bindings. Due to the ability to make unspecific bindings, BSA is often used to block active binding sites [194] and as negative control to test the selectivity of a biosensor [172]. The detection procedure is schematically shown in Fig. 10.3.

Protocol

The protocol of the pre-treatment and the measurement is as follows.

1. Anti-mouse immunoglobulin G (IgG) (whole molecule) biotin conjugate [0.46 mg/ml] is diluted 1:5000 with phosphate buffered saline (PBS) [10 mM].

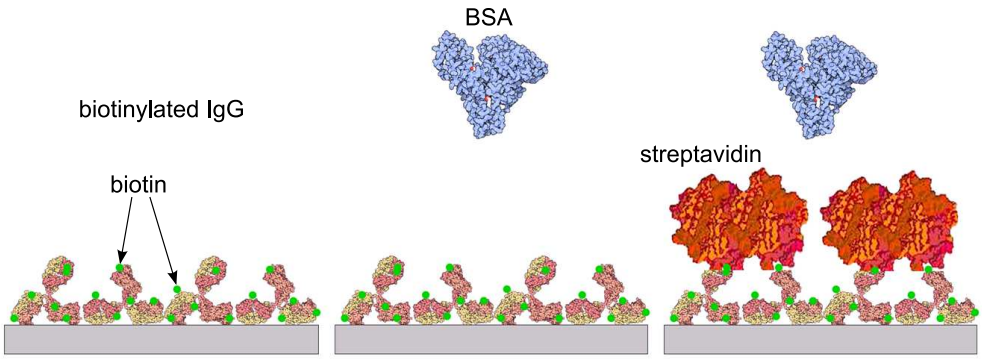

Figure 10.3: Measurement procedure for the detection of streptavidin; SU-8 microbeams are covered with biotinylated immunoglobulin G (IgG). Bovine serum albumin (BSA) is used as a negative test. The analyte streptavidin (SA) is binding to the biotin of the IgG.

2. The sample with the resonant structures is put into a droplet of this solution and stored at 37 °C for 60 min.
3. The sample is rinsed for 20 min with tris buffered saline with tween 20 (TBST) to remove unspecific bindings.
4. TBST is replaced by water.
5. Blocking unbound surface sites: Bovine serum albumin [5 μg/ml] diluted in water is applied.
6. The sample is rinsed with water.
7. Starting of measurement.
8. Negative test: Sample environment is replaced by bovine serum albumin [5 μg/ml] diluted in water.
9. Positive test: The Sample environment is replaced by the analyte streptavidin from streptomyces adidinii [5 μg/ml].

10.3 Results

In Fig. 10.4, the amplitude response of the self-sustained oscillation of the resonant sensor in water is shown before and after streptavidin detection.

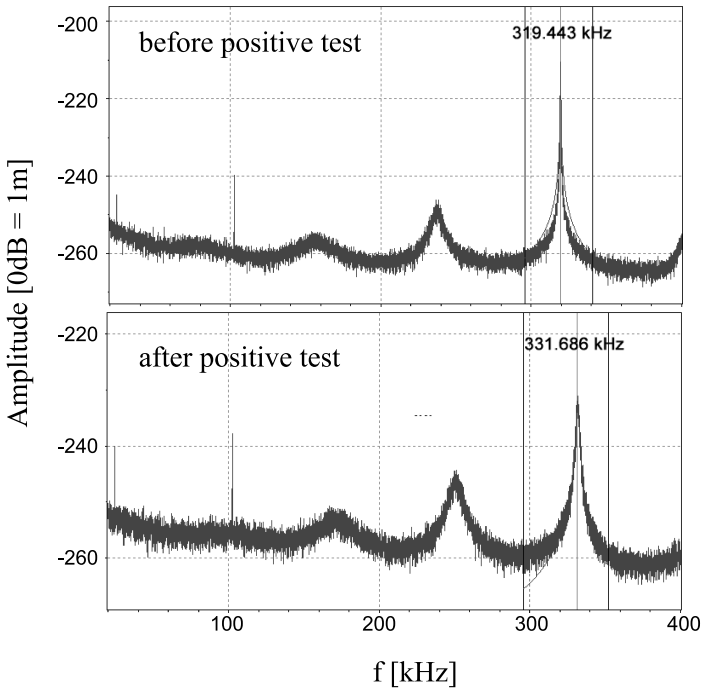

Figure 10.4: Frequency response before and after streptavidin detection (5.0 g/ml) with a biotinylated SU-8 resonant double-clamped microbeam (sample: d-c 1).

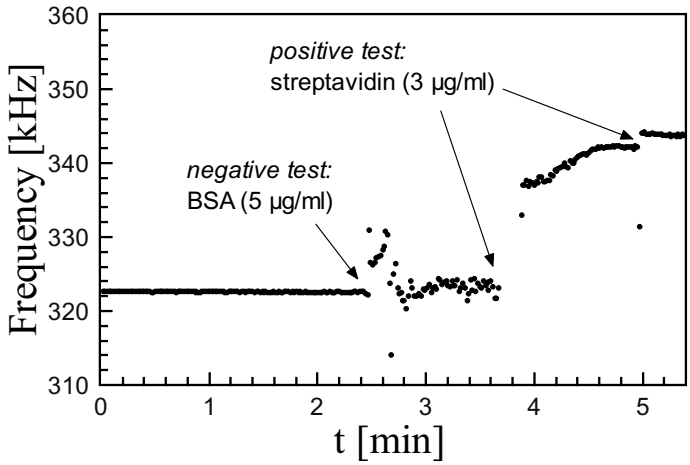

Figure 10.5: Detection of 3 μg/ml streptavidin with a thin double-clamped SU-8 microbeam (L=80 μm, h=1.45 μm, w=14 μm) at $T = 24.1 \pm 0.2$ °C (sample: d-c 2).

Fig. 10.5 shows the monitored oscillation frequency of a SU-8 double-clamped microbeam during the sequential exposure to aqueous solutions containing 5 μg/ml of BSA as a negative test and 3.0 μg/ml of streptavidin as a positive test causing a frequency shift of 6.1%. A minimum frequency resolution of 58 Hz was determined for a constant signal over a time period of 1 minute by taking twice the standard deviation.

The sample was functionalized prior to the measurement with immunoglobulin G conjugated with biotin which has a high affinity to streptavidin. Minimum streptavidin concentrations of 0.025 μg/ml (this is equal to 430 pM assuming a molecular weight of 58 kDa per streptavidin protein) were detected with a corresponding frequency shift 1.9% (Fig. 10.6).

Fig. 10.7 shows the detection of 0.25 μg/ml of streptavidin causing a frequency shift of 15.6%, which is the highest measured relative frequency shift.

Fig. 10.8 shows the relative frequency change of single-clamped (s-c) and double-clamped (d-c) microbeams for the detection of different concentrations of streptavidin. Maximum frequency shifts of 15.6% for the positive test were measured whereas the maximum measured frequency shift of the negative test was 0.4%. Details about the microbeams used for the streptavidin detection are listed in table 10.1.

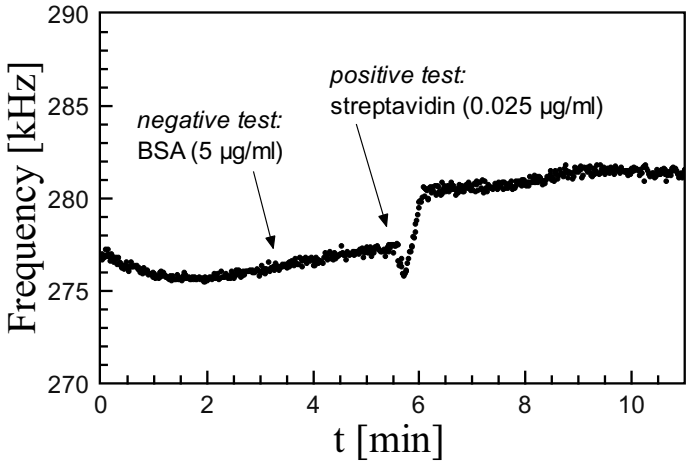

Figure 10.6: Detection of 0.025 μg/ml streptavidin with a thin double-clamped SU-8 microbeam (L=200 μm, h=1.45 μm, w=14 μm) at $T = 24.9 \pm 0.2$ °C (sample: d-c 4).

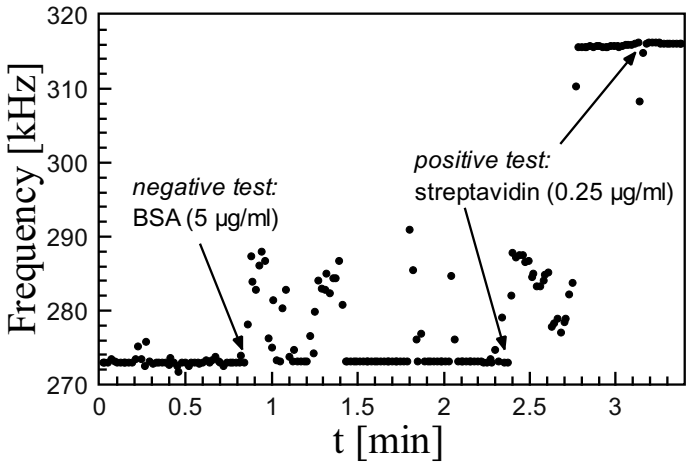

Figure 10.7: Detection of 0.25 μg/ml streptavidin with a thin double-clamped SU-8 microbeam (L=100 μm, h=1.45 μm, w=14 μm) at $T = 24.5 \pm 0.2$ °C (sample: d-c 3).

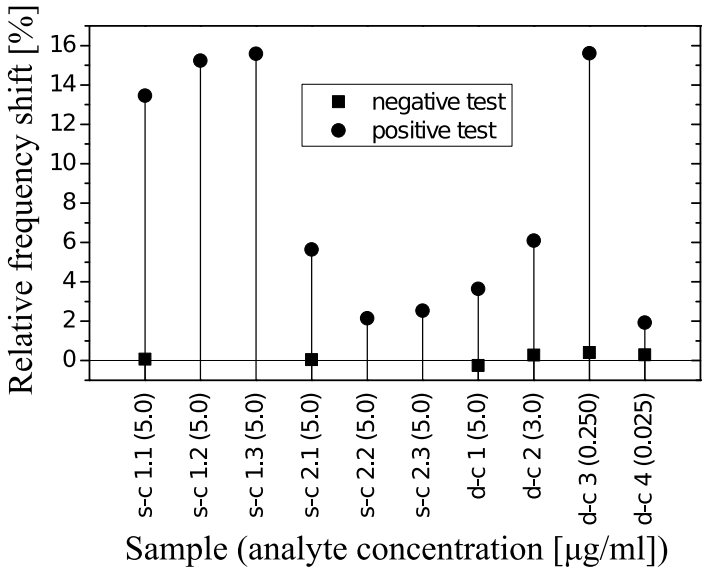

Figure 10.8: Relative frequency shift of single-clamped (s-c) and double-clamped (d-c) SU-8 microbeams for the detection of streptavidin. The oscillation frequencies vary between 272-322 kHz.

Table 10.1: Samples used for the detection of streptavidin.

Label	Clamping	Length [μm]	Start frequency [kHz]	Streptavidin concentration [μg/ml]
s-c 1.1	single	100	272.7	5.0
s-c 1.2	single	100	315.1	5.0
s-c 1.3	single	100	314.4	5.0
s-c 2.1	single	60	269.9	5.0
s-c 2.2	single	60	310.8	5.0
s-c 2.3	single	60	306.2	5.0
d-c 1	double	100	320.2	5.0
d-c 2	double	80	322.6	3.0
d-c 3	double	100	273.1	0.25
d-c 4	double	200	276.1	0.025

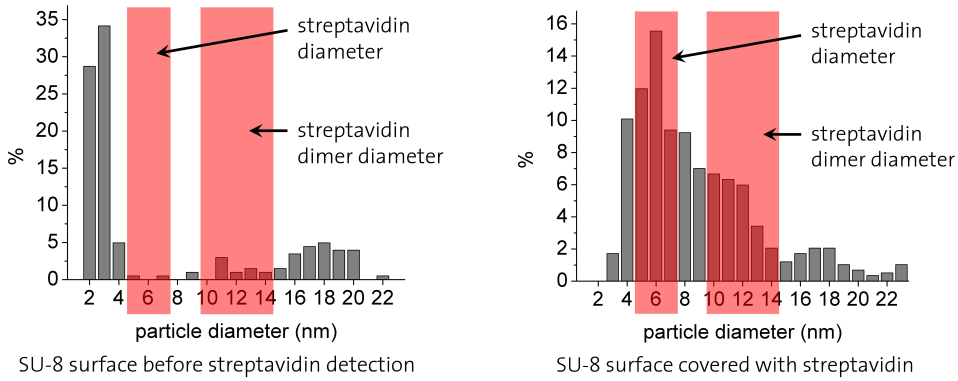

Figure 10.9: AFM histogram of particle diameter on SU-8 surface before (a) and after (b) streptavidin detection.

10.4 Discussion

To verify, that the analyte molecules actually bind to the biotinylated SU-8 surface, a histogram of the particle size on the beam surface before the measurements and after the streptavidin detection was calculated from the topographical information of an AFM scan (Fig. 10.9). The majority of the particles after the streptavidin detection have a diameter of 6 nm which corresponds to the size of the analyte molecules. Streptavidin builds dimers [195, 196], entities of two equal streptavidin monomers, which have a diameter of around 10-13 nm. This explains the increased levels of particle diameters of this dimension in the histogram. It is concluded that the shift of the oscillation frequency is caused by the adsorption of the analyte molecules.

As shown in Fig. 10.8, the frequency shift of the streptavidin detection is always positive. Among other effects, this might be due to an increase of the flexural rigidity of the soft polymer microbeams caused by the adsorbate stiffness as theoretically explained in [30]. A positive frequency shift was measured for bacteria adsorption on silicon cantilevers in air by placing the bacteria layer near the clamping of the microbeam where the additional layer has a significant influence on the flexural rigidity and the mass effect is minimal. Consequently, the frequency increased [197]. Positive frequency shifts of up to +50% were measured with 30 nm thick silicon cantilevers after the adsorption of proteins in air [198]. For a similar experiment where 0.2 mg/ml neutravidin was detected in aqueous solution with a onesided biotinylated silicon nitride cantilever with a thickness between 0.7 to 1 μm the resonant frequency showed a negative shift of -19% after the adsorption of the analyte molecules [157] due to the

mass uptake. The silicon nitride microbeam is too stiff to be sensitive to a change of the adsorbate stiffness. With (10.6), the relative frequency change due to the adsorbed layer on the microbeam can be evaluated. The exact film thickness h_a, film stiffness Y_a, and film mass density ρ_a are unknown and thus have to be guessed. Assuming the streptavidin layer to be $h_a = 12$ nm thick (see Fig. 10.9b), a relative frequency change of +0.35% for a protein layer ($\rho_a = 183$ kg/m^3 and $Y_a = 0.7$ GPa [30]) and +8.2% for a self-assembled monolayer ($\rho_a = 675$ kg/m^3 and $Y_a = 12.9$ GPa [30]) results. This estimation of the frequency shift due to an adsorbed layer is lower than the maximal measured frequency shifts of up to +15.6%. In air, the d-c SU-8 microbeams are pre-stressed and they would be insensitive to a change in the flexural rigidity. But in water the polymer swells, the pre-stress is released and the d-c structures can also become sensitive to changes of the flexural rigidity.

As discussed in the introduction, in addition to the stiffness increase, the adsorbed streptavidin molecules also increase the effective mass m_{eff} which can trigger a positive frequency shift too if the damping is high enough, that is if $c^2/(k\, m_{eff}) > 1$. Unfortunately, the analytical model presented in [190] for the frequency response of a microbeam near a solid wall is not valid for damping close to the critical damping ratio. The frequency response of the polymeric microcantilevers would thus needed to be simulated by means of the finite element method in order to get an accurate frequency response description. Instead, the damping ratio is estimated for a beam in a viscous fluid of infinite extent. The damping coefficient of a rectangular beam in water is given by [199]

$$c_{water} = \frac{L}{2}\left(3\pi\mu + \frac{3}{4}\pi w\sqrt{4\rho_{liq}\mu\pi f_{res}}\right) \tag{10.10}$$

where $\mu = 10^{-3}$ N s m^{-2} is the viscosity and $\rho_{liq} = 997$ kg/m^3 is the mass density of water. The eigenfrequency of a 60 μm long thin ($h = 1.3$ μm) s-c microbeam is 105 kHz. In [192] it was shown, that the added mass coefficient for small gaps is $\alpha_m > 12$. With (10.9) the resonant frequency in water is $\omega_{liq} \approx 0.25\,\omega_0$. The resonant frequency in water is thus assumed to be approximately 25 kHz. This results in a damping coefficient of $c_{water} = 8.4 \times 10^{-7}$ Pa s. In water, the effective mass of a cantilever beam increases due to the coupling to the surrounding water which is moved during vibration. It is given by [199]

$$m_{eff,water} = \frac{L}{4}\left(\rho w h + \frac{3}{4}\pi w\sqrt{\frac{\rho_{liq}\mu}{\pi f_{res}}}\right). \tag{10.11}$$

For a resonant frequency of 25 kHz an effective mass of $m_{eff} = 2.1 \times 10^{-12}$ kg is obtained for the 60 μm long thin s-c microbeam. The spring constant can be calculated from (4.20) and a value of $k = 0.15$ N/m is obtained assuming a Young's

modulus of 4 GPa. With these values, a damping ratio (10.1) $\zeta \approx 0.74$ results. This is above the critical damping ratio of $\zeta = 0.707$. Thus, the first resonant mode of a thin s-c microbeam immersed in a viscous fluid of infinite extent is already overdamped. FEM simulation [192] and measurement results [191] of the damping ratio with respect to the gap distance have clearly shown, that the damping is significantly increased upon approaching towards the substrate. Thus, the polymeric thin s-c microbeams are already overdamped far away from a surface, but they are even more damped because of the squeeze film effect in the gap with a height of only 3 μm. This estimation coincides with observations made during measurements that the first resonance mode is overdamped and thus no resonance is observed. Consequently, the polymer microbeams were driven at a higher resonant mode where the damping is smaller [165, 192]. From the fact, that all measured frequency shifts are positive, it can be hypothesized that $0.5 < \zeta < 0.707$ for the measured microbeams vibrating at a higher resonance mode.

Furthermore, the influence of a change of the resonator parameters on the positive feedback is discussed. For an increasing spring constant and an additional mass caused by the adsorbed biomolecules, the damping ratio (10.1) becomes smaller. Since the operation point of the driving signal does not perfectly match the phase of the sensor resonance, the oscillation frequency will be different from the resonant frequency of the sensor, as explained in section 9.4. For a constant phase offset, this causes the oscillation frequency to be sensitive to the system damping. The oscillation frequency is below the resonant frequency of the microbeam which is caused by the signal delay of the feedback circuit as can be seen in Fig. 9.10. Based on (9.5) it can be concluded, that a decreasing damping ratio caused by the additional mass from the adsorbed biomolecules thus would increase the oscillation frequency. For small Q values, this effect is most pronounced. The quality factor of the polymer microresonators in water is primarily defined by the squeeze film damping between beam and substrate. Therefore, the relative small additional mass from the adsorbed biomolecules will not significantly change the quality factor and the effect of the feedback on the oscillation frequency is assumed to be insignificant.

In Fig. 10.8 it can be seen, that the frequency shifts from microbeams from the same chip (chip 1 and 2) are similar. This suggests that the sensor sensitivity mainly depends on the resonant mode of each sample at which is was operated and the quality of the functionalization rather than on the feedback control. In summary, no systematic difference in the sensitivity could be observed between the single- and double-clamped beams.

The biotin-streptavidin bond is durable and only breaks at temperature above 70 °C [200], that means the streptavidin molecules that are bound to the biotiny-

lated polymer microbeams are fixed there. In Fig. 10.5 it can be seen, that additional analyte only slightly increased the resonant frequency. This behavior was observed at several measurements. After a first flush with 3.0 or 5.0 μg/ml of streptavidin, the streptavidin molecules seem to almost cover the whole surface of the beam, such that only little free biotin molecules remain available. All receptor binding sites are saturated. Hence, for the second injection of streptavidin there are quasi no biotin binding sites available anymore.

The minimal detected streptavidin concentration of 25 ng/ml which is equal to 430 pM (assuming a molecular weight of 58 kDa for streptavidin molecules) is compared to minimal concentrations measured by other techniques. This comparison is presented in Table 10.2. Methods such as the surface plasmon resonance or the use of silicon nanowires are highly sensitive and are able to detect analytes in picomolar concentrations. The presented detection based on resonant polymer microbeams captures one of the top positions in the list. The minimal detected concentration of 430 pM streptavidin is one order of magnitude higher than the most sensitive methods in the list. The measurement with the resonant polymer microbeams shown in Fig. 10.7 exhibits a signal to noise ratio of around 10. Thus it should be possible to detect even lower concentrations of analyte. From a geometrical point of view, the sensitivity can further be enhanced by decreasing the polymer beam thickness. The response time can not be directly compared between different biosensing assays because it depends on the sensor sensitivity but also mainly on the experimental conditions such as the sample volume. The small liquid volume of 5 ml might be a reason for the fast response time for the streptavidin detection with the polymer microresonators which is one of the fastest in the list.

10.5 Conclusion

In conclusion, we have demonstrated the feasibility of polymer microbeam resonators as biosensors. The experimental results show that streptavidin can be selectively detected against BSA with a high sensitivity resulting in a very fast response time of less than 30 sec for a sample volume of 5 ml. The minimal concentration of 430 pM of streptavidin that are measured is comparable to the minimal detected concentrations measured with state-of-the-art techniques. A main advantage of a resonant polymer microbeam biosensor is the possibility to directly adsorb biomolecules on the polymer without the need of an additional functional coating. All-polymer resonant microbeams have thus a high potential as low-cost system for disposable and label-free biosensing applications. The dynamic response of the polymeric microbeams immersed in water can not be exactly explained with analytical models. The dynamic

Table 10.2: A comparison of minimal measured streptavidin concentrations (C_{SA}) by means of the biotin/streptavidin system.

C_{SA} [M]	Response time [sec]	Sensor gauge	Reference
2.5×10^{-11}	~ 40	conductance of silicon nanowire	Science, 2001 [183]
1×10^{-10}	n.a.	absorbance intensity of colloidal surface plasmon resonance	Anal. Chem., 2003 [177]
4.3×10^{-10}	10 - 30	resonant frequency of polymer microbeam	**this work**
8.3×10^{-10}	>1800	absorbance intensity of colloidal surface plasmon resonance	Anal. Chem., 2004 [179]
1×10^{-9}	~1000	conductance of silicon nanoribbon	Nanotechn., 2008 [184]
$\sim1\times10^{-8}$	120	conductance of single protein pore	Nat. Biotechnol., 2000 [182]
1×10^{-8}	500	deflection of silicon nitride microcantilever	Biosens. Bioelectron., 2007 [201]
5×10^{-8}	1800	absorbance intensity of colloidal surface plasmon resonance	Biosens. Bioelectron., 2008 [180]
8×10^{-8}	~ 500	deflection of polymer microbeam	Appl. Phys. Lett., 2006 [172]
1×10^{-7}	> 600	deflection of silicon microcantilever	Sens. Actuators, B, 2001 [176]
1×10^{-7}	~ 30	conductance of carbon nanotubes	PNAS, 2003 [187]
1.7×10^{-7}	~ 50	absorbance spectrum of optical resonance in dielectric microparticle	Appl. Phys. Lett., 2002 [178]
5×10^{-7}	6	conductuance of silicon nanostructure	Nanomed. Nanotechnol. Biol. Med., 2006 [185]
3.4×10^{-6}	900	resonant frequency of silicon-nitride microcantilever	Appl. Phys. Lett., 2001 [157]
3.4×10^{-6}	n.a.	reflection spectrum of porous silicon semiconductor	Science, 1997 [181]

behavior would need to be analyzed computationally in order to take account of the high damping in water and its effect on the resonant frequency and damping ratio.

11 Electronic readout

All the measurements in the previous chapters have been performed with a laser-Doppler vibrometer. This optical readout method allows the detection of a vertical vibration with picometer resolution. Furthermore, the optical readout system is electrically decoupled from the device under test. This decoupling allows the measurement of arbitrary micromechanical devices without the need for a sophisticated electronic readout circuitry. Therefore, the use of a laser-Doppler vibrometer can be favorable for vibration measurements in basic research, such as the determination of material properties or investigating the feasibility of a microsystem as a sensor as done in the previous chapters. But for the development of a sensor device, e.g. based on the findings from research, a readout setup is needed that can be directly integrated to the sensor unit. This is usually done by transducing the micromechanical sensor response into an electrical signal by means of an electronic readout circuit, e.g. by measuring a capacitance change. The electrostatic actuation principle of the all-polymer microresonators present a microsystem design on which a standard readout schema can not be applied. In this chapter, the electronic readout by means of a capacitance change of the all-polymer microresonators is investigated.

The dielectric force used to actuate the polymer microbeams is an electrostatic force which implies a change of the resonator capacitance when the dielectric polymer beam changes its distance relative to the electrodes. Consequently, the vibrational amplitude of the resonant micro beam can be monitored by measuring the capacitance change [202]. Fig. 11.1 shows the readout scheme. In order to measure this change, which is orders of magnitude smaller than the fixed feedthrough capacitance C_{ft}, a differential design is needed. This is done by building a half-bridge with the resonator and a fixed reference capacitance C_{ref} which is equal to the fixed feedthrough capacitance. The half-bridge is driven by two sinusoidal signals with 180 °C phase difference in order to cancel out the influence of the fixed feedthrough capacitance. A large bias voltage U_{DC} at the resonator is used to generate a larger sinusoidal output. When the dielectric polymer microresonator is excited by the input voltage U_{in} the vibration creates a time-varying capacitance between the coplanar electrode pair. The bias voltage which is applied across the time-varying capacitance produces a motional output current I_{out}. The output current is maximum when the vibration is at resonance. The bridge output current is readout by means of a

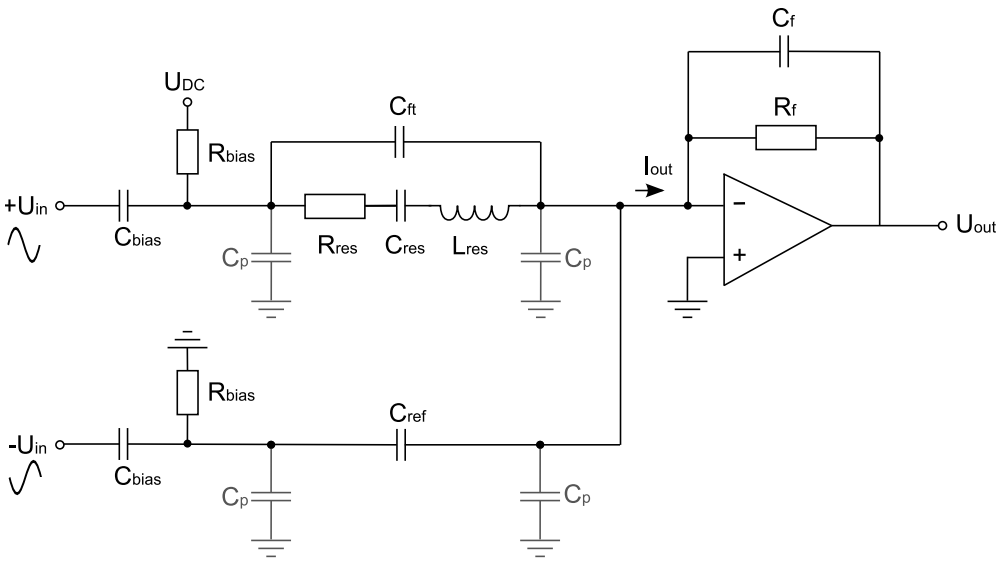

Figure 11.1: Schematic of the experimental setup for the electronic readout including the small-signal electromechanical LCR model of the oscillating microbeam resonator.

transimpedance amplifier [203]. With this setup, the bridge output is held at virtual ground by an operational amplifier shorting the parasitic capacitances C_p of the output node. A reduction of the parasitic capacitances C_p is still favorable to reduce the overall noise. The I/U amplification is amplifying I_{out} to $U_{out} = R_f I_{out}$, where R_f is the feedback resistance.

11.1 Electromechanical model

Assuming the DC-bias voltage U_{DC} to be much larger than the AC-excitation voltage U_{in}, the electrostatic resonator can be modelled as a inductor-capacitor-resistor (LCR) circuit with the impedance of [202]

$$Z_{res}(s) = R_{res} + sL_{res} + \frac{1}{sC_{res}} \tag{11.1}$$

with the following equation for the particular elements

$$R_{res} = \frac{m_{eff}\,\omega_0}{Q\,U_{DC}^2\left(\frac{\partial C}{\partial z}\right)^2} \tag{11.2}$$

$$C_{res} = \frac{1}{Q\ \omega_0\ R_{res}} \tag{11.3}$$

$$L_{res} = \frac{Q\ R_{res}}{\omega_0} \tag{11.4}$$

where m_{eff} is the effective mass of the resonator, ω_0 is the radian natural frequency, z is the displacement of the beam during vibration and $\partial C/\partial z$ is the change of the resonator capacitance per unit displacement of the microbeam. The total impedance of the microresonator device $Z_{res,ft}$ is the parallel combination of (11.1) with the feedthrough capacitance C_{ft} existing over the two electrodes placed below the polymer microbeam

$$Z_{res,ft}(s) = \frac{U_{in}}{I_{out}} = \frac{1 + sC_{res}(R_{res} + sL_{res})}{s(C_{res} + C_{ft}(1 + sC_{res}(R_{res} + sL_{res})))}. \tag{11.5}$$

The impedance of the transimpedance amplifier is given by

$$Z_f(s) = \frac{U_{out}}{I_{out}} = -\frac{R_f}{1 + sC_f R_r}. \tag{11.6}$$

Neglecting the reference electrode, the transfer function of the electronic circuit is

$$H_{noRef}(s) = \frac{U_{out}}{U_{in}} = \frac{Z_f}{Z_{res,ft}} \tag{11.7}$$

and with the reference electrode, the total transfer function becomes

$$\begin{aligned} H(s) = \frac{U_{out}}{U_{in}} &= Z_f \left(\frac{1}{Z_{res,ft}} - sC_{ref} \right) \\ &= Z_f \left(\frac{sC_{res}}{1 + sC_{res}(R_{res} + sL_{res})} + sC_{ft} - sC_{ref} \right). \end{aligned} \tag{11.8}$$

As already mentioned above, the influence of the feedthrough capacitance C_{ft} on the transfer function can be fully suppressed when the capacitance C_{ref} of the reference electrode has the same magnitude as C_{ft}. Hence, the transfer function of the pure resonator remains as a result.

In order to create the electromechanical model of the resonator by means of (11.8) and (11.7), the required parameters have to be determined. The microbeams which is going to be used in the capacitive readout experiments is characterized optically by means of the laser-Doppler vibrometer. The resonance response of the thin d-c microbeam is shown in Fig. 11.2. A resonant frequency of f_{res}=279.2 kHz and a quality factor of Q=6.7 are measured.

A change in capacitance per unit displacement of 60 aF/μm was calculated by means of a finite element simulation assuming an electrode gap distance $g = 2\mu m$,

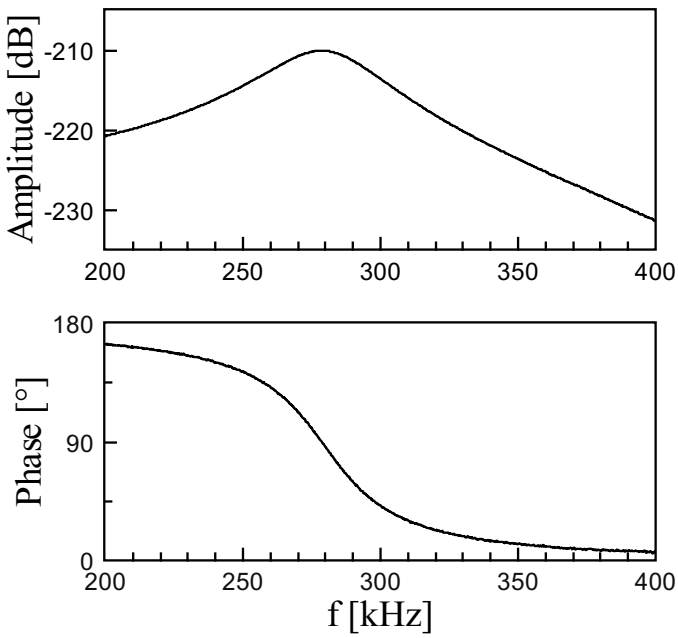

Figure 11.2: Measured vibration spectrum for a long thin d-c microbeam (150 μm) at atmospheric pressure at room temperature measured with a laser-Doppler vibrometer. An actuation voltage of U_{AC}=10 V and U_{DC}=10 V was applied. The vibration has a resonant frequency of f_{res}=279.2 kHz and a quality factor of Q=6.7.

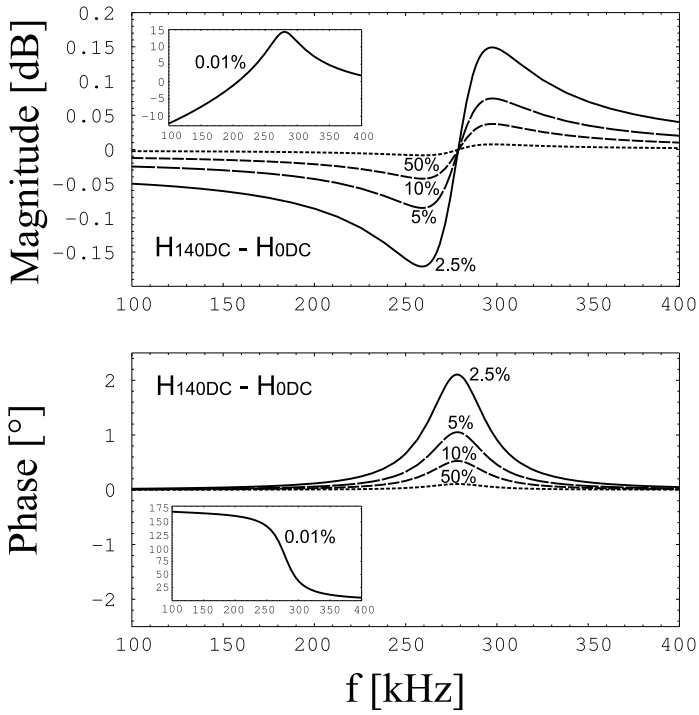

Figure 11.3: The differential transfer function according to (11.8) for different C_{ref} to C_{ft} ratios in percent for a bias voltage of U_{DC} =140 V, an effective mass m_{eff} = 1.83×10^{-12} kg, a sensitivity of 60 aF/μm, a quality factor of $Q = 6.7$, a resonant frequency of $f_{res} = 279.2$ kHz and a feedthrough capacitance of $C_{ft} = 100$ fF. For the transimpedance amplifier, a resistance and capacitance of R_f=22 MOhm and C_f=1 pF are used.

and a distance from the beam to the substrate of $d = 3\mu m$. The change of capacitance is not constant. The obtained value is only valid close around the working point at the distance d. The sensitivity of 60 aF/μm is three orders of magnitude smaller than a typical sensitivity of a capacitive sensor interface e.g. of an accelerometer [204].

The differential transfer function (11.8) is shown in Fig. 11.3 for different C_{ref} to C_{ft} ratios given in percent. The smaller the missmatch between the reference capacitance and the feedthrough capacitance the higher becomes the output signal. The goal would be to perfectly match these two capacitances. In the insert it can be seen that for a capacitance match of 0.01 % the curves take the form of the resonance response of a resonator, as shown in the vibrometer measurement (Fig. 11.2).

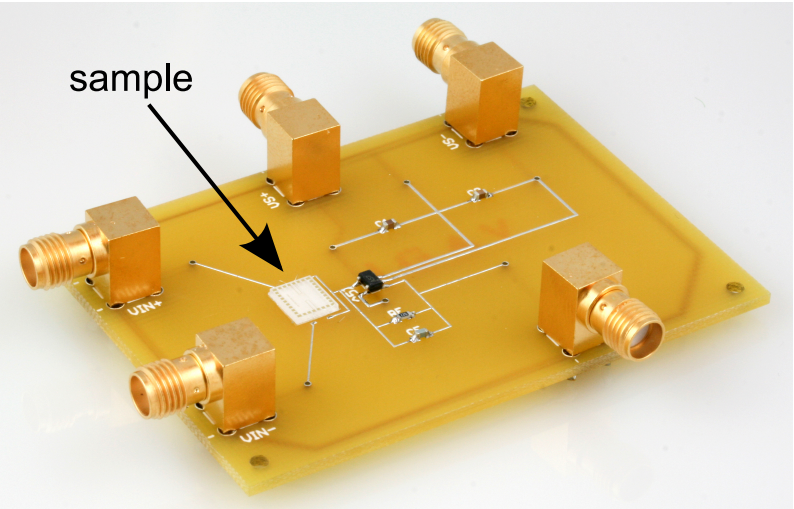

Figure 11.4: Photograph of a PCB for the electric readout of a polymer microbeam by means of a transimpedance amplifer setup.

11.2 Experimental

For the implementation of the electrical readout according to the transimpedance amplifier readout scheme, samples were fabricated with a reference electrode pair on the chip along with the polymer resonator. The chip containing one resonator is directly die and wire bonded onto a printed-circuit board (PCB) containing the readout circuitry. This solution is advantageous over a chip-carrier chip-socket system and reduces parasitic capacitances. An image of the PCB with a sample wire-bonded onto it is shown in Fig. 11.4. A high gain bandwidth (gain bandwidth product of 1.6 GHz), low-noise voltage-feedback op amp was used which is suitable for wide-band transimpedance applications (Burr-Brown OPA657). The feedback resistance was set to 22 MOhm and a feedback capacitance of 1 pF was selected for stability reason. Bias-Ts are used with a capacitance C_{bias} of 14.1 μF and a resistance R_{bias} of 11.7 kOhm. The transmission measurements are done with a network analyzer from Hewlett Packard. A 180 °C phase shifter from Mini-Circuits is used to split the input voltage U_{in} coming from the Network Analyzer. For the measurements, the PCB is placed in a grounded aluminum box. The device under test was a thin stringlike d-c microbeam with a length of 150 μm throughout the measurements.

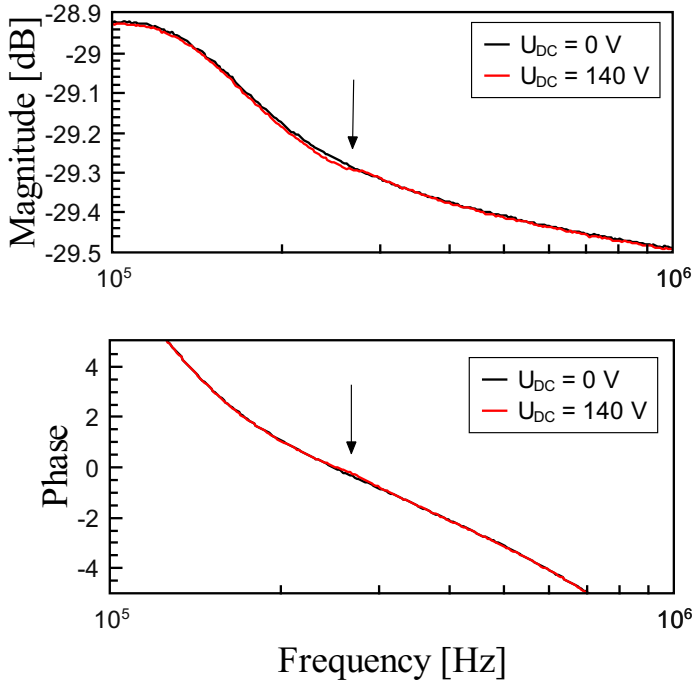

Figure 11.5: Measured absolute transmission spectrum H for a long thin d-c microbeam (150 μm) at atmospheric pressure at room temperature measured with a network analyzer.

11.3 Results

Fig. 11.5 shows the absolute transmission spectrum for a thin d-c microbeam. The transmission was measured for a bias voltage of 0 V and 140 V. The resonant peak is slightly visible at a frequency just below 300 kHz (as indicated by the arrow).

The difference of the transmission spectrum for the measurement with and without bias voltage is small. Therefore, a differential measurement was performed and the measured transmission spectrum with zero bias voltage is subtracted from the spectrum with applied bias voltage. In Fig. 11.6 the differential transmission spectrum of the same sample is shown. The measured data is compared to the model which is shown as a grey line.

In Fig. 11.7, the differential transmission spectrum was measured without the reference electrode. Here, the signal from the network analyzer was directly fed to the input of the microresonator without using the half-bridge to cancel out the large feedthrough capacitance.

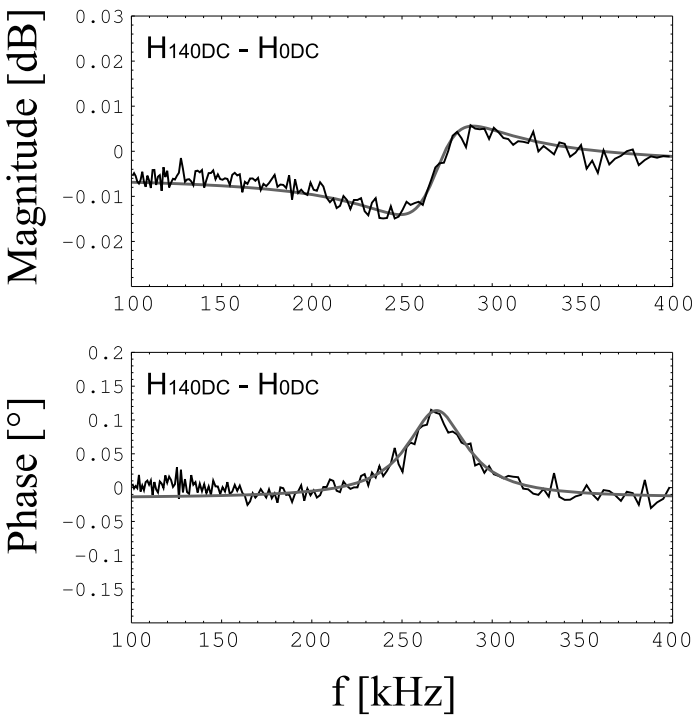

Figure 11.6: Measured differential transmission spectrum H (black line) with a bias voltage of $U_{DC} = 140$ V for a long thin d-c microbeam (150 μm) at atmospheric pressure at room temperature measured with a network analyzer. The grey line is the corresponding transfer function (11.8) for an effective mass $m_{eff} = 1.83 \times 10^{-12}$ kg, a sensitivity of 60 aF/μm, a quality factor of $Q = 6.7$, a feedthrough capacitance of $C_{ft} = 100$ fF, and a C_{ref} to C_{ft} match of 40%. The frequency and magnitude (offset) of the model are adapted to match the measured data.

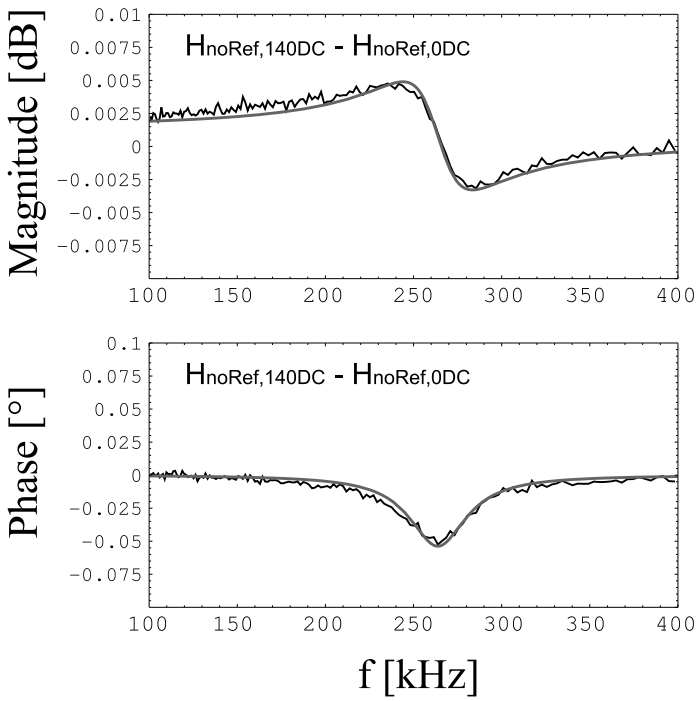

Figure 11.7: Measured differential transmission spectrum with a bias voltage of $U_{DC} = 140$ V for a long thin d-c microbeam (150 μm) without reference electrode (and without passing the signal through the phase-shifter) at atmospheric pressure at room temperature measured with a network analyzer. The grey line is the corresponding transfer function (11.7) for an effective mass $m_{eff} = 1.83 \times 10^{-12}$ kg, a sensitivity of 60 aF/μm, a quality factor of $Q = 6.7$, and a feedthrough capacitance of $C_{ft} = 100$ fF. The frequency and magnitude (offset) of the model are adapted to match the measured data.

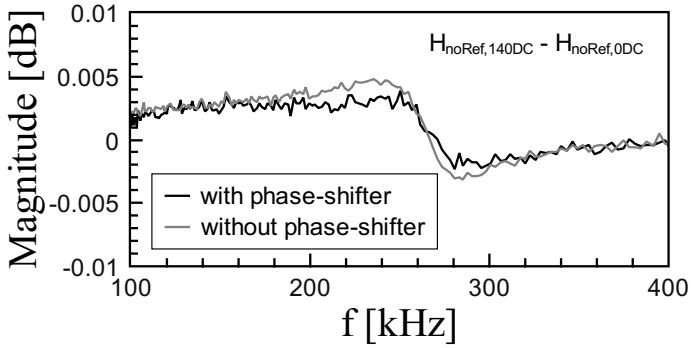

Figure 11.8: The differential transmission spectrums without reference capacitance with a bias voltage of $U_{DC} = 140$ V at atmospheric pressure at room temperature measured with a network analyzer. In one measurement the signal passes through the phase-shifter and in the other measurement not.

In Fig. 11.8, the influence of the phase-shifter in the signal path on the transfer function is shown.

11.4 Discussion

By comparing the measured transmission, shown in Fig. 11.6, with the electromechanical model it can be seen, that the compensation of the feedthrough capacitance corresponds approximately to $C_{ref} = 1.4\ C_{ft}$. This inequality of the reference capacitance most probably comes from geometry differences of the wire bonds. Due to the relative big reference capacitance missmatch, the transfer function signal is small with a magnitude in the range of 0.01 dB.

If the transfer function is measured without the compensation of the feedthrough capacitance, as shown in Fig. 11.7, the measured signal is smaller than with the reference capacitance. But the signal to noise ratio is enhanced compared to the measurement in Fig. 11.6. The higher noise seems to be caused by the half-bridge design which adds the signals from the resonator and reference path. Furthermore, the phase-shifter is slightly damping the actuation signal of the network analyzer as can be seen in Fig. 11.8. Therefore it can be assumed that the signal response of the measurement with the compensation of the feedthrough capacitance (Fig. 11.6) would be larger without a damping phase-shifter. Consequently, the capacitance match might be better than 40%.

In Fig. 11.3, the importance of the exact match of the reference capacitance C_{ref}

with the feedthrough capacitance C_{ft} is made clear. From Fig. 11.5 it can be seen, that the transmission spectrum is not totally flat but it varies for less than 0.6 dB over a bandwidth from 100 kHz to 1 MHz. Thus, in order to get a total maximum in the absolute transmission spectrum from the resonance peak, the peak magnitude has to exceed 0.6 dB. The model (11.8) predicts a resonance peak magnitude of around 0.7 dB for a feedthrough capacitance compensation better than 0.5%. But to obtain a 0.5% accuracy of the two capacitances (C_{ref} and C_{ft}) with wire-bonding might be impossible.

11.5 Conclusion

The electronic readout by means of a transimpedance amplifier of the presented all-polymer microresonators with a change in capacitance per unit displacement of 60 aF/μm is presented. High bias voltages of up to 140 V are needed to measure the very small capacitance change during vibration. The transmission spectrum of a resonator without the compensation of the feedthrough capacitance can be measured but the magnitude of the resonance peak is only 0.005 dB for a bias voltage of 140 V. The application of a half-bridge design for the compensation of the feedthrough capacitance was shown feasible. But in order to obtain the resonance peak magnitudes of more than 0.7 dB the reference capacitance has to match the feedthrough capacitance better than 0.5%. This is very difficult to achieve with conventional wire-bonding and might only be possible by a CMOS integration of the entire readout circuit. In order to minimize the feedthrough capacitance, the signal path was kept as short as possible and the transimpedance amplifier was therefore placed directly after the half-bridge output. These requirements make it rather difficult to readout an array of different polymer microresonators on a single chip. Furthermore, when compared with the optical readout, the precise determination of the resonant frequency and quality factor is more difficult with the electronic readout. The optical readout allows the fast and ultra precise readout of an array of polymer resonators all connected to the same input electrodes. The established laser-photodiode readout system known from atomic force microscopy might be an alternative optical readout system to the expensive laser-Doppler vibrometer.

12 Conclusion and outlook

The viscoelastic material properties of polymers are very different compared to quasi elastic stiff and brittle silicon based crystalline materials. In this work, the potential benefits and limitations of polymer based materials for microsystem actuators are explored. Therefore, as a first step, a novel actuation principle is developed for the actuation of polymer microstructures which are purely made from one polymer material. The electrostatic actuation method based on the Kelvin polarization force is significantly weaker than a conventional electrostatic force acting normal on parallel capacitor plates for a comparable setup. However, it is suitable to actuate soft polymer microbeams and presents an alternative solution to drive micro structures made from arbitrary polymer materials. Thus, the greater flexibility in terms of material selection virtually allows for the full exploration of the exceptional variety of polymer materials for microscaled actuators and sensors without the need of a lifetime limiting conducting layer by means of a metalization.

The sacrificial layer processes which are developed allow the fabrication of suspended microstructures made from SU-8. The fabrication processes are based on only 2 and 3 photolithography steps, respectively. The processes could also be used as basis for the fabrication of suspended structures made from other polymer materials, such as polymer nanocomposites or thermoplasts.

The polymer microbeams are characterized regarding the Young's modulus, prestress and damping by means of the resonant method. This simple and most accurate method allows the characterization of macroscopic samples at frequencies up to approximately 10 kHz which is given by the scaling behavior of the eigenfrequency of thin beams (4.12). With the polymer microresonators presented in this work, the frequency range of the mechanical characterization can be extended to frequencies of up to approximately 6 MHz. In Fig. 12.1, the common experimental methods for the mechanical characterization of hard viscoelastic materials in the macroscale are compared to the resonance method of polymer microbeams. It can be seen, that in macroscopic samples, the frequency range between 10 kHz to 6 MHz can only be reached by wave propagation because the wavelength of the stress waves is in the same order of magnitude as the length of the macroscopic sample. With the microsamples, the frequency range of the very accurate resonant method can be extended to much higher frequencies.

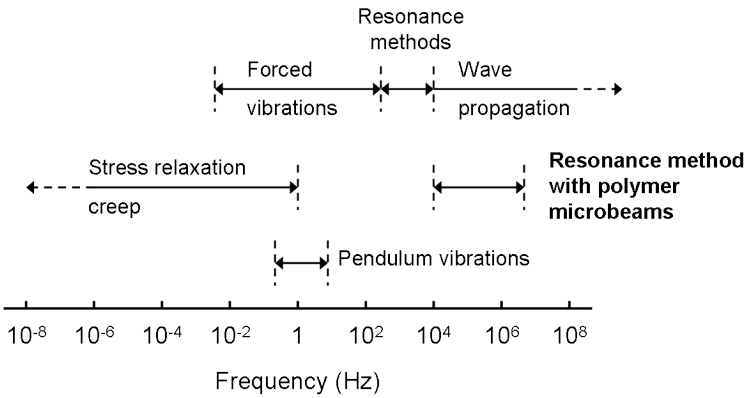

Figure 12.1: Frequency scales for different experimental techniques for the determination of viscoelastic behavior in polymer materials. Image adapted from [42].

In order to achieve a high frequency resolution, resonators need to have a high quality factor. A main limitation for the application of resonant polymer microstructures is thus the relatively large material damping which is responsible for the main intrinsic damping of the s-c polymer microbeams. But, this limitation can be avoided with the stringlike microstructures. Here, the material damping is not directly affecting the resonator damping, but the dominant damping was found to be the energy loss due to radiation of the elastic waves into the suspended anchor plates. Therewith, quality factors of almost 1000 are obtained with d-c microbeams with a length of 300 μm in high vacuum. By designing an optimized clamping without suspended anchor edges, quality factors values of several thousand can be theoretically obtained with polymeric resonators. At atmospheric pressure however, the air damping becomes dominant at low frequencies. At high frequencies, the material damping is limiting the quality factor of s-c microbeams. Only the stringlike polymer microbeams have the potential to yield high quality factors at high frequencies where air damping diminishes. Therefore, long strings with a high resonant frequency, that is with a high tensile stress, could be used. Here, the relatively low tensile strength of polymer materials and the high relaxation rate at high tensile stress are the limiting parameters.

In MEMS, on the one hand it is often desired to have a constant resonant frequency, e.g. for micromirrors or AFM cantilevers. But for sensors on the other hand, the resonant frequency should be as sensitive as possible to a certain parameter. The Young's modulus of SU-8, which is a highly crosslinked glassy polymer, has found to be highly sensitive to temperature. The resonant frequency can change up to al-

most 0.2 %/ °C. The influence of humidity on the Young's modulus is below 1 % over a relative humidity range from 3 to 60 %. Being a viscolastic material, the Young's modulus is frequency dependent, but operating at a fixed frequency this will not be a issue for a resonator. SU-8 was found to change its stiffness with time due to aging. A change of 2 to 4 % relative resonant frequency change was observed by actuation at room temperature and cycling the temperature below the glass transition temperature, respectively. Resonators based on a polymeric strings were found to be extremely sensitive to temperature (0.5%/ °C) and humidity (0.8%/%RH). This is because the substrate is relatively insensitive to temperature and humidity changes. This results in a change of the tensile stress which strongly influences the resonant frequency. Furthermore, the tensile stress is relaxing with time which implies a resonant frequency drop with time. As a consequence, on the one hand, for the design of a resonator where a stable frequency is desired it is of advantage to avoid structures where the resonant frequency is defined by a tensile stress. It would be favorable to make only polymeric resonator structures which are dependent on the stiffness which is less sensitive to temperature or humidity. On the other hand, stringlike polymer microbeams could be applied as highly sensitive temperature or humidity sensors. The small structure size results in small response times.

The application of resonant polymer microbeams as biosensors has many advantages. In a liquid, water in particular, a polymer microresonator is relatively stable. For the duration of the measurement, the temperature can assumed to be constant and the polymer is fully soaked with water and humidity will not change the resonant frequency. Furthermore, in water, polymer microresonators have no drawback concerning the low quality factor; the quality factor of a polymeric resonators is in the same range as the quality factor of silicon based beam resonators. A positive-feedback loop has shown to be an efficient way to self-excite polymer microbeams in water by means of the Kelvin polarization force. The biotinylated polymer microresonators are highly sensitive and selective against BSA in the detection of streptavidin molecules. A main advantage is also the simple functionalization of the polymer surface with proteins such as IgG which can directly bind to SU-8. The detection of biomolecules is a very promissing application of resonant polymer microbeams. In particular polymeric microbeams which vibrate near the point of critical damping could be interesting new sensors with a high sensitivity.

In the last chapter it was shown, that the resonance of such polymeric resonators can be detected by an electronic readout. The readout of the vibration is challenging and needs an integrated circuit in order to use the measured signal for the application of a feedback-signal. This integration would make this technology more expensive and a disposable biosensor unit would not be feasible. Instead of having a point of

care application, the sensor might have a future in a laboratory environment, where an optical readout station would be used. Instead of a very expensive laser-Doppler vibrometer, a inexpensive and established laser-photodiode readout which in well known in atomic force microscopes could be used.

12.1 Outlook

The characterization by means of the resonant method of polymer microbeams has only been performed for SU-8. Based on the presented electrostatic actuation of dielectric materials and the surface micromachining fabrication process, other polymer materials such as polyimide, PMMA or PC could be characterized. It would be interesting from a fundamental point of view but also from a technical point of view in order to find the most suitable polymer material for specific dynamic micromechanical applications.

Stringlike d-c polymer microbeams have shown to allow insight into the intrinsic damping mechanisms, the clamping loss in particular. Therefore, such structures could be used to study the influence of the anchor geometry on the clamping loss in microresonators. There are analytical models describing clamping loss. The experimental verification of these models turns out to be rather difficult because usually it is not possible to separate the influence of the clamping loss on the resonator damping from other damping sources.

Beside the high sensitivity, the main advantage of a resonant polymer microbeam biosensor is the possibility to directly adsorb the receptor biomolecules on the polymer without the need of an additional functional coating. All-polymer resonant microbeams have thus a high potential as low-cost system for disposable and label-free biosensing applications. The sensitivity of the SU-8 microresonators can be optimized, e.g by making the beam thinner. It can be also investigated if s-c or d-c microbeams are more sensitive. Beside streptavidin, it would be interesting to detect other biomolecules, e.g. detect base missmatches of single-stranded DNA sequences. Furthermore, it would be interesting to test different polymer materials and consequently adapt the functionalization process. In order to obtain an easy and inexpensive readout, the use of a laser-photodiode system known from atomic force microscopy would be favorable. Facing the problem of a diminishing electrostatic force in a highly concentrated buffer solution, the investigation of applying a different actuation principle could be of interest.

Being aware of polymer materials to be highly sensitive to environmental influences, it would be nice to see polymers as mechanical parts in future MEMS applications thereby making use of their unique material properties.

Part III

Appendix

A Validation of electrostatic actuation

Electrical forces on macroscopic media in an electroquasistatic system with one degree of freedom ξ depend on the derivative of capacitance C with respect to ξ times the applied voltage U squared $F(\xi) = (1/2)\, U^2\, dC/d\xi$ [54]. Upon fitting the amplitude as a function of the driving voltage in Fig. A.1, a squared dependency of F_{KPFn} on the applied voltage, i.e. $|\nabla(\mathbf{E} \cdot \mathbf{E})| \propto U^2$, was demonstrated.

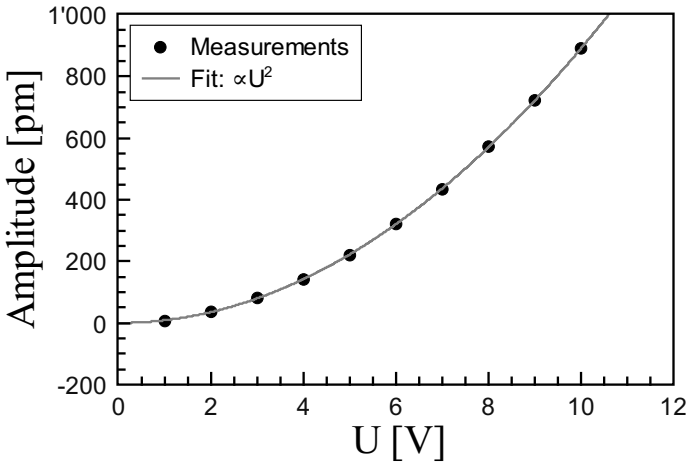

Figure A.1: Vibration amplitude as a function of driving voltage for thin single-clamped microbeam (55 μm long) actuated by the Kelvin polarization force at high vacuum ($p < 0.05$ Pa) measured with a laser-Doppler vibrometer.

B Run sheets

Table B.1: Ti/Au or Cr/Au electrode structuring by lift-off on borosilicate glass wafer.

Process step	**Parameters**
O_2 plasma	10 min at 600 W
HMDS	60 sec N_2 40 sec HMDS 60 sec N_2
Spin Futurrex NR7-1000P	3 ml Ramp (100 rpm/sec) to 500 rpm for 3 sec Ramp (1000 rpm/sec) to 3000 rpm for 40 sec
Prebake	Ramp to 150 °C with 80% 3 min at 150 °C Cool down on Al plate
Exposure	Softcontact 600 mJ/cm^2
Post exposure bake	Ramp to 100 °C with 80% 3 min at 100 °C Cool down on Al plate
Development	RD6:H_2O (5:1) for 220 sec
Rinse	DI water
Dry	Nitrogen gun
Ti or Cr evaporation	E-beam Deposition: 25 nm E-beam current: 115 mA
Au evaporation	E-beam Deposition: 100 nm E-beam current: 90 mA
Rinse	13 min in Acetone
US bath	20 min in Acetone 10 min in IPA
QDR	Rinse $>$ 12 MOhm

Rinser/Dryer	Program 2
Alumina layer (optional)	Atomic layer deposition Thickness: 120 nm at 185 °C

Table B.2: Fabrication runsheet for thin SU-8 microbeams.

Process step	**Parameters**
O_2 plasma	10 min at 150 W
Spin LOR 30B	4 ml Ramp (100 rpm/sec) to 500 rpm for 1 sec Ramp (300 rpm/sec) to 3000 rpm for 40 sec
Prebake	Ramp from 100 °C to 170 °C with 90% 12 min at 170 °C Slowly cool down on glass plate
Spin SU-8 2002	4 ml Ramp (100 rpm/sec) to 500 rpm for 1 sec Ramp (300 rpm/sec) to 3000 rpm for 30 sec
Softbake	Ramp to 105 °C with 80% 5 min at 105 °C Cool down on glass plate
Exposure	Softcontact 100 mJ/cm^2
Post exposure bake	Ramp to 105 °C with 70% 10 min at 105 °C Cool down on glass plate
Development	Mr-Dev 600 for 4 min 30 sec
Rinse	IPA, then DI water
Dry	Nitrogen gun
Dicing	Hubless Blade to chuck distance: 250 μm Index 1, 2: 5550 and 6550 Speed: 25000 rpm Feed rate: 5 μm/s Wafer size: 4 inch Wafer thickness: 500 μm

Rinse	DI water
Hardbake	Ramp to 170 °C with 80% 10 min at 170 °C Cool down on glass plate
Release	First bath: 351:H_2O (1:3) for 2 min 20 sec Second bath: 351:H_2O (1:3) for 30 sec Transfer to water baths Transfer to IPA bath
Supercritical point drying	

Table B.3: Fabrication runsheet for thick SU-8 microbeams.

Process step	**Parameters**
O_2 plasma	10 min at 600 W
HMDS	60 sec N_2 40 sec HMDS 60 sec N_2
LOR spin coat	4 ml LOR 30B Ramp (100 rpm/sec) to 500 rpm for 1 sec Ramp (300 rpm/sec) to 3000 rpm for 45 sec
Prebake	Ramp to 170 °C at 90% 15 min at 170 °C on hotplate then slowly cool down
ma-N 405	3 ml Ramp (100 rpm/sec) to 500 rpm for 1 sec Ramp (300 rpm/sec) to 3000 rpm for 30 sec
Softbake	1 min at 100 °C Cool down
Exposure	Softcontact 600 mJ /cm^2
Develop	20 % Shipley 351 for 15 min
Strip ma-N 405	Rinse in acetone
Rinse	In IPA, 2 min ultrasound
Rinse	In DI-water

Dry	Blow dry in nitrogen
SU-8 2005	4 ml Ramp (100 rpm/sec) to 500 rpm for 1 sec Ramp (300 rpm/sec) to 3000 rpm for 30 sec
Softbake	Ramp to 95 °C with 30% then hold for 15 min
Exposure	Softcontact 150 mJ/cm^2
PEB	Ramp to 95 °C with 30% then hold for 4 min Cool down slowly
Develop	In PGMEA
Rinse	in IPA, then in Di-Water
Dry	Blow dry with nitrogen
Dicing	Hubless Blade to chuck distance: 250 μm Index 1, 2: 5550 and 6550 Speed: 25000 rpm Feed rate: 5 μm/s Wafer size: 4 inch Wafer thickness: 500 μm
Release	15 min in 100% 351
Rinse	15 min in DI water
Rinse	in IPA
Supercritical point drying	

C HiQLab source code

HiQLab is an open source finite element simulation tool written in C++. The FEM mesh is defined with LUA and Matlab is used as the interface which gives access to powerful visualization and pre- and postprocessing capabilities.

Lua file defining the mesh:

```
 -- Include function definition file
require 'common.lua'

-- Define physical dimension of mesh
mesh = Mesh:new(2)

-- Define mesh related global parameters
order   = 3  -- Order of element
dense   = 3.5e-6      -- Approximate element size 2e-6
meshtol = dense/100   -- Default mesh tolerance

-- Define geometry of domain
l  =  30e-6  -- Beam length
w  =   20e-6  -- Beam width
t  =    3.5e-6  -- Beam thickness
at =    3e-6  -- Anchor height
al =   40e-6  -- Anchor length
aw =   20e-6  -- Anchor width
sw =  600e-6  -- Substrate Width
sh =  300e-6  -- Substrate Height
spml =240e-6  -- PML Depth
spmlx= sw/2-spml
spmly= sh  -spml

-- Define PML paramter
f0 = f0 or 40
f0 = 28
```

```
-- Define element type
su8 = fill_mech({
  -- SU-8
  rho = 1200,
  E   = 4e9,
  nu  = 0.26
})

celt = make_material_e('su8', 'planestress')
selt = make_material_e('siox', 'planestress')

densex = dense*2
densey = dense*2
-- Define mesh using block command
mesh:blocks2d( {       -al/2, al/2, l+al/2},
{         at, at + t}, celt, order ,dense, dense)
mesh:blocks2d( {       -al/2, al/2        },
{      0, at        }, celt, order ,dense, dense)
mesh:blocks2d( {-spmlx, -al/2, al/2,  spmlx},
{ -spmly, 0        }, selt, order ,dense, dense)

mesh:blocks2d( {-sw/2, -spmlx},
{ -spmly, 0        }, selt, order ,densex, dense)
mesh:blocks2d( {-sw/2, -spmlx},
{ -sh, -spmly      }, selt, order ,densex, densey)
mesh:blocks2d( { spmlx,  sw/2},
{ -spmly, 0        }, selt, order ,densex, dense)
mesh:blocks2d( { spmlx,  sw/2},
{ -sh, -spmly      }, selt, order ,densex, densey)
mesh:blocks2d( {-spmlx, -al/2, al/2,   spmlx},
{ -sh, -spmly     }, selt, order ,dense, densey)

-- Tie mesh together
mesh:tie()

function stretch_function(x,y)
    local xs = 0   -- x stretch value
```

```
    local ys = 0   -- y stretch value
    if abs(x) > sw/2-spml and meshleq(y,0)
then xs =  f0*(abs(x)-(sw/2-spml))/(spml) end
    if y < -(sh-spml)
then ys = -f0*(y+sh-spml)/(spml) end
    return xs, ys
end
selt:set_stretch(stretch_function)



-- Define boundary condition
function bc_function(x,y)
    if mesheq(y,-sh)                    then return 'uu', 0, 0; end
    if mesheq(x,-sw/2)                    then return 'uu', 0, 0; end
    if mesheq(x,sw/2) and meshleq(y,0)     then return 'uu', 0, 0; end
    --if mesheq(x, l) and mesheq(y, at+t)   then return ' f', 1; end
end
mesh:set_bc(bc_function)
```

Matlab file starting the FEM simulation:

```
 clear;
close all;
% -- Parameters
%for i = [5,6,7,8,9,10,11,12,13,14,15]
    params.f0    = 40;

% -- Load mesh from Lua input file
[mesh, L] = Mesh_load('su8_cant_tk.lua',params);
numid = Mesh_get_numid(mesh);
fprintf('Node num:%d\n',numid);

% -- Display the mesh
figure(1);
popt.axequal = 1;
plotmesh(mesh,popt);
```

```
% -- Plot the stretch function
figure(2);
psopt.cfields = 'stretch_function';
psopt.ncfields= 2;
psopt.axequal = 1;
psopt.cbias   = 1;
plotfield2d(mesh,psopt);

popt.deform  = 2e-5; %/Mesh_get_scale(mesh,'L');
popt.axequal = 1;
popt.animate = 1;


% -- Compute frequencies, Qs, and eigenvectors
if 1==1
w0      = 9e5*2*pi;
nev     = 1;
%mopt.use_matlab = 1;
[V,w,Q] = mechmode(mesh,w0,nev);

% -- Show modes
figure(3);
popt.cbias = 10000;
popt.nframes = 64;
popt.fpcycle = 32;
plot_mode(mesh,V,w,popt);
% -- Clean up
%Mesh_delete(mesh);
end
%end
```

D Iterative FEM analysis

The Young's modulus of the thin s-c microbeams is calculated with a iterative finite element method. The eigenfrequency of the polymer structure yielding a suspended anchor plate is simulated with Comsol for a given Young's modulus. The obtained eigenfrequency is then compared to the measured resonant frequency and the Young's modulus is iteratively adjusted until the difference of the computed and measured frequency value are below a defined threshold of 0.1% of the measured resonant frequency.

The algorithm which is given below is schematically explained in Fig. D.1. The eigenfrequencies f_{upper} and f_{lower} are calculated from FEM for given lower and upper maximum Young's modulus values Y_{upper} and Y_{lower}. An approximate value of the real Young's modulus Y_{approx} is obtained by introducing the measured eigenfrequency f_0 into the linearized eigenfrequency function. The corresponding eigenfrequency f_{approx} is then calculated with FEM. Depending on weather the obtained eigenfrequency value is bigger or smaller than the measured eigenfrequency, the corresponding Young's modulus becomes the new upper or lower limit. This goes on while the difference of the obtained approximated eigenfrequency to the measured resonant frequency is below the defined threshold.

Matlab file controlling the iteration:

```
function YoungsModulus =
calculateModulus(pLength, pMeasuredResonantFrequency)
% Material data
poissonRatio = 0.26;
massDensity = 1200;

% Geometry data
thickness = 1.45e-6;
width = 14e-6;
undercut = 16.9e-6;

% Accuracy of approximation
frequencyAccuracy = pMeasuredResonantFrequency/1000;
```

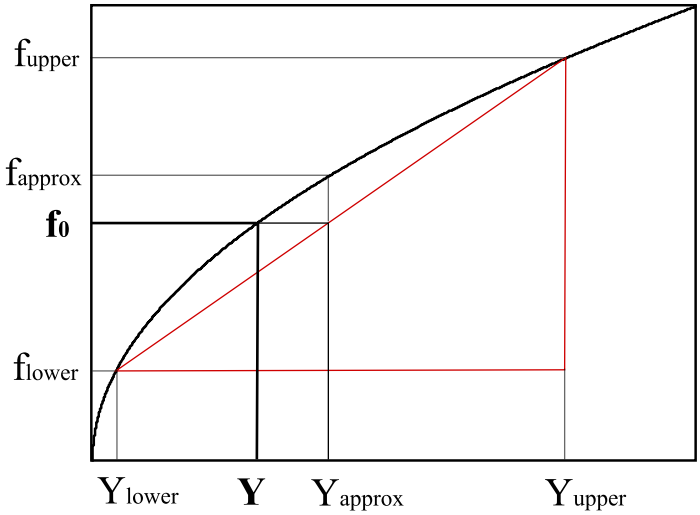

Figure D.1: Iterative FEM

```
% Start Values
f = 0;
YoungsModulusLower = 3e9;
YoungsModulusUpper = 6e9;

% call Comsol to simulate start eigenfrequency
fLower = cantilever(undercut, pLength, thickness, width,
poissonRatio, massDensity, YoungsModulusLower);

ENew = YoungsModulusUpper;

% while definded accuracy is not reached...
while abs(f - pMeasuredResonantFrequency) > frequencyAccuracy

    % call Comsol to simulate new eigenfrequency
    fNew = cantilever(undercut, pLength, thickness, width,
poissonRatio, massDensity, ENew);

    % define new upper and lower modulus
    if fNew > pMeasuredResonantFrequency
```

```
        fUpper = fNew;
        YoungsModulusUpper = ENew;
    else
        fLower = fNew;
        YoungsModulusLower = ENew;
    end
    f = fNew;

    % calculate new Youngs Modulus
    k = (fUpper-pMeasuredResonantFrequency)
/(pMeasuredResonantFrequency-fLower);
    ENew = (YoungsModulusUpper + k*YoungsModulusLower)/(k+1);
    disp(ENew)
end
%save data_b6_nu0.txt datana '-ascii' '-tabs' ;

YoungsModulus = ENew;
```

Comsol file defining the FEM model:

```
 function eigenfreq =
cantilever(pUndercut,pLength,pThickness,pWidth,pNu,pRho,pE)
% COMSOL Multiphysics Model M-file
% Generated by COMSOL 3.2b

flclear fem

% COMSOL version
clear vrsn
vrsn.name = 'COMSOL 3.2';
vrsn.ext = 'b';
vrsn.major = 0;
vrsn.build = 304;
vrsn.rcs = '$Name:  $';
vrsn.date = '$Date: 2006/04/04 14:56:13 $';
fem.version = vrsn;

% Geometry
g1=block3(pLength,pWidth,pThickness,'base','center','pos',
```

```
{'0','0','0'},'axis',{'0','0','1'},'rot','0');
g2=block3(pUndercut,'200e-6',pThickness,'base','center','pos',
{pLength/2 + pUndercut/2,'0','0'},'axis',{'0','0','1'},'rot','0');
clear s
s.objs={g1,g2};
s.name={'Beam','Anchor'};
s.tags={'g1','g2'};

fem.draw=struct('s',s);
fem.geom=geomcsg(fem);

% Initialize mesh
fem.mesh=meshinit(fem);

% Refine mesh
%  fem.mesh=meshrefine(fem, ...
%                      'mcase',0, ...
%                      'rmethod','longest');

% (Default values are not included)

% Application mode 1
clear appl
appl.mode.class = 'FlSolid3';
appl.gporder = 4;
appl.cporder = 2;
appl.assignsuffix = '_sld';
clear prop
prop.analysis='eigen';
appl.prop = prop;
clear bnd
bnd.Hy = {0,1};
bnd.Hx = {0,1};
bnd.Hz = {0,1};
bnd.ind = [1,1,1,1,1,1,1,1,1,1,1,1,2];
appl.bnd = bnd;
clear equ
equ.alphadM = 0;
```

```
equ.betadK = 0;
equ.rho = 'mat1_rho';
equ.nu = 'mat1_nu';
equ.E = 'mat1_E';
equ.ind = [1,1];
appl.equ = equ;
fem.appl{1} = appl;
fem.frame = {'ref'};
fem.border = 1;
fem.units = 'SI';

% Solution form
fem.solform = 'general';

% Library materials
clear lib
lib.mat{1}.name='SU-8';
lib.mat{1}.varname='mat1';
lib.mat{1}.variables.rho=pRho;
lib.mat{1}.variables.nu=pNu;
lib.mat{1}.variables.E=pE;


fem.lib = lib;

% Multiphysics
fem=multiphysics(fem);

% Extend mesh
fem.xmesh=meshextend(fem);

% Solve problem
%                     fem.sol=femeig(fem, ...
%                         'symmetric','on', ...
%                         'solcomp',{'w','u','v'}, ...
%                         'outcomp',{'w','u','v'}, ...
%                         'neigs',2, ...
%                         'linsolver','spooles');
```

```
% Solve problem
fem=adaption(fem, ...
             'symmetric','on', ...
             'solcomp',{'w','u','v'}, ...
             'outcomp',{'w','u','v'}, ...
             'neigs',1, ...
             'solver','eigenvalue', ...
             'eigselect',[1], ...
             'l2scale',[1], ...
             'l2staborder',[2], ...
             'maxt',10000000, ...
             'ngen',1, ...
             'resorder',[0], ...
             'rmethod','longest', ...
             'tppar',1.1, ...
             'linsolver','spooles', ...
             'geomnum',1);

% Save current fem structure for restart purposes
fem0=fem;

% Transform eigenvalue in eigenfrequency [Hz]

eigenfreq=sqrt(fem.sol.lambda(1))/(2*pi);
```

E Eigenfrequency of beams with suspended anchors

E.1 Introduction

Fig. E.1 shows the geometry of a microbeam with underetching at the clamped end. A common technique to evaluate the Young's modulus Y of thin films in microelectromechanical systems (MEMS) is to measure the resonant frequency of microbeams. The Bernoulli-Euler beam theory assumes perfectly clamped end which is not given in real structures. Thus, an extended model is needed which includes the typical nonideal suspended anchors.

E.2 Bernoulli-Euler beam: Ideally clamped resonators

Assuming linear elastic bending waves in thin beams with infinitesimal small deformations, the bending oscillation of beams can be approximated by the Bernoulli-Euler equation [205]:

$$\rho A \frac{\partial^2 v}{\partial t^2} + Y I_z \frac{\partial^4 v}{\partial x^4} = q \tag{E.1}$$

where ρ, A, Y, I_z are the mass density, the beam cross-sectional area, the Young's modulus, and the geometrical moment of inertia, respectively. v is the displacement perpendicular to the axis x and q is the load per unit length perpendicular to the axis.

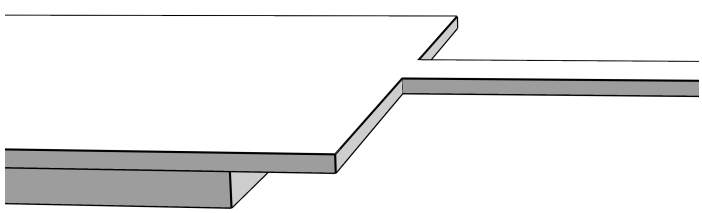

Figure E.1: Geometry of a microbeam with underetching at the clamped end.

To calculate the eigenfrequencies of the beam, the load term q is set to zero and equation E.1 is solved for non-trivial functions by separation of variables with the ansatz:

$$v(x,t) = \phi(x)e^{i\omega t} \tag{E.2}$$

Using the dispersion relationship:

$$\beta^4 = \frac{\rho A}{Y I_z}\omega^2 \tag{E.3}$$

equation E.1 can be written as follows:

$$\varphi_{,xxxx} - \beta^4\varphi = 0 \tag{E.4}$$

The solution of the common differential equation E.4 is:

$$\varphi(x) = A\cos(\beta x) + B\sin(\beta x) + C\cosh(\beta x) + D\sinh(\beta x) \tag{E.5}$$

where A to D are the integration constants depending on the boundary conditions, and β and ω are the wave number and frequency, respectively.

The eigenfrequencies are determined by introducing the boundary conditions. This results in a homogeneous linear system of equations for the integration constants A to D. A non-trivial solution can only be found if the determinant of the coefficient matrix is zero. This results in specific frequency equation for different boundary conditions which can be solved numerically, resulting in a specific wave number β and consequently in the eigenfrequency ω_0.

E.3 Extended resonator model

To approximate the complete eigenmodes of the resonator model as illustrated in Fig. E.2, the assumed-modes method is used [206]. It is assumed that beam theory (Sec. E.2) is applicable and that the beam oscillation fulfills Eq. E.1. We choose a parameterized approximation for the eigenmode that fulfills the kinematic boundary conditions, in this case:

$$w(x,t) = \vec{v}(x)^T \cdot \vec{q}(t) \tag{E.6}$$

where $w(x,t)$ is the vertical displacement, $\vec{v}(x)$ is the shape function vector and $\vec{q}(t)$ is the vector containing the time dependent coefficients that are to be determined. Following the principle of stationary action (or Hamilton's principle), the coefficients should be determined such as to minimize the action functional:

$$I(w(x,t)) = \int (Y_k(w) - Y_p(w))\mathrm{d}t \tag{E.7}$$

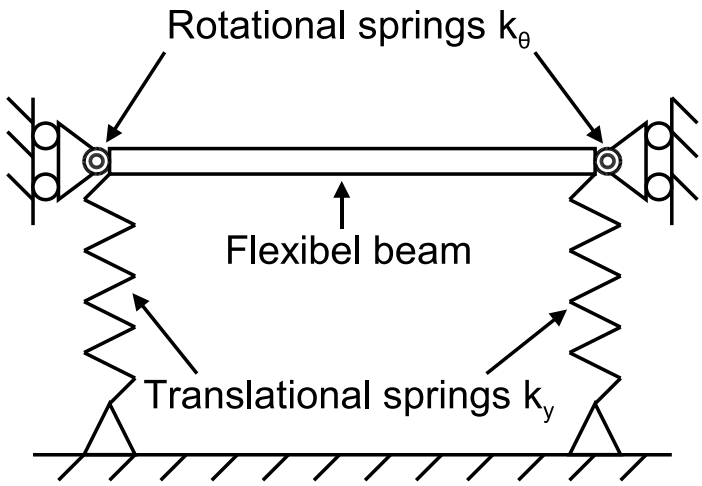

Figure E.2: Resonator model including flexible beam and rotational and translational stiffness of the anchor

The necessary condition for minimizing the action functional is that the Lagrange equation for such systems, namely,

$$\frac{\mathrm{d}}{\mathrm{d}t}\left(\frac{\partial Y_k}{\partial \dot{\vec{q}}}\right)^T - \left(\frac{\partial Y_k}{\partial \vec{q}}\right)^T + \left(\frac{\partial Y_p}{\partial \vec{q}}\right)^T = 0 \tag{E.8}$$

is satisfied.

The eigenmode will be build up of the four terms of Eq. E.5, but the coefficients will be different, i.e. the coefficients A to D will be replaced by the time-dependent coefficient vector, as indicated in Eq. E.6:

$$\vec{v}(x) = \begin{pmatrix} \cos(\beta x) & \sin(\beta x) & \cosh(\beta x) & \sinh(\beta x) \end{pmatrix}^T \tag{E.9}$$

$$\vec{q}(t) = \begin{pmatrix} q_1(t) & q_2(t) & q_3(t) & q_4(t) \end{pmatrix}^T \tag{E.10}$$

Particularly, the weighting of the coefficients relative to each other will be different from the ideally clamped beam resonator, since the anchored ends also have a velocity.

First, the kinetic energy is calculated:

$$\begin{aligned} Y_k &= \frac{1}{2}\int_0^L \rho A \dot{w}^2 \mathrm{d}x \\ &= \frac{1}{2}\rho A \int_0^L \left(\vec{v}(x)^T \cdot \dot{\vec{q}}(t)\right)^2 \mathrm{d}x \end{aligned} \tag{E.11}$$

where ρA is the mass load per length and L is the length of the beam.

The potential energy for a clamped-clamped resonator is given by:

$$\begin{aligned} Y_p &= \frac{1}{2}\int_0^L YI_z w_{,xx}^2 \mathrm{d}x + \frac{1}{2}k_\theta w_{,x}^2(0) + \frac{1}{2}k_\theta w_{,x}^2(L) + \frac{1}{2}k_y w^2(0) + \frac{1}{2}k_y w^2(L) \\ &= \frac{1}{2}\int_0^L YI_z \left(\vec{v}_{,xx}(x)^T \cdot \vec{q}(t)\right)^2 \mathrm{d}x + \\ &\quad + \frac{1}{2}k_\theta \left(\vec{v}_{,x}(0)^T \cdot \vec{q}(t)\right)^2 + \frac{1}{2}k_\theta \left(\vec{v}_{,x}(L)^T \cdot \vec{q}(t)\right)^2 + \\ &\quad + \frac{1}{2}k_y \left(\vec{v}(0)^T \cdot \vec{q}(t)\right)^2 + \frac{1}{2}k_y \left(\vec{v}(L)^T \cdot \vec{q}(t)\right)^2 \end{aligned} \tag{E.12}$$

The first term in the potential energy represents the energy stored in the deformed beam, the second and third the energy stored in the rotational springs at both ends, and the last two terms represent the energy stored in the translational springs at both ends. In the case of a clamped-free resonator, only one term for the rotational and one for the translational spring at on end are included in Eq. E.12.

Next, the Lagrange equation (Eq. E.8) is evaluated term by term.

$$\begin{aligned} \frac{\mathrm{d}}{\mathrm{d}t}\left(\frac{\partial Y_k}{\partial \dot{\vec{q}}}\right) &= \frac{\mathrm{d}}{\mathrm{d}t}\left(\frac{\partial}{\partial \dot{\vec{q}}}\left(\frac{1}{2}\rho A \int_0^L \left(\vec{v}(x)^T \cdot \dot{\vec{q}}(t)\right)^2 \mathrm{d}x\right)\right) \\ &= \frac{\mathrm{d}}{\mathrm{d}t}\left(\rho A \int_0^L \left(\vec{v}(x) \cdot \vec{v}(x)^T\right) \mathrm{d}x \cdot \dot{\vec{q}}\right) \\ &= \rho A \int_0^L \left(\vec{v}(x) \cdot \vec{v}(x)^T\right) \mathrm{d}x \cdot \ddot{\vec{q}} \end{aligned} \tag{E.13}$$

$$\frac{\partial Y_k}{\partial \vec{q}} = 0 \tag{E.14}$$

$$\begin{aligned} \frac{\partial Y_p}{\partial \vec{q}} = \Big(YI_z \int_0^L \left(\vec{v}_{,xx} \cdot \vec{v}_{,xx}^T\right) \mathrm{d}x + \\ + k_\theta \left(\vec{v}_{,x}(0) \cdot \vec{v}_{,x}(0)^T + \vec{v}_{,x}(L) \cdot \vec{v}_{,x}(L)^T\right) + \\ + k_y \left(\vec{v}(0) \cdot \vec{v}(0)^T + \vec{v}(0) \cdot \vec{v}(0)^T\right) \Big) \cdot \vec{q} \end{aligned} \tag{E.15}$$

Based on these results, a mass matrix M

$$M = \rho A \int_0^L \left(\vec{v}(x) \cdot \vec{v}(x)^T\right) \mathrm{d}x \tag{E.16}$$

and a stiffness matrix K

$$\begin{aligned} K = YI_z \int_0^L \left(\vec{v}_{,xx} \cdot \vec{v}_{,xx}^T\right) \mathrm{d}x + k_\theta \left(\vec{v}_{,x}(0) \cdot \vec{v}_{,x}(0)^T + \vec{v}_{,x}(L) \cdot \vec{v}_{,x}(L)^T\right) + \\ + k_y \left(\vec{v}(0) \cdot \vec{v}(0)^T + \vec{v}(0) \cdot \vec{v}(0)^T\right) \end{aligned} \tag{E.17}$$

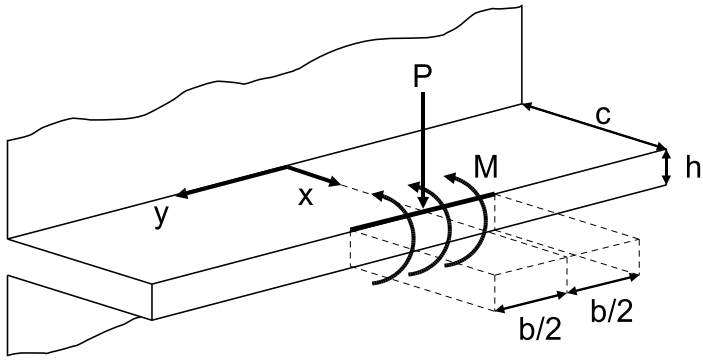

Figure E.3: Infinitely long cantilever plate with loading

can be defined. This simplifies the Lagrange equation to a simple matrix equation:

$$M \cdot \ddot{\vec{q}} + K \cdot \vec{q} = 0 \tag{E.18}$$

Since only eigenfrequencies are to be determined, all components of $\vec{q}$ can be assumed harmonic functions with the same frequency and the second derivative of $\vec{q}$ can be rewritten as:

$$\ddot{\vec{q}} = -\omega^2 \cdot \vec{q} \tag{E.19}$$

Then, the equation of motion can further be simplyfied to:

$$(K - \omega^2 \cdot M) \cdot \vec{q} = 0 \tag{E.20}$$

Eq. E.20 is a special form of an eigenvalue problem: finding a non-trivial $\vec{q}$ is only possible if $(K - \omega^2 M)$ is singular, thus the eigenfrequencies can be found by solving the following equation for ω:

$$\det(K - \omega^2 \cdot M) = 0 \tag{E.21}$$

E.4 Determination of the anchor spring constants

The bending of a long cantilever plate as shown in Fig. E.3 can be determined by applying the *Kirchhoff's* theory of flat plates. It will be assumed that: (1) The long sides of the plate extend to infinity; (2) the plate is rigidly clamped along $x = 0$; (3) the deflection of the plate is small compared to its thickness; and (4) that the thickness h is small compared with the width c. The latter assumption means that the effect of shear on the deflection are not regarded. Under these assumptions, the problem can

be solved with the homogeneous biharmonic equation for the deflection $w = f(x, y)$ of a plate with constant rigidity [207].

$$\nabla^4 w = 0 \tag{E.22}$$

where ∇^4 is the biharmonic operator:

$$\nabla^4 = \frac{\partial^4}{\partial x^4} + 2\frac{\partial^4}{\partial x^2 \partial y^2} + \frac{\partial^4}{\partial y^4} \tag{E.23}$$

The flexural rigidity D of a plate is defined by

$$D = \frac{Yh^3}{12(1-\nu^2)} \tag{E.24}$$

The deflection w can be represented by a Fourier integral of the form [208]:

$$w = \int_0^\infty X(x, \alpha) \cos(\alpha y) \mathrm{d}\alpha \tag{E.25}$$

where $X(x, \alpha)$ is consists of four terms containing hyperbolic functions with four constants A to D to be determined from the specific boundary conditions.

$$X = (A + Bx)\cosh(\alpha x) + (C + Dx)\sinh(\alpha x) \tag{E.26}$$

E.4.1 Vertical Force Loading at Free Edge

The intensity of the vertical force loading as illustrated in Fig. E.3 is given by $p(y) = P/b$ for $-b/2 < y < b/2$ and by zero elsewhere, we have the Fourier integral representation for $p(y)$

$$p(y) = -\frac{2P}{\pi b} \int_0^\infty \frac{1}{\alpha} \sin\left(\frac{\alpha b}{2}\right) \cos(\alpha y) \mathrm{d}\alpha \tag{E.27}$$

With the boundary conditions

$$w(0, y) = 0 \tag{E.28}$$

$$w_{,x}(0, y) = 0 \tag{E.29}$$

$$D\left[w_{,xxx}(c, y) + (2-\nu) w_{,xyy}(c, y)\right] = p(y) \tag{E.30}$$

$$w_{,xx}(c, y) + \nu w_{,yy}(c, y) = 0 \tag{E.31}$$

the constants A to D are determined and Eq. E.26 gives

$$X(c, \alpha) = \frac{4P}{D\pi b} \cdot \cdot \frac{\sin\left(\frac{b\alpha}{2}\right)(\sinh(2c\alpha) - 2c\alpha)}{\alpha^4\left(5 + 2\nu + \nu^2 + 2c^2(\nu-1)^2\alpha^2 - (\nu-1)(3+\nu)\cosh(2c\alpha)\right)} \tag{E.32}$$

The maximal spring constant k_y of the plate clamping support is calculated by

$$k_y = \frac{P}{w(c,0)} = c_y Y h^3 \tag{E.33}$$

with

$$c_y^{-1}(b,c,\nu) = \frac{48(1-\nu^2)}{\pi b} \cdot \\ \cdot \int_0^\infty \frac{\sin\left(\frac{b\alpha}{2}\right)(\sinh(2c\alpha) - 2c\alpha)}{\alpha^4\left(5+2\nu+\nu^2+2c^2(\nu-1)^2\alpha^2-(\nu-1)(3+\nu)\cosh(2c\alpha)\right)} \mathrm{d}\alpha \tag{E.34}$$

The spring constant coefficient c_y is obtained by numerical integration.

E.4.2 Boundary Conditions for Moment Loading at Free Edge

The intensity of the vertical moment loading as illustrated in Fig. E.3 is given by $m(y) = M/b$ for $-b/2 < y < b/2$ and by zero elsewhere, we have the Fourier integral representation for $m(y)$

$$m(y) = -\frac{2P}{\pi b}\int_0^\infty \frac{1}{\alpha}\sin(\frac{\alpha b}{2})\cos(\alpha y)\mathrm{d}\alpha \tag{E.35}$$

With the boundary conditions

$$w(0,y) = 0 \tag{E.36}$$

$$w_{,x}(0,y) = 0 \tag{E.37}$$

$$w_{,xxx}(c,y) + (2-\nu)w_{,xyy}(c,y) = 0 \tag{E.38}$$

$$D\left[w_{,xx}(c,y) + \nu w_{,yy}(c,y)\right] = m(y) \tag{E.39}$$

the constants A to D are determined and Eq. E.26 gives

$$X_{,x}(b,\alpha) = -\frac{4M}{D\pi b\alpha^2} \cdot \\ \cdot \frac{\sin\left(\frac{b\alpha}{2}\right)(\sinh(2c\alpha) + 2c\alpha)}{5+2\nu+\nu^2+2c^2(\nu-1)^2\alpha^2-(\nu-1)(3+\nu)\cosh(2c\alpha)} \tag{E.40}$$

The maximal spring constant k_θ of the plate clamping support is calculated by

$$k_\theta = \frac{M}{w_{,x}(c,0)} = c_\theta Y h^3 \tag{E.41}$$

with

$$c_\theta^{-1}(b,c,\nu) = \frac{48(1-\nu^2)}{\pi b} \cdot \\ \cdot \int_0^\infty \frac{\sin\left(\frac{b\alpha}{2}\right)(\sinh(2c\alpha) + 2c\alpha)}{\alpha^2\left(5+2\nu+\nu^2+2c^2(\nu-1)^2\alpha^2-(\nu-1)(3+\nu)\cosh(2c\alpha)\right)} \mathrm{d}\alpha \tag{E.42}$$

The spring constant coefficient c_θ is obtained by numerical integration.

E.5 Calculation of the eigenfrequency

For a beam with a square cross-section

$$A = b\,h \tag{E.43}$$

where b and h are the width and the height, respectively, the geometrical moment of inertia is:

$$I_z = \frac{b\,h^3}{12} \tag{E.44}$$

Substituting equations E.33 and E.41 into Equation E.17 and the substituting equations E.16 and E.17 into equation E.21 results in the frequency equations for a one side clamped beam

$$\begin{aligned}\frac{b^2\beta^4 + 144c_y c_\theta}{\cosh(\beta L)} &= \cos(\beta L)(b^2\beta^4 - 144c_y c_\theta) + \\ &+ 12b\beta\sin(\beta L)(c_\theta\beta^2 + c_y) + 12b\beta\cos(\beta L)\sinh(\beta L)(c_\theta\beta^2 - c_y)\end{aligned} \tag{E.45}$$

and a double side clamped beam, respectively.

$$\begin{aligned}\frac{b^2\beta^4 + 144c_y c_\theta}{\cosh(\beta L)} &= \cos(\beta L)(20736c_y^2c_\theta^2 - 864b^2c_y c_\theta\beta^4 + b^4\beta^8) + \\ &+ 24b\beta(c_\theta\beta^2 + c_y)\sin(\beta L)(b^2\beta^4 - 144c_y c_\theta) + \\ &+ 24b\beta(c_\theta\beta^2 - c_y)\cos(\beta L)(b^2\beta^4 - 144c_y c_\theta) + \\ &+ 12b\beta(c_\theta\beta^2 + c_y)\sin(\beta L)\sinh(\beta L)\end{aligned} \tag{E.46}$$

These frequency equations (E.45 & E.46) are transcendental and can only be solved numerically. The resulting wave number $\beta = f(L, b, c, \nu)$ is only a function of the geometry and the Poisson's ratio ν. The eigenfrequency is obtain with the dispersion relationship given in Eq. E.3

$$\omega = \sqrt{\frac{YI_z}{\rho A}}\beta^2 \tag{E.47}$$

E.6 Validation with FEM

The extended model is compared to the eigenfrequencies obtained with finite element method simulation. The comparison is shown in Fig. E.4.

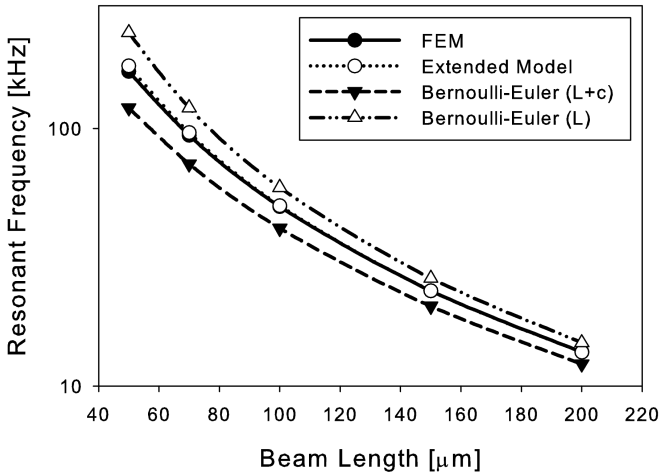

Figure E.4: Eigenfrequencies of single clamped beams calculated with extended resonator model compared with FEM results and Bernoulli-Euler model ($h = 2\mu m$, $b = 14\mu m$, undercut $c = 20\mu m$, $\nu = 0.2$, $Y = 4GPa$).

F Hydrophilic/Hydrophobic: Contact Angle Measurements on SU-8

The contact angle can be determined by producing a drop of pure liquid on a solid. The angle formed between the solid-liquid interface and the liquid-vapor interface is defined as the contact angle.

To describe the relation between surface energy and contact angle the Young's equation is used as given below:

$$\gamma_{SV} = \gamma_{SL} + \gamma_{LV} \cos \Theta \tag{F.1}$$

As shown in figure F.2a a droplet showing a large contact angle is hydrophobic. This condition is illustrated by poor wetting, poor adhesiveness and low solid surface free energy. A drop with a small contact angle is hydrophilic as presented in figure F.2b. This condition is referred to better wetting, better adhesiveness, and higher surface energy.

Goniometric measurements of a droplet of water on a SU-8 layer, passed through all the process steps like the resonant structures, were performed as shown in figure F.3. what indicates the surface of the resonant structures is hydrophilic.

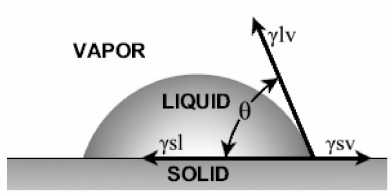

Figure F.1: Liquid droplet on solid surface in ambient air. Θ is the contact angle, γ_{SL} is the solid-liquid interfacial free energy, γ_{SV} the solid surface free energy and γ_{LV} denotes the liquid surface free energy

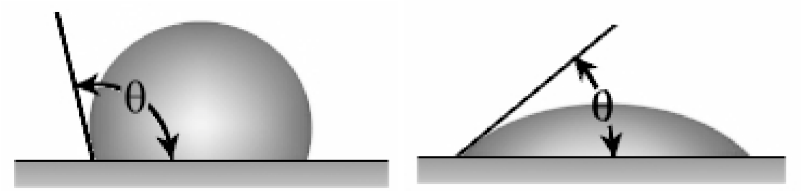

(a) Hydrophobic drop. (b) Hydrophilic drop.

Figure F.2: Droplet in contact with solid in ambient vapor.

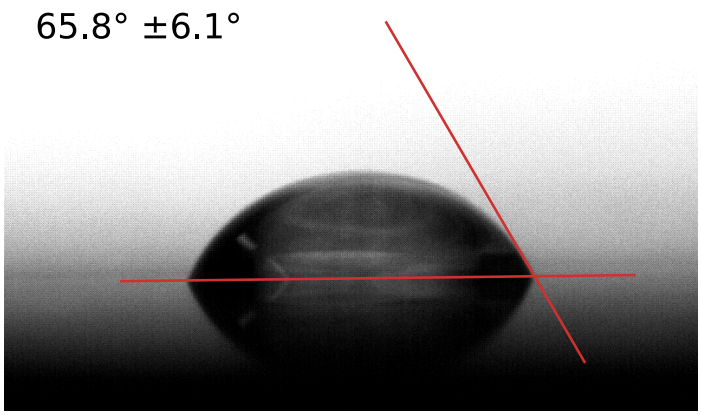

Figure F.3: Contact angle measurement of a drop of water (10μl) on SU-8 surface treated exactly as the beam structures.

G Case study: Stringlike humidity sensor

Polymers often play a key role in chemical sensing applications. Gas-detection sensors can be coated with a functional polymer layer. The absorption of an analyte, water vapor in particular, alters the physical properties of the polymer film which can be measured. There are several transduction techniques [126] such as the gravimetric technique which detects the mass load of the polymer film by resonant cantilevers [31,127] or by quartz crystal microbalances [128]. The change of the dielectric constant can be measured by a capacitive technique [127,129,130] and the amount of heat that is generated in the polymer during absorption can be detected by a calorimetric transducer [127]. The absorption of an analyte can also change the resistance of a conductive polymer [130].

One of the oldest techniques to measured humidity is the hygrometric method, where the change of the volume of the polymer due to the absorbed water vapor is detected. This can be done by coating a silicon membrane [131,132] or thin single-clamped beam [31] with an absorbent polymer layer. With increasing air humidity, the polymer swells and the mechanical bi-layer structure deflect due to the different coefficient of expansion of the two materials. But the combination of a stiff support structure with a soft polymer film restrains the expansion due to swelling of the polymer. This limits the maximal strain and thus limits the sensitivity of such a humidity sensor.

In this case study the feasibility of an all-polymer resonant humidity sensor based on string-like double-clamped polymer microbeams made of SU-8 with an intrinsic stress is investigated. Without a stiff support structure the expansion of the polymer is not restrained. These structures have a high gravimetric sensitivity due to their own low mass density. But in particular, polymer microstrings are highly sensitive to the change of the intrinsic stress and thus to the change of the volume due to swelling as explained in section 8.4.2.

In Fig. 8.7, the shift of the resonant frequency of a stringlike thin d-c microbeam is shown with a linearized relative frequency shift -0.78%/%RH. The sensitivity is more than one order of magnitude higher than the sensitivity of a resonant glass cantilever humidity sensor covered with a polymer layer with a sensitivity of -0.024%/%RH

[209] and more than two orders of magnitude higher than the sensitivity of a polymer coated silicon cantilevers with a sensitivity of -0.003%/%RH [31].

As discussed in section 7.2.1, temperature has a big influence on the resonant frequency of the stringlike SU-8 microbeams. A temperature sensitivity of 0.51% relative frequency change per 1 °C temperature change is obtained from the measurements shown in Fig. 7.7. Thus, in order to compensate for the temperature influence the temperature needs to be known accurately. Roughly, the temperature sensitivity per °C (0.51%/ °C) of the resonant frequency is about the same as the relative humidity sensitivity per %RH (0.79%/%RH). Consequently, the accuracy of a relative humidity measurement in %RH with such a stringlike polymer microbeam depends one-to-one on the temperature measurement accuracy in °C. Furthermore, it has to be assumed, that the total absorption coefficient of the polymer changes with temperature. Thus, such a sensor would need a thorough calibration.

SU-8, which was used for the fabrication of the microstructures, is a highly crosslinked polymer. Nevertheless, it shows a relaxation behavior which is typical for polymer materials, as discussed in section 7.2. The stringlike d-c microbeams show an exponential relaxation behavior with a relaxation time of 113.7 days, as shown in Fig. 7.8. Based on the exponential fit, the time after the fabrication that has to be waited until the relaxation is slow enough such that the relative resonant frequency change is less than 0.0062% (which corresponds to a relative humidity change of 0.01%) over a period of 7 days can be calculated. It results, that after 402 days after fabrication, the relaxation theoretically is slow enough such that the relative humidity can be measured over a week with an accuracy of 0.01%. Thus in order to optimize the long-term stability, the samples need to be stored prior to their application. To accelerate the relaxation process, the polymer sensors could be stored at elevated temperatures. At higher temperatures, the molecular rearrangement processes in the polymer are accelerated and the material relaxes faster, as depicted in Fig. 7.9.

Summing up, stringlike SU-8 microbeams can be used as highly sensitive humidity sensors with certain restrictions. They require an accurate temperature compensation and need to be calibrated in relative short time intervals of several days in order to guarantee accurate humidity measurements. The polymer string humidity sensor presents a sensor design for applications with the need of an enhanced sensitivity over a short period of time.

H Matlab/Simulink model

The nonlinear differential equation (9.3) can not be solved analytically, therefore the solution was simulated with simulink.

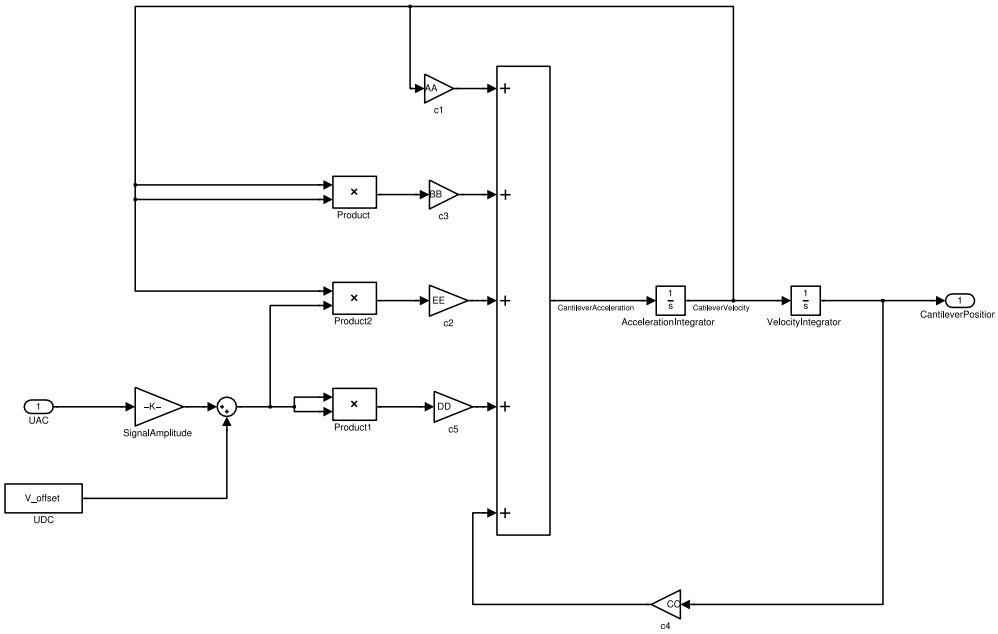

Figure H.1: Simulink model for solving the nonlinear differential equation without taking the diode into account.

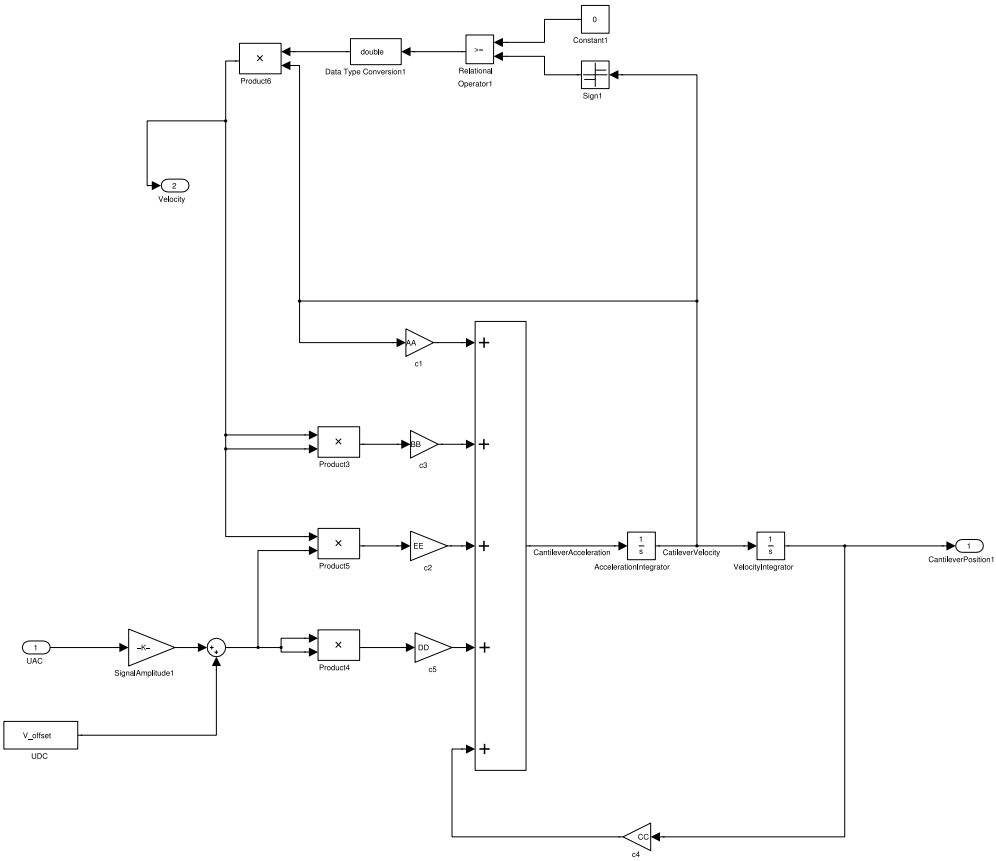

Figure H.2: Simulink model for solving the nonlinear differential equation with taking the diode into account.

I Electronic Feedback Circuit

The detailed circuit diagram is shown in Fig. I.1.

- The supply voltage can be varied up to 18 volts and is equal to the maximal output voltage.
- The voltage supply port as well as the signal input ports are filtered to avoid noise.
- Due to an inverting and non inverting output is required the circuit shows tow parallel parts; once showing an inverting and once a non inverting amplifier (High Speed Comparator, Texas Instruments 3116C).
- The delay time can be adjusted by a potentiometer due to the variation of the switching threshold of the following Schmitt-Trigger (National 9612).
- The digital output signal of the Schmitt-Trigger is used to control a switch which puts through zero or the supply voltage to the output.

In Fig. I.2, the circuit used for the positive feedback based on the circuit diagram is shown.

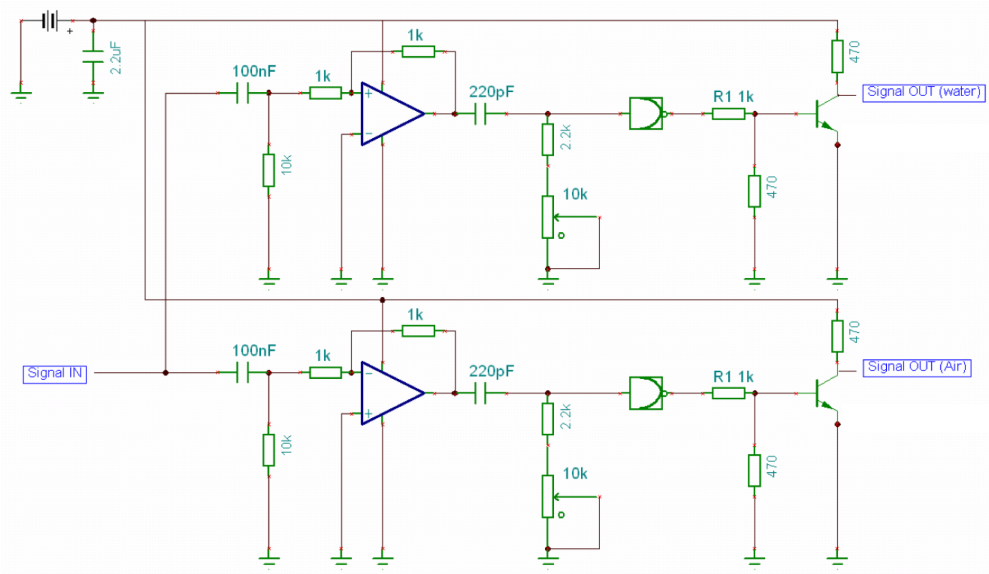

Figure I.1: Circuit diagram of the closed loop control.

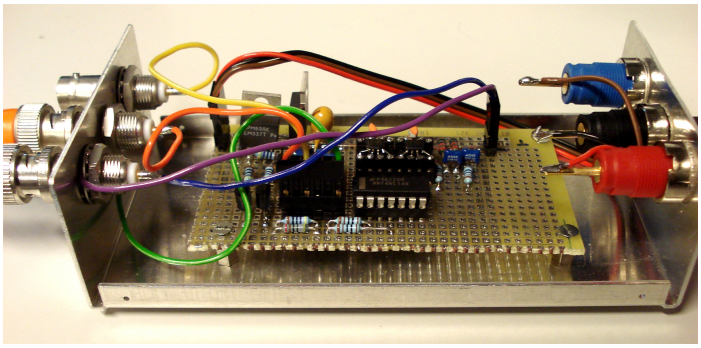

Figure I.2: Electrical parts soldered on circuit board mounted in the screening enclosure.

J Ethanol dissolved in water

In order to test the application of the self-excitation technique introduced in chapter 9.4 in aqueous environment, the oscillation frequency of a microbeam is determined for varying concentrations of ethanol dissolved in water. Hossenlopp et al. [109] describe a plasticization of SU-8 for increasing concentrations of organic solvents such as acetone and ethanol in aqueous solution. Consequently, the resonant frequency of the microbeam is expected to decrease for an increasing solvent concentration. In Fig. J.1, the average oscillation frequency is shown for varying ethanol concentrations between 0 to 6%. At 6%, a relative frequency change of 4.15%/% ethanol is evaluated.

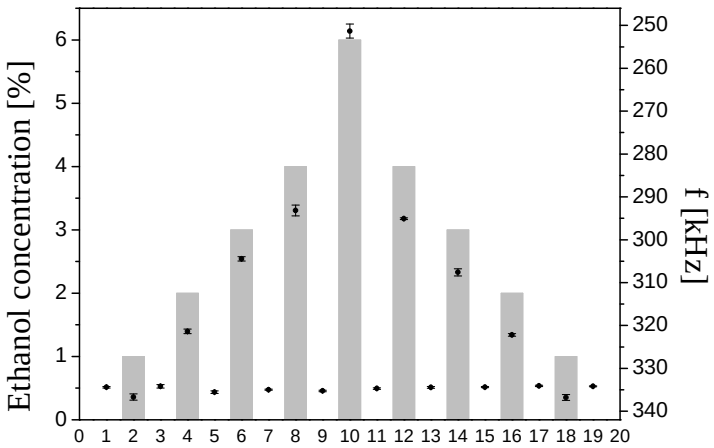

Figure J.1: Average oscillation frequencies (of 5 single measurements for each concentration) of a thin d-c SU-8 microbeam ($L = 100\ \mu$m) as a function of varying ethanol concentration in DI-water. The microbeam is actuated by means of a self-excitation. The measurments were performed at 24.4 °C.

Bibliography

[1] V. T. Srikar and S. M. Spearing, "Materials selection in micromechanical design: An application of the Ashby approach," *Journal of Microelectromechanical Systems*, vol. 12, no. 1, pp. 3–10, 2003.

[2] S. R. Quake and A. Scherer, "From micro- to nanofabrication with soft materials," *Science*, vol. 290, no. 5496, pp. 1536–1540, 2000.

[3] J. Gaspar, V. Chu, and J. P. Conde, "Electrostatically actuated thin-film amorphous silicon microbridge resonators," *Journal of Applied Physics*, vol. 97, no. 9, p. 094501, 2005.

[4] N. T. Nguyen, S. S. Ho, and C. L. N. Low, "A polymeric microgripper with integrated thermal actuators," *Journal of Micromechanics and Microengineering*, vol. 14, no. 7, pp. 969–974, 2004.

[5] V. T. Srikar and S. M. Spearing, "Materials selection for microfabricated electrostatic actuators," *Sensors and Actuators A: Physical*, vol. 102, no. 3, pp. 279–285, 2003.

[6] I. M. Ward and J. Sweeney, *An Introduction to the Mechanical Properties of Solid Polymers*, 2nd ed. John Wiley & Sons, 2004.

[7] L. R. G. Treloar, *The physics of rubber elasticity*. Oxford university press, 1975.

[8] J. W. L. Zhou, H. Y. Chan, T. K. H. To, K. W. C. Lai, and W. J. Li, "Polymer MEMS actuators for underwater micromanipulation," *IEEE-ASME Transactions on Mechatronics*, vol. 9, no. 2, pp. 334–342, 2004.

[9] N. Chronis and L. P. Lee, "Electrothermally activated SU-8 microgripper for single cell manipulation in solution," *Journal of Microelectromechanical Systems*, vol. 14, no. 4, pp. 857–863, 2005.

[10] E. Smela, "Conjugated polymer actuators for biomedical applications," *Advanced Materials*, vol. 15, no. 6, pp. 481–494, 2003.

[11] J. D. Madden, R. A. Cush, T. S. Kanigan, and I. W. Hunter, "Fast contracting polypyrrole actuators," *Synthetic Metals*, vol. 113, no. 1-2, pp. 185–192, 2000.

[12] C. Goll, W. Bacher, B. Bustgens, D. Maas, R. Ruprecht, and W. K. Schomburg, "An electrostatically actuated polymer microvalve equipped with a movable membrane electrode," *Journal of Micromechanics and Microengineering*, vol. 7, no. 3, pp. 224–226, 1997.

[13] V. Seidemann, S. Butefisch, and S. Buttgenbach, "Fabrication and investigation of in-plane compliant SU8 structures for MEMS and their application to micro valves and micro grippers," *Sensors and Actuators A: Physical*, vol. 97-8, pp. 457–461, 2002.

[14] M. Calleja, P. Rasmussen, A. Johansson, and A. Boisen, "Polymeric Mechanical Sensors with Integrated Readout in a Microfluidic System," in *Proceedings of the SPIE*, vol. 5116, 2003, pp. 314–321.

[15] M. Calleja, J. Tamayo, A. Johansson, P. Rasmussen, L. Lechuga, and A. Boisen, "Polymeric cantilever arrays for biosensing applications," *Sensor Letters*, vol. 1, pp. 1–5, 2003.

[16] M. Calleja, M. Nordstrom, M. Alvarez, J. Tamayo, L. M. Lechuga, and A. Boisen, "Highly sensitive polymer-based cantilever-sensors for DNA detection," *Ultramicroscopy*, vol. 105, no. 1-4, pp. 215–222, 2005.

[17] J. Thaysen, A. D. Yalcinkaya, P. Vettiger, and A. Menon, "Polymer-based stress sensor with integrated readout," *Journal of Physics D-Applied Physics*, vol. 35, no. 21, pp. 2698–2703, 2002.

[18] X. R. Zhang and X. F. Xu, "Development of a biosensor based on laser-fabricated polymer microcantilevers," *Applied Physics Letters*, vol. 85, no. 12, pp. 2423–2425, 2004.

[19] T. Xu, M. Bachman, F. G. Zeng, and G. P. Li, "Polymeric micro-cantilever array for auditory front-end processing," *Sensors and Actuators A: Physical*, vol. 114, no. 2-3, pp. 176–182, 2004.

[20] G. Genolet, J. Brugger, M. Despont, U. Drechsler, P. Vettiger, N. F. de Rooij, and D. Anselmetti, "Soft, entirely photoplastic probes for scanning force microscopy," *Review Of Scientific Instruments*, vol. 70, no. 5, pp. 2398–2401, 1999.

[21] E. W. H. Jager, E. Smela, and O. Inganas, "On-chip microelectrodes for electrochemistry with moveable PPy bilayer actuators as working electrodes," *Sensors and Actuators B: Chemical*, vol. 56, no. 1-2, pp. 73–78, 1999.

[22] E. W. H. Jager, E. Smela, O. Inganas, and I. Lundstrom, "Polypyrrole microactuators," *Synthetic Metals*, vol. 102, no. 1-3, pp. 1309–1310, 1999.

[23] E. W. H. Jager, E. Smela, and O. Inganas, "Microfabricating conjugated polymer actuators," *Science*, vol. 290, no. 5496, pp. 1540–1545, 2000.

[24] M. Roemer, T. Kurzenknabe, E. Oesterschulze, and N. Nicoloso, "Microactuators based on conducting polymers," *Analytical and Bioanalytical Chemistry*, vol. 373, no. 8, pp. 754–757, 2002.

[25] J. M. Sansinena, J. B. Gao, and H. L. Wang, "High-performance, monolithic polyaniline electrochemical actuators," *Advanced Functional Materials*, vol. 13, no. 9, pp. 703–709, 2003.

[26] E. Smela, W. Lu, and B. R. Mattes, "Polyaniline actuators - Part 1. PANI(AMPS) in HCl," *Synthetic Metals*, vol. 151, no. 1, pp. 25–42, 2005.

[27] D. Bachmann, B. Schoeberle, S. Kuehne, Y. Leiner, and C. Hierold, "Fabrication and characterization of folded SU-8 suspensions for MEMS applications," *Sensors and Actuators A: Physical*, pp. 379–386, 2006.

[28] D. Bachmann, S. Kühne, and C. Hierold, "MEMS scanning mirror supported by soft polymeric springs and actuated by electrostatic charge separation," *Micro Electro Mechanical Systems, 2007. MEMS. IEEE 20th International Conference on*, pp. 723–726, Jan. 2007.

[29] G. Zhang, J. Gaspar, V. Chu, and J. P. Conde, "Electrostatically actuated polymer microresonators," *Applied Physics Letters*, vol. 87, no. 10, p. 104104, 2005.

[30] J. Tamayo, D. Ramos, J. Mertens, and M. Calleja, "Effect of the adsorbate stiffness on the resonance response of microcantilever sensors," *Applied Physics Letters*, vol. 89, p. 224104, 2006.

[31] F. Battiston, J.-P. Ramseyer, H. Lang, M. Baller, C. Gerber, J. Gimzewski, E. Meyer, and H.-J. Güntherodt, "A chemical sensor based on a microfabricated cantilever array with simultaneous resonance-frequency and bending readout," *Sensors and Actuators B: Chemical*, vol. 77, pp. 122–131, 2001.

[32] B. D. Jensen, M. P. de Boer, and S. L. Miller, "IMaP: Interferometry for material property measurment in MEMS," in *Modeling and Simulation of Microsystems*, San Juan, Puerto Rico, 1999, pp. 206–209.

[33] P. M. Osterberg and S. D. Senturia, "M-TEST: A Test Chip for MEMS Material Property Measurement Using Electrostatically Actuated Test Structures," *Journal of Microelectromechanical Systems*, vol. 6, no. 2, pp. 107–118, 1997.

[34] K. E. Petersen and C. R. Guarnieri, "Young's Modulus Measurements of Thin Films Using Micromechanics," *Journal of Applied Physics*, vol. 50, no. 11, pp. 6761–6766, 1979.

[35] J. Yang, T. Ono, and M. Esashi, "Energy Dissipation in Submicrometer Thick Single-Crystal Cantilevers," *Journal of Microelectromechanical Systems*, vol. 11, no. 6, pp. 775–783, 2002.

[36] K. Y. Yasumura, T. D. Stowe, E. M. Chow, T. Pfafman, T. W. Kenny, B. C. Stipe, and D. Rugar, "Quality Factors in Micron- and Submicron-Thick Cantilevers," *Journal of Microelectromechanical Systems*, vol. 9, no. 1, pp. 117–125, 2000.

[37] D. Valtorta, J. Lefevre, and E. Mazza, "A New Method for Measuring Damping in Flexural Vibration of Thin Fibers," *Experimental Mechanics*, vol. 45, no. 5, pp. 433–439, 2005.

[38] Z. Hao, A. Erbil, and F. Ayazi, "An Analytical Model for Support Loss in Micromachined Beam Resonators with In-plane Flexural Vibrations," *Sensors and Actuators A: Physical*, vol. 109, pp. 156–164, 2003.

[39] V. T. Srikar and S. M. Spearing, "A Critical Review of Microscale Mechanical Testing Methods Used in the Design of Microelectromechanical Systems," *Experimental Mechanics*, vol. 43, no. 3, pp. 238–247, 2003.

[40] R. Feng and R. J. Farris, "Influence of processing conditions on the thermal and mechanical properties of SU8 negative photoresist coatings," *Journal of Micromechanics and Microengineering*, vol. 13, no. 1, pp. 80–88, 2003.

[41] W. R. Vieth, *Diffusion In and Through Polymers*. Hanser, 1991.

[42] I. Ward, *Mechanical Properties of Solid Polymers*. John Wiley & Sons, 1983.

[43] Y. N. Xia and G. M. Whitesides, "Soft lithography," *Annual Review of Materials Science*, vol. 28, pp. 153–184, 1998.

[44] M. Brehmer, L. Conrad, and L. Funk, "New developments in soft lithography," *Journal Of Dispersion Science And Technology*, vol. 24, no. 3-4, pp. 291–304, 2003.

[45] H. Lorenz, M. Laudon, and P. Renaud, "Mechanical characterization of a new high-aspect-ratio near UV- photoresist," *Microelectronic Engineering*, vol. 42, pp. 371–374, 1998.

[46] H. Becker and U. Heim, "Hot embossing as a method for the fabrication of polymer high aspect ratio structures," *Sensors and Actuators A: Physical*, vol. 83, no. 1-3, pp. 130–135, 2000.

[47] G. Fichet, N. Stutzmann, B. V. O. Muir, and W. T. S. Huck, "Microembossing of elastomeric triblock copolymers," *Advanced Materials*, vol. 14, no. 1, pp. 47–51, 2002.

[48] N. Stutzmann, T. A. Tervoort, C. W. M. Bastiaansen, K. Feldman, and P. Smith, "Solid-state replication of relief structures in semicrystalline polymers," *Advanced Materials*, vol. 12, no. 8, pp. 557–562, 2000.

[49] V. Studer, A. Pepin, and Y. Chen, "Nanoembossing of thermoplastic polymers for microfluidic applications," *Applied Physics Letters*, vol. 80, no. 19, pp. 3614–3616, 2002.

[50] J. W. L. Zhou, H.-Y. Chan, T. K. H. To, K. W. C. Lai, and W. J. Li, "Polymer MEMS Actuators for Underwater Micromanipulation," *IEEE/ASME Transactions on Mechatronics*, vol. 9, no. 2, pp. 334–342, 2004.

[51] G. M. Atkinson, R. E. Pearson, Z. Ounaies, C. Park, J. S. Harrison, and S. Dogan, "Novel piezoelectric polyimide MEMS," in *Digest of Technical Papers of the TRANSDUCERS'03*, Boston, USA, 2003, pp. 782–785.

[52] C. Friese, M. Wissmann, and H. Zappe, "Polymer-based Membrane Mirrors for Micro-optical Sensors," in *Proceedings of IEEE Sensors*, vol. 1, 2003, pp. 667– 672.

[53] Y.-J. Kim and M. Allen, "In situ measurement of mechanical properties of polyimide films using micromachined resonant string structures," *IEEE Transactions on Components and Packaging Technology*, vol. 22, no. 2, pp. 282–290, 1999.

[54] H. A. Haus and J. R. Melcher, *Electromagnetic Fields and Energy*. Prentice Hall, 1989, chapter 11: Energy, Power Flow, and Forces.

[55] T. B. Jones, *Electromechanics of Particles*. Cambridge University Press, 1995, chapter 2: Fundamentals.

[56] J. N. Israelachvili, *Intermolecular and Surface Forces*. Academic Press Inc, 1991.

[57] V. Kuz'min, V. Romanov, and E. Obraztsov, "Permittivity of suspensions," *Optics and Spectroscopy*, vol. 93, no. 6, pp. 1000–1006, 2002.

[58] S. Schmid, M. Wendlandt, D. Junker, and C. Hierold, "Nonconductive polymer microresonators actuated by the Kelvin polarization force," *Applied Physics Letters*, vol. 89, p. 163506, 2006.

[59] S. Margulies, "Force on a dielectric slab inserted into a parallel-plate capacitor," *American Journal of Physics*, vol. 52, no. 6, pp. 515–518, 1984.

[60] J. Thorpe, D. Steenson, and R. Miles, "High frequency transmission line using micromachined polymer dielectric," *Electronics Letters*, vol. 34, no. 12, pp. 1237–1238, Jun 1998.

[61] M. Bao, *Analysis and Design Principles of MEMS Devices*. Elsevier, 2005.

[62] H. Lorenz, M. Despont, N. Fahrni, N. LaBianca, P. Renaud, and P. Vettiger, "SU-8: a low-cost negative resist for MEMS," *Journal of Micromechanics and Microengineering*, vol. 7, no. 3, pp. 121–124, 1997.

[63] Y.-J. Chuang, F.-G. Tseng, J.-H. Cheng, and W.-K. Lin, "A Novel Fabrication Method of Embedded Micro-channels by Using SU-8 Thick-film Photoresists," *Sensors and Actuators A: Physical*, vol. 103, pp. 64–69, 2003.

[64] A. Hartley, R. Miles, N. Dimitrakopoulos, and R. D. Pollard, "SU-8 Beams and Membranes," in *Proceedings of the 1st EMRS DTC Technical Conference*, 2004.

[65] L. J. Guerin, M. Bossel, M. Demierre, S. Calmes, and P. Renaud, "Simple and Low Cost Fabrication of Embedded Micro-Channels by Using a New Thick-Film Photoplastic," in *Digest of Technical Papers of the Transducers' 97*, 1997, pp. 1419–1422.

[66] C. Chung and M. Allen, "Uncrosslinked SU-8 as a sacrificial material," *Journal of Micromechanics and Microengineering*, vol. 15, pp. N1–N5, 2005.

[67] B. E. J. Alderman, C. M. Mann, D. P. Steenson, and J. M. Chamberlain, "Microfabrication of Channels Using an Embedded Mask in Negative Resist," *Journal of Micromechanics and Microengineering*, vol. 11, pp. 703–705, 2001.

[68] F. Ceyssens and R. Puers, "Two Methods for Creating Multi-Layered Structures with Freestanding Parts in SU-8," in *Technical Digest of the MicroMechanics Europe Workshop*, 2005, pp. 115–118.

[69] D. Haefliger and A. Boisen, "Contact Printed Masks for 3D Microfabrication in Negative Resists," in *Proceedings of the 18th IEEE International Conference on Micro Electro Mechanical Systems. MEMS 2005.*, 2005, pp. 556–559.

[70] W. H. Teh, U. Duerig, G. Salis, R. Harbers, U. Drechsler, R. F. Mahrt, C. G. Smith, and J. H. Guentherodt, "SU-8 for Real Three-dimensional Subdiffraction-limited two-photon Microfabrication," *Applied Physics Letters*, vol. 84, pp. 4095–4097, 2004.

[71] F. J. Blanco, M. Agirregabiria, J. Garcia, J. Berganzo, M. Tijero, M. T. Arroyo, J. M. Ruano, I. Aramburu, and K. Mayora, "Novel Three-dimensional Embedded SU-8 Microchannels Fabricated Using a Low Temperature Full Wafer Adhesive Bonding," *Journal of Micromechanics and Microengineering*, vol. 14, pp. 1047–1056, 2004.

[72] M. Agirregabiria, F. J. Blanco, J. Berganzo, M. T. Arroyo, A. Fullaondo, K. Mayora, and J. M. Ruano-Lopez, "Fabrication of SU-8 Multilayer Microstructures Based on Successive CMOS Compatible Adhesive Bonding and Releasing Steps," *Lab on a Chip*, vol. 5, pp. 545–552, 2005.

[73] R. J. Jackman, T. M. Floyd, R. Ghodssi, M. A. Schmidt, and K. F. Jensen, "Microfluidic Systems with On-line UV Detection Fabricated in Photodefinable Epoxy," *Journal of Micromechanics and Microengineering*, vol. 11, pp. 263–269, 2001.

[74] J. Bühler, F.-P. Steiner, and H. Baltes, "Silicon dioxide sacrificial layer etching in surface micromachining," *Journal of Micromechanics and Microengineering*, vol. 7, pp. R1–R13, 1997.

[75] V. Linder, B. D. Gates, D. Ryan, B. A. Parviz, and G. M. Whitesides, "Water-Soluble Sacrificial Layers for Surface Micromachining," *Small*, vol. 1, no. 7, pp. 730–736, 2005.

[76] R. Stöckle, C. Fokas, V. Deckert, R. Zenobia, B. Sick, B. Hecht, and U. P. Wild, "High-quality near-field optical probes by tube etching," *Applied Physics Letters*, vol. 75, no. 2, pp. 160–162, 1999.

[77] V. Seidemann, J. Rabe, M. Feldmann, and S. Buettgenbach, "SU8-micromechanical structures with in situ fabricated movable parts," *Microsystem Technologies*, vol. 8, pp. 348–350, 2002.

[78] J. P. Jayachandran, H. A. Reed, H. Zhen, L. F. Rhodes, L. Henderson, S. A. B. Allen, and P. A. Kohl, "Air-Channel Fabrication for Microelectromechanical Systems via Sacrificial Photosensitive Polycarbonates," *Journal of Microelectromechanical Systems*, vol. 12, no. 2, pp. 147–157, 2003.

[79] S. Metz, S. Jiguet, A. Bertsch, and P. Renaud, "Polyimide and SU-8 Microfluidic Devices Manufactured by Heat-depolymerizable Sacrificial Material Technique," *Lab on a Chip*, vol. 4, pp. 114–120, 2004.

[80] K. Williams, K. Gupta, and M. Wasilik, "Etch rates for micromachining processing-Part II," *Journal of Microelectromechanical Systems*, vol. 12, no. 6, pp. 761– 778, 2003.

[81] H. Lorenz, M. Despont, N. Fahrni, J. Brugger, P. Vettiger, and P. Renaud, "High-aspect-ratio, ultrathick, negative-tone near-UV photoresist and its applications for MEMS," *Sensors and Actuators A: Physical*, vol. 64, no. 1, pp. 33–39, 1998.

[82] J. M. Shaw, J. D. Gelorme, N. C. LaBianca, W. E. Conley, and S. J. Holmes, "Negative photoresists for optical lithography," *IBM Journal of Research Development*, vol. 41, no. 1/2, pp. 81–94, 1997.

[83] R. Feng and R. J. Farris, "The characterization of thermal and elastic constants for an epoxy photoresist SU8 coating," *Journal of Materials Science*, vol. 37, no. 22, pp. 4795–4801, 2002.

[84] C. Luo, T. Schneider, R. White, J. Currie, and M. Paranjape, "A simple deflection-testing method to determine Poisson's ratio for MEMS applications," *Journal of Micromechanics and Microengineering*, vol. 13, p. 129133, 2003.

[85] B. Schöberle, "Evaluation of viscoelastic materials for MEMS by creep compliance analysis," Ph.D. dissertation, ETH Zurich, 2008.

[86] C. Mattsson, G. Thungstrom, K. Bertilsson, H.-E. Nilsson, and H. Martin, "Development of an infrared thermopile detector with a thin self-supporting SU-8 membrane," in *Proceedings of IEEE Sensors*, 2007, pp. 836–839.

[87] *SU-8 2000 permanent epoxy negative photoresist. Application notes.*, MicroChem Corp.

[88] M. B. Sayir and S. Kaufmann, *Ingenieurmechanik 3 : Dynamik*. Teubner, 2005, chapter 34: Dynamik einfacher kontinuierlicher Strukturen.

[89] K. Magnus and K. Popp, *Schwingungen*, 7th ed. Teubner, 2005, chapter 7: Kontinuumsschwingungen.

[90] R. S. Lakes, *Viscoelastic Solids*. CRC Press, 1999.

[91] I. M. Ward and J. Sweeney, *An Introduction to the Mechanical Properties of Solid Polymers*, 2nd ed. Wiley, 2004.

[92] S. Schmid and C. Hierold, "Damping mechanisms of single-clamped and prestressed double-clamped resonant polymer microbeams," *Journal of Applied Physics*, vol. 104, no. 9, p. 093516, 2008.

[93] P. Mohanty, D. A. Harrington, K. L. Ekinci, Y. T. Yang, M. J. Murphy, and M. L. Roukes, "Intrinsic dissipation in high-frequency micromechanical resonators," *Physical Review B*, vol. 66, no. 8, p. 085416, 2002.

[94] K. Y. Yasumura, T. D. Stowe, E. M. Chow, T. Pfafman, T. W. Kenny, B. C. Stipe, and D. Rugar, "Quality factors in micron- and submicron-thick cantilevers," *Journal of Microelectromechanical Systems*, vol. 9, no. 1, pp. 117–125, 2000.

[95] K. Naeli, P. Tandon, and O. Brand, "Geometrical optimization of resonant cantilever sensors," in *Digest of Technical Papers of Transducers'07 & Eurosensors XXI*, 2007, pp. 245–248.

[96] J. Gaspar, V. Chu, and J. P. Conde, "Amorphous silicon electrostatic microresonators with high quality factors," *Applied Physics Letters*, vol. 84, no. 4, pp. 622–624, 2004.

[97] S. S. Verbridge, J. M. Parpia, R. B. Reichenbach, L. M. Bellan, and H. G. Craighead, "High quality factor resonance at room temperature with nanostrings under high tensile stress," *Journal of Applied Physics*, vol. 99, p. 124304, 2006.

[98] S. S. Verbridge, D. Finkelstein Shapiro, H. G. Craighead, and J. M. Parpia, "Macroscopic tuning of nanomechanics: Substrate bending for reverisble control of frequency and quality factor of nanostring resonators," *Nano Letters*, vol. 7, no. 6, pp. 1728–1735, 2007.

[99] G. Zhang, V. Chu, and J. P. Conde, "Conductive blended polymer MEMS microresonators," *Journal of Microelectromechanical Systems*, vol. 16, no. 2, pp. 329–335, 2007.

[100] M. Bao, H. Yang, H. Yin, and Y. Sun, "Energy transfer model for squeeze-film air damping in low vacuum," *Journal of Micromechanics and Microengineering*, vol. 12, pp. 341–346, 2002.

[101] R. G. Christian, "The theory of oscillating-vane vacuum gauges." *Vacuum*, vol. 16, pp. 175–178, 1966.

[102] P. Li and R. Hu, "On the air damping of flexible microbeam in free space at the free-molecule regime," *Microfluidics and Nanofluidics*, vol. 3, pp. 715–721, 2007.

[103] "Hiqlab project page," http://www.cims.nyu.edu/~dbindel/hiqlab/.

[104] T. Koyama, D. Bindel, H. Wei, E. Quevy, S. Govindjee, J. Demmel, and R. Howe, "Simulation tools for damping in high frequency resonators," in *Proceedings of IEEE Sensors*, 2005, pp. 349–352.

[105] D. S. Bindel and S. Govindjee, "Elastic PMLs for resonator anchor loss simulation," *International Journal for Numerical Methods in Engineering*, vol. 64, pp. 789–818, 2005.

[106] H. Hosaka, K. Itao, and S. Kuroda, "Damping Characteristics of Beam-shaped Micro-oscillators," *Sensors and Actuators A: Physical*, vol. 49, pp. 87–95, 1995.

[107] C. Zener, "Internal friction in solids I. Theory of internal friction in reeds." *Physical Review*, vol. 52, pp. 230–235, 1937.

[108] R. Lifshitz and M. L. Roukes, "Thermoelastic Damping in Micro- and Nanomechanical Systems," *Physical Review B*, vol. 61, no. 8, pp. 5600–5609, 2000.

[109] J. Hossenlopp, L. H. Jiang, R. Cernosek, and F. Josse, "Characterization of epoxy resin (SU-8) film using thickness-shear mode (TSM) resonator under various conditions," *Journal of Polymer Science Part B-Polymer Physics*, vol. 42, no. 12, pp. 2373–2384, 2004.

[110] L. Monnerie, F. Laupretre, and J. L. Halary, "Investigation of solid-state transitions in linear and crosslinked amporphous polymers," *Advanced Polymer Science*, vol. 187, pp. 35–213, 2005.

[111] L. Heux, J. L. Halary, F. Lauprêtre, and L. Monnerie, "Dynamic mechanical and ^{13}C n.m.r. investigations of molecular motions involved in the β relaxation of epoxy networks based on DGEBA and aliphatic amines," *Polymer*, vol. 38, pp. 1767–1778, 1997.

[112] J. R. Fried, A. Letton, and W. J. Welsh, "Secondary relaxation processes in bisphenol-A polysulphone," *Polymer*, vol. 31, pp. 1032–1037, 1990.

[113] W. Weaver, S. P. Timoshenko, and D. H. Young, *Vibration Problems in Engineering*. Wiley Interscience, 1990.

[114] B. S. Berry, "Damping mechanisms in thin-layer materials," in *M3D: Mechanics and Mechanisms of Material Damping*, V. K. Kinra and A. Wolfenden, Eds. ASTM, 1992, pp. 28–44.

[115] M. C. Cross and R. Lifshitz, "Elastic wave transmission at an abrupt junction in a thin plate with application to heat transport and vibrations in mesoscopic systems," *Physical Review B*, vol. 64, p. 085324, 2001.

[116] J. D. Ferry, *Viscoelastic Properties of Polymers*, 3rd ed. John Wiley & Sons, 1980.

[117] E. Mazza, S. Abel, and J. Dual, "Experimental determination of mechanical properties of Ni and Ni-Fe microbars," *Microsystem Technologies*, pp. 197–202, 1996.

[118] J. D. Ferry, *Viscoelastic Properties of Polymers, Chapter 15*, 3rd ed. John Wiley & Sons, 1980.

[119] G. Zhang, V. Chu, and J. P. Conde, "Electrostatically actuated conducting polymer microbridges," *Journal of Applied Physics*, vol. 101, p. 064507, 2007.

[120] M. Kühlmeyer, *Statistische Auswertungsmethoden für Ingenieure*. Springer, 2001.

[121] B. Kim, R. Candler, M. Hopcroft, M. Agarwal, W.-T. Park, and T. Kenny, "Frequency stability of wafer-scale encapsulated MEMS resonators," *Digest of Technical Papers. The 13th International Conference on TRANSDUCERS '05.*, vol. 2, pp. 1965–1968, 2005.

[122] L. C. E. Struik, "Physical aging in plastics and other glassy materials," *Polymer Engineering and Science*, vol. 17, no. 3, pp. 165–173, 1977.

[123] J. D. Ferry, *Viscoelastic properties of polymers*. New York: John Wiley and Sons, 1980.

[124] S. Schmid, S. Kühne, and C. Hierold, "Influence of air humidity on polymeric microresonators," *Journal of Micromechanics and Microengineering*, vol. 19, p. 065018 (9pp), 2009.

[125] C.-Y. Lee, C.-H. Lin, and L.-M. Fu, *MEMS/NEMS, Techniques in MEMS Devices for Micro Humidity Sensors and Their Applications*. Springer US, 2006.

[126] Z. M. Rittersma, "Recent achievements in miniaturised humidity sensorsa review of transduction techniques," *Sensors and Actuators A: Physical*, vol. 96, no. 2-3, pp. 196–210, 2002.

[127] P. Kurzawski, C. Hagleitner, and A. Hierlemann, "Detection and discrimination capabilities of a multitransducer single-chip gas sensor system," *Analytical Chemistry*, vol. 78, no. 19, pp. 6910 –6920, 2006.

[128] T. Pascal-Delannoy, B. Sorli, and A. Boyer, "Quartz crystal microbalance (QCM) used as humidity sensor," *Sensors and Actuators A: Physical*, vol. 84, no. 3, pp. 285–291, 2000.

[129] Y. Sakai, Y. Sadaoka, and M. Matsuguchi, "Humidity sensors based on polymer thin films," *Sensors and Actuators B: Chemical*, vol. 35, no. 1-3, pp. 85–90, 1996.

[130] Y. Li, M. J. Yanga, N. Camaionib, and G. Casalbore-Miceli, "Humidity sensors based on polymer solid electrolytes: investigation on the capacitive and resistive devices construction," *Sensors and Actuators B: Chemical*, vol. 77, no. 3, pp. 625–631, 2001.

[131] K. Sager, G. Gerlach, and A. Schroth, "A humidity sensor of a new type," *Sensors and Actuators B: Chemical*, vol. 18, no. 1-3, pp. 85–88, 1994.

[132] R. Buchhold, A. Nakladal, G. Gerlach, K. Sahre, K.-J. Eichhorn, and M. Müller, "Reduction of mechanical stress in micromachined components caused by humidity-induced volume expansion of polymer layers," *Microsystem Technologies*, vol. 5, pp. 3–12, 1998.

[133] G. Dlubek, R. Buchhold, C. Hübner, and A. Nakladal, "Water in local free volume of polyimides: A positron lifetime study," *Macromolecules*, vol. 32, pp. 2348–2355, 1999.

[134] Y. Diamant, G. Marom, and L. J. Broutman, "The effect of network structure on moisture absorption of epoxy resins," *Journal of Applied Polymer Science*, vol. 26, pp. 3015–3025, 1981.

[135] D. W. Galipeau, C. Feger, J. F. Vetelino, and R. Lec, "The study of polyimide films and adhesion using a surface acoustic wave sensor," in *Proceedings of the Ultrasonic Symposium*, 1990, pp. 1087–1090.

[136] M. Matsuguchi, M. Shinmoto, Y. Sadaoka, T. Kuroiwa, and Y. Sakai, "Effect of the degree of cross-linking on the characteristics of a PVCA capacitive-type humidity sensor," *Sensors and Actuators B: Chemical*, vol. 34, pp. 349–355, 1996.

[137] J. M. Barton, "Effect of absorbed water on the thermal relaxation of biaxially stretched crosslinked poly(methyl methacrylate)," *Polymer*, vol. 20, pp. 1018–1024, 1979.

[138] E. Dermitzaki, B. Wunderle, J. Bauer, H. Walter, and B. Michel, "Structure property correlation of epoxy resins under the influence of moisture; and comparison of diffusion coefficient with MD-simulation," in *Proceedings of the International Conference on Thermal, Mechanical and Multiphysics Simulation and Experiments in Micro-Electronics and Micro-Systems*, 2008, pp. 1–8.

[139] H. Ardebili, E. H. Wong, and M. Pecht, "Hygroscopic swelling and sorption characteristics of epoxy molding compounds used in electronic packaging," *IEEE Transactions on Components and Packaging Technologies*, vol. 26, no. 1, pp. 206–214, 2003.

[140] M. R. Vanlandingham, R. F. Eduljee, and J. W. Gillespie, "Moisture diffusion in epoxy systems," *Journal of Applied Polymer Science*, vol. 71, pp. 787–798, 1999.

[141] S. S. Lawrence, J. L. Willett, and C. J. Carriere, "Effect of moisture on the tensile properties of poly(hydrxy ester ether)," *Polymer*, vol. 42, pp. 5643–5650, 2001.

[142] S. Ito, M. Hashimoto, B. Wadgaonkar, N. Svizero, R. M. Carvalho, C. Yiu, F. A. Rueggeberg, S. Foulger, T. Saito, Y. Nishitani, M. Yoshiyama, F. R. Tay, and D. H. Pashley, "Effects of resin hydrophilicity on water sorption and changes in modulus of elasticity," *Biomaterials*, vol. 26, pp. 6449–6459, 2005.

[143] W. J. Cousins, "Elastic modulus of lignin as related to moisture content," *Wood Science and Technology*, vol. 10, pp. 9–17, 1976.

[144] C. Ishiyama and Y. Higo, "Effects of humidity on Young's modulus in poly(methyl methacrylate)," *Journal of Polymer Science: Part B: Polymer Physics*, vol. 40, pp. 460–465, 2002.

[145] A. S. Zerda and A. J. Lesser, "Characteristics of antiplasticized thermosets: Effects of network architecture and additive chemistry on mechanical fortification," *Polymer Engineering and Science*, vol. 44, no. 11, pp. 2125–2133, 2004.

[146] M. Rapp, B. Böss, A. Voigt, H. Gemmeke, and H. J. Ache, "Development of an analytical microsystem for organic gas detection based on surface acoustic wave resonators," *Fresenius' Journal of Analytical Chemistry*, vol. 352, pp. 699–704, 1995.

[147] G. Dlubek, F. Redmann, and R. Krause-Rehberg, "Humidity-induced plasticization and antiplasticization of polyamide 6: A positron lifetime study of the local free volume," *Journal of Applied Polymer Science*, vol. 84, pp. 244–255, 2002.

[148] J. Crank, *The Mathematics of Diffusion*, 2nd ed. Clarendon Press, Oxford, 1975.

[149] G. C. Hill, R. Melamud, F. E. Declercq, A. A. Davenport, I. H. Chan, P. G. Hartwell, and B. L. Pruitt, "SU-8 MEMS Fabry-Perot pressure sensor," *Sensors and Actuators A: Physical*, vol. 138, pp. 52–62, 2007.

[150] A. Hierlemann and R. Gutierrez-Osuna, "Higher-order chemical sensing," *Chemical Reviews*, vol. 108, pp. 563–613, 2008.

[151] R. Marie, S. Schmid, A. Johansson, L. Ejsing, M. Nordstroem, D. Haefliger, C. B. V. Christensen, A. Boisen, and M. Dufva, "Immobilisation of DNA to polymerised SU-8 photoresist," *Biosensors and Bioelectronics*, vol. 21, pp. 1327–1332, 2006.

[152] C. Ziegler, "Cantilever-based biosensors," *Analytical and Bioanalytical Chemistry*, vol. 379, no. 7-8, pp. 946–959, 2004.

[153] J. Tamayo, A. D. L. Humphris, A. M. Malloy, and M. J. Miles, "Chemical sensors and biosensors in liquid environment based on microcantilevers with amplified quality factor," *Ultramicroscopy*, vol. 86, pp. 167–173, 2001.

[154] J. Tamayo, M. Alvarez, and L. M. Lechuga, "Digital tuning of the quality factor of micromechanical resonant biological detectors," *Sensors and Actuators B: Chemcial*, vol. 89, pp. 33–39, 2003.

[155] E. Colinet, J. Juillard, S. Guessab, and R. Kielbasa, "Actuation of resonant MEMS using short pulsed forces," *Sensors and Actuators A: Physical*, vol. 115, pp. 118–125, 2004.

[156] R. Sunier, Y. Li, K.-U. Kirstein, T. Vancura, H. Baltes, and O. Brand, "Resonant magnetic field sensor with frequency output," in *Proceedings of the MEMS Conference*, 2005, pp. 339–342.

[157] A. Mehta, S. Cherian, D. Hedden, and T. Thundat, "Manipulation and controlled amplification of brownian motion of microcantilever sensors," *Applied Physics Letters*, vol. 78, no. 11, pp. 1637–1639, 2001.

[158] A. Vidic, D. Then, and C. Ziegler, "A new cantielver system for gas and liquid sensing," *Ultramicroscopy*, vol. 97, pp. 407–416, 2003.

[159] J. Tamayo, "Study of the noise of micromechanical oscillators under quality factor enhancement via driving force control," *Journal of Applied Physics*, vol. 97, p. 044903, 2005.

[160] U. Dürig, H. R. Steinauer, and N. Blanc, "Dynamic force microscopy by means of the phase-controlled oscillator method," *Journal of Applied Physics*, vol. 82, no. 8, pp. 3641–3651, 1997.

[161] T. R. Albrecht, P. Grütter, D. Horne, and D. Rugar, "Frequency modulation detection using high-Q cantilevers for enhanced force microscope sensitivity," *Journal of Applied Physics*, vol. 69, no. 2, pp. 668–673, 1991.

[162] J. Tamayo, M. Calleja, D. Ramos, and J. Mertens, "Underlying mechanisms of the self-sustained oscillation of a nanomechanical stochastic resonator in a liquid," *Physical Review B*, vol. 76, p. 180201, 2007.

[163] S. Schmid, P. Senn, and C. Hierold, "Electrostatically actuated nonconductive polymer microresonators in gaseous and aqueous environment," *Sensors and Actuators: A. Physical*, vol. 145-146, pp. 442–448, 2008.

[164] U. Tietze and C. Schenk, *Halbleiterschaltungstechnik*. Springer, 2002.

[165] M. K. Ghatkesar, T. Braun, V. Barwich, J.-P. Ramseyer, C. Gerber, M. Hegner, and H. P. Lang, "Resonating modes of vibrating microcantilevers in liquid," *Applied Physics Letters*, vol. 92, no. 4, p. 043106, 2008.

[166] A.-S. Rollier, B. Legrand, D. Collard, and L. Buchaillot, "The stability and pull-in voltage of electrostatic parallel-plate actuators in liquid solutions," *Journal of Micromechanics and Microengineering*, vol. 16, pp. 794–801, 2006.

[167] N. M. Alford, J. Breeze, X. Wang, S. Penn, S. Dalla, S. Webb, N. Ljepojevic, and X. Aupi, "Dielectric loss of oxide single crystals and polycrystalline analogues from 10 to 320 K," *Journal of the European Ceramic Society*, vol. 21, pp. 2605–2611, 2001.

[168] N. V. Lavrik, M. J. Sepaniak, and P. G. Datskos, "Cantilever transducers as a platform for chemical and biological sensors," *Review of Scientific Instruments*, vol. 75, no. 7, pp. 2229–2253, 2004.

[169] Y. Arntz, J. D. Seelig, H. P. Lang, J. Zhang, P. Hunziker, J. P. Ramseyer, E. Meyer, M. Hegner, and C. Gerber, "Label-free protein assay based on a nanomechanical cantilever array," *Nanotechnology*, vol. 14, pp. 86–90, 2003.

[170] R. Marie, H. Jensenius, J. Thaysen, C. B. Christensen, and A. Boisen, "Adsorption kinetics and mechanical properties of thiol-modified DNA-oligos on gold investigated by microcantilever sensors," *Ultramicroscopy*, vol. 91, no. 1-4, pp. 29–36, 2002.

[171] P. Bergese, E. Bontempi, M. Chiari, P. Colombi, F. Damin, L. E. Depero, G. Oliviero, G. Pirri, and M. Zucca, "Investigation of a biofunctional polymeric coating deposited onto silicon microcantilevers," *Applied Surface Science*, vol. 253, pp. 4226–4231, 2007.

[172] M. Calleja, J. Tamayo, M. Nordström, and A. Boisen, "Low-noise polymeric nanomechanical biosensors," *Applied Physics Letters*, vol. 88, p. 113901, 2006.

[173] M. Nordström, S. Keller, M. Lillemose, A. Johansson, S. Dohn, D. Haefliger, G. Blagoi, M. Havsteen-Jakobsen, and A. Boisen, "SU-8 cantilevers for bio/chemical sensing; fabrication, characterisation and development of novel read-out methods," *Sensors*, vol. 8, pp. 1595–1612, 2008.

[174] G. Blagoi, S. Keller, A. Johansson, A. Boisen, and M. Dufva, "Functionalization of SU-8 photoresist surfaces with IgG proteins," *Applied Surface Science*, vol. 255, pp. 2896–2902, 2008.

[175] R. Gabl, H.-D. Feucht, H. Zeininger, G. Eckstein, M. Scheiter, R. Priming, D. Pitzer, and W. Wersing, "First results on label-free detection of DNA and protein molecules using a novel integrated sensor technology based on gravimetric detection principles," *Biosensors and Bioelectronics*, vol. 19, pp. 615–620, 2004.

[176] R. Raiteri, M. Grattarola, H.-J. Butt, and P. Skladal, "Micomechanical cantilever-based biosensors," *Sensors and Actuators B: Chemical*, vol. 79, pp. 115–126, 2001.

[177] S.-F. Cheng and L.-K. Chau, "Colloidal cold-modified optical fiber for chemical and biochemical sensing," *Analytical Chemistry*, vol. 75, no. 1, pp. 16–21, 2003.

[178] F. Vollmer, D. Braun, A. Libchaber, M. Koshsima, I. Teraoka, and S. Arnold, "Protein detection by optical shift of a resonant microcavity," *Applied Physics Letters*, vol. 80, no. 21, pp. 4057–4059, 2002.

[179] N. Nath and A. Chilkoti, "Label-free biosensing by surface plasmon resonance of nanoparticles on glass: optimization of nanoparticle size," *Analytical Chemistry*, vol. 76, no. 18, pp. 5370–5378, 2004.

[180] W. Y., W. Qian, Y. Tan, and S. Ding, "A label-free biosensor based on gold nanoshell monolayers for monitoring biomolecular interactions in diluted whole blood," *Biosensors and Bioelectronics*, vol. 23, pp. 1166–1170, 2008.

[181] V. S.-Y. Lin, K. Motesharei, K.-P. S. Dancil, M. J. Sailor, and M. R. Ghadiri, "A porous silicon-based optical interferometric biosensor," *Science*, vol. 278, pp. 840–843, 1997.

[182] L. Movileanu, S. Howorka, O. Braha, and H. Bayley, "Detecting protein analytes that modulate transmembrane movement of a polymer chain within a single protein pore," *Nature Biotechnology*, vol. 18, pp. 1091–1095, 200.

[183] Y. Cui, Q. Wei, H. Park, and C. M. Lieber, "Nanowire nanosensors for highly sensitive and selective detection of biological and chemical species," *Science*, vol. 2939, pp. 1289–1292, 2001.

[184] N. Elfström and J. Linnros, "Biomolecule detection using a silicon nanoribbon: Accumulation mode versus inversion mode," *Nanotechnology*, vol. 19, p. 235201, 2008.

[185] J. Lund, R. Mehta, and B. A. Parviz, "Label-free direct electronic detection of biomolecules with amorphous silicon nanostructures," *Nanomedicine: Nanotechnology, Biology, and Medicine*, vol. 2, pp. 230–238, 2006.

[186] M. Shim, N. W. S. Kam, R. J. Chen, Y. Li, and H. Dai, "Functionalization of carbon nanotubes for biocompatibility and biomolecular recognition," *Nano Letters*, vol. 2, no. 4, p. 285288, 2002.

[187] R. J. Chen, S. Bangsaruntip, K. A. Drouvalakis, N. W. S. Kam, M. Shim, Y. Li., W. Kim, P. J. Utz, and H. Dai, "Noncovalent functionalization of carbon nanotubes for highly specific electronic biosensors," *Proceedings of the National Academy of Sciences*, vol. 100, no. 9, pp. 4984–4989, 2003.

[188] R. Sandberg, W. Svendsen, K. Mølhave, and A. Boisen, "Temperature and pressure dependence of resonance in multi-layer microcantilevers," *Journal of Micromechanics and Microengineering*, vol. 15, pp. 1454–1458.

[189] J. E. Sader, "Frequency response of cantilver beams immersed in viscous fluids with applictions to the atomic force microscope," *Journal of Applied Physics*, vol. 84, no. 1, pp. 64–76, 1998.

[190] C. P. Green and J. E. Sader, "Frequency resonse of cantilever beams immersed in viscous fluids near a solid surface with applications to the atomic force microscope," *Journal of Applied Physics*, vol. 98, p. 114913, 2005.

[191] T. Naik, E. K. Longmire, and S. C. Mantell, "Dyanmic response of a cantilever in liquid near a solid wall," *Sensors and Actuators A: Physical*, vol. 102, pp. 240–254, 23.

[192] S. Basak, A. Raman, and S. V. Garimella, "Hydrodynamic loading of microcantilevers vibrating in viscous fluids," *Journal of Applied Physics*, vol. 99, p. 114906, 2006.

[193] M. Gonzalez, C. E. Argarana, and G. D. Fidelio, "Extremly high thermal stability of streptavidin and avidin upon biotin binding," *Biomolecular Engineering*, vol. 16, pp. 67–72, 1999.

[194] A. Johansson, "SU-8 cantilever sensor with integrated readout," Ph.D. dissertation, Technical University of Denmark, 2006.

[195] Y. Pazy, Y. Eisenberg-Domovich, O. H. Laitinen, M. S. Kulomaa, E. A. Bayer, M. Wilchek, and O. Livnah, "Dimer-tetramer transition between solution and crystalline states of streptavidin and avidin mutants," *Journal of Bacteriology*, vol. 185, pp. 4050–4046, 2006.

[196] F. M. Aslan, Y. Yu, S. Vajda, S. C. Mohr, and C. . R. Cantor, "Engineering a novel, stable dimeric streptavidin with lower isoelectric point," *Journal of Biotechnology*, vol. 128, pp. 213–225, 2007.

[197] D. Ramos, J. Tamayo, J. Mertens, M. Calleja, and A. Zaballos, "Origin of the response of nanomechanical resonators to bacteria adsorption," *Journal of Applied Physics*, vol. 100, p. 106105, 2006.

[198] A. K. Gupta, P. R. Nair, D. Akin, M. R. Ladisch, S. Broyles, M. A. Alam, and R. Bashir, "Anomalous resonance in a nanomechanical biosensor," *Proceedings of the National Academy of Sciences (PNAS)*, vol. 103, no. 36, pp. 13 362–13 367, 2006.

[199] N. Scuor, P. Gallina, O. Sbaizero, H. V. Panchawagh, and R. L. Mahajan, "Dynamic characterization of MEMS cantilevers in liquid environment using a low-cost optical system," *Measurement Science Technology*, vol. 17, pp. 173–180, 2006.

[200] A. Holmberg, A. Blomstergren, O. Nord, M. Lukacs, J. Lundeberg, and M. Uhlen, "The biotin-streptavidin interaction can be reversibly broken using water at elevated temperatures," *Electrophoresis*, vol. 26, pp. 501–510, 2005.

[201] W. Shu, E. D. Laue, and A. A. Seshia, "Investigation of biotin-streptavidin binding interactions using microcantilever sensors," *Biosensors and Bioelectronics*, vol. 22, pp. 2003–2009, 2007.

[202] C. T.-C. Nguyen and R. T. Howe, "An integrated CMOS micromechanical resonator high-Q oscillator," *IEEE Journal of Solid-State Circuits*, vol. 34, no. 4, pp. 440–455, 1999.

[203] N. Yazdi, H. Kulah, and K. Najafi, "Precision readout circuits for capacitive microaccelerometers," in *Proceedings of IEEE Sensors*. IEEE, 2004, pp. 28–31.

[204] B. E. Boser, "Electronics for micromachined inertial sensors," in *Proceedings of the Transducers 97*, 1997, pp. 1169–1172.

[205] M. B. Sayir, J. Dual, and S. Kaufmann, *Ingenieurmechanik*. Teubner, 2004-2005.

[206] L. Meirovitch, *Elements of Vibration Analysis*. McGraw-Hill Internationl Editions, 1986.

[207] E. Ventsel and T. Krauthammer, *Thin plates and shells : theory, analysis, and applications*. New York : Marcel Dekker, 2001.

[208] C. W. MacGregor, "Deflection of a long helical gear tooth," *Mechanical Engineering*, vol. 57, pp. 225–227, 1935.

[209] A. Glück, W. Halder, G. Lindner, H. Müller, and P. Weindler, "PVDF-excited resonance sensors for gas flow and humidity measurements," *Sensors and Actuators B: Chemical*, vol. 18/19, pp. 554–557, 1994.

Acknowledgements

First of all, I would like to thank Prof. Christofer Hierold for the possiblity to perform this work at the group of Micro and Nanosystems. I thank my enthusiastic students who successfully worked for my project. Namely these are Pablo Stefan Dörig, Andreas Leimbacher, Yves Leiner, Philipp Senn, Pedro Thomi and Philip Wägli. I also would like to say thank you to all members and former members of the Micro and Nanosystems group for the pleasing atmosphere.

I gratefully acknowledge Tsuyoshi Koyama from Prof. Sanjay Govindjee's group for his support with HiQLab. Many thanks go to Prof. Herbert Shea from LMTS: Microsystems for Space Technologies Laboratory at the EPFL who let me perform my first vibration measurements at his laboratory. Thank you Ivo Zemp from Prof. Dr. Ulrike Kutay's group at the Institute of Biochemistry at ETH Zurich for the biochemistry discussion. I highly acknowledge the support in the electronic readout design of Prof. Bernhard Boser from the University of California at Berkeley. I also would like to thank Dominik Hassler from Prof. Dr. Johann Walter Kolar's group (Power Electronic Systems Laboratory) at the Departement Informationstechnologie und Elektrotechnik at ETH Zurich for the hot-air soldering of the surface mounted devices. I highly appreciate the help of Hansruedi Benedickter from Prof. Colombo Bolognesi's group for the transimpedance measurements. I would like to thank Ueli Marti from IMES ETH Zurich for the help in realizing the electronic feedback circuit. Furthermore, I also thank Prof. Mazza from the IMES ETH Zurich for the discussion about the model based analysis for the evaluation of the Youngs' modulus.

Last but not least, I would like to thank my family and my friends for their mental support and distraction when needed.

This project has been financed by the Swiss National Science Foundation (Project No. 200020-113350/1 and 200021-103954/1).

Publications

Journal Papers & Conference Proceedings

P1 R. Marie, S. Schmid, A. Johansson, L. Ejsing, M. Nordström, D. Häfliger, C. B. V. Christensen, A. Boisen and M. Dufva, Immobilisation of DNA to polymerised SU-8 photoresist", *Biosensors & Bioelectronics*, vol. 21, pp. 1327-1332, 2006.

P2 S. Schmid and C. Hierold, "Two Sacrificial Layer Techniques for the Fabrication of Freestanding Polymer Micro Structures", *in Proceedings of the 17th Workshop on Micromachining, Micromechanics and Microsystems (MME06)*, 2006.

P3 S. Schmid, M. Wendlandt, D. Junker, and C. Hierold, "Nonconductive Polymer Microresonators Actuated by the Kelvin Polarization Force", *Applied Physics Letters*, vol. 89, pp. 163506/1-3, 2006.

P4 S. Schmid, P. Senn and C. Hierold, "Electrostatically actuated nonconductive polymer microresonators with amplified quality factor in gaseous and aqueous environment", *in Proceedings of the TRANSDUCERS & EUROSENSORS 07: The 14th international conference on solid-state sensors, actuators and microsystems*, 2007, vol. 1, pp. 443-446.

P5 S. Schmid, P. Senn and C. Hierold, "Electrostatically actuated nonconductive polymer microresonators in gaseous and aqueous environment", *Sensors and Actuators A: Physical*, vol. 145-146, pp. 442-448, 2008.

P6 S. Schmid, A. Leimbacher and C. Hierold, "Integrated Dynamic Mechanical Testing of Polymer Micro Structures", *in Proceedings of the euspen International Conference*, 2008, vol. 2, pp. 473-477.

P7 S. Schmid, P. Wägli and C. Hierold, "All-Polymer Microstring Resonant Humidity Sensor with Enhanced Sensitivity due to Change of Intrinsic Stress", *in Proceedings of the EUROSENSORS XXII*, 2008, pp. 697-700.

P8 S. Schmid and C. Hierold, "Damping mechanisms of single-clamped and prestressed double-clamped resonant polymer microbeams", *Journal of Applied Physics*, vol. 104, pp. 093516/1-12, 2008.

P9 S. Schmid, P. Wägli, and C. Hierold, "Biosensor based on all-polymer resonant microbeams", *in Technical Digest of the MEMS Conference*, 2009, pp. 300-303.

P10 M. Suter, S. Graf, O. Ergeneman, S. Schmid, A.Camenzind, B. J. Nelson and Ch.Hierold, "Superparamagnetic Photosensitive Polymer Nanocomposite for Microactuators", *Transducers 2009: The 15th international conference on solid-state sensors, actuators and microsystems*, , Denver, CO, USA, June 21-25, 2009, pp. 869-872.

P11 S. Schmid, S. Kühne, and C. Hierold, "Influence of air humidity on polymeric microresonators", *Journal of Micromechanics and Microengineering*, vol. 19, pp. 065018 (9pp), 2009.

Talks

T1 *Micro Actuators Made of Polymer Materials Driven by the Net Electromechanical Force Resulting from Electric Field Nonuniformities*, Seminar Talk at the group of Micro and Nanosystems ETH Zurich, Switzerland (2004).

T2 *Non-Conductive Polymer Microresonators Actuated by the Kelvin Polarization Force*, Seminar Talk at the group of Micro and Nanosystems ETH Zurich, Switzerland (2006).

T3 *Towards Total Polymer Microsystems: Micro Actuators for the Characterization of Micro Mechanical Properties of Polymers under Dynamic Load Conditions*, Seminar Talk at the group of Micro and Nanosystems ETH Zurich, Switzerland (2005).

T4 *Dynamic mechanical measurements of SU-8 micro beams*, Seminar Talk at the group of Micro and Nanosystems ETH Zurich, Switzerland (2007).

T5 *Dynamic Mechanical Testing of Polymer Microstructures*, Invited Talk at the 6th MEMUNITY - Worshop Grenoble, France (2007).

T6 *Electrostatically actuated nonconductive polymer microresonators with amplified quality factor in gaseous and aqueous environment*, Transducers'07 & Eurosensors XXI in Lyon, France (2007).

T7 *Dynamic mechanical characterization of polymer microbeams and their application as resonant sensors*, Seminar Talk at the group of Micro and Nanosystems ETH Zurich, Switzerland (2008).

T8 *All-Polymer Microstring Resonant Humidity Sensor with Enhanced Sensitivity due to Change of Intrinsic Stress*, Eurosensors XXII in Dresden, Germany (2008).

T9 *Electrostatically Actuated All-Polymer Microbeam Resonators: Characterization and Application*, Seminar Talk at the group of Micro and Nanosystems ETH Zurich, Switzerland (2008).

T10 *Characterization of Electrostatically Actuated All-Polymer Microbeam Resonators*, Invited Talk at the Micro and Nano Systems Laboratory, Tel Aviv University, Israel (2009).

CV

Personal details

Born: March 17, 1977 — Lucerne, Switzerland
Nationality: Swiss
Civil status: unmarried

Education

2004–2009 **PhD** at ETH Zurich, Switzerland
Dissertation at the Chair of Micro and Nanosystems

1998–2003 **Mechanical engineer** at ETH Zurich, Switzerland (Dipl. Ing. ETH)

Diploma thesis performed at the Institute of Micro and Nanotechnology, Technical University of Denmark, Copenhagen: *"Immobilization of DNA and protein to polymerized SU-8 photoresist investigated with microarray assays"*

Semester thesis performed at the Nanotechnology Group, ETH Zurich: *"Dielectrophoretic Tweezers"*

Semester thesis performed at the Center for Product Development, ETH Zurich: *"Realisierung interaktiver Formeln innerhalb des e-learning Umfeldes thekey"*

1990–1997 **High School** at Kantonsschule Hochdorf and Reussbühl, Switzerland

---

Language Skills

German: native, **English**: fluent, **French**: Seven years school knowledge, basic

---

Working Experience

2004–2009 **Research and teaching assistant**, Chair of Micro and Nanosystems, ETH Zurich
Secured CHF 150'000.- funding for polymer MEMS research projects.
Supervision of 4 master theses, 4 semester theses and 1 scientific assistant.

2000–2003 **Team leader development**, Triloga Knowledge AG, Switzerland, part-time
SCODi 4P: Java based tool for corporate management (process-, personal-, product- and project-management)

1998 **Software developer**, Triloga Knowledge AG, Switzerland, 7 months
Web programming, interface design

1997–2002 **Webdesigner** as a freelancer, part-time
Website design and programming (dynamic HTML, databases server-side scripting)
